Springer Proceedings in Materials

Saluru Baba Krupanidhi
Vinay Gupta
Anjali Sharma Kaushik
Anjani Kumar Singh *Editors*

Advanced Functional Materials and Devices

Select Proceedings of AFMD 2021

Springer

Springer Proceedings in Materials

Volume 14

Springer Proceedings in Materials publishes the latest research in Materials Science and Engineering presented at high standard academic conferences and scientific meetings. It provides a platform for researchers, professionals and students to present their scientific findings and stay up-to-date with the development in Materials Science and Engineering. The scope is multidisciplinary and ranges from fundamental to applied research, including, but not limited to:

- Structural Materials
- Metallic Materials
- Magnetic, Optical and Electronic Materials
- Ceramics, Glass, Composites, Natural Materials
- Biomaterials
- Nanotechnology
- Characterization and Evaluation of Materials
- Energy Materials
- Materials Processing

To submit a proposal or request further information, please contact one of our Springer Publishing Editors according to your affiliation:

European countries: **Mayra Castro** (mayra.castro@springer.com)
India, South Asia and Middle East: **Priya Vyas** (priya.vyas@springer.com)
South Korea: **Smith Chae** (smith.chae@springer.com)
Southeast Asia, Australia and New Zealand: **Ramesh Nath Premnath** (ramesh.premnath@springernature.com)
The Americas: **Michael Luby** (michael.luby@springer.com)
China and all the other countries or regions: **Mengchu Huang** (mengchu.huang@springer.com)

More information about this series at https://link.springer.com/bookseries/16157

Saluru Baba Krupanidhi · Vinay Gupta ·
Anjali Sharma Kaushik · Anjani Kumar Singh
Editors

Advanced Functional Materials and Devices

Select Proceedings of AFMD 2021

Springer

Editors
Saluru Baba Krupanidhi
Indian Institute of Science Bangalore
Bengaluru, India

Anjali Sharma Kaushik
Department of Physics
Atma Ram Sanatan Dharma College
University of Delhi
New Delhi, India

Vinay Gupta
Department of Physics and Astrophysics
University of Delhi
New Delhi, India

Anjani Kumar Singh
Department of Physics
Atma Ram Sanatan Dharma College
University of Delhi
New Delhi, India

ISSN 2662-3161 ISSN 2662-317X (electronic)
Springer Proceedings in Materials
ISBN 978-981-16-5970-6 ISBN 978-981-16-5971-3 (eBook)
https://doi.org/10.1007/978-981-16-5971-3

This Springer imprint is published by the registered company Springer Nature Singapore Pte Ltd.
The registered company address is: 152 Beach Road, #21-01/04 Gateway East, Singapore 189721, Singapore

This book is dedicated to Late Prof. Vinay Gupta

Organizers

Partner

Springer Nature

Editorial Board

Prof. Saluru Baba Krupanidhi
Prof. Vinay Gupta
Dr. Anjali Sharma Kaushik
Dr. Anjani Kumar Singh

Patrons

Prof. Pradeep Burma
Prof. Prem Lal Uniyal

Chairman

Dr. Gyantosh Kumar Jha, (Principal, ARSD College)

International Advisory Board

Prof. Vinay Gupta, University of Delhi
Prof. S. Murugavel, University of Delhi
Dr. Shekhar Mande, Director, CSIR
Dr. Seema Vinayak, Director, SSPL-DRDO
Dr. A. K. Aswal, Director, NPL
Dr. H. B. Srivastava, Director, LASTEC-DRDO
Dr. Ashutosh Sharma, Secretary, DST
Dr. Hiro Amekura, NIMS, Ibaraki, Japan
Prof. Milan Radovic, PSI, Switzerland
Prof. Amar Bhalla, UTSA, USA
Prof. Ruyan Guo, UTSA, USA
Prof. Saluru Baba Krupanidhi, IISC Bangalore
Prof. S. Annapoorni, University of Delhi
Dr. Manoj Sharma, CEO, STARC, Bangalore

National Advisory Board

Dr. D. Kanjilal, Director, IUAC
Dr. O. P. Thakur, NSUT, Delhi
Prof. Kedar Singh, JNU, Delhi
Dr. Shiv Kumar, SSPL-DRDO
Dr. Monika Tomar, Miranda House, University of Delhi
Dr. P. K. Jha, DDU, University of Delhi
Dr. Fouran Singh, IUAC, Delhi
Dr. Ajay Agarwal, CEERI Pilani
Dr. Bipin Kumar Gupta, NPL, Delhi
Dr. A. L. Sharma, Central University of Punjab
Dr. Ashok Kumar, NPL, Delhi
Dr. Renu Sharma, SSPL-DRDO
Prof. S. S. Islam, Jamia Millia Islamia University
Prof. S. K. Dhawan, Emeritus, NPL, Delhi
Dr. Ravinder Pal, SSPL-DRDO
Dr. Shibu Saha, NPL, Delhi
Dr. H. K. Mallik, IIT Delhi

Convener

Dr. Vinta Tuli

Organizing Secretaries

Dr. Anjali Sharma Kaushik
Dr. Raghvendra
Dr. Anjani Kumar Singh
Dr. Shankar Subramanian
Dr. Manish Kumar
Mr. Mohd. Sadiq

Finance Committee

Convener
Ms. Swati
Co-conveners
Dr. Rakesh Malik
Dr. Rita Singh

Publication Committee

Convener
Dr. Ashutosh Vishwa Bandhu
Co-conveners
Dr. Avanish Pratap Singh
Dr. Arvind Kumar

Oral Session Committee

Convener
Dr. Manisha
Co-conveners
Dr. Yogesh Kumar
Dr. Rajveer Singh

Technical Programme Committee

Convener
Dr. Devender Rana
Co-conveners
Mr. Ashok
Mr. Bhupender Singh
Dr. B. L. Prashant

Poster Session Committee

Convener
Mr. Lalit Kumar
Co-conveners
Dr. Amit Kumar
Dr. Abid Hussain

Local Organizing Committee

Dr. Pinky Dureja
Dr. Nutan Mishra
Dr. Geeta Sanon
Dr. Pankaj Narang
Mr. Pravata Kumar Behera

Session Chairs

Dr. Vinita Tuli
Dr. Anjali Sharma Kaushik
Dr. Anjani Kumar Singh
Mr. Sadiq
Dr. Raghvendra
Dr. Manish Kumar
Dr. Manisha
Dr. S. Shankar
Dr. Ashutosh Vishwabandhu
Dr. Arvind Kumar
Dr. Avanish Pratap Singh

Dr. Yogesh
Dr. Lokesh Rana
Dr. Abid
Dr. Amit
Ms. Swati
Dr. Rakesh Malik
Mr. Lalit
Dr. Rita
Dr. Kajal Jindal
Dr. Ayushi Paliwal
Dr. Rajveer Singh
Dr. Devender Rana
Mr. Bhupendra

Foreword

I would like to congratulate the Department of Physics for the successful organization of three-day online International Conference on "*Advanced Functional Materials and Devices (AFMD 2021)*" under the IQAC. The department has been at the forefront in research activities in college, and this new endeavour has proved to highlight their commitment to the same.

Atma Ram Sanatan Dharma College has become synonymous with equity and excellence in the last few years. Established in 1959, the college underwent upheaval and transformation in the post-independence years. Yet, the ability to adapt while holding onto one's cultural identity, built into its foundations early on, has held ARSD in good stead. A NAAC-accredited A-grade institution and holding NIRF All India Rank of 13, the college stands testament to this community's dedication towards creating an educational ecosystem that is holistic and all-embracing. In the last five years, the college has gone from strength to strength, developing existing facilities to maximize their potential and keep pace with rapid shifts in the global economy. ARSD is evolving into an excellent centre for research. The departments of physics, chemistry, biology and mathematics are funded by the Department of Biotechnology, GOI, under the Star College Scheme, attesting to the high quality of work being undertaken at the campus. The establishment of the DBT Science Centre in addition to the Centre for Innovation and Entrepreneurial Leadership (CIEL) in collaboration with M/oMSME, a first for any University of Delhi college, showcases ARSD's commitment to research and innovation. The college has been the recipient of several prestigious grants and is fast emerging as a hub of research. The aim of ARSD College is, therefore, to produce bright young minds in synergy with their ecosystem and maximizing their potential in an ethically sound manner. I wish this institution the very best and hope it continues to light the way towards the creation of a knowledge society.

AFMD 2021 was enriched with 20 invited lectures from eminent researchers and also received 94 abstracts for oral and poster presentations from all over the world. The conference began with the inaugural ceremony by respected Guests of Honour, Prof. Vinay Gupta (Dean, FOT, University of Delhi); Prof. Prem Lal Uniyal, Treasurer, ARSD College; and Chief Guest, Prof. Pradeep Burma, Chairman, ARSD

College followed by a plenary talk by Prof. R. S. Katiyar, University of Pureto Rico, USA. I would like to thank all the invited speakers and participants for sharing their valuable knowledge and research work on this platform. The theme of the conference was very relevant to the present day of technology. Researchers from each and every corner of the globe are working very efficiently in the advancement of the technology for the benefit of the common people.

I am happy to announce that this proceeding book is the outcome of the papers received in AFMD 2021. I would like to congratulate all the authors whose papers have been selected for the publication. My sincere gratitude to the respected reviewers and editors for putting their efforts and time. The editorial board of this proceeding book was led by renowned researchers Prof. Saluru Baba Krupanidhi (Emeritus Scientist, IISc Bangalore) and Late Prof. Vinay Gupta (Professor, University of Delhi). I thank both Prof. Krupanidhi and Prof. Gupta for their valuable cooperation. I really appreciate the hard work of other editors Dr. Anjali Sharma Kaushik and Dr. Anjani Kumar Singh for giving shape to this book. At last, I appreciate the convener of the conference, Dr. Vinita Tuli, and the organizing team for the grand success of AFMD 2021. I wish them all the very best for future endeavours and may many such more feathers of accomplishments be added in their hat of success.

Coming together is a beginning. Keeping together is progress. Working together is success.

June 2021

Gyantosh Kumar Jha
Principal, Atma Ram Sanatan Dharma College
University of Delhi
New Delhi, India

Preface

The book titled *Advances in Functional Materials* presents the selected proceedings of the International Conference on "Advanced Functional Materials and Devices" (AFMD 2021). AFMD 2021 was organized by the Department of Physics and Internal Quality Assurance Cell of Atma Ram Sanatan Dharma College, University of Delhi, New Delhi, India, from 3 to 5 March 2021 via online mode. Papers published in this book highlight the advancements in functional materials which include electronic, magnetic, optical, adaptive, dielectric materials, etc., that are required to develop new functionalities with better performance in the present era based on technology. The topics covered include the knowledge of a wide range of materials for energy harvesting, biomedical applications, environmental monitoring, photonics and opto-electronic devices, strategic applications and high energy physics. This book can be a valuable addition reference for beginners, researchers, and academicians regarding the new functional materials for device applications.

The conference consisted of invited as well as technical sessions along with the discussions with eminent speakers covering a wide range of topics: multifunctional materials, 2D materials, biomaterials, materials for environmental studies, DFT and solar simulation of materials, perovskite and double perovskite materials, luminescent materials, smart materials, materials for energy conversion and storage, smart materials, advanced functional materials, polymeric materials, composites, liquid crystals, materials for sustainable development, nanomaterials and thin films, smart devices and quantum dot synthesis technique, and characterization tools with application in smart devices. On this occasion, one plenary speaker, 2 keynote speakers and 20 invited speakers delivered their outstanding research works in various fields of material science. There were 54 oral presentations and about 40 poster presentations by participants which brought great opportunity to share their recent research work among each other graciously.

A total of 94 abstract submissions were received from all over the world including countries like Singapore, USA, Mexico, Iran, South Korea, Japan, etc., from which 62 full-paper submissions materialized. All papers were reviewed by two experts in the field, and after intense review, only 33 papers were accepted for the publication. This proceeding book mainly focuses on the material science, but few papers are

from nuclear and particle physics also as the scope of the conference. Efforts taken by peer reviewers in the form of constructive critical comments, improvements and corrections to the authors contributed to improve the quality of papers which is gratefully appreciated. Our sincere gratitude to all the authors who submitted papers because of which the conference became a story of success.

We hope the papers published in the proceeding book will not only expand readers' knowledge but also open a new platform for research to grow. Last but not least, we thank the respected editors, International/National Advisory Committees, session chairs, programme committee members and external reviewers, who invested time and effort in the selection process to ensure the scientific quality of the programme. We also thank Springer Nature for their support towards our journey of success. Their support was not only the strength but also an inspiration for organizers.

Bengaluru, India — Saluru Baba Krupanidhi
New Delhi, India — Vinay Gupta
New Delhi, India — Anjali Sharma Kaushik
New Delhi, India — Anjani Kumar Singh

Contents

About the Editors

Prof. Saluru Baba Krupanidhi is a materials scientist who integrates in an exemplary manner fundamental science with engineering of materials and devices. He has worked as Professor at Indian Institute of Science, Bangalore for more than 22 years. At present he is serving as Emeritus Professor at IISc. He is internationally recognized in the areas of integrated ferroelectrics and compound semiconductor technology as evidenced by invited lectures at international meetings and memberships of editorial boards. Professor Krupanidhi's research is focused on developing expitaxial thin films of complex oxides for electro-optic, ferroelectric, and high permittivity dielectric applications and hetero epitaxial compound semiconductors for opto-electronic applications. His major contributions in the area of complex perovskites include ECR plasma assisted development of low temperature epitaxy, rapid thermal processing, modeling of crystallization in perovskite thin films under strong thermal gradients, and engineered properties in the superlattices of ferroelectric peroksites. Professor S. B. Krupanidhi has been honored with many awards and positions like 2 Engineering Invention Awards at Motorola, USA (1986), MRSI Medal, India (1997), Fellow of Indian Academy of Sciences (2003), VASVIK Medal (2004), MRSI Superconductivity-Materials Science Award (2004), Tatachem Chair Professor, Indian Institute of Science (2006), Rustum Choksi medal for research excellence, IISc (2006) J. C. Bose Fellow, DST (2009–2019), Prof. C. N. R. Rao Lecture Prize, MRSI (2010), Fellow of Indian National Science Academy (2012), Fellow of Indian National Academy of Engineering (2012) D. S. Kothari Research Professor (2016–2020), INSA Senior Scientist (Indian Institute of Science) (2018–2021) and MRSI Distinguished Materials Scientist Of The Year Award (2019). He has published more than 600 research papers in journals of high repute. He has also guided more 55 research Scholars who are holding good position in leading institutes.

Prof. Vinay Gupta received the B.Sc., M.Sc., and Ph.D. degrees in physics in 1987, 1989, and 1995, respectively, from the University of Delhi, New Delhi, India. Presently, he is a professor in the Department of Physics and Astrophysics and Dean of Faculty of Science, University of Delhi. His current research area includes semiconductor and surface acoustic wave (SAW) sensors for gas/chemical/radiations/biomolecules, amperiometric/photometric biosensors, surface plasmon resonance (SPR) technique for dielectric studies and sensing applications, micro-fluidics, nanostructured materials, piezoelectric and multiferroic thin films/ceramics for energy harvesting applications, pressure sensors, RF and microwave resonators, photonic devices, non-linear optical studies, SAW devices, MEMS transducers and Microheaters, Molecular Simulations and device modeling. He is engaged towards the development of integrated devices having strategic as well as commercial applications. His research group has successfully integrated piezoelectric ZnO thin film with MEMS structures fabricated by CEERI, India for acoustic sensor as per specification desired by Indian Space Research Organization (ISRO). These Acoustic sensors have been installed in PSLV flights of ISRO from C9—onwards. He has published more than 370 research papers in high impact factor SCI journals. He has been granted one US and 3 Indian patents along with one successful technology transfer of Indigenously developed table top SPR system which is being used in various academic and research institutes. He is an active member of various reputed research societies like IEEE, MRSI, EMSI etc. At present he has project grants of more than Rs. 4 Crores. He is recipient of BOYSCAST fellow, MRSI Medal-2012 presented by Material Research Society of India and also recently received Distinguished Teacher's Award by University of Delhi. Recently he has been ranked amongst top 2% scientists by Stanford Ranking of world's Best Scientist.

Dr. Anjali Sharma Kaushik received her B.Sc., M.Sc. and Ph.D. degrees in Physics in the year 2006, 2008 and 2013, respectively, from University of Delhi. At present, she is serving as Assistant Professor at Atma Ram Sanatan Dharma College, University of Delhi. Her research interests are in gas sensor systems that include sensor characterization and development of metal oxide films for sensor coatings. She is working towards the fabrication of MEMS based electronic-nose for gas sensing applications. Her area of interest also includes the metal oxide based thermoelectric energy harvesters and fabrication of 2D materials like MoS_2 for sensing applications. She is recipient of Dr. G. C. Jain Memorial Award for best Ph.D. thesis by Material Research Society of India in year 2015 and Shri Ram Arora Award at 141st Annual meeting of The Metals, Minerals and Materials Society, Orlando USA in year 2012 for her excellence in Materials and Engineering. She has published more than 55 papers in journals of high repute with h-index of 17 and has published two Indian Patents. She is also working as Co-PI in two DRDO and DST sponsored projects. She is also actively involved in many students and administrative activities of the college.

Dr. Anjani Kumar Singh is an Assistant professorin the Department of Physics, Atma Ram Sanatan Dharma College, University of Delhi. He has done his M.Sc. from UP Autonomous College, Varanasi and Ph.D. from Delhi University in the year 2010. He worked as a Teaching cum Research Fellow at N.S.I.T., New Delhi. During his Ph.D. work and afterwards he has published twenty 22 research papers in peer reviewed international journals and International Conference. He is a life member of The Materials Research Society of India (MRSI). His major research interests are Electrostriction Based Dielectric Materials, Fuel cells.

Electrocatalytic Properties of ZnO Thin Film Based Biosensor for Detection of Uric Acid

Kajal Jindal, Vinay Gupta, and Monika Tomar

Abstract A novel uric acid biosensor employing ZnO thin film as matrix is developed using pulsed laser deposition technique. The dependence of electrocatalytic properties of ZnO thin films on the ZnO processing pressure during growth is studied. It has been observed that the growth kinetics of ZnO matrix play a critical role in governing the electron transfer characteristics of ZnO thin film based biosensors. It is found from the cyclic voltammetric measurements that the peak oxidation current of ZnO/ITO/glass electrode increases with a rise in pressure of ambient gas from 1 to 100 mT and is maximum (548 μA) for ZnO thin film based electrode prepared in an oxygen ambient of 100 mT. The variation in peak current with change in processing pressure is attributed to the change in surface properties, which largely depends on the mean free path and kinetic energy of ablated species arriving at the substrate. The optimized ZnO thin film (100 mT) offers high surface coverage (9.74×10^{-9} mol/cm^2) during immobilization of uric acid resulting in a sensitivity of 122 μA/(mM-cm^2). In addition, the prepared ZnO based biosensor exhibit high affinity towards detection of uric acid (K_m~0.07 mM), low limit of detection (0.01 mM) along a storage stability of more than 20 weeks. Thus, the present work suggests an important role of plume kinetics for the fabrication of ZnO thin film based biosensors.

Keywords Uric acid · Zinc oxide · Biosensor

1 Introduction

Recent years have witnessed a growing trend in the research on biosensors as the development of biosensors has facilitated a common man to keep track of the levels

K. Jindal
Department of Physics, Kirori Mal College, University of Delhi, Delhi 110007, India

V. Gupta
Department of Physics and Astrophysics, University of Delhi, Delhi 110007, India

M. Tomar (✉)
Department of Physics, Miranda House, University of Delhi, Delhi 110007, India

S. B. Krupanidhi et al. (eds.), *Advanced Functional Materials and Devices*, Springer Proceedings in Materials 14, https://doi.org/10.1007/978-981-16-5971-3_1

of various metabolites related to his health at home [1]. Out of the various components of biosensors, Matrix forms the most crucial element as it governs the charge transfer characteristics from the enzyme active center to the electrode. Various literature studies suggest that metal oxide based matrices are preferred due to their high stability, excellent electron communication features, and ease of enzyme immobilization via physical adsorption due to their high isoelectric point (IEP) [2]. Out of the various metal oxide matrices, Zinc oxide (ZnO) has been widely employed for applications in biosensing due to its biocompatible nature, low toxicity, ease of deposition, good electron transfer characteristics, and high IEP for binding of enzymes (~9.0) [3]. It has been used for detection of various bio-analytes in human blood including glucose [4], cholesterol [5], H_2O_2 [6], urea [7], DNA [8], etc. Recently, ZnO finds great applications in development of reagentless biosensors by doping [9], forming *p–n* junction heterostructures [1], or making hybrid composites [10]. Wu et al. [11] have reported a photoelectrochemical and self-powered biosensor based on *p–n* junction of ZnO and Cu_2O. Uddin et al. [12] have reported the development of a chemisensor based on GCE modified with ZnO/RuO_2 NPs for detection of 2-nitrophenol in different water samples. Thus, ZnO forms the constituent of most of the biosensors exhibiting high stability and sensitivity. Particularly, ZnO grown by physical deposition techniques such as pulsed laser deposition (PLD) is exploited for biosensing applications due to the stoichiometric, and nanocrystalline growth of thin films, small turnaround time, good reproducibility and high chemical stability [13]. The electron transfer characteristics of a matrix are strongly dependent on the growth parameters and thus, it is important to critically analyze the role of growth parameters of ZnO thin film on its biosensing response [14]. Despite the fact that ZnO is the most widely used matrix for the development of biosensors, an insight into its growth kinetics in governing its electrocatalytic properties has not been provided in literature.

Uric acid (UA) is chosen as a model analyte in the present work to analyze the critical role of processing parameters of ZnO thin film on its electrocatalytic properties. Uric acid is an important constituent of biofluids including urine and blood serum which is released as a consequence of breakdown of purines [15]. Purine is a key constituent of some common foods and drinks that are consumed in our daily life, such as sweet breads, seafood, meat extracts, dried beans, peas, and beer. A major portion of the uric acid (~70%) in human body dissolves in blood and is transported through the bloodstream to the kidneys which is then degraded with the help of urate oxidase (uricase) enzyme into allantoin and excreted out of the body in the form of urine [16]. Nevertheless, UA level in our human serum can become elevated if our body produces in excess or if it doesn't efficiently dispose it. In human blood, men and women should have a reference range of uric acid between 0.214–0.506 mM and 0.137–0.393 mM respectively [1]. UA levels outside the physiological range on either side can be considered as an alarming sign related to several diseases [9]. Therefore, development of sensitive, selective, cost-effective, and reproducible biosensors for detecting the level of uric acid is the concern of research community. Thus, in the present work, role of growth kinetics in Pulsed

laser deposition technique on the electrocatalytic properties of ZnO thin film based electrode has been studied towards the detection of uric acid.

2 Experimental

Preparation of uric acid biosensor mainly involves the following process steps.

2.1 Preparation of Various Reagents

2.1.1 Electrolyte Solution

Firstly, the electrolyte for electrochemical sensing measurements is prepared. 0.2 M stock solutions of NaH_2PO_4 and Na_2HPO_4 were mixed and phosphate buffer saline (PBS) solution (50 mM) was obtained. 5 mM potassium ferrocyanide $[K_4Fe(CN)_6]$ and potassium ferricyanide $[K_3Fe(CN)_6]$ were added as an external mediator in the PBS solution to facilitate the transfer of electrons from the enzyme active sites to the electrode. The pH of the solution was adjusted by adding 0.9% sodium chloride (NaCl).

2.1.2 Enzyme and Analyte Solutions

Uricase (Ur) (*Candida sp.,* 4.9 U) enzyme was employed as receptor for detection of uric acid (analyte). PBS solution was used to prepare (1 mg/ml) enzyme solutions. To prepare different concentrations of uric acid solution in the range of 0.05–1.0 mM, required amounts of uric acid were dissolved in de-ionized water.

2.2 Preparation of ZnO Based Bioelectrode: Ur/ZnO/ITO/Glass

ITO coated glass (ITO/glass) substrates having dimensions of (2 cm × 1 cm) were taken and cleaned thoroughly. ZnO thin film was grown by PLD (fourth harmonic of Nd:YAG laser; 266 nm, repetition rate = 10 Hz) onto cleaned ITO coated glass substrates via a shadow mask over an area of (1 cm × 1 cm) to obtain ZnO/ITO/glass electrode. Electrochemical measurements were carried out by taking electrical connections from the ITO layer which was covered during ZnO thin film deposition (i.e., remaining 1 cm × 1 cm). A one inch dia. ceramic ZnO target prepared by solid state reaction route is used as described in our previous work

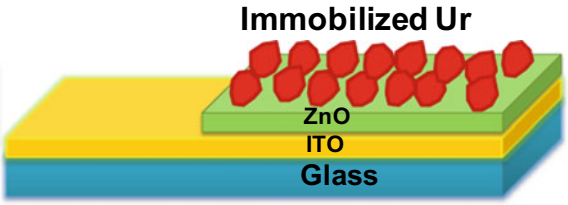

Fig. 1 Schematic of uric acid bioelectrode based on ZnO thin film

[2] to obtain ZnO thin films having a thickness of 90 nm. Ambient pressures (100% O_2) were varied in the range of 1–100 mT to analyze the effect of growth kinetics on biosensing response. In our previous work, it has been reported that the laser fluence influences the defect profile in ZnO films, and native defects are maximum in ZnO thin films deposited at low laser energy density (1.0–1.5 J/cm^2) [17]. Since presence of defects in metal oxide matrix enhanced the electron communication property and are useful for obtaining good biosensing response characteristics [14]; ZnO thin films are grown at low laser fluence (1.2 J/cm^2) in the present work for biosensing applications [17]. Since the ablated species require minimum energy to settle down on the desired nucleating sites on the substrates, ZnO thin films were intentionally deposited without heating the substrates so that large number of defects may be introduced. Uricase is immobilized via physical adsorption by drop casting 10 µl of Ur solution (0.049 Units) on the surface of ZnO/ITO/glass electrode to prepare bioelectrode. Uricase possesses a low IEP $\approx$ 6.06 and is thus easily attached on the surface of ZnO thin film having high IEP (~9.5). The prepared bioelectrode was kept overnight for drying and thereafter rinsed with buffer solution to remove the uricase which was loosely bound. The schematic diagram of the developed bioelectrode is shown in Fig. 1.

3 Results and Discussion

3.1 Characteristics of ZnO Based Uric Acid Bioelectrode

The biosensing response characteristics of all prepared Ur/ZnO/ITO/glass bioelectrodes are investigated using the cyclic voltammetric (CV) measurements which are performed using a Potentiostat/Galvanostat in a three-electrode electrochemical cell configuration (Gamry Inc. 600). Here, Ag/AgCl, Pt foil, and Ur/ZnO/ITO/glass bioelectrode were used as reference, counter, and working electrode respectively. 10 ml PBS solution with a mediator was used as electrolyte (Sect. 2.1).

Developing a matrix is highly critical as it provides the base for the immobilization of enzymes and provides a pathway for the transfer of electrons to the bottom electrode. Since the electron transfer characteristics of the matrix are strongly governed by growth kinetics, it is important to optimize its deposition condition. In the present

work, O_2 gas pressure has been optimized for deposition of ZnO thin film matrix using CV studies.

3.1.1 Effect of Oxygen Gas Pressure for Growth of ZnO Matrix

Different electrodes were prepared for the CV measurements by preparing ZnO thin film at different oxygen gas pressures (1, 10, 50, 100 mT) and under the conditions described in Sect. 2.2. The obtained cyclic voltammograms for ZnO electrodes prepared under different O_2 gas pressures are shown in Fig. 2.

It may be observed from Fig. 2 that CV spectra of ZnO electrodes fabricated at higher pressures (10 to 100 mT) are well defined and exhibit good oxidation and reduction peaks which may be attributed to the presence of $[Fe(CN)_6]^{3-/4-}$ in the buffer solution and serves as a mediating species for the transfer of electrons from enzyme active site to electrode. However, no redox peaks are observed when CV spectra were recorded for ZnO thin film electrode fabricated at an ambient pressure of 1 mT (Fig. 2). The peak oxidation current is found to increase continuously for ZnO/ITO/glass electrodes as ZnO films are fabricated at higher pressure from 10 to 100 mT. The peak value of oxidation current (I_{po}) is plotted by varying processing pressure for ZnO matrix as shown in Fig. 3. The magnitude of I_{po} increases from 160 to 548 μA as the oxygen gas pressure in PLD chamber is raised from 10 to 100 mT (Fig. 3) for deposition of ZnO thin film matrix for electrode.

Since biosensing is a process that predominantly occurs at the surface, roughness of the ZnO matrix surface is important as it provides increased surface area for loading of the enzyme and hence, improved response characteristics. The surface roughness of ZnO thin films grown at different oxygen gas pressures is studied using surface profilometer (Dektak 150A), and its variation is shown in Fig. 4. ZnO thin films grown at lower pressures (1–10 mT) are quite smooth having a low surface roughness of

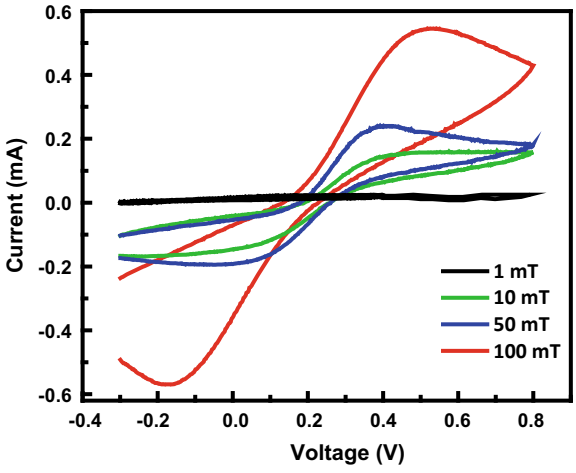

Fig. 2 CV spectra of ZnO based electrodes fabricated at different oxygen gas pressures

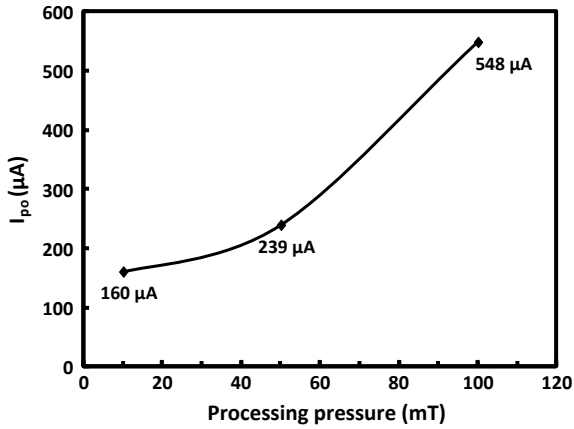

Fig. 3 Variation in peak oxidation current of ZnO/ITO/glass electrode with ZnO thin film prepared at different pressures

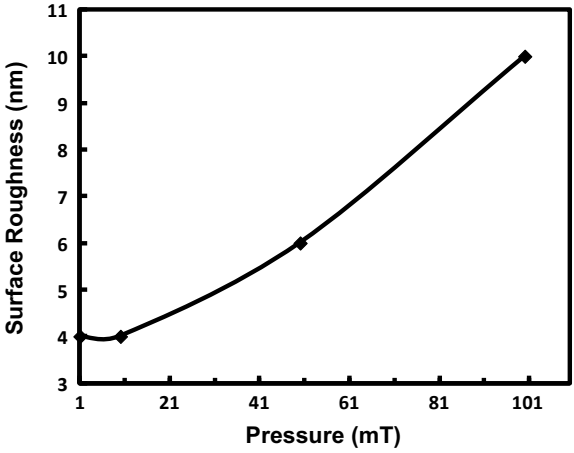

Fig. 4 Variation in surface roughness of ZnO thin film matrix as a function of oxygen pressure

4 nm (Fig. 4) and may be due to large mean free path of species present in plume. Therefore, the ablated species condense on the surface of substrate resulting in the formation of a continuous film with minimal native defects and dense morphology. The dense morphology of the ZnO film at low pressures ($\leq$10 mT) leads to small value of I_{po} with weak CV response (Fig. 2) due to poor electron communication property of ZnO matrix. Surface roughness of ZnO thin film increases significantly to 10 nm as the oxygen gas pressure during film growth is increased to 100 mT (Fig. 4). This is due to the large number of collisions of ablated species with background oxygen gas molecules which results in deposition of ZnO matrix having large amount of native defects and formation of irregular grains with increased surface roughness. The rough microstructure with large defects in ZnO thin film electrode prepared at high processing pressure of 100 mT results in increased value of I_{po} (Fig. 3) due to enhanced charge transfer features, and therefore, it is considered as a suitable matrix

for further study. Thus, it is evident from above studies that growth kinetics of matrix as altered by varying processing pressure play an important role in the development of biosensor and needs to be studied well before the matrix is applied for practical applications.

3.2 Electrochemical Property of Ur/ZnO/ITO/glass Bioelectrode

Uricase (Ur) is immobilized electrostatically over ZnO matrix grown at an optimized processing pressure of 100 mT, and Ur/ZnO/ITO/glass bioelectrode is fabricated as discussed in Sect. 2.2. Figure 5a illustrates the CV spectrums measured for ITO/glass electrode, ZnO/ITO/glass electrode and Ur/ZnO/ITO/glass bioelectrode, and are found to be well defined for all samples. Though the electrical conductivity of ITO is higher than that of ZnO thin film of semiconducting nature, it is important to note from Fig. 5a that the value of I_{po} for ZnO/ITO/glass electrode (548 μA) is much greater as compared to that of bare ITO/glass electrode (178 μA). The obtained high value of I_{po} may be related to the excellent charge conduction taking place through the semiconducting ZnO matrix. The magnitude of I_{po} decreases considerably (Fig. 5a) due to the immobilization of uricase on the electrode (ZnO/ITO/glass) surface (125 μA). The decrease in I_{po} upon immobilization of uricase onto ZnO/ITO/glass electrode (125 μA) is due to the hindrance in the transfer of electrons caused by non-conducting uricase.

3.2.1 pH Studies

pH of buffer solution may largely affect the activity of immobilized enzyme. Thus, the effect of pH of PBS buffer solution on its biosensing response was studied by varying it from 6.0 to 8.0, and the variation in I_{po} for Ur/ZnO/ITO/glass bioelectrode is demonstrated in Fig. 5b. The magnitude of $I_{po} \approx 125$ μA was maximum when pH of buffer solution was set to 7.0 and decreases by reducing and increasing it. Thus, further studies were carried out by maintaining the pH of PBS buffer solution at 7.0.

3.2.2 Effect of Scan Rate

The magnitude of current measured in CV studies for bioelectrodes depends on turnover rate of enzyme, reaction kinetics between redox couple and enzyme, flux of mediator to surface of enzyme, surface coverage of enzyme, and flux of analyte to enzyme surface [18]. Thus, it is important to investigate the kinetics of reaction and surface coverage of uricase on the electrode surface for the development of biosensor.

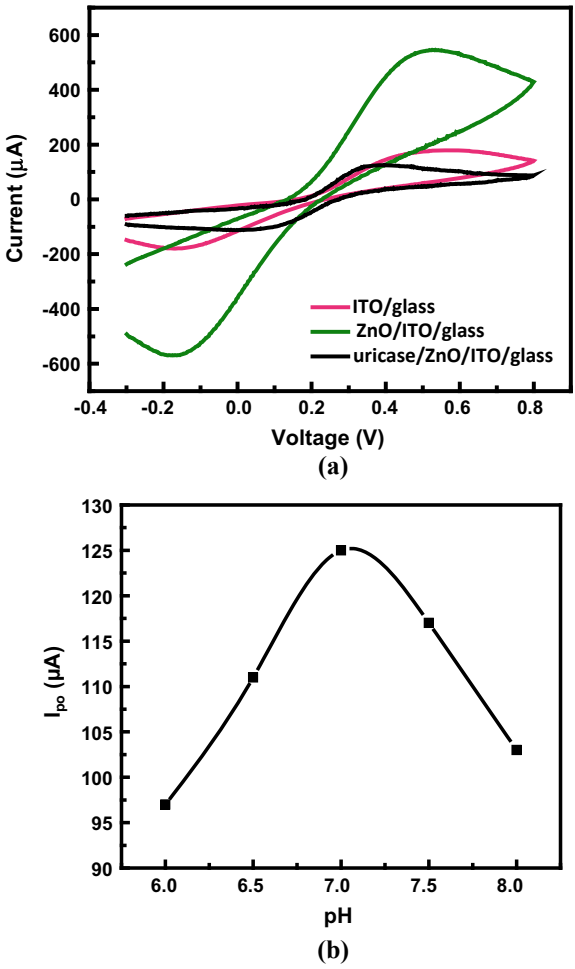

Fig. 5 **a** CV response of ITO/glass electrode, ZnO/ITO/glass electrode before and after uricase immobilization. **b** Influence of pH on the I_{po} for Ur/ZnO/ITO/glass bioelectrode

The CV measurements of Ur/ZnO/ITO/glass bioelectrode were conducted at different scan rates from 90 to 150 mV/s as shown in Fig. 6.

It is interesting to note the quasi-reversibility of system from Fig. 6(a) where the separation between the oxidation (E_{po}) and reduction (E_{pr}) peak potential for the bioelectrode increases due to an increase in scan rate [19]. Figure 6b shows the dependence of peak oxidation (I_{po}) and reduction (I_{pr}) current for the Ur/ZnO/ITO/glass bioelectrode on the scan rate. The peak currents obtained during the oxidation and reduction reactions for ZnO based bioelectrode are found to vary linearly with the scan rate (Fig. 6b). This explains that the electrochemical process at the bioelectrode is surface controlled mechanism [9]. The linear variation of peak currents may be represented in the form of equations given by:

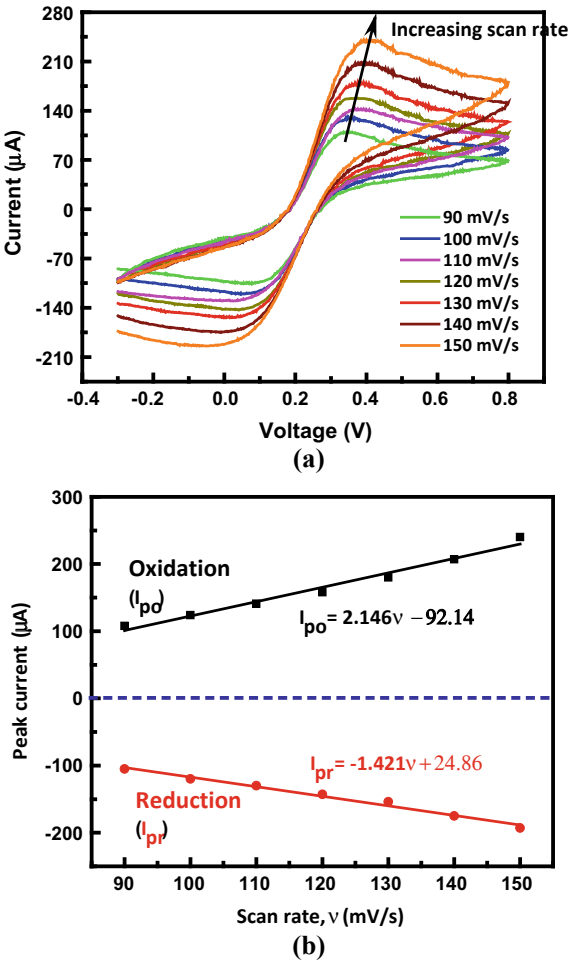

Fig. 6 **a** Scan rate studies showing the cyclic voltammograms of Ur/ZnO/ITO/glass bioelectrode in PBS solution containing $[Fe(CN)_6]^{3-/4-}$. **b** Variation in peak currents obtained by varying scan rate

$$I_{\text{po}}\,(\mu\text{A}) = 2.146v - 92.14\,(r = 0.99, \text{S.D.} = 7.31\,\mu\text{A}) \tag{1}$$

$$I_{\text{pr}}\,(\mu\text{A}) = -1.421v + 24.86\,(r = 0.99, \text{S.D.} = 3.95\,\mu\text{A}) \tag{2}$$

Here, r indicates the coefficient of regression and S.D. corresponds to the standard deviation. Since the value of regression coefficient is found to be close to 1, it indicates a good linear fit of the dependence of peak currents on scan rate. Also, the value of standard deviation is very small.

3.2.3 Surface Coverage

Brown–Anson model was used to estimate the surface coverage (I^*) [20] per unit area of the electroactive uricase (mol cm^{-2}) immobilized on ZnO/ITO/glass electrode as given by the equation:

$$I_{po} = \frac{n^2 F^2 I^* A \nu}{4RT} \tag{3}$$

In this equation, n corresponds to the number of electrons per reactant molecule (= 1 in present work) which are exchanged in the reaction, F is the Faraday constant (96,485 C/mol), R is gas constant (8.314 J^{-1} mol^{-1} K^{-1}), A is surface area of the bioelectrode (1 cm^2), and T is the temperature (300 K). The value of surface coverage of Ur/ZnO/ITO/glass bioelectrode is calculated to be ~9.74 × 10^{-9} mol/cm^2. The obtained value of surface coverage (I^*) is significantly higher in comparison to that reported for uricase bioelectrodes by other workers in literature (2.69 × 10^{-9} mol/cm^2 [21]) which provides a confirmation of the efficient immobilization of the biomolecule on the matrix surface based on ZnO grown under optimized conditions.

3.3 Sensing of Uric Acid

Sensing of uric acid is carried out using the prepared Ur/ZnO/ITO/glass bioelectrode by varying the concentrations of uric acid in the electrolyte solution. Figure 7a shows the CV spectra when uric acid solution of different concentrations from 0.05 to 1.0 mM is mixed with buffer solution.

The behavior of CV curves remains similar with defined oxidation and reduction peaks, however, the magnitude of redox peaks increases significantly for Ur immobilized ZnO thin film electrode with an increase in uric acid concentration (Fig. 7a). The oxidation peak potential is obtained to be 0.4 V which corresponds to the oxidation of mediating species [$(Fe(CN)_6]^{3-/4-}$ in the present work] (Fig. 7a). Figure 7b demonstrates that the variation of I_{po} is linear with uric acid concentration where the value of I_{po} is found to increase from 125 to 247 μA for the corresponding rise in uric acid concentration from 0 to 1.0 mM. Wang et al. [22] has recently worked on the development of a calorimetric biosensor for detection of uric acid on the basis of redox reaction between 3,3′,5,5′-tetramethylbenzidine (TMB) and $HAuCl_4$, however, the sensing response of the developed biosensor was linear upto 80 μM which is far below the physiological range in humans. Thus, the ZnO thin film based biosensor developed by Pulsed laser deposition technique is a potential candidate for uric acid detection owing to good linearity over wide range of UA concentrations. The linearity of current with UA concentrations can be described by equation:

$$I_{po}\,(\mu A) = 122 \times \text{UA concentration (mM)} + 129\,(r = 0.996, \text{S.D.} = 3.8\,\mu A) \tag{4}$$

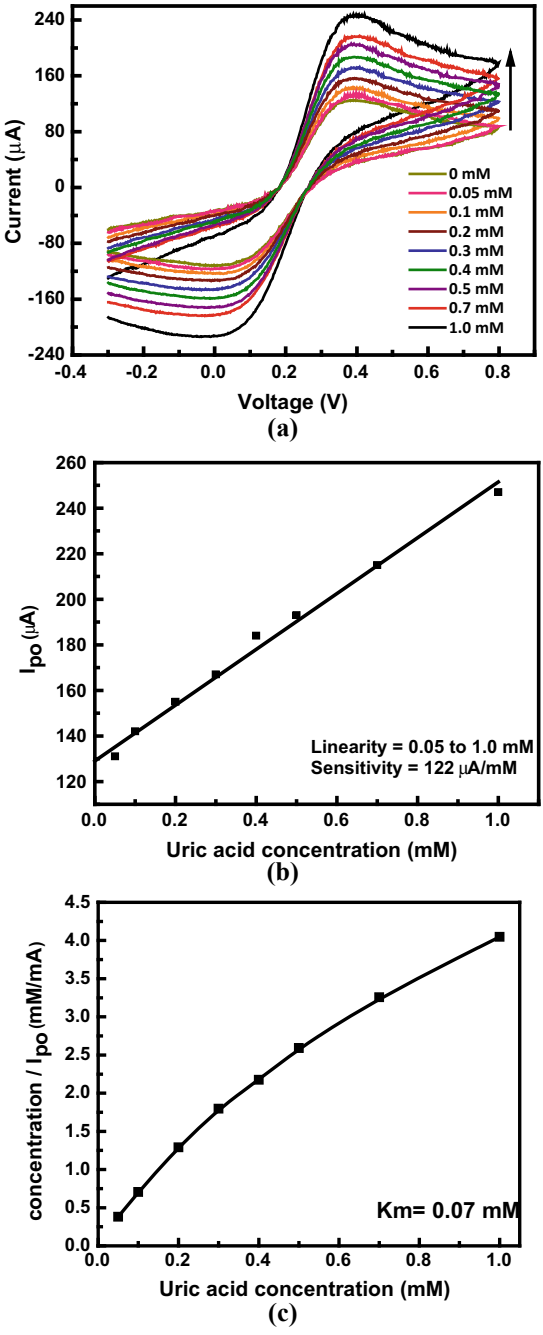

Fig. 7 **a** Sensing response of the prepared bioelectrode towards uric acid with its concentration varying in the range of 0.05–1.0 mM, **b** Variation of peak oxidation current with uric caid concentration, and **c** Hanes plot showing affinity of uricase towards analyte

The slope of the linearity curve provides an estimate of sensitivity of the developed biosensor which is obtained to be about 122 μA/(mM). The obtained value of sensitivity is much higher than the ones reported in literature (3 to 40 (μA)mM^{-1}) for other uric acid biosensors [23, 24]. Ya et al. [25] has recently reported a uric acid biosensor based on Cu_2O nanoparticles on glassy carbon electrode and further decorated with ferrocene and reported a sensitivity of 1.9 μA/(mM-cm^2). Kudo et al. [26] reported a uric acid biosensor based on the measurement of H_2O_2 produced in the enzymatic reaction and obtained a sensitivity of 170 nA/mM in saliva. Thus, uric acid biosensors developed under optimized growth parameters exhibits high sensitivity towards detection of uric acid. Hence, it may be concluded that growth kinetics play an important role in governing the response characteristics of a biosensor.

Sensing mechanism is based on the transfer of electrons through mediating species due to the absence of any redox couple in ZnO. Uricase immobilized on the surface of ZnO matrix reacts with the analyte (uric acid), converts it into product (allantoin), and gets reduced (Fig. 8). The electron released during its re-oxidation is taken up by the mediator ($K_3[Fe(CN)_6]$) and reduces itself. The reduced mediator releases an electron during its re-oxidation which is then transferred to the ITO electrode.

$$\underset{\text{(relatively insoluble)}}{\text{Uric acid}} + 2H_2O + O_2 \xrightarrow{\text{uricase}} \underset{\text{(relatively soluble)}}{\text{Allantoin}} + CO_2 + H_2O_2 \tag{5}$$

As the uric acid concentration increases, more oxidation of uricase take place which in turn releases more electrons. Thus, the obtained current signal varies directly with the analyte concentration. The catalytic oxidation of uricase is increasing with a rise in concentration of uric acid in the electrolyte, thereby resulting in current signal (I_{po}) which is directly proportional to the uric acid concentration.

The Michaelis–Menten kinetic parameter (K*m*) was calculated from the linear region of the Hanes plot (Fig. 8) to analyze the affinity of immobilized uricase on the surface of matrix. The value of K*m* is about 0.07 mM which is much lower than the corresponding values (0.17 to 7.83 mM) reported by other workers for uric acid biosensors [27]. Jirakunakorn et al. [28] in his recent work on screen printed electrode

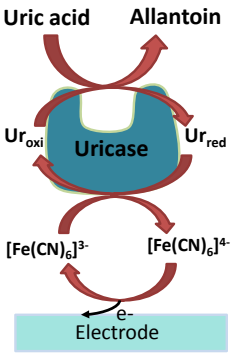

Fig. 8 Schematic of the sensing mechanism taking place at Ur/ZnO/ITO/glass bioelectrode for the detection of uric acid

prepared using Prussian blue and a cryogel prepared from the composite of chitosan and graphene has reported a uric acid biosensor which exhibits a K*m* of 0.23 mM. Also, the linear range is limited to 0.4 mM [28]. In another report, Numnuam et al. [29] developed a uric acid biosensor based on electrospun nanocomposite of chitosan with nanofibers of CNTs and obtained a Michaelis–Menten constant of 0.21 mM. The obtained low value of K*m* suggests that the immobilized uricase shows high affinity towards uric acid because of the biocompatible environment and favorable conformation offered by ZnO matrix to the receptor. Thus, ZnO matrix prepared under optimized conditions possess high potential for biosensing applications.

3.4 Shelf Life

The shelf life or storage capability of the prepared bioelectrode is an important concern and is thus analyzed by recording the CV measurements repeatedly after 15 days for 20 weeks. The concentration of uric acid was kept to be fixed at 0.30 mM, and peak current is measured. Activity is then calculated with respect to the peak current obtained for uric acid concentration of 0.30 mM for the ZnO based biosensor on 0th day and the obtained variation in activity is plotted in Fig. 9. The obtained results suggest that the immobilized uricase presents more than 90% of its activity even after 20 weeks when stored at 4 °C (Fig. 9), indicating better stability of the Ur/ZnO/ITO/glass bioelectrode. The results obtained in the present study are promising compared to those reported by other workers for uric acid biosensors in literature [24].

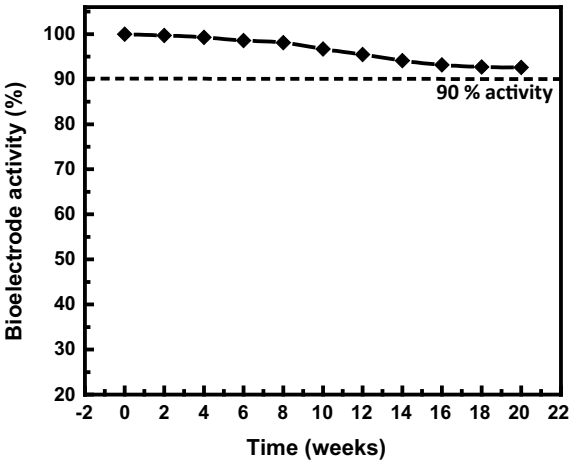

Fig. 9 Analysis of shelf life of the Ur/ZnO/ITO/glass bioelectrode

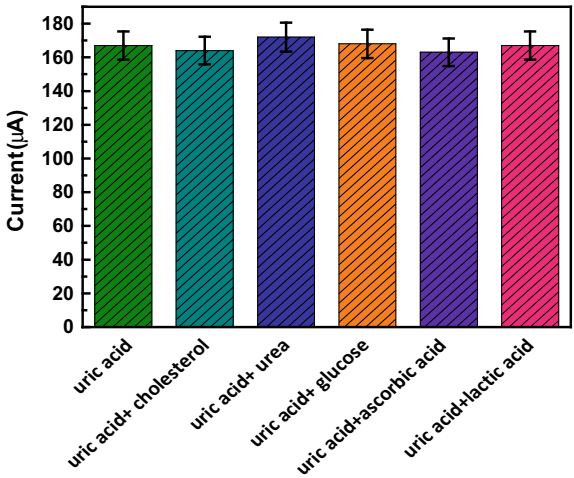

Fig. 10 Selectivity of Ur/ZnO/ITO/glass biosensor towards uric acid

3.5 Selectivity of Bioelectrode

Selectivity is a major concern as any false signal which may interfere with the original signal will lead to wrong conclusions. The selectivity of biosensor was studied wherein, the effect of possible common interferants present in serum on the sensing response of the prepared bioelectrode towards uric acid was tested. In order to perform the experiment, a fixed concentration of uric acid (0.30 mM) and the possible interferent having concentration within physiological range are taken in the same ratio and then subsequently added to the buffer solution. The peak current was recorded after addition of common interferents such as glucose, cholesterol, urea, ascorbic acid, and lactic acid. The fluctuation in the peak current for buffer solution having both interferents and uric acid with respect to uric acid only gave an estimate of selectivity of the biosensor. Error bars were added which represented the error in repeatability in experiment. The selectivity study presented in Fig. 10 suggests that the response characteristics of Ur/ZnO/ITO/glass bioelectrode towards uric acid are not affected by the presence of other interferents in blood. Thus, the sensor exhibited high selectivity towards uric acid due to the presence of receptor uricase which is specific to uric acid.

4 Conclusion

In this paper, ZnO thin film matrix prepared using Pulsed laser deposition has been exploited for the development of biosensor. The role of processing parameters in governing the electrocatalytic parameters of the matrix has been highlighted. As the growth pressure is varied from 1 to 100 mT, it is found that the peak oxidation

current increases to 100 mT. This may be attributed to the reduction in mean free path and increased roughness at high pressures which provide more surface area for immobilization of enzyme. The optimized ZnO thin film electrode is applied to the detection of uric acid where a high sensitivity of 122 μA/mM is obtained with a low K*m*~0.07 mM with a high shelf life of 20 weeks. Thus, careful control of ZnO parameters may lead to the development of highly sensitive and stable matrix which can be used as a platform for development of biosensors.

Acknowledgements Authors are thankful to University of Delhi for providing research facilities.

References

1. Jindal K, Tomar M, Gupta V (2017) A novel low-powered uric acid biosensor based on arrayed p-n junction heterostructures of ZnO thin film and CuO microclusters. Sens Actuators B Chem 253. https://doi.org/10.1016/j.snb.2017.06.146
2. Jindal K, Tomar M, Gupta V (2013) Nitrogen-doped zinc oxide thin films biosensor for determination of uric acid. Analyst 138(15). https://doi.org/10.1039/c3an36695b
3. Beitollahi H, Tajik S, Nejad FG, Safaei M (2020) Recent advances in ZnO nanostructure-based electrochemical sensors and biosensors. J Mater Chem B 8(27):5826–5844
4. Baruah S, Maibam B, Borah CK, Agarkar T, Kumar A, Kumar S (2021) A highly receptive ZnO based enzymatic electrochemical sensor for glucose sensing. IEEE Sens J
5. Batra N, Tomar M, Gupta V (2012) Realization of an efficient cholesterol biosensor using ZnO nanostructured thin film. Analyst 137(24):5854–5859
6. Yang Z, Zong X, Ye Z, Zhao B, Wang Q, Wang P (2010) The application of complex multiple forklike ZnO nanostructures to rapid and ultrahigh sensitive hydrogen peroxide biosensors. Biomaterials 31(29):7534–7541
7. Tak M, Gupta V, Tomar M (2015) A highly efficient urea detection using flower-like zinc oxide nanostructures. Mater Sci Eng C 57:38–48
8. Kaur G, Paliwal A, Tomar M, Gupta V (2016) Detection of Neisseria meningitidis using surface plasmon resonance based DNA biosensor. Biosens Bioelectron 78:106–110
9. Jindal K, Tomar M, Gupta V (2014) Inducing electrocatalytic functionality in ZnO thin film by N doping to realize a third generation uric acid biosensor. Biosens Bioelectron 55. https://doi.org/10.1016/j.bios.2013.11.015
10. Antony N, Mohanty S, Nayak SK (2020) Electrochemical inspection of polypyrrole/chitosan/zinc oxide hybrid composites. J Appl Polym Sci 137(47):49561
11. Wu I-C et al (2017) Nano-structure ZnO/Cu 2 O photoelectrochemical and self-powered biosensor for esophageal cancer cell detection. Opt Express 25(7):7689–7706
12. Uddin MT, Alam MM, Asiri AM, Rahman MM, Toupance T, Islam MA (2020) Electrochemical detection of 2-nitrophenol using a heterostructure ZnO/RuO 2 nanoparticle modified glassy carbon electrode. RSC Adv 10(1):122–132
13. Batra N, Tomar M, Gupta V (2015) ZnO–CuO composite matrix based reagentless biosensor for detection of total cholesterol. Biosens Bioelectron 67:263–271
14. Saha S, Gupta V (2011) Influence of surface defects in ZnO thin films on its biosensing response characteristic. J Appl Phys 110(6):64904
15. Ghanbari K, Moloudi M (2016) Flower-like ZnO decorated polyaniline/reduced graphene oxide nanocomposites for simultaneous determination of dopamine and uric acid. Anal Biochem 512:91–102
16. RoyChoudhury S et al (2018) Continuous monitoring of wound healing using a wearable enzymatic uric acid biosensor. J Electrochem Soc 165(8):B3168

17. Jindal K, Tomar M, Katiyar RS, Gupta V (2015) Transition from diamagnetic to ferromagnetic state in laser ablated nitrogen doped ZnO thin films. AIP Adv 5(2). https://doi.org/10.1063/1.4908040
18. Zoski CG (2006) Handbook of electrochemistry. Elsevier
19. Matharu Z, Pandey P, Pandey MK, Gupta V, Malhotra BD (2009) Functionalized Gold nanoparticles–Octadecylamine hybrid Langmuir-Blodgett film for enzyme sensor. Electroanal Int J Devoted to Fundam Pract Asp Electroanal 21(14):1587–1596
20. Bard AJ, Faulkner LR (2001) Fundamentals and applications. Electrochem Methods 2(482):580–632
21. Li J, Lin X-Q (2007) Electrodeposition of gold nanoclusters on overoxidized polypyrrole film modified glassy carbon electrode and its application for the simultaneous determination of epinephrine and uric acid under coexistence of ascorbic acid. Anal Chim Acta 596(2):222–230
22. Wang J et al (2018) A simple and rapid colorimetric probe for uric acid detection based on redox reaction of 3, 3′, 5, 5′-tetramethylbenzidine with HAuCl4. Colloids Surf, A 555:565–571
23. Wang J, Zhang W-D (2011) Sputtering deposition of gold nanoparticles onto vertically aligned carbon nanotubes for electroanalysis of uric acid. J Electroanal Chem 654(1–2):79–84
24. Puri N, Sharma V, Tanwar VK, Singh N, Biradar AM (2013) Enzyme-modified indium tin oxide microelectrode array-based electrochemical uric acid biosensor. Prog Biomater 2(1):1–7
25. Yan Q et al (2020) A highly sensitive uric acid electrochemical biosensor based on a nano-cube cuprous oxide/ferrocene/uricase modified glassy carbon electrode. Sci Rep 10(1):1–10
26. Kudo H, Takagi Y (2018) Electrochemical biosensor for simplified determination of salivary uric acid. Sens Mater 30(5):1187–1195
27. Liu Y, Yuan M, Liu L, Guo R (2013) A facile electrochemical uricase biosensor designed from gold/amino acid nanocomposites. Sens Actuators B Chem 176:592–597
28. Jirakunakorn R, Khumngern S, Choosang J, Thavarungkul P, Kanatharana P, Numnuam A (2020) Uric acid enzyme biosensor based on a screen-printed electrode coated with Prussian blue and modified with chitosan-graphene composite cryogel. Microchem J 154:104624
29. Numnuam A, Thavarungkul P, Kanatharana P (2014) An amperometric uric acid biosensor based on chitosan-carbon nanotubes electrospun nanofiber on silver nanoparticles. Anal Bioanal Chem 406(15):3763–3772

Investigation of Magnesium Ion and Cellulose Acetate-Based Conducting Biopolymers: Electrical and Ion Transport Properties

Mohd Sadiq, Mohammad Moeen Hasan Raza, Mohammad Zulfequar, Mahboob Ali, and Javid Ali

Abstract The conducting biopolymer based on cellulose acetate with various concentration of magnesium perchlorate were prepared by standard solution cast technique. The electrical properties and electrochemical performance of as-prepared biopolymer films were investigated by electrochemical impedance technique. The maximum ionic conductivity of biopolymer electrolytes films approximately of order 10^{-4} S/cm at 30 °C. The voltage stability limit of biopolymer electrolyte films was examined by linear voltammetry and cyclic voltammetry for use in energy storage device applications. The highest electrochemical window 4.5 V is achieved at 50% of Mg $(ClO_4)_2$.

Keywords Biopolymer · Electrolytes · Cyclic voltammetry · Cellulose acetate · Magnesium perchlorate

1 Introduction

In this current time, a lot of energy is required to full fill the need of modern lifestyle and industry. So, the entire population of the world depends on fossil fuels. There are many disadvantages of the fossil fuels like limited resources, non-renewable, and producing massive air pollution [1, 2]. All these factors motivate the research community to find an alternative resource in terms of renewability and sustainability. There are many renewable energy sources like fuel cells, wind, and solar cells [3, 4]. The new and emerging science of polymer electrolytes becoming a promising candidate to store energy and replace non-renewable resources. Polymer electrolyte extensively gets used in many applications like energy storage, supercapacitor, solar

M. Sadiq
Department of Physics, A R S D College, University of Delhi, Delhi, India

M. Sadiq · M. M. H. Raza · M. Zulfequar · J. Ali (✉)
Department of Physics, Jamia Millia Islamia University, Delhi, India
e-mail: jali1@jmi.ac.in

M. Ali
Department of Physics and Astrophysics, University of Delhi, Delhi, India

S. B. Krupanidhi et al. (eds.), *Advanced Functional Materials and Devices*, Springer Proceedings in Materials 14, https://doi.org/10.1007/978-981-16-5971-3_2

cells, and fuel cells [5]. In 1975, P. V. Wright reported the properties of ion conduction in the polymers but practically, it is reported by Armand et al. in 1979 [6]. Extensive research work has been carried out in the polymer field for making different types of polymers like gel polymer, solid polymer, and liquid polymer. Some polymers have been obtained from nature, and a lot of new synthetic polymers are synthesized in the laboratory in terms of modification in their physical and chemical properties [7, 8]. Biopolymer is a new class of polymer, and they are eco-friendly. Biopolymers are having high mechanical and thermal stability, high ionic conductivity, and large area window of electrochemical. Biopolymer family containing the carboxy methylcellulose (CMC), CMC/PVA, (Na-CMC), potato starch, seaweeds, tamarind seed polysaccharide, starch–chitosan, starch, and gelatine [9–16]. These are used in the biopolymer-based electrolyte for energy storage and energy generation. Electrolyte films based on cellulose acetate are having many advantages like low cost, eco-friendly, flexibility, biodegradability, biocompatibility, and easily film formation, etc. over the other natural biopolymers [17]. Like other natural polymers, they have also some limitations such as semi-crystalline, low ionic conductivity at room temperature, low electrochemical window, and mechanical stability which hindering the application in electrochemical devices. In the cellulose acetate biopolymer, polar functional group presents like carboxyl group C=O which makes the cellulose acetate useful as a separator between the two electrodes in the electrochemical battery application [18]. Separators help in separating the cations and anion between the electrodes. The cations of dopant salt can move through the polar functional groups and induced ionic conductivity. While the anion is free to move in the host polymer matrix [19]. Currently, cellulose is widely studying for making the separators, electrode, gel, and solid polymer electrolytes worth for the enhanced parameter in the energy storage device/conversion applications. The fast ionic movements of ions within the host polymer are highly dependable on the doping salts ions species. The doping salt highly influencing the ionic mobility, conductivity, thermal stability and amorphous nature of the polymer electrolytes material [20]. Most of the work has been done on the Li-ion-based cellulose acetate polymer electrolytes separators for application in the supercapacitor and batteries. But divalent salt like Mg-based polymer electrolytes has some advanced advantage over the Li-based polymer electrolytes like the better performance, negligible hazards nature, easily available, high melting point, non-reactive in air, high negative standard potential, and many more [21–24].

In the present report, we prepared the biopolymer films based on various compositions of cellulose acetate (CA) with varying different salt concentrations $Mg(ClO_4)_2$ by standard solution casting technique. The electrical properties, voltage stability, and magnesium ion transference number of the as-prepared biopolymer films were measured by an electrochemical impedance analyzer.

Table 1 Designation of biopolymer electrolyte BPE films

Composition (cellulose acetate CA: $Mg(ClO_4)_2$) (wt%)	Designation
90:10	CA-Mg(10)
80:20	CA-Mg(20)
70:30	CA-Mg(30)
60:40	CA-Mg(40)
50:50	CA-Mg(50)

2 Experiment Section

2.1 Material Used

The following materials were used under present work like magnesium salt magnesium percholorate ($Mg(ClO_4)_2$) (m.w. 223.2 g/mol), biopolymer cellulose acetate (CA) (m.w = 30,000 g/mol), and solvent dimethylformamide (DMF) of m.w. = 73.09 g/mol and density 944 kg/m^3 of purity > 99%. All the chemicals are high quality and purity > 99%).

2.2 Sample Preparation Method

The detailed synthesis of biopolymer films and techniques are used in the present works [25, 26]. The designation biopolymer electrolytes films are shown in Table 1.

2.3 Measurements

The impedance measurements have been carried out using potentiostat/galvanostat and impedance analyzer PALMSENS (The Netherlands) model PalmSens4 controlled by a computer through the PSTRACE version software. All the electrochemical performances were performed in the frequency range from 0.1 Hz to 1 MHz at room temperature. The sample was sandwich between two stainless steel blocking electrodes.

3 Results and Discussion

3.1 Electrical Properties

The a–c impedance analysis of biopolymer electrolyte films was studied at room temperature. From the impedance plot, the real part of the sample is Z', and the imaginary part of the sample is Z''. This impedance plot is a structured relationship between the real and imaginary parts of the data. The impedance spectra are evaluated by the Nyquist plot by using mathematical formalism [27]. The complex form of the impedance is calculated by the equation;

$$Z^*(\omega) = (Z^{'} - jZ'') \tag{1}$$

where $Z' = |Z| \cos\theta,\ Z'' = |Z| \sin\theta$.

The *a–c* impedance performance of biopolymer electrolyte and calculated by the equation,

$$\sigma = \frac{t}{R_b A} \tag{2}$$

where t (cm) is the thickness of the biopolymer electrolytes, A (cm^2) is the contact area, and R_b (ohm) is the bulk resistance of biopolymer electrolytes, which is obtained from the electrical properties [28]. Figure 1 shows the room temperature ionic conductivity plot of biopolymer with various mg salt contents. Therefore, the overall conductivity of biopolymer electrolyte films is shown in Table 2. The addition of magnesium perchlorate $Mg(ClO_4)_2$ salts results in an increase in conductivity has been observed. The maximum ionic conductivity of biopolymer electrolytes remained at 10^{-4} S/cm. The existence of the conduction medium is possibly related to the dissociation of ion aggregates into the polymer chain, which enhanced the conductivity. In the CA + 20 wt% of $Mg(ClO_4)_2$ bioplymer film shows no semicircle in the impedance spectra, which means that they are indicating the residual resistive part in the biopolymer electrolyte films. However, the low-frequency side shows spike this is due to ionic conduction in materials. Figure 1 shows that the semicircles validate the electrode effect and electrode–electrolyte interface effect. The enhance in the conductivity can be used to help for better understanding the conduction in the electrolytes, which is a basic requirement parameter of energy storage systems [29, 30].

3.2 Electrochemical Performance

The electrochemical performance is an important parameter of the energy storage system. The electrochemical window stability of the biopolymer films was examined

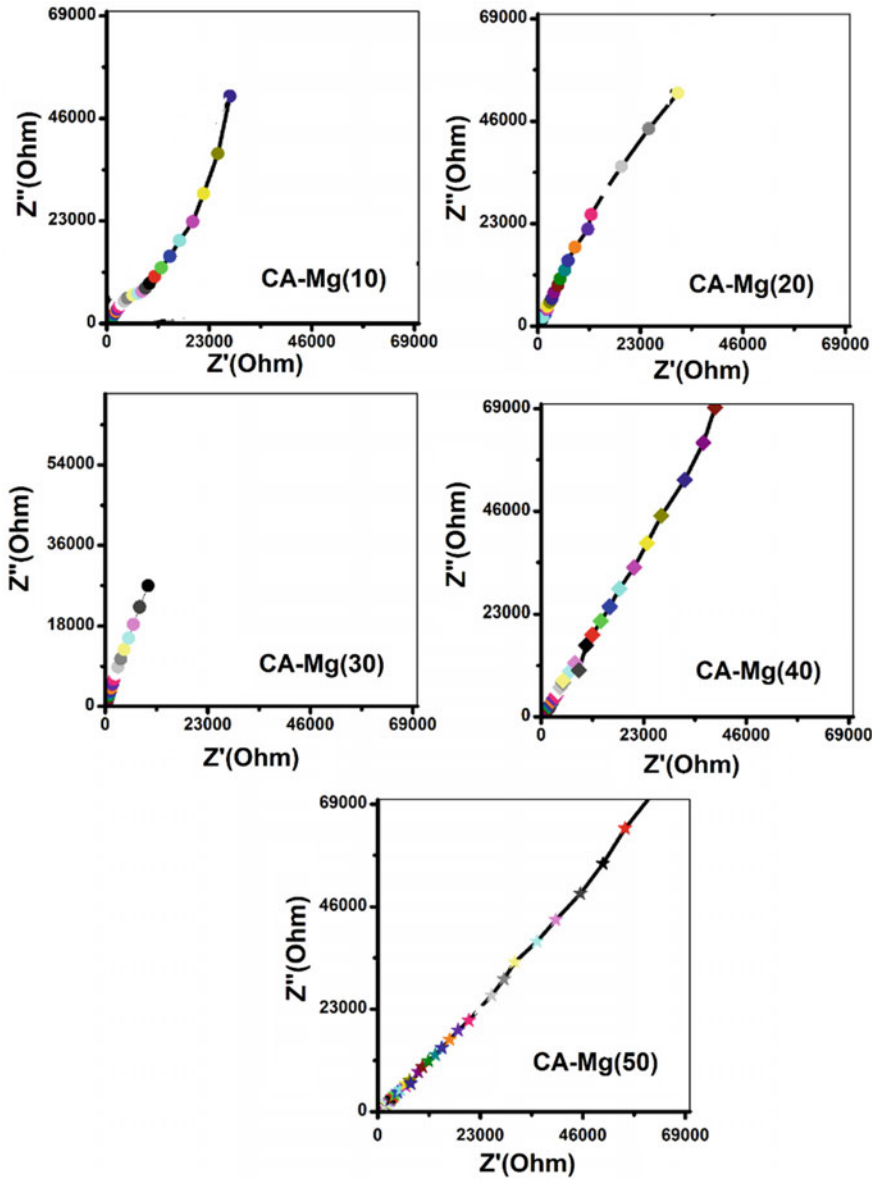

Fig. 1 Ionic conductivity of magnesium ion-based biopolymer electrolytes films at room temperature

Table 2 Ionic conductivity of magnesium ion-based biopolymer electrolytes films at room temperature

Sample code	t_{ion}	t_e	R_b	Conductivity (S cm^{-1})
CA-Mg(10)	0.98	0.018	806.65	1.205×10^{-4}
CA-Mg(20)	0.84	0.15	1075.544	9.979×10^{-5}
CA-Mg(30)	0.96	0.030	313.70	3.734×10^{-5}
CA-Mg(40)	0.97	0.028	1165.17	7.79×10^{-4}
CA-Mg(50)	0.75	0.24	495.95	2.401×10^{-4}

by linear sweep voltammetry (LSV) [31, 32]. The biopolymer films were sandwich between the two stainless steel blocking electrodes with scan rate 10 mV s^{-1} and voltage range from −3 to +3 V. Figure 2 shows the linear sweep voltammetry curve at room temperature. The highest stability window was 4.55 V at CA-Mg(40).

This stability window is highly used in energy storage systems. The cyclic voltammetry (CV) performs at room temperature, under the scan rate of 20 mV S^{-1}, and was carried out for two cycles at the same scan rate with the sample sandwich between two stainless steel electrodes [30]. This absence of oxidation–reduction peaks in the CV plots is due to the stability of the biopolymer electrolyte films as shown in Fig. 3.

This result could be used for its application in the energy storage system.

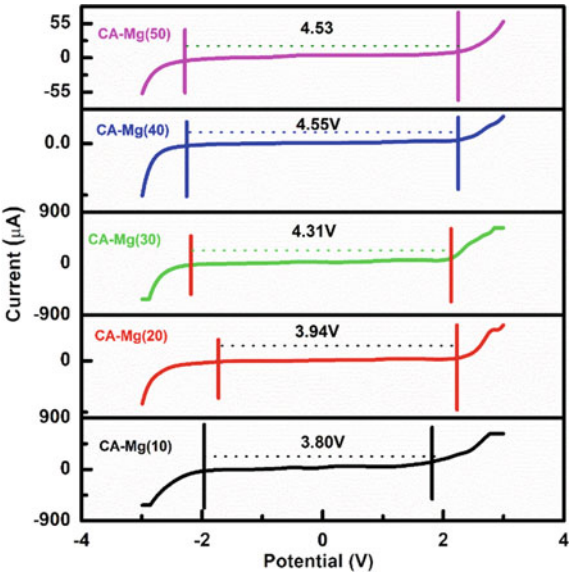

Fig. 2 Linear sweep voltammetry (LSV) of biopolymer electrolyte films

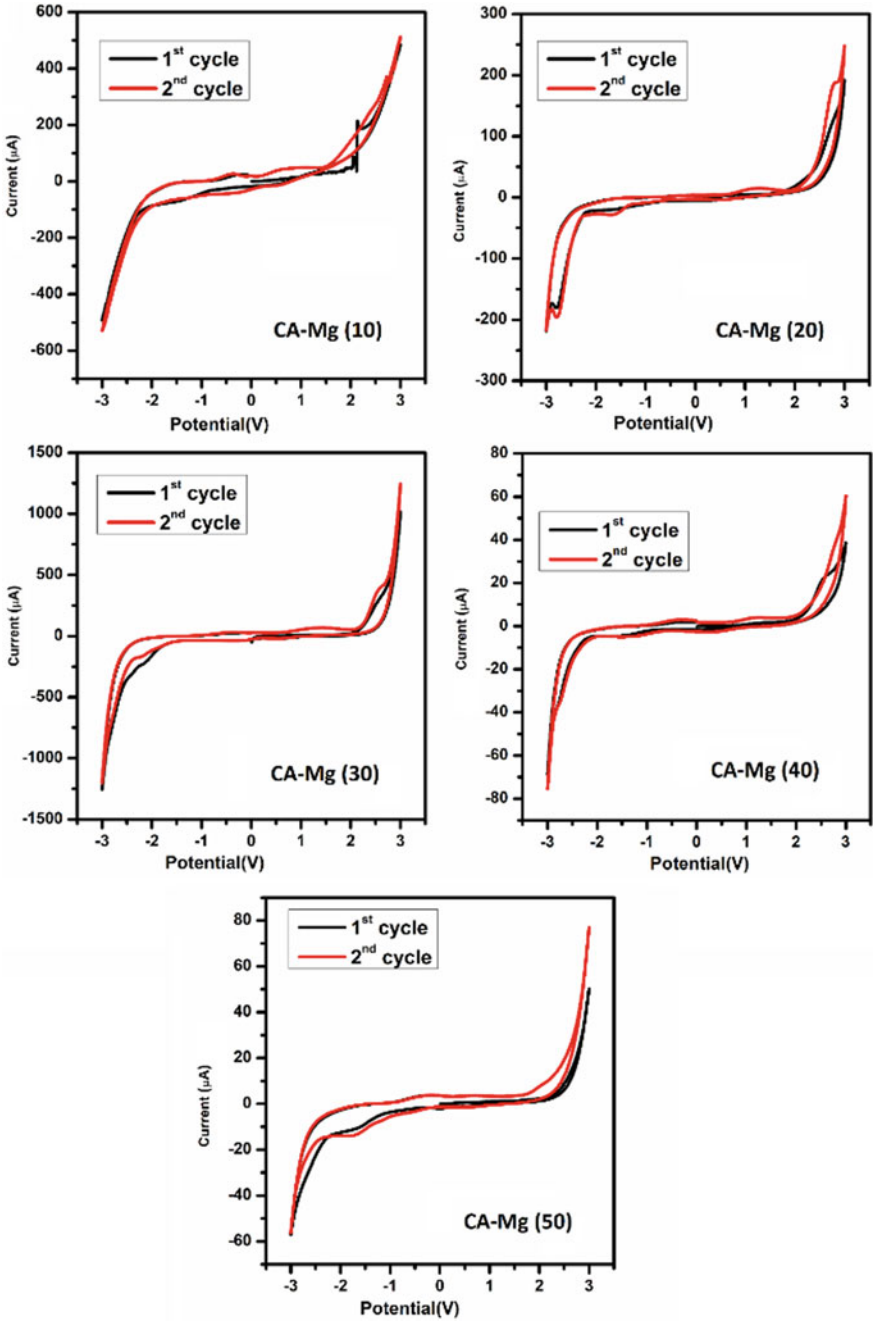

Fig. 3 Cyclic voltammetry (CV) of biopolymer electrolyte films

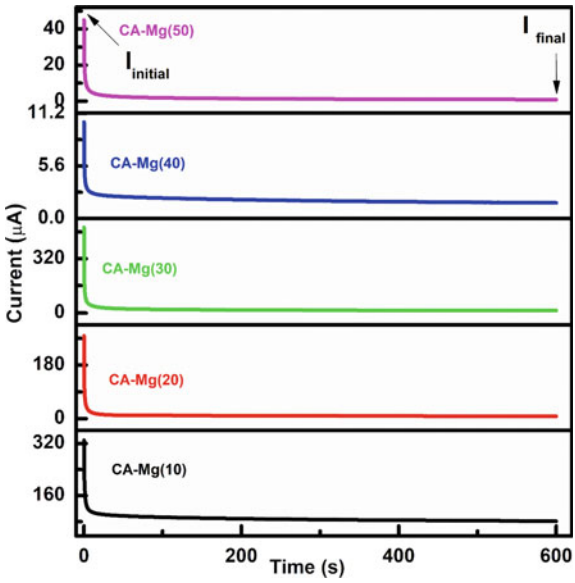

Fig. 4 Ion transference number of biopolymer electrolyte films

3.3 Chronoamperometry

Chronoamperometry is a technique that uses to study the ionic transference number by measuring the direct current (DC) as a function of time. The study was carried out by applied the 2 V across the cell. The ion transference number across the cell configuration SS/biopolymer films/SS at room temperature are shown in Fig. 4.

The ion transference number was examined by

$$t_{\text{ion}} = \left(\frac{I_{\text{initial}} - I_{\text{final}}}{I_{\text{initial}}} \right), \quad t_{\text{e}} = \frac{I_{\text{final}}}{I_{\text{initial}}} \tag{3}$$

where I_{initial} (initial) is the total current, and I_{final} (final) is the residual electronic current, respectively [33–36]. The maximum transference number for this system is 0.98. The ion transference and electronic transference numbers were summarized in Table 2. This result is highly used in electrochemical devices.

4 Summary

The biopolymer-based CA: magnesium perchlorate Mg $(ClO_4)_2$ was successfully prepared by the standard solution casting technique. The maximum ionic conductivity at room temperature is achieved ~10^{-4} S cm^{-1}. The electrochemical stability window of CA-Mg(50) stables up to ~4.5 V. No oxidation–reduction peak is observed in the

system, which is confirmed by CV analysis. Maximum ion transference number values up to 0.98. This highly enhanced parameter is demand for application in energy storage devices such as; batteries, fuel cell, and supercapacitors.

References

1. Arya A, Sharma AL (2020) J Mater Sci 55:6242–6304
2. Perera K, Dissanayake MAKL, Bandaranayake PWSK (2004) Mater Res Bull 39:1745–1751
3. Sadiq M, Raza MMH, Murtaza T, Zulfequar M, Ali J (2021) J Electron Mater 50:403–418
4. Kiruthika S, Malathi M, Selvasekarapandian S, Tamilarasan K, Moniha V, Manjuladevi R (2019) J Solid-State Electrochem 23:2181–2193
5. Arya A, Sadiq M, Sharma AL (2019) Polym Bull 76:5149–5172
6. Armand M (1994) Solid State Ionics 69:309–319
7. Arya A, Sadiq M, Sharma AL (2017) Ionics 23(3):497–540
8. Mobarak NN, Jumaah FN, Ghani MA, Abdullah MP, Ahmad A (2015) Electrochim Acta 175:224–231
9. Samsudin AS, Isa MIN (2012) J Appl Sci 12:174–179
10. Arya A, Sharma AL (2019) J Solid-State Electrochem 23:997–1059
11. Mazuki NF, Fuzlin AF, Saadiah MA, Samsudin AS (2019) Ionics 25:2657–2667
12. Iboroma SD, Cookey GA, Obunwo CC (2018) J Appl Sci Environ Manag 22:1591–1594
13. Rani MSA, Isa NS, Sainorudin MH, Abdullah NA, Mohammad M, Asim N, Ibrahim MA (2021) Int J Electrochem Sci 16:1–10
14. Shukur MF, Ithnin R, Kadir MFZ (2016) Ionics 22:1113–1123
15. Raymundo- E, Leroux F, Béguin F (2006) Adv Mater 18:1877–1882
16. Perumal P, Abhilash KP, Sivaraj P, Selvin PC (2019) Mater Res Bull 118:110490
17. Shukur MF, Ithnin R, Kadir MFZ (2014) Ionics 20:977–999
18. Wang W, Wang K, Xiao J, Liu Y, Zhao Z, Liu A (2017) Int J Biol Macromol 94:258–265
19. Noor NAM, Isa MIN (2019) Int J Hydrogen Energy 44:8298–8306
20. Samsudin AS, Khairul WM, Isa MIN (2012) J Non-Cryst Solids 358:1104–1112
21. Samsudin AS, Lai HM, Isa MIN (2014) Electrochim Acta 129:1–13
22. Kiruthika S, Malathi M, Selvasekarapandian S, Tamilarasan K, Maheshwari T (2019) Polym Bull 46:1–19
23. Rudhziah S, Ahmad A, Ahmad I, Mohamed INS (2015) Electrochim Acta 175:162–168
24. Lizundia E, Kundu D (2021) Adv Func Mater 31:2005646
25. Sadiq M, Chaurasia SK, Singh AK, Pandey R, Yadav HS, Raza MH, Ali J (2020) Mater Today: Proc 1–8
26. Samsudin AS, Saadiah MA (2018) J Non-Cryst Solids 497:19–29
27. Mahalakshmi M, Selvanayagam S, Selvasekarapandian S, Chandra ML, Sangeetha P, Manjuladevi R (2020) Ionics 26:4553–4565
28. Arya A, Sharma AL (2020) Ionics 26:745–766
29. Sangeetha P, Selvakumari TM, Selvasekarapandian S, Srikumar SR, Manjuladevi R, Mahalakshmi M (2020) Ionics 26:233–244
30. Mahalakshmi M, Selvanayagam S, Selvasekarapandian S, Moniha V, Manjuladevi R, Sangeetha P (2019) J Sci: Adv Mater Devices 4:276–284
31. Selvalakshmi S, Mathavan T, Selvasekarapandian S, Premalatha M (2017) Ionics 23:2791–2797
32. Winie T, Arof AK (2016) Biopolymer electrolytes for energy devices. Nanostruct Polym Membr: Appl 2:311–356

33. Sadiq M, Hasan Raza MM, Zulfequar, Ali J (20201) J Nanosci Nanotechnol 21:3203–3217
34. Monisha S, Mathavan T, Selvasekarapandian S, Benial AMF, Aristatil G, Mani N, Premalatha M (2017) Carbohyd Polym 157:38–47
35. Monisha S, Mathavan T, Selvasekarapandian S, Benial AMF (2017) Ionics 23:2697–2706
36. Kamboj V, Arya A, Tanwar S, Kumar V, Sharma AL (2020) J Mater Sci 51:6167–6187

Phase Formation and Ionic Conduction in Potassium-Doped Strontium Metasilicate

Hera Tarique, Raza Shahid, Anjani Kumar Singh, Pragati Singh, Raghvendra Pandey, and Prabhakar Singh

Abstract Alkali metal-doped strontium metasilicate has been reported as ion-conducting materials. Here, we report the phase formation in potassium-doped strontium metasilicate ($SrSiO_3$) and also explored the conduction mechanism that is responsible for high ionic conductivity in this system. The phase evolution also explains the conduction behavior. The coexistence of crystalline along with few amount amorphous phases was also found to be responsible for high ionic conduction in the material. The high level of conductivity observed may be due to the oxygen vacancies in these structures generated through the mobile defects.

Keywords $SrSiO_3$ · Ionic conduction · Phase formation · SOFCs

1 Introduction

Due to non-renewable nature of fossil fuels and an ever-increasing demand of energy generation sources, there has been a lot of research for a cleaner alternative. Solid oxide fuel cells (SOFCs) are a potential alternative to the conventionally used fossil fuels. SOFC is an electrochemical device which directly converts the chemical energy of the fuel into electrical energy. Even though SOFCs offer high efficiency, fuel flexibility and cleaner energy generation, its commercial implementation is hampered due to its high operating temperature. SOFCs consist of an electrolyte sandwiched between porous anode and cathode. Electrolyte determines operating temperature of a SOFC. Conventionally available yttria-stabilized zirconia has a very high operating temperature of 1000 °C. Researchers have been looking for an electrolyte

H. Tarique · R. Shahid
Department of Physics, Jamia Millia Islamia (Central University), New Delhi 110025, India
e-mail: rshahid1@jmi.ac.in

H. Tarique · A. K. Singh · R. Pandey (✉)
Department of Physics, A.R.S.D College, University of Delhi, New Delhi 110021, India

P. Singh · P. Singh
Department of Physics, IIT (BHU) Varanasi, Varanasi 221005, India

S. B. Krupanidhi et al. (eds.), *Advanced Functional Materials and Devices*, Springer Proceedings in Materials 14, https://doi.org/10.1007/978-981-16-5971-3_3

with intermediate operating temperature ($T < 700$ °C) for commercial realization of SOFCs.

Singh et al. [1] reported high ionic conductivity in intermediate temperature range in alkali-doped strontium silicate system $Sr_{1-x}K_xMO_{3-0.5x}$ (M = Si or Ge) for the first time. They reported single monoclinic phase in the doped samples. For $Sr_{1-x}K_xGeO_{3-0.5x}$ ($0 < x < 0.25$), conductivity increases with increase in dopant concentration. Potassium doping in $SrSiO_3$ also shows similar increase in conductivity on increasing dopant concentration. Substitution of Ge on the Si sites further increased the conductivity. Maximum conductivity values are reported for $Sr_{0.8}K_{0.2}Si_{0.5}Ge_{0.5}O_{2.9}$ of $\sigma_o = 10^{-2}$ Scm^{-1} at 625 °C. Later on, they investigated the conductivity for sodium-doped strontium metasilicate ($Sr_{1-x}Na_xSiO_{3-0.5x}$). It was reported that sodium-doped oxides were less hygroscopic compared to potassium-doped oxides which created interstitial oxide ions instead of oxide ion vacancies which resulted in better conductivity [2].

Sodium and potassium-doped strontium silicates were reported to show competitive conductivity values which makes them a candidate for the electrolyte for solid oxide fuel cells. Even though it shows high conductivity, the widespread implementation could not be done due to the discrepancy in the nature of the ionic conductivity. It was reported by Baylis et al. [3] that an amorphous potassium silicate phase was present in potassium-doped strontium silicate system. Phase formation for $Sr_{0.8}K_{0.2}Si_{0.5}Ge_{0.5}O_{2.9}$ system was re-investigated, and it was reported that there was negligible or no potassium present in the crystalline part indicating toward low oxide ion vacancies. Instead of just one crystalline phase, an additional amorphous phase with high potassium concentration was reported. They reported low concentration of oxygen vacancies hence low level of oxide ion conduction in $Sr_{0.8}K_{0.2}Si_{0.5}Ge0.5O_{2.9}$ system.

Xu et al. [4] investigated phase formation and conductivity in $Sr_{0.8}K_{0.2}SiO_{2.85}$ system. Using an internal standard, the Rietveld refinement was carried out for the system. It was reported that 13.25 weight% amorphous phase was present in the sample suggesting that majority of the potassium ions were incorporated in the amorphous phase and not the crystalline phase. Additional amorphous phases of K_2SiO_3 and SiO_2 reported in the analysis are responsible for high ionic conductivity in the sample. On crystallization of these amorphous phases at high temperature, decrement in the conductivity is also observed. It was suggested that K^+ ions are responsible for the high ionic conductivity values instead of the oxide ions.

Sood et al. [5] re-investigated sodium-doped strontium silicate system. The detailed structural analysis of the samples implied the presence of an additional amorphous phase along with the crystalline phase. SEM analysis showed that the amorphous phase was segregated along the grain boundaries and was sodium rich. It was reported that amorphous grain boundaries are responsible for the ionic conductivity. The sample shows very low ionic conductivity and is insulating in the measured temperature range.

In our work, we have synthesized a new potassium-doped metasilicate $Sr_{3-3x}K_{3x}Si_3O_{9-\delta}$ ($x = 0.0, 0.20$) system. We have investigated its phase formation using diffraction (XRD). We have carried out UV–visible spectroscopy to study the

absorbance characteristics and have determined the optical band gap energy. To study the molecular structure of the system, Fourier transform–infrared spectroscopy has been performed. Scanning electron microscopy (SEM) is performed to study the microstructure of the samples and to investigate if the electrolytes are dense. Electrical conductivity measurements are taken for the system to study the variations with the introduction of the dopant in intermediate temperature range.

2 Experimental Procedure

Samples with nominal compositions $Sr_{3-3x}K_{3x}Si_3O_{9-\delta}$ ($x = 0.0$, 0.20; SKS30—$Sr_3Si_3O_9$, SKS34—$Sr_{2.4}K_{0.6}Si_3O_{9-\delta}$) were prepared by solid-state route method. Stoichiometric amount of $SrCO_3$ (99.9%), K_2CO_3 (99.9%) and SiO_2 (99.9%) were weighed and grinded in an agate mortar pestle. Samples were calcined in a muffle furnace by heating them at 1223 K for 6 h with heating rate of 5 °C per minute. After calcination, the samples were allowed to cool down and were crushed and ground for 1 h in the mortar pestle. The structure of the calcined samples was investigated by X-ray diffraction (XRD). XRD was carried out in room temperature in the 2° range of 10°–80° with Cu-Kα radiation ($\lambda = 1.5415$ Å. Disk-shaped pellets of 10 mm diameter were made using uniaxial cold press under 4 $Kgcm^{-2}$ pressure. Pellets were sintered at 1323 K for 6 h in a muffle furnace with the heating rate of at 5 °C per minute, and SKS samples were synthesized.

UV–visible spectroscopy was carried out on the samples in wavelength range of 200–1000 nm. Absorbance characteristics were studied as a function of wavelength, and optical band gap energy is calculated using UV–vis spectra.

Fourier transform–infrared spectroscopy (FT-IR) was carried out on the samples to investigate their structural features. The FT-IR spectroscopy was performed using PerkinElmer FT-IR system spectrum GX to study the transmittance characteristics as a function of wave number.

Microstructure was analyzed using scanning electron microscopy (SEM). SEM was performed to observe the surface morphology. Imaging was done at 5, 10, 20, 50, 100, 200 and 500 μm for the sintered samples.

Electrical impedance spectroscopy was carried out in laboratory environment at different temperature (573–973 K) using two-probe method by Kiethley 2450 source meter. The pellets were coated with silver paint on two faces and were dried at 700 °C in the muffle furnace for 30 min in order to make two silver blocking electrodes. Measurements were taken in the voltage range of −1 to 1 V with a step of 0.05 V in the temperature range of 300 °C–700 °C at an interval of 50 °C.

3 Results and Discussion

X-ray diffraction (XRD) conducted at the room temperature for the calcined samples is shown in Fig. 1. In the XRD pattern obtained, one of the phases is identified as monoclinic phase with space group C12/c1 for $SrSiO_3$. Apart from the monoclinic phase, some additional peaks were also observed in both the samples which may be attributed to the polymorphism in the prepared samples. The additional peaks at 20.13°, 20.9°, 31.6°, 30.3°, 42.3° and 48.4° have been star marked in the figure and have been identified as the triclinic polymorph of $SrSiO_3$ as reported by Shahid et al. [6].

Figure 2 shows the Fourier transform–infrared spectroscopy spectra of the samples carried out at room temperature in the scan range of 4000–400 cm^{-1}. Band present at 506.51 is due to vibrational stretching of Si–O. Band at 970.14 cm^{-1} is due to Si–O–Si asymmetric stretch with a red shift, and band at 881.40 cm^{-1} is due to Si–O

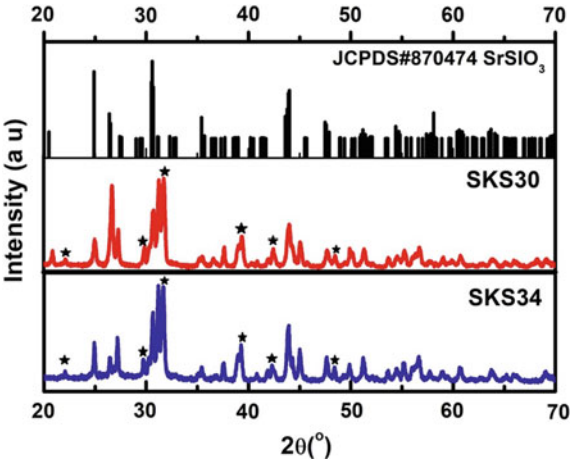

Fig. 1 X-ray diffraction (XRD) pattern for $Sr_{3-3x}K_{3x}Si_3O_{9-\delta}$ (x = 0, 0.20)

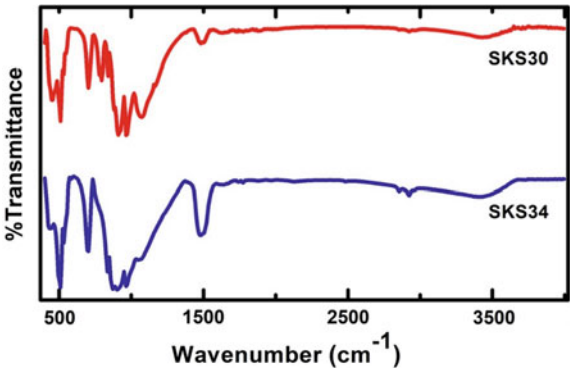

Fig. 2 FT-IR images for $Sr_{3-3x}K_{3x}Si_3O_{9-\delta}$ (x = 0, 0.20)

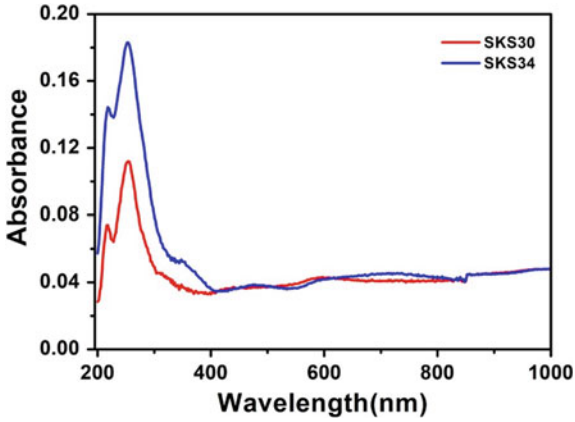

Fig. 3 UV–vis absorption spectra for $Sr_{3-3x}K_{3x}Si_3O_{9-\delta}$ (x = 0, 0.20)

symmetric stretch with a blue shift. Band at 1489 cm^{-1} (with a blue shift) is assigned due to Sr^{2+}. Bands present at 704.18 (with a red shift) and 915.63 $cm^{-1}$are due to the presence of SiO4 group. Band at 797.67 cm^{-1} (with a blue shift) is due to bending vibration of O–Si–O. The band at 3440 cm^{-1} is due to the stretching vibrations of OH^- which indicates hydration of the sample resulting from the absorption of atmospheric moisture [7–9].

UV–visible spectra for the samples are shown in Fig. 3 in the wavelength range of 200–1000 nm. Using the absorbance data, we have determined the optical band gap energy for the samples.

Tauc's equation states that

$$\alpha h\nu = A(h\nu - Eg)^n$$

where α = absorption coefficient, $h\nu$ = energy of the incident light is given by, A = constant, n = constant, and its value depends on the type of electron transition.

By plotting $(\alpha h\nu)^{1/n}$ on the x-axis and $h\nu$ on the y-axis, we can determine the optical band gap energy of the system. Linear part of the Tauc plot is extrapolated, and the optical band gap of the samples has been calculated as shown in Fig. 4.

Figure 5 shows the SEM micrographs of the samples. In SKS30 sample, it is observed that the most of the grains are small in size compared to the SKS34 sample. Some of the grains appear to have been agglomerated. In SKS30 sample, the grains do not have good contact, hence making the sample porous and decreasing its density. In the SKS34, the grains are relatively bigger in size and grains show better contact compared to the undoped sample. In SKS34 sample, another glassy phase is observed at the boundaries which is absent in the parent compound. The undoped SKS30 sample appears to be porous compared to the doped SKS34. On the addition of the dopant, the sample is dense, and the grains have good contact. In earlier literature, it has been stated that this glassy/amorphous phase may be the reason for the increment in the conductivity of these samples.

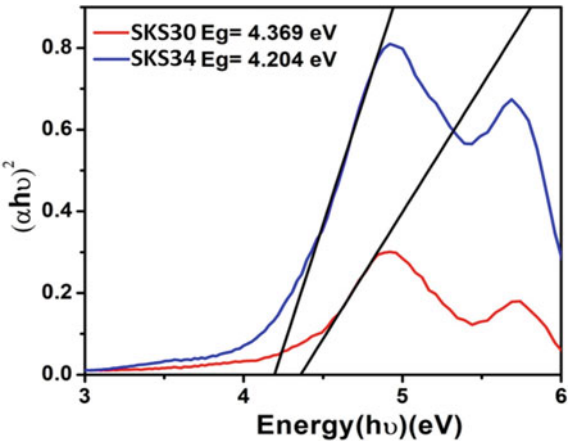

Fig. 4 Tauc plot obtained from UV–vis spectra for $Sr_{3-3x}K_{3x}Si_3O_{9-\delta}$ (x = 0, 0.20)

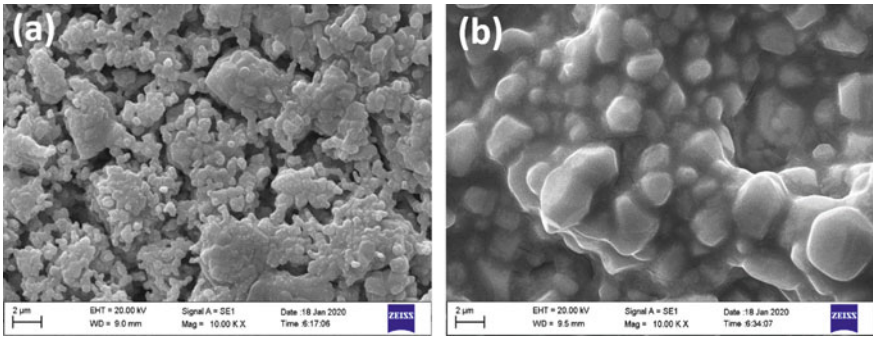

Fig. 5 SEM micrographs for $Sr_{3-3x}K_{3x}Si_3O_{9-\delta}$ (x = 0.0, 0.20), **a** SKS30; **b** SKS34

The electrical conductivity for both the samples was measured in the intermediate temperature range (300–700 °C). Table 1 shows the variation of conductivity with the temperature for both parent and doped concentration. It can be noted with the addition of the dopant, there is sharp increase in the conductivity values at all temperatures. The conductivity values increase by order of two on addition of the dopant till 650 °C, and it increases by order of three at 700 °C. Arrhenius plot for total conductivity for both the samples is shown in Fig. 6, and it is observed that there is an evident increase in the conductivity of the samples with increase in the temperature. The maximum conductivity is reported for SKS34 at 700 °C with conductivity value of 1.06×10^{-4} Scm^{-1}.

Table 1 Conductivity variation for the system in the intermediate temperature range

Compound	Conductivity (Scm^{-1})								
	300 °C	350 °C	400 °C	450 °C	500 °C	550 °C	600 °C	650 °C	700 °C
$Sr_3Si_3O_9$	2.5×10^{-10}	1.92×10^{-9}	8.10×10^{-9}	2.44×10^{-8}	4.29×10^{-8}	1.25×10^{-7}	2.66×10^{-7}	4.19×10^{-7}	5.42×10^{-7}
$Sr_{2.4}K_{0.6}Si_3O_9$	1.12×10^{-8}	6.34×10^{-8}	2.65×10^{-7}	1.13×10^{-6}	3.86×10^{-6}	1.10×10^{-5}	2.92×10^{-5}	6.34×10^{-5}	1.06×10^{-4}

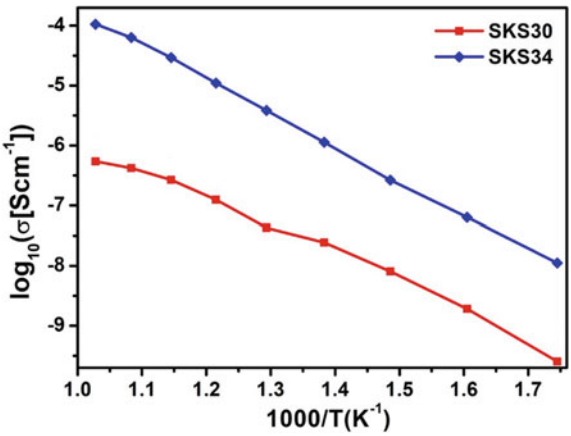

Fig. 6 Arrhenius plot for total conductivity for $Sr_{3-3x}K_{3x}Si_3O_{9-\delta}$ (x = 0, 0.20)

4 Conclusion

Potassium-doped strontium silicate samples were synthesized via solid-state reaction route. The phase formation was investigated via XRD and FTIR. In XRD, monoclinic phase was identified for the system. Ft-IR analysis further supplemented the phase structure. SEM analysis indicated good grain contact in the sintered samples. The sample prepared was dense. It was also observed that two phases were present in the doped sample. The phase present in the grain boundary corresponded to the potassium-rich amorphous sample. Electrical conductivity measurements showed that the conductivity increases on increasing the temperature. It was observed that on doping there was a sharp increase in the conductivity value. Since system shows high conductivity in intermediate temperature range, it may be used as electrolyte for IT-SOFCs.

Acknowledgements Authors acknowledge the support of DST-SERB for the ECRA project (ECR/2016/001152).

References

1. Singh P, Goodenough JB (2012) Energy Environ Sci 5:9626–9631
2. Singh P, Goodenough JB (2013) J Am Chem Soc 135:10149–10154
3. Bayliss RD, Cook SN, Fearn S, Kilner JA, Greaves C, Skinner SJ (2014) Energy Environ Sci 7:2999–3005
4. Xu J, Liu S, Wang Q, Xiaofeng J, Li X, Kuang X (2016) J Mater Chem A 4:6313–6318
5. Basu S, Sood K (2016) RSC Adv 6:20211–20218
6. Katyayan S, Agrawal S (2019) JOM 71:2899–2905
7. Shahid R, Pandey R, Singh P (2020) J Phys Chem Solids 147:109641
8. Ueno A, Hayashi S, Okada K, Otsuka N (1990) J Mater Sci Lett 9:9–12
9. Sahu IP, Bisen DP, Brahme N, Tamrakar RK (2015) J Radiat Res Appl Sci 8:104–109

Variable Dielectric and Ferroelectric Properties in Size-Controlled Cobalt Ferrite

S. Shankar, Vinita Tuli, S. Gaurav, O. P. Thakur, and M. Jayasimhadri

Abstract The nano-form of cobalt ferrite ($CoFe_2O_4$) is fascinating for fabrication of nano-magnets and miniaturized electronic devices. A comparative structural, dielectric, and ferroelectric study of size-controlled cobalt ferrite has been reported. The nanoparticles of cobalt ferrite (CFNP) were prepared via sol–gel method and subsequent heat treatments. With the altering of reaction reactants and temperature, the size has been varied from 10 to 80 nm. The XRD studies confirm the variation of size in CFNPs. The frequency variation of dielectric permittivity of CFNP display dependence of crystallite size. The thermal variation of dielectric constant indicates the presence of relaxation phenomena. The P–E ferroelectric hysteresis loop measurements display enhanced ferroelectricity in CFNP with improved properties.

Keywords XRD · Dielectric · Ferroelectric

1 Introduction

Nanomaterial is the heart of nanotechnology which can offer benefits of remarkable relative surface area and ultra-small size. These features assist in attaining excellent electrical, mechanical, optical, magnetic properties, and chemical reactivity [1–5]. Among nanoparticles, synthesis of spinel-type ferrite structures has gain immense

S. Shankar (✉) · V. Tuli
Experimental Research Laboratory, Department of Physics, ARSD College, University of Delhi, Dhaula Kuan, New Delhi 110021, India
e-mail: sssubramaniam@arsd.du.ac.in

S. Shankar · M. Jayasimhadri
Luminescent Materials Research Laboratory, Department of Applied Physics, Delhi Technological University, Bawana Road, Delhi 110042, India

S. Gaurav
Department of Applied Physics, Amity Institute of Applied Sciences, Amity University, Noida, Uttar Pradesh 201313, India

O. P. Thakur
Materials Analysis and Research Laboratory, Department of Physics, NSUT Dwarka, New Delhi 110078, India

S. B. Krupanidhi et al. (eds.), *Advanced Functional Materials and Devices*, Springer Proceedings in Materials 14, https://doi.org/10.1007/978-981-16-5971-3_4

attention in recent years in the field of ceramics. These nano-spinel ferrites are attractive because of remarkable electrical as well magnetic characteristics, which are relatively less in their bulk counter parts. Consequently, they are exciting because of characteristics as well as potential ability in the areas of semiconductor technology, biotechnology, and medical facilities [1–4].

Cobalt ferrite ($CoFe_2O_4$) is one of the best ferromagnetic materials that has been considered as vital component because of strong semiconducting nature and minimum losses [2, 6]. Nanosized $CoFe_2O_4$ possesses spinel cubic structure with widely explored electric and magnetic characteristics. These features are dependent on ionic distribution at octahedral and tetrahedral sites in cubic unit cell. $CoFe_2O_4$ nanoparticles (CFNPs) exhibit electric nature because of manifestation of dipoles via transferring of charges among multivalent Fe ions. These CFNPs parade robust structure stability and is vital for device applications [1, 7–9].

The synthesis of CFNP with essential physical characteristics and constituent reactivity play key role in devices. Over the last two decades, different methods like co-precipitation, sol–gel, and auto-combustion have evolved for preparation of CFNPs [1, 7–9]. In all these methods, by controlling the mixing extent, homogenous-sized particles can be prepared. In additions, these procedures offer regulation of sizes and shapes of CFNPs. Particularly high-quality yield of CFNPs is preparation as well as synthesis parameters dependent such as like fuel ratio, pH, mixing temperature and sintering temperature. The combustion process mainly affects the size, purity, and coagulation. In this work, we have adopted sol–gel auto-combustion method along with variation of the mixing temperature of the solutions. The corresponding changes in structure as well electrical properties are observed.

2 Experimental

11.6 gm of cobaltous nitrate ($Co(NO_3)_2.6H_2O$) and 16 gm of ferric nitrate ($Fe(NO_3)_3.9H_2O$) were mixed separately in 20 ml of deionised water. The metal salt solutions were stirred and mixed together with the help of citric acid and ethylene glycol in ratio of l:6:4. The temperature required for the synthesis of cobalt ferrite nanoparticles was kept low and maintained between 50 and 110 °C in steps of 20°. The sol was heated to until dried and was followed by auto-combustion. The nanoparticles prepared were labeled as A, B, C, and D at 110, 90, 70, and 50 °C, respectively. The samples were ground properly and were sintered at 700 °C for 4 h.

3 Results and Discussions

3.1 Structural Analysis

The powder X-ray diffraction pattern of different CFNPs is plotted in Fig. 1a. The XRD spectra of CFNPs A–D shows clearly resolved peaks and confirm the high-purity single phase. The XRD peaks are labeled using JCPDS # 08-0234 for face-centered CFO. Figure 1b shows the enlarged XRD pattern of CFNPs in the 2θ range of 34–37°. It can be observed that the peaks shift to lower 2θ side with increasing crystallite size. The particle size t of CFNPs was computed with the help of Debye–Scherrer's relation

$$\beta = \frac{k\lambda}{t \cdot \cos\theta} + 4\varepsilon \cdot \tan\theta$$

where t, λ, ε, and β denote the size of nanoparticles, wavelength, and full width at half maxima, respectively. The constant k takes value of 0.9 [6, 10–12].

The crystallite size is observed to increase from 10 nm for CFNP-D to 80 nm for CFNP-A as temperature is increased from 50 to 110 °C. The effect of increase in temperatures is to increase the lattice parameters and decrease β. In other words, we can say the decrease in β is mainly due to increase in crystallite size and decrease in the strains due to mixing at higher temperatures [5] (Table 1).

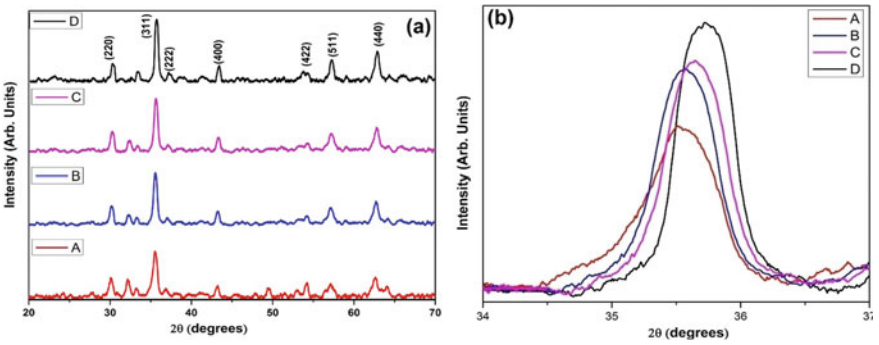

Fig. 1 **a** XRD pattern of CNFPs; **b** enlarged XRD pattern of CNFPs

Table 1 Crystallite size and micro-strain of CFNPs

Sample	Mixing temperature (°C)	Crystallite size (t) (nm)	Micro-strain
A	110	80	0.531
B	90	53	0.594
C	70	28	0.652
D	50	10	0.738

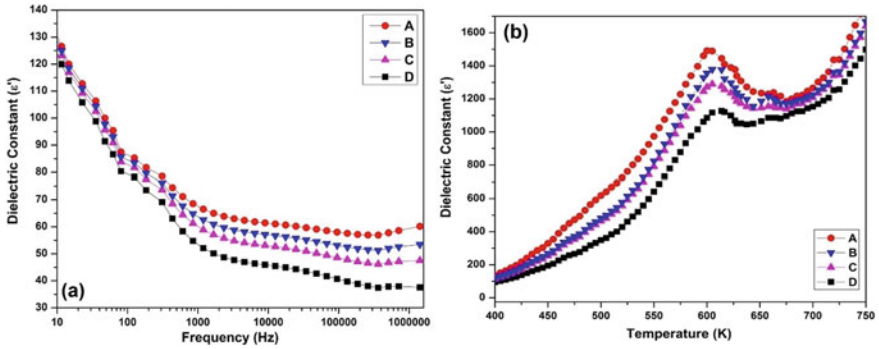

Fig. 2 **a** Dielectric permittivity of CFNPs at room temperature; **b** dielectric permittivity of CFNPs at different temperatures

3.2 Dielectric Properties

Figure 2a displays the variation of dielectric permittivity with frequency for CFNPs. These alterations are understood with the help of space charge phenomena of multivalent Fe ions as explained by Maxwell–Wagner and Koop. As these Fe ions are completely polarized, at low frequency, the dielectric permittivity is high. On the contrary, permittivity tends to decrease on increasing the frequency since the charges are incapable of following the oscillations. It can also be observed that CFNP-A has higher dielectric constant as compared to CFNP-D because of larger crystallite size and improved crystallinity [10, 11].

The plot of temperature-dependent dielectric permittivity in CFNPs is shown in Fig. 2b. It can be observed from the plot that all CFNPs exhibit an anomaly near 600 K and indicate the presence of relaxation process in CFNPs. This anomaly is attributed to ferroelectric transition temperature and matches with earlier works. Further, it is noted that the transition temperature increases from 600 K in CFNP-D to 615 K in CFNP-A due to increase in size of grains. The increase in grain size results in increased conductivity and subsequently dielectric constant. The magnitude of permittivity increases from 1100 in CFNP-D to 1500 in CFNP-A because of increased density in CFNPs. In addition, as the charge suffers thermal activation, increased hopping also contributes to enhanced dielectric permittivity [10, 11, 13, 14].

3.3 Ferroelectric Properties

P–E hysteresis loops of CFNPs at room temperature measured are displayed in Fig. 3. These ferroelectric loops exhibit oval non-saturated behavior, and P–E loops have rounded corners and imply low ferroelectric nature of CFNPs. This large leaky behavior is due to strong magnetic nature of CFNPs which results in coagulation of

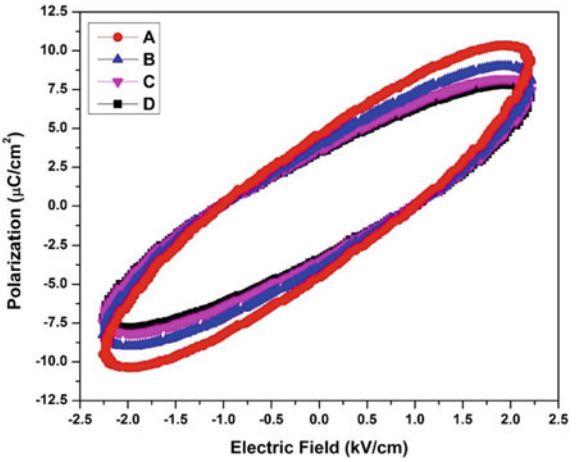

Fig. 3 Ferroelectric hysteresis plot of CFNPs

nanoparticles to one another. In addition, CNFP-A exhibits higher maximum polarization as compared to CNFP-D due to the improvement in grain size, crystallite size and improved crystallinity [15, 16].

4 Conclusion

The nanoparticles of cobalt ferrite (CFNP) were prepared via sol–gel method and subsequent heat treatments. With the altering of temperature, the size has been varied from 10 to 80 nm. The XRD studies confirm the variation of size in cobalt ferrite. The thermal variation of dielectric constant indicates presence of relaxation phenomena. The frequency variation of dielectric permittivity display dependence of crystallite size. The P–E ferroelectric hysteresis loop measurements display enhanced ferroelectricity in CFNP with improved properties. The size dependency of CFNPs on structural, dielectric, and ferroelectric properties makes them suitable for tunable electric devices.

Acknowledgements This work is funded by Research Scheme no. 03(1427)/18/EMR-II, CSIR, New Delhi, and supported by USIC, University of Delhi, New Delhi, India, for characterization facilities.

References

1. Cernea M, Radu R, Amorín H, Greculeasa SG, Vasile BS, Surdu VA, Ganea P, Trusca R, Hattab M, Galassi C (2020) Nanomaterials 10:672
2. Lather S, Gupta A, Dalal J, Verma V, Tripathi R, Ohlan A (2017) Ceram Int 43:3246–3251

3. Mo HL, Jiang DM, Wang CM, Zhang WG, Sen Jiang J (2013) J Alloys Compd 579:187–191
4. Wang J, Zhao F, Wu W, Cao S, Zhao G (2012) Phys Lett A 376:547–549
5. Kumar M, Shankar S, Thakur OP, Ghosh AK (2015) Mater Lett 143:241–243
6. Ranjith Kumar E, Jayaprakash R, Arunkumar T, Kumar S (2013) J Phys Chem Solids 74:110–114
7. Zhang D, Cheng J, Chai J, Deng J, Ren R, Su Y, Wang H, Ma C, Lee CS, Zhang W, Zheng GP, Cao M (2018) J Alloys Compd 740:1067–1076
8. Kumar M, Shankar S, Tuli V, Mittal S, Joshi V, Jha MK, Gupta G (2020) Natl Acad Sci Lett
9. Bhagwat VR, Humbe AV, More SD, Jadhav KM (2019) Mater Sci Eng B Solid-State Mater Adv Technol 248:114388
10. Shankar S, Thakur OP, Jayasimhadri M (2020) J Mater Sci Mater Electron 31:12226–12237
11. Shankar S, Maurya I, Raj A, Singh S, Thakur OP, Jayasimhadri M (2020) Appl Phys A 126:686
12. Thankachan S, Jacob BP, Xavier S, Mohammed EM (2013) J Magn Magn Mater 348:140–145
13. Balavijayalakshmi J, Suriyanarayanan N, Jayaprakash R, Gopalakrishnan V (2013) Phys Procedia 49:49–57
14. Krishna Surendra M, Kannan D, Ramachandra Rao MS (2011) Mater Res Soc Symp Proc 1368:66–71
15. Kumar M, Shankar S, Kumar S, Thakur OP, Ghosh AK (2016) J Mater Sci Mater Electron 27:6849–6853
16. Shankar S, Kumar M, Kumar S, Thakur OP, Ghosh AK (2017) J Alloys Compd 694:715–720

Investigation on Ionic Conductivity and Raman Spectroscopic Studies of Ionic Liquid Immobilized PEO-Based Polymer Electrolytes

Sujeet Kumar Chaurasia, Abhishek Kumar Gupta, Sarvesh Kumar Gupta, Shivani Gupta, Pramod Kumar, and Manish Pratap Singh

Abstract The ionic conductivity and Raman spectroscopic studies are reported for ionic liquid (IL)-based polymer electrolyte [PEO:$LiPF_6$ (as salt)] + $BMIMPF_6$ (as IL) in which the dopant salt and IL have common anion PF_6^-. These results are compared with another IL-based polymer electrolyte system with mixed anions (ClO_4^- & PF_6^-). X-ray diffraction (XRD) results showed that the structural modification in the polymer PEO matrix due to the change in its crystalline structure after the incorporation of salt and/or IL that gives reduced crystallinity (or enhanced amorphous content) of the polymer electrolyte films which, in turn, is accountable for enhancement in ionic conductivity. Raman spectroscopic analysis confirmed the occurrence of ion–polymer and ion–ion association/interaction phenomena in these polymer electrolyte membranes which is partly responsible for determining the number of mobile ions concentrations and hence ionic mobility. Furthermore, composition-dependent ionic conductivity results are discussed on the basis of changes in ion–polymer and ion–ion interactions as well as changes in the degree of crystallinity/amorphicity of the membranes.

Keywords Polymer electrolyte · Ionic liquid · Raman study · Ion–ion interaction

S. K. Chaurasia (✉)
Centre for Nanoscience and Technology, Professor Rajendra Singh (Rajju Bhaiya) Institute of Physical Sciences for Study and Research, V.B.S. Purvanchal University, Jaunpur 222003, India

A. K. Gupta · S. K. Gupta · S. Gupta
Department of Physics and Material Science, Madan Mohan Malviya University of Technology, Gorakhpur 273010, India

P. Kumar
Department of Chemistry and Chemical Science, School of Physical and Material Sciences, Central University of Himachal Pradesh, Dharamshala 176215, India

M. P. Singh
Department of Physics, Faculty of Engineering and Technology, V.B.S. Purvanchal University, Jaunpur 222003, India

S. B. Krupanidhi et al. (eds.), *Advanced Functional Materials and Devices*, Springer Proceedings in Materials 14, https://doi.org/10.1007/978-981-16-5971-3_5

1 Introduction

Over the last few decades, lithium (Li)-ion batteries have seen instant development with different applications in energy storage, hybrid vehicles and wearable electronic devices [1, 2]. Polymer electrolytes play key role in determining the performances of the variety of electrochemical devices like rechargeable batteries, supercapacitors, etc., by enhancing safety and cycling stability of these devices [3]. Ionic conductivity has been discovered in polar polymers such as poly (ethylene oxide) PEO complexes with appropriate ionic salts (cations as ions of lithium, sodium or ammonium) [4]. The polymer matrix amorphicity and flexibility of the polymeric backbone both play a major role in regulating the conductivity by suppressing the crystallization dynamics of the polymeric matrix. Plasticizers which are low molecular weight organic solvents were earlier used comprehensively for suppressing the crystalline phases in the polymer matrix to give more amorphous and flexible backbone giving high ionic conductivity [5]. With the advent of ionic liquids, which are low melting point molten salts having some remarkable properties such as high ionic conductivity, wide electrochemical window and wider temperature range of operation used for achieving the same goal [6]. When ionic liquid is incorporated into a polymer matrix, it increases amorphicity and the mobile ions number that emerge from the dissociated cations and anions of ionic liquid [7]. In recent years, amalgamations of polymer and ion conducting electrochemically stable ionic liquids with or without dopant ionic salt have been discovered as suitable polymer electrolytes [8–11]. In our recent study [12] on (PEO:$LiClO_4$) + ionic liquid (1-butyl-3-methylimidazolium hexafluorophosphate, $BMIMPF_6$), we got that conductivity first decreased with dopant ionic liquid concentration and afterward increased, while the amorphicity monotonically decreased with cumulative ionic liquid content. To explain this, we invoked the establishment of solvent separated contact ion pairing (Li^+ - - - - ClO_4^-; $BMIM^+$ - - - - PF_6^-) between dopants and cross-contact ion pairing (Li^+ - - - - PF_6^-; $BMIM^+$ - - - - ClO_4^-) in co-dopants (i.e., combination of salt cation with IL anion and IL cation with salt anion). Note that such type of IL-based polymer electrolyte is a 'mixed anion system'. It is known that mixed cation and anion effects in polymer electrolytes have significant role in controlling overall ionic conductivity of the membranes [13]. To resolve the role of cross-contact ion pairs, this paper reports conductivity and Raman studies on IL-containing polymer electrolyte PEO:$LiPF_6$ + IL (as $BMIMPF_6$) membranes in which the complexing salt and IL have common anions (PF_6^-) with no prospect of developing cross-contact ion pairs. Interestingly, it is found that the conductivity does show a regular increasing trend with increasing IL content (which increases amorphicity) in these same anion systems, and Raman spectral analysis is used as a supporting tool to identify the existence of contact ion pairs.

2 Experimental

The polymer PEO (mol. wt. 6×10^5 g/mol, Aldrich) as host polymeric matrix and lithium hexafluorophosphate ($LiPF_6$, Aldrich) as the dopants salt and ionic liquid (IL) (1-butyl-3-methylimidazolium hexafluorophosphate, $BMIMPF_6$, Sigma Aldrich, Germany) were used as starting materials. The polymer electrolyte films (PEs) PEO: 10 wt% $LiPF_6 + x$ wt% IL for $x = 0$, 5, 10, 15 and 20 were synthesized by using standard solution casting procedure as described by us earlier [14]. Abbreviations of the PEs used in the present study are as follows: '**PE*x*:** (PEO: $LiPF_6$) + x wt% IL, **PE0:** PEO:10 wt% IL, **PE1:** PEO:10 wt% $LiPF_6$, **PE2:** PEO:10 wt% $LiPF_6$ + 5 wt% IL, **PE3:** PEO:10 wt% $LiPF_6$ + 10 wt% IL, **PE4:** PEO: 10 wt% $LiPF_6$ + 15 wt% IL, **PE5:** PEO: 10 wt% $LiPF_6$ + 20 wt% IL.'

The X-ray diffraction patterns of the polymer electrolyte films were recorded by using Philips X-ray diffractometer (PW 1710). The complex impedance spectroscopic technique is used for measuring the ionic conductivity of polymeric films using Wayne Kerr impedance analyzer model 6500B in the frequency range 20 Hz–5 MHz. Raman spectra of PEs films were recorded in the region 700–1200 cm^{-1} by using Renishaw micro-Raman setup (Model RM1000) with an Ar ion laser of wavelength 514.5 nm as excitation source.

3 Results and Discussion

The polymer PEO–salt complex system is generally semicrystalline in nature in which cation of the dopant salt complexes with the ether oxygen of polymer PEO backbone and the dissociated anion reside outside the polymeric chain. The cations move by hopping to different sites in the polymer chain while the anions generally move in amorphous phase [15]. The structural modification in the polymer PEO backbone due to the incorporation of ionic salt and/or ionic liquid (IL) involves changes in its crystalline structure which is reflected in terms of enhanced amorphicity (or decreased crystallinity) and hence partly responsible for enhanced ionic conductivity of the polymer electrolytes.

3.1 X-ray Diffraction (XRD) Study

The XRD pattern of pure PEO along with typical polymer electrolyte membranes (**PE0**: PEO + 10 wt% $LiPF_6$, **PE5:** PEO + 10 wt% $LiPF_6$ + 20 wt% IL) is shown in Fig. 1. The polymer PEO consists of the predominant peaks mainly in the range $2\theta = 15°–25°$ along with some minor peaks beyond this range [16, 17]. These crystalline peaks are essentially the signature of the presence of crystalline phases in the polymer PEO. It can also be seen that in the XRD pattern of pure PEO, these crystalline peaks

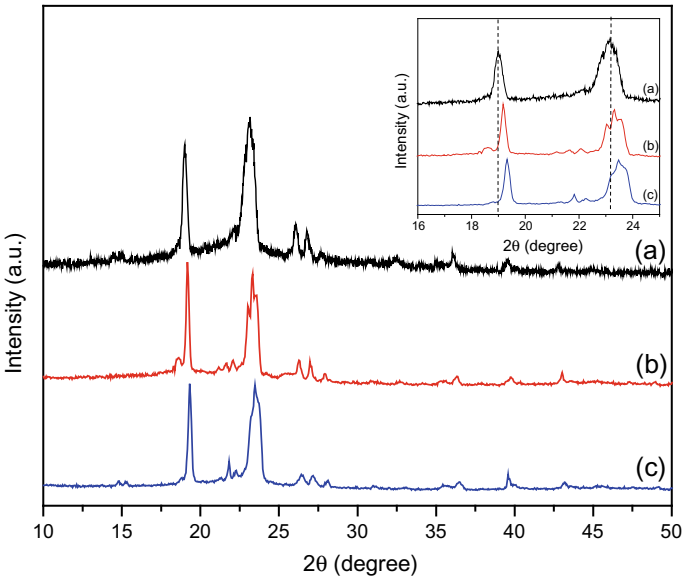

Fig. 1 X-ray diffraction patterns of **a** pure PEO, **b PE0:** PEO + 10 wt% $LiPF_6$ and **c PE5:** PEO + 10 wt% $LiPF_6$ + 20 wt% IL

are riding over a small broad 'halo' which is essentially representing the amorphous phase present in the membranes. This confirms the overall semicrystalline nature of the polymer PEO [18]. Upon incorporation of the salt $LiPF_6$ and/or IL to the pure polymer PEO, the following two observations can be clearly observed:

(1) "Halo" is less prominent in pure PEO than the polymer electrolyte membranes PE0 or PE5. The increasing area of the halos upon addition of salt and/or IL to the PEO is an indicative of the increase in the amorphicity (or decreased crystallinity) of the polymer electrolyte membranes.

(2) Intensities of the predominant crystalline peaks of PEO are found to decrease along with disappearance of some minor diffraction peaks, and only two broaden peaks observed near $2\theta = 19°$ and 23° remain. The reduction in intensities of the peaks infers to an enhancement in the amorphous content in the polymer electrolyte membranes PE0 and PE5.

On the closer observations of the diffraction peaks of PEO, we also observed that electrolytes PE0 and PE5 exhibited slightly shifted and split broaden peaks with reduced intensity (as shown in inset of Fig. 1). This shift could be because of the slight change in the PEO structure geometry because of the interaction/complexation of the polymer PEO with the added salt $LiPF_6$ and/or IL ($BMIMPF_6$).

3.2 *Effect of IL on Polymer Electrolyte's Conductivity*

For a polymer electrolyte "PEO + wt.% $LiPF_6$" with added IL, both amorphicity and number of charge carrier ions are expected to improve with increasing IL content. The assessed magnitudes of σ of PEx along with the results for another mixed anion-type IL-based polymer electrolyte system 'PEO:$LiClO_4$ + *x* wt% IL' [12] for distinct '*x*' values are shown in Fig. 2.

The conductivity results for the present electrolyte system PEx follow the expected behavior as observed for many polymer–salt and/or ionic liquid complexes [19–22] and can be explained on the basis of change in amorphicity of the membranes with IL content. However, this is in contradiction to earlier obtained conductivity results for the polymeric system of mixed anions: (PEO: $LiClO_4$) + IL. The latter was explained by us [23] invoking the existence of neutral contact ion pairs: (Li^+ - - - - ClO_4^- & $BMIM^+$ - - - - PF_6^-) and cross-contact ion pairs: (Li^+ - - - - PF_6^- & $BMIM^+$ - - - - ClO_4^-) between dopants and co-dopants, respectively. It may be remarked here that in the existing arrangement both the salt and IL have same anions (PF_6^-), while our previous analyzed system was a mixed anion arrangement, and the two anions were different (ClO_4^- & PF_6^-). So, there is no chance of the creation of cross-contact ion pairing in the present case while it exists in the latter case. To confirm the contention outlined above, it is important to study polymer–salt complexation (i.e., ion–polymer interaction) and the ion pairing (i.e., ion–ion interaction) which has been done by Raman studies discussed below.

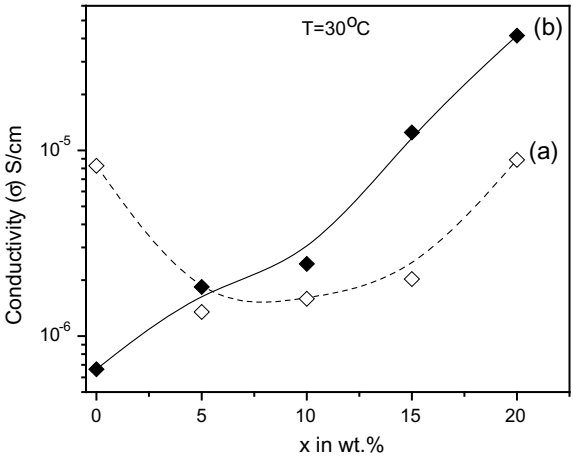

Fig. 2
Composition-dependent conductivity for **a** PEO:10 wt% $LiClO_4$ + *x* wt% IL and **b PE***x*: PEO:10 wt% $LiPF_6$ + *x* wt% IL for distinct values of '*x*'

3.3 Raman Study on Polymer Electrolytes

3.3.1 Complexation of Polymer Chain with the Cations (Li^+ and $BMIM^+$) of Ionic Salt and Ionic Liquid

When the ionic salt and/or IL or both are mixed simultaneously with PEO to get a polymer electrolyte, then there is a possibility of ether oxygen of PEO (i.e., C–O–C bond) to complex with the cations of added dopants as salt and IL. This complexation will be reflected by the changes in the vibrational bands involved in the complexation, i.e., C–O–C, CH_2 and CO bands in PEO. The Raman spectra of pristine PEO and PE0, PE1 and PE5 in the region 700–1200 cm^{-1} are shown in Fig. 3.

The vibrations related to the combined C–C bond stretching + CH_2 bond wagging and (C–O–C + C–C) bonds stretching of pure PEO lie at 1126 and 1142 cm^{-1}, respectively [24]. These bands shift in the Raman spectrum of PE0, PE1 and PE5 (for detail see inset of Fig. 3). Because of the coordination of cations salt (Li^+) and IL ($BMIM^+$) with the ether oxygen, i.e., C–O–C bond of the polymer PEO chain, these detected spectral alterations show changes in the configurational states of the PEO–salt and/or IL.

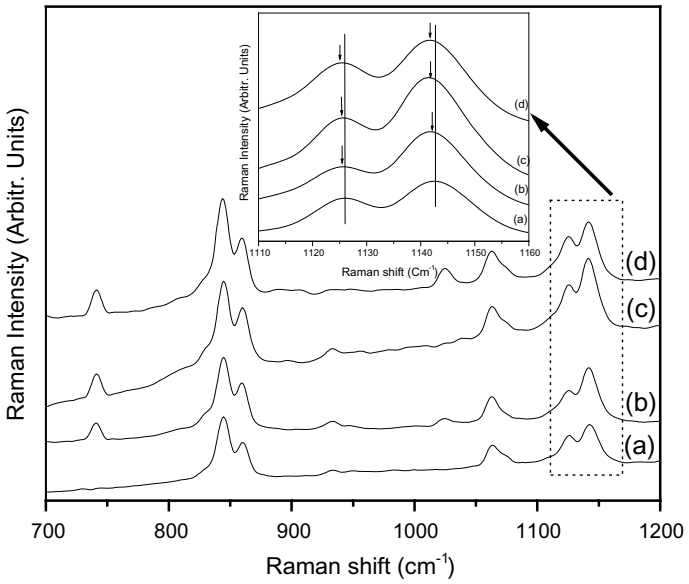

Fig. 3 Raman spectra of polymer electrolyte films **a** PEO, **b** PE0, **c** PE1 and **d** PE5 in the spectral region 700–1200 cm^{-1}

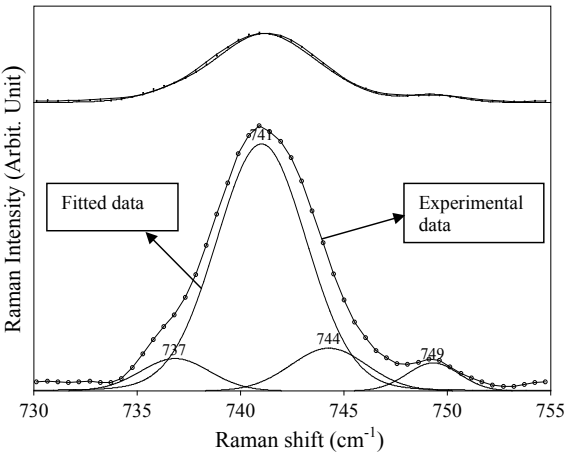

Fig. 4 Deconvoluted Raman peaks of PF_6^- anion symmetric stretching vibrations in PE5

3.3.2 Ion Pairing Effect in PEx

In polymer electrolytes, symmetric modes of vibration of anions have been widely used to investigate the different ionic configurations that result in the establishment of ion pairs with or without higher-order ionic clusters [25]. The free anion in the polymer electrolyte used in this study is PF_6^-. It can form ion pairs with Li^+ (Li^+ - - - - PF_6^-) or $BMIM^+$ ($BMIM^+$ - - - - PF_6^-). Consequently, observing the symmetric vibrational stretching mode of anion PF_6 observed at 741 cm^{-1} [26] will be very useful for studying ion pairing. With the assistance of PeakFit 4.12 software, different peak positions were achieved by deconvolution of this peak. The expanded typical Raman spectra in the region 730–755 cm^{-1} for monitoring the PF_6 vibration at 741 cm^{-1} for PE5 polymer electrolytes are exhibited in Fig. 4.

There are four peaks in the spectra of PE5 as (i) 741 cm^{-1} because of the symmetric stretching vibration of free PF_6 anion, (ii) 744 cm^{-1} due to the existence of contact ion pairs $BMIM^+$ - - - - PF_6^- (iii) 749 cm^{-1} due to the development of contact ion pairs Li^+ - - - - PF_6^- and (iv) a smaller frequency side peak at 737 cm^{-1} due to the formation of more complex ionic clusters. As expected, both of the ion pair peaks due to Li^+ - - - - PF_6^- and $BMIM^+$ - - - - PF_6^- appear in spectra of PE5 (see Fig. 4 for detail) alongside the free PF_6^- and ionic clusters peak. Interestingly, no additional peak due to the cross-contact ion pairing is neither expected nor seen in the existing electrolyte system because the anions of the two dopants as ionic liquid ($BMIMPF_6$) and lithium salt ($LiPF_6$) are identical. Moreover, in mixed anion system which was earlier studied by us [12, 23] showed the formation of cross-contact ion pair peak whose existence significantly affected the overall ionic conductivity of the polymer electrolytes.

4 Conclusions

Polymer electrolyte films PEx based on polymer PEO and lithium salt ($LiPF_6$) with various amount of dopant ionic liquid (IL) concentration 'x,' have been synthesized and studied. The chosen salt and dopants IL have common anion PF_6^-. The conductivity increased with varying amounts of IL in (PEO + salt) polymer electrolyte system which was explained on the basis of increase in amorphicity of the polymeric membranes. The conductivity vs. IL content behavior of the present IL-based electrolyte is found to be different from our earlier reported [12] electrolyte where the salt anion was ClO_4^- and the IL-anion was PF_6^- (mixed anion system). Raman spectroscopic studies are also reported for obtaining information about ion–polymer and ion–ion interactions and their role in controlling overall conductivity of the present electrolyte system.

Acknowledgements Authors acknowledge Prof. Rajendra Kumar Singh, Department of Physics, Institute of Science, Banaras Hindu University, Varanasi, India, for providing the experimental facilities and fruitful discussions.

References

1. Armand M, Endres F, MacFarlane DR, Ohno H, Scrosati B (2009) Nat Mater 8:621–629
2. Zhou W, Li Y, Xin S, Goodenough JB (2017) ACS Cent Sci 3:52–57
3. Chen N, Zhang H, Li L, Chen R, Guo S (2018) Adv Energy Mater 8:27. 1702675
4. Mindemark J, Lacey MJ, Bowden T, Brandell D (2018) Prog Polym Sci 81:114–143
5. Maheshwaran C, Kanchan DK, Mishra K, Kumar D, Gohe K (2020) J Mater Sci: Mater Electron 31:15013–15027
6. Ohno H (ed) (2005) Electrochemical aspects of ionic liquids. Wiley, New Jersey
7. Watanabe M, Thomas ML, Zhang S, Ueno K, Yasuda T, Dokko K (2017) Chem Rev 117:7190–7239
8. Lewandoski A, Swiderska A (2004) Solid State Ionics 169:21–24
9. Kim SK, Park SJ (2009) J Electrochim Acta 54:3775–3780
10. Singh VK, Shalu, Chaurasia SK, Singh RK (2016) RSC Adv 6:40199-402010
11. Lin D, Liu W, Liu Y, Lee HR, Hsu PC, Liu K, Cui Y (2016) Nano Lett 16:459–465
12. Chaurasia SK, Sing RK, Chandra S (2011) J Poly Sci Part B: Polym Phys 49:291–300
13. Chandra A, Chandra S (1994) J Phys D: Appl Phys 27:2171–2179
14. Chaurasia SK, Singh RK, Chandra S (2011) Solid State Ionics 183:32–39
15. Papke BL, Ratner MA, Shriver DF (1981) J Phys Chem Solids 42:493–500
16. Arya A, Sharma AL (2020) Polym Bull 77:2965–2999
17. Huang Y, Ma M, Guo Y (2020) J Polym Sci 58:466–477
18. Karmakar A, Ghosh A (2014) AIP Adv 4:087112–087117
19. Ye YS, Rick J, Hwang BJ (2013) J Mater Chem A 1:2719–2743
20. Arya A, Sharma AL (2018) J Solid State Electrochem 22:2725–27451
21. Singh P, Bharati DC, Gupta PN, Saroj AL (2018) J Non-Cryst Solids 494:21–30
22. Chaurasia SK, Chandra A (2017) Solid State Ionics 307:35–43

23. Chaurasia SK, Singh RK, Chandra S (2011) J Raman Spectrosc 42:2168–2172
24. Chrissopoulou K, Andrikopoulos KS, Fotiadou S, Bollas S, Karageorgaki K, Christofilos D, Voyiatzis GA, Anastasiadis SH (2011) Macromolecules 44:9710–9722
25. Branca C, Faraone A, Magazu S, Maisano G, Migliardo P, Villari V (2000) J Mol Liq 87:21–23
26. Morales D, Ruther RE, Nanda J, Greenbaum S (2019) Electrochim Acta 304:239–245

Investigating the Defective Structural Sites in Ge–Sb–Te-Based Phase Change Memory Materials

Manisha Upadhyay and Sevi Murugavel

Abstract GeTe is an important ingredient of GeTe–Sb_2Te_3 pseudo-binary alloy having important applications in phase change memory (PCM) applications. Electronic information storage applications have found PCMs as the emerging successors which are presently employed in rewritable data storage devices due to their fast crystallization speed (Meijer in Science 319:1625, 2007 [1]; Kolobov et al. in Nat Mater 3:703, 2004 [2]; Caravati et al., Appl Phys Lett 91:171906, 2007 [3]). In spite of great technological interest several of the microscopic properties such as local environment of the constituent species and presence of atomic vacancies/defects in amorphous and crystalline phases are still under debate (Mazzarello et al. Phys. Rev. Lett. 104:085503, 2010 [4]; Kohara et al., Appl Phys Lett 89: 201910, 2006 [5]; Upadhyay et al., J Appl Phys 110:083711, 2011 [6]). The concept of highly disordered crystalline phase predicts interrelation of defects (as inherited) in phase change property and atomic vacancies which might cause the phase change process to proceeds on a sub-nanosecond timescale. The present work has provided detailed structural analysis in various GST alloys in thin film and bulk form. These results have provided us a deeper insight on the effect of atomic structural rearrangements of the switched crystal phase to better recognize the PCM structure.

1 Introduction

Chalcogenide materials based on stoichiometric GeTe and Sb_2Te_3 are the currently favored collection for phase change memory applications. These materials are promising candidates for the emerging electronic information storage applications

M. Upadhyay (✉)
Atma Ram Sanatan Dharma College, South Campus, University of Delhi, New Delhi 110021, India

S. Murugavel
Department of Physics & Astrophysics, University of Delhi, New Delhi 110007, India

S. B. Krupanidhi et al. (eds.), *Advanced Functional Materials and Devices*, Springer Proceedings in Materials 14, https://doi.org/10.1007/978-981-16-5971-3_6

and are presently employed in rewritable data storage devices due to their fast crystallization speed [1]. In spite of great technological interest several of the microscopic properties such as local environment of the constituent species and presence of atomic vacancies/defects in amorphous and crystalline phases are still under debate. For example, EXAFS studies performed by Kolobov et al. on amorphous and crystalline states of $Ge_2Sb_2Te_5$ reveals that coordination changes from six to four for Ge/Sb atoms while moving from crystalline to amorphous state with a subsequent shortening of covalent bond lengths [2]. Subsequently, first principle simulation and ab initio methods have been used to explore the local environment of Ge atoms in both the switching states, i.e., amorphous as well as crystalline [3, 4]. These studies revealed about the simultaneous existence of tetrahedral as well as octahedral Ge coordination corresponding to amorphous stoichiometric GeTe and $Ge_2Sb_2Te_5$.

On the other hand, the models based on reverse Monte-Carlo (RMC) lead to larger uncertainties when fitted to the total scattering function for a-$Ge_2Sb_2Te_5$ [5]. Apart from the distorted octahedral environment of Ge/Sb sites, presence of different defective tetrahedral germanium units ($GeTe_{4-n}Ge_n$, $n = 2$) has been detected in crystalline state of PCM which supports the existence of very high density of inherent defects along with vacancies [6]. The size of defect volume (cavity) has been quantified and is of the order of about 70–90 $Å^3$ in amorphous and crystalline state of binary Ge–Te system by theoretical and experimental methods [7, 8]. Furthermore, these studies have found that defect concentration is larger in crystalline state, and hence, crystalline state is more disordered as compared to the amorphous state. Subsequently, these results are further supported by the XANES and density functional theory (DFT) studies on Ge–Sb–Te (GST) alloys which reveal that the bonds become shorter and stronger and more importantly, 'locally ordered' on amorphization for typically covalently bonded solids [2, 9]. These results further conclude that the presence of defects in crystalline state has bond energy hierarchy promoting the presence of stronger bonds and further destruction of weaker bonds which implies the loss of long-range order. The concept of highly disordered crystalline phase has raises the question if there is a some relation among defects in phase change property and present small voids in the form of vacancies which might cause the phase change process to proceeds on a sub-nanosecond timescale. Therefore, in the last few years, research on crystalline state of PCM is seeking great attention. The crystallization process in GST alloys is represented using optical [10, 11], electrical [12, 13], x-ray diffraction [14, 15] and microscopic studies [16–18]. The aim for all these studies is to determine the energy required for phase transformation process which would enable to correlate the crystallization speed and power consumption. In-depth investigations and more compelling characterization of amorphous and crystalline state of PCM would further facilitate the search for better performing materials. Generally, one can summarize GST-based Sb_2Te alloys as shown in Fig. 1 showing few stoichiometric compositions.

GST-based phase change materials are basically mGeTe$-n$$Sb_2Te_3$ where $m{:}n =$ 1:1, 1:2, 2:1 called as GST-147, GST-124 and GST-225, respectively. Depending upon the crystallization temperature, these compositions have two crystalline states, one is meta-stable state having NaCl like structure and another is stable state having

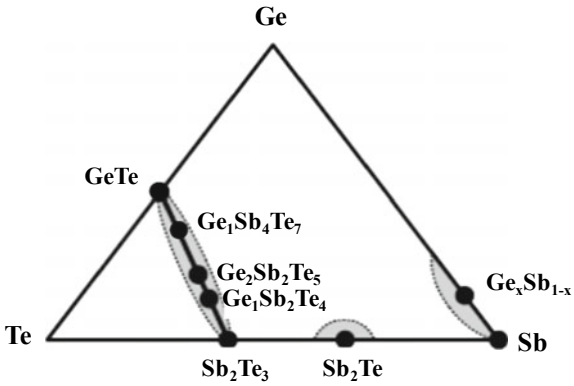

Fig. 1 Ternary phase diagram representing the location for various stoichiometric compositions of GST alloys [19]

hexagonal phase. The stable hexagonal phase for these GST-based alloys shows alternative layered structure of Ge (or Sb) and Te atoms. But this stable hexagonal structure has no role in rewritable phase change memory devices used in optical data storage. Switching between the two states, viz. amorphous and crystalline state takes place between the meta-stable and the amorphous states. Therefore, a complete understanding about the meta-stable state needs clarification so as to get the more information about the nucleation sites and their promotion with the help of certain dopants so as to enhance the crystallization rate [20, 21]. Understanding the structural rearrangements in these materials is a prerequisite for improved performance of device applications. In the present work, we have extended structural studies on pseudo-binary GeTe:xSb_2Te_3 system with $x = 0.5$, 1 and 2 by using Raman spectroscopic and X-ray diffraction (XRD) methods.

2 Experimental Details

The bulk samples of $Ge_2Sb_2Te_5$ (GST-225), $Ge_1Sb_2Te_4$ (GST-124) and $Ge_1Sb_4Te_7$ (GST-147) were prepared by melt quench method. As-quenched compositions were annealed at various temperatures for 5 h in order to get the stable phase which was obtained at 723 K, 848 K and 823 K for GST-225, GST-124 and GST-147, respectively.

XRD studies were recorded at room temperature by using Bruker X-ray diffractometer with CuK_α radiation. Rietveld refinement of the obtained data was made using fullprof software. The Raman spectra of bulk samples were recorded at room temperature using a 514 nm excitation of air-cooled argon ion laser (Renishaw InVia Reflex Micro Raman Spectrometer) in the 180° back scattering geometry with incident laser power about 2 mW. The backscattered light was analyzed by Raman spectrometer equipped with triple mono-chromator. In addition, we have carried out Raman polarization studies in two kinds of polarization geometries, i.e., parallel (VV) and perpendicular (VH) configurations.

3 Results and Discussion

3.1 X-Ray Diffraction Studies

Figure 2a–c is representing the XRD pattern of bulk GST-225, GST-147 and GST-124 samples in their stable crystalline phase, respectively. In order to attain their stable phase, the melt derived samples were annealed at various temperatures. The obtained XRD pattern for all three GST samples has been compared with JCPDS data and it is in agreement with each other (Fig. 2a–c). On the basis of these results, we identify that GST-225 and GST-147 are in hexagonal phase with space group $P\bar{3}m1$ and GST-124 sample exists in rhombohedral phase with $R\bar{3}m$ space group.

3.2 Raman Spectroscopic Studies on Bulk GST Samples

In the present work, we observe three different characteristic bands for the hexagonal phase of GST-225 and they are relatively sharper than the FCC phase as well as shift in the peak maxima. The shift in the wavenumber of hexagonal phase is due to the change in the number of layers as well as the absence of vacancies. The Raman band at 170 cm^{-1} is assigned to vibrations of $A_{1g}(4)$ modes of crystalline Sb_2Te_3 structure [22]. The band at 118 cm^{-1} has been assigned as $E_g(3)$ vibrating phonon modes of the tetrahedral $GeTe_4$ and/or pyramidal Sb_2Te_3 units [23]. On the other hand, the peaks in the low frequency range are called as E-type modes which are vibrating in the *ab* plane, whereas peaks in the higher frequency region, i.e., above 150 cm^{-1} are labeled as A-type phonons vibrating along the *c* direction. Lower frequency vibration at ~68 cm^{-1} has been assigned as $E_g(2)$ vibrational phonons. A schematic sketch of displacement pattern of E_g and A_{1g} vibrational phonons is shown in Fig. 3a, b. These assignments have been made on the basis of density functional perturbation theory performed by Sosso et al. [24].

Hexagonal structures of GST-147, GST-124 and GST-225 are the most stable bulk phases for GST-based alloys which are characterized by a layered structure of stoichiometric GeTe and Sb_2Te_3. Figure 4 is representing the Raman spectra of bulk crystalline GST-147, GST-124 and GST-225 samples in their stable hexagonal phase. In all the samples, two strong bands are observed at ~114–118 and ~166–167 cm^{-1}. At low frequencies, the appearance/disappearance of vibrational modes depends basically upon the molar ratio of Ge/Sb content. For the case of crystalline GST-124 and GST-147 samples, we observe the presence of two additional bands at 51 cm^{-1} along with 66 cm^{-1} and is absent in GST-225.

The Raman bands at 118 cm^{-1} along with 140 cm^{-1} have been assigned as $E_g(3)$ and $E_g(4)$ phonon vibrational modes. Additionally, we observe the emergence of new Raman bands at ~50 cm^{-1} and simultaneous occurrence at 68 cm^{-1} in GST-147 and have been assigned as $A_{1g}(1)$ and $E_g(2)$ vibrational modes, respectively. The Raman band at 170 cm^{-1} has been assigned as vibrations of $A_{1g}(4)$ modes of crystalline

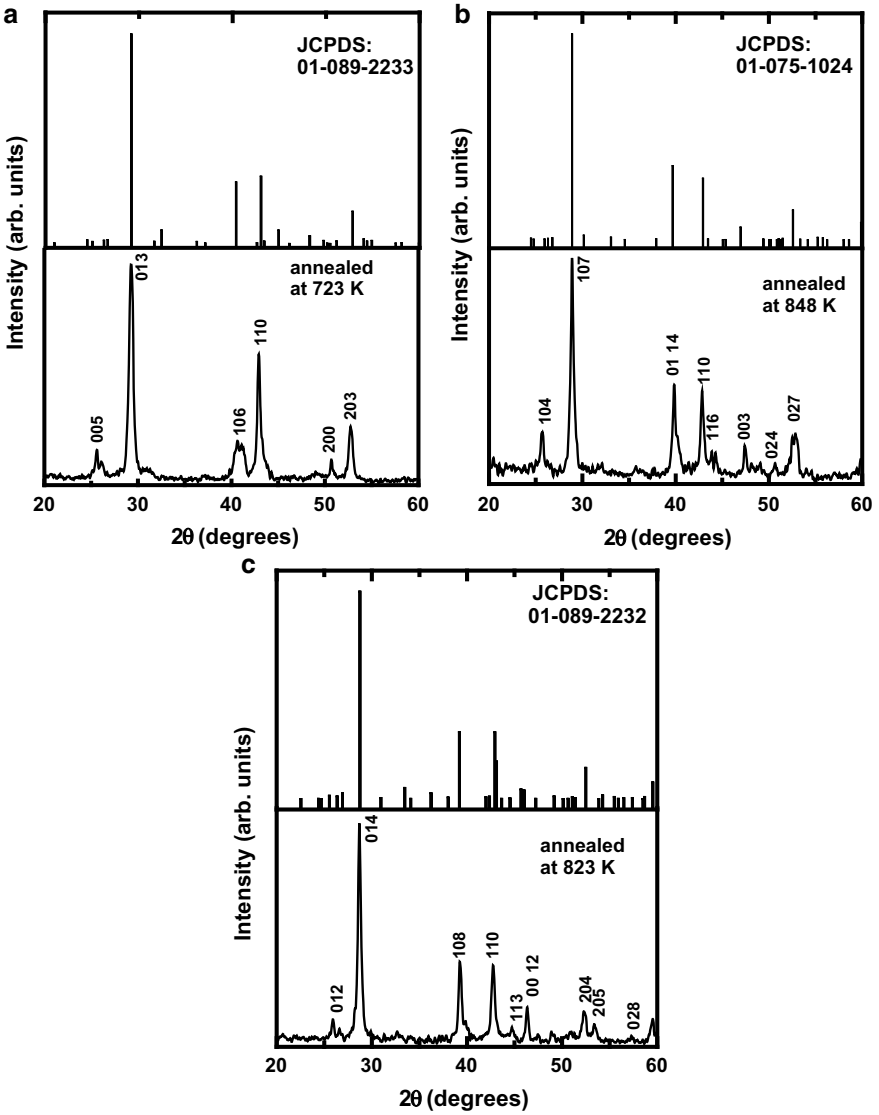

Fig. 2 **a** Powdered XRD pattern of bulk crystalline GST-225 (re-crystallized at 723 K). Obtained peaks are compared with JCPDS data number-01-089-2233. **b** Powdered XRD pattern of bulk crystalline GST-124 (re-crystallized at 848 K). Obtained peaks are compared with JCPDS data number- 01–075-1024. **c** Powdered XRD pattern of bulk crystalline GST-147 (re-crystallized at 823 K). Obtained peaks are compared with JCPDS data number-01-089-2232

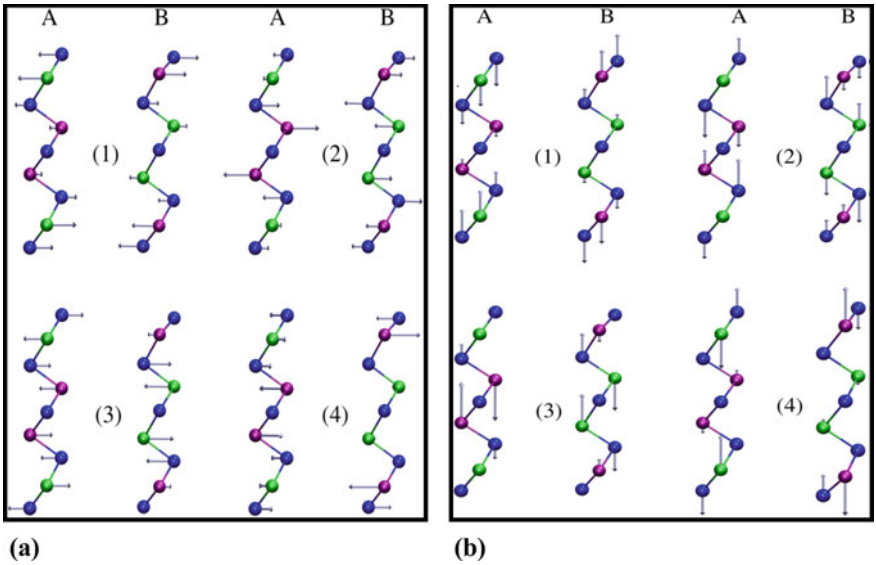

Fig. 3 Schematic of the displacement patterns of **a** E_g phonons **b** A_{1g} phonons, at the Γ point for phases A and B [24]

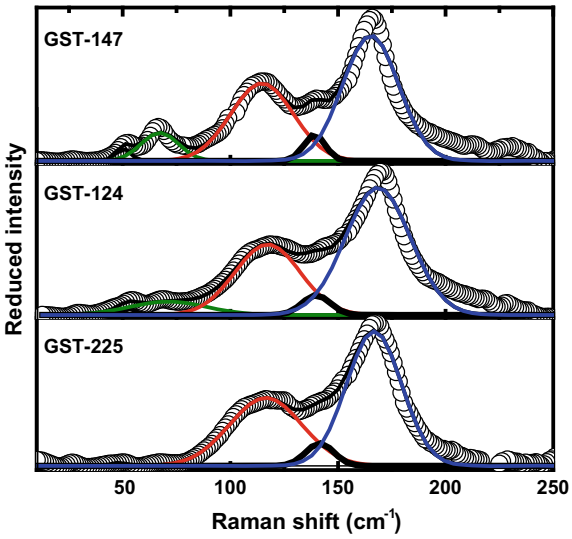

Fig. 4 Deconvoluted reduced Raman spectra of GST-225, 124 and 147 samples in the stable crystalline phases

Sb_2Te_3 structure [22]. It is worthwhile to note that as the ratio of GeTe:Sb_2Te_3 enhances from 1:0.5 in GST-225 to 1:2 in GST-147, there is progressive rise in $A_{1g}(1)$ and $E_g(2)$ phonon modes. The Raman spectra approach more toward stacking A which is more ordered as compared to stacking C for the case of GST-225 [24].

Energy associated with stack A is minimum and hence, Ge/Sb–Te bond lengths do not vary over a large range. Furthermore, the presence/absence of low-frequency features is independent of the other bands at ~118, 140 and 170 cm^{-1} in all the compositions. However, narrowing of the peaks is observed as the Sb_2Te_3 content is increased, which again supports the presence of more ordered structure in GST-147.

4 Conclusions

In the present work, the crystallization kinetics of mGeTe−$n$$Sb_2Te_3$ where $m{:}n = 1{:}1$, 1:2, 2:1 is investigated. The structure of meta-stable FCC and stable hexagonal phase of GST-225 has been studied by X-ray diffraction method and Raman studies. The obtained Raman results reveal that an increase in Sb_2Te_3 content causes an increase in order among the nine-layer atom where same layer is not randomly occupied by Ge or Sb atoms, i.e., each site is independently occupied by each atom (either Ge or Sb). The present work has provided detailed structural analysis in various GST alloys in thin film and bulk form. These results have provided us a deeper insight on the atomic and structural arrangements of the crystalline phases and will further help us to identify with the phase change mechanism of GST-based alloys.

References

1. Meijer GI (2007) Science 319:1625
2. Kolobov AV, Fons P, Frenkel AI, Ankudinov AL, Tominaga J, Uruga T (2004) Nat Mater 3:703
3. Caravati S, Bernasconi M, Kühne TD, Krack M, Parrinello M (2007) Appl Phys Lett 91:171906
4. Mazzarello R, Caravati S, Angioletti-Uberti S, Bernasconi M, Parrinello M (2010) Phys Rev Lett 104:085503
5. Kohara S et al (2006) Appl Phys Lett 89:201910
6. Upadhyay M, Murugavel S, Anbarasu M, Ravindran TR (2011) J Appl Phys 110:083711
7. Akola J, Jones RO (2008) Phys Rev Lett 100:205502
8. Upadhyay M, Abhaya S, Murugavel S, Amarendra G, J Solid State Chem (Submitted)
9. Kolobov AV, Krbal M, Fons P, Tominaga J, Uruga T (2011) Nat Chem 3:311
10. Mendoza-Galvdn A, Gonzlez-Herndndez J (2000) J Appl Phys 87:1
11. Volker CA, Wutting M (1999) J Appl Phys 86:1808
12. Friedrich I, Weidenhof V, Njoroge W, Franz P, Wutting M (2000) J Appl Phys 87:4130
13. Gonzdlez-Herndndez J, Castafio V, del Real A, Morales-Sdnchez E, Garsia-Garsia E, Mendoza-Galvdn A, Prokhorov E, Vorobiev Yu (2000) Inorganic Mat 36:1219
14. Gonzdlez-Hernmndez J, Chao BS, Strand D, Ovshinsky SR, Pawik D, Gasiorowski P (1992) Appl Phys Com 11:557
15. Yamada N, Matsunaga T (2000) J Appl Phys 88:7020
16. Oshima N (1998) J Appl Phys 83:5244
17. Nobukuni N, Takashima M, Ohnoa T, Horie M (1995) J Appl Phys 78:6980
18. Weindenhof V, Fiedrich I, Ziegler S, Wutting M (1999) J Appl Phys 86:5879
19. Lencer D, Salinga M, Grabowski B, Hickel T, Neugebauer J, Wuttig M (2008) Nat Mat 7:972
20. Seo H, Jeong T-H, Park J-W, Yeon C, Kim S-J, Kim S-Y (2000) J Appl Phys 39:745
21. Ebina A, Hirasaka M, Nakatani K (1999) J Vac Sci Technol A 37(6):3463

22. Sosso GC, Caravati S, Bernasconi M (2009) J Phys Condens Mater 21:095410
23. Tsunetomo K, Sugishima T, Imura T, Osaka Y (1987) J Non-Cryst Solids 95 & 96:509
24. Sosso GC, Caravati S, Gatti C, Assoni S, Bernasconi M (2009) J Phys Condens Mater 21:245401

Monolayer Transition Metal Oxides (MTMOs): CoO, FeO and NiO—A First Principles Study

Sanju Meena and Jyotika Jogi

Abstract In the last few years, a large number of two-dimensional materials (2D) have been demonstrated to exhibit unprecedented characteristics or unique functionality. 2D materials have unique optical, electronic and mechanical properties, due to which these materials may exhibit a tremendous potential in nano-electronics and optoelectronics. With every passing year, the use of 2D materials is increasingly being explored for potential in various fields. This work specifically focuses on monolayer of Transition Metal Oxides (TMOs) such as NiO, CoO and FeO which are the Mott insulators and relatively less expensive, thus useful in reducing the cost in addition to their various other salient features. The present study focuses on the electronic and magnetic properties of monolayer of NiO (100), FeO (100) and CoO (100) done using first principles approach. The planar structure of monolayer of TMOs is investigated and found to be unstable whereas the buckle structures are seen to be relatively stable with minimum ground state energy. Also, the FeO (100), CoO (100) and NiO (100) buckle monolayer structures exhibit different magnetic phases from antiferromagnetic (Bulk) to ferromagnetic phase.

Keywords MTMOs (Monolayer Transition Metal Oxides) · FeO · NiO · CoO · Density Functional Theory (DFT) · Spin Orbital Coupling (SOC)

1 Introduction

Two-dimensional (2D) materials with strong and weak interaction between the interlayers have attracted increasing attention in recent years in various fields [1, 2]. 2D materials-based nanostructures have attracted a wide range of research interests in the field of nanoscience because of their exceptional nanoscale structures and extraordinary properties [3]. Among these 2D materials, Transition Metal Oxides (TMOs) such as FeO, CoO and NiO are classic examples of strongly correlated systems [4, 5]. Electronic, magnetic and optoelectronic properties of transition metal oxide thin

S. Meena · J. Jogi (✉)
Micro-electronics Research Laboratory, Department of Electronics Science, ARSD College, University of Delhi, South Campus, New Delhi 110021, India

S. B. Krupanidhi et al. (eds.), *Advanced Functional Materials and Devices*, Springer Proceedings in Materials 14, https://doi.org/10.1007/978-981-16-5971-3_7

films are different from the bulk properties. This behaviour has attracted tremendous interest from researchers [6–8]. FeO, NiO and CoO have been seen to show typical rock salt or NaCl structure as Mott insulators [7]. **The *d*-levels in most Mott-insulator such as TMOs (FeO NiO) are partially filled with an electronic configuration varying from $3d^6$ to $3d^8$. Convectional Band Theory predicts electron delocalization and metallic properties in TMOs. TMOs (FeO, NiO and CoO) have been investigated as Mott insulators by experiments** [4, 5]. **Strong e-e Coulomb repulsion (U) and 3*d*-electrons localization are present in TMOs. TMOs show metal-insulator phase transition, which has been confirmed by both experiments and theoretical studies** [9–11]. **The effect of the e-e Coulomb repulsion (U) makes even the half-filled *d*-band insulating when the bandwidth (W) is smaller than the U. The major difficulty occurs when (U) and (W) have the same or comparable values** [9–11]. The theoretical studies of transition metal oxides have been a challenge to the researchers due to the interaction of strong correlated electrons, metal-insulator phase transition and exchange coupling in 3*d* orbital [4, 5, 9–11]. Metallic behaviour has been reported in bulk transition metal oxides (TMOs) using Density Functional Theory (DFT) which is contradictory to the experimental results [5, 12, 13]. Generalized Gradient Approximation (GGA) has failed to completely break the degeneracy of the 3*d* orbital at the Fermi level [13]. **Several high-temperature experiments have confirmed that the TMOs (FeO, NiO and CoO) exhibit a pressure induced Mott transition in their paramagnetic (PM) phase with cubic rock salt (B1) crystal structure** [4, 5, 9–15]**. Below the Neel temperatures (T_n), ranging from 116 to 523 K for MnO to NiO, these materials exhibit a structural phase transition from cubic structure to distorted rhombohedral structure at ambient pressure** [4, 5, 9–16]. Recent works have shown that synthesis of various single-layer and multiple layer monoxide nanocrystals (MgO, CaO, NiO, CuO and MnO) is possible [6, 8, 18]. The monolayer and thin films of TMOs have shown excellent magnetic, catalytic, gas sensing, optical and tuneable band gap properties [4–8, 14, 15, 17] which provide a platform for studies on 2D-monoxide in the fabrication of nanosheets [6, 8, 18], spintronics [19, 20], solar cell [21, 22], catalysis [23, 24] and energy storage [25]. Though a large number of studies on the planar thin films of monoxides electronic, structural and optical properties have been reported [4–8], the buckling effect and magnetic or nonmagnetic properties of monolayers of CoO, FeO and NiO have not been explored which are actively debated in the literature. In this present work, the focus is on distorted crystal structures of TMOs; the structural properties, electronic structure, magnetic properties of buckle monolayer (100) and planar monolayer (100) of TMOs (FeO, NiO and CoO) were investigated using DFT with Generalized Gradient Approximation (DFT+ GGA) approach. In this research, the authors have developed an efficient methodology for theoretical investigation of the buckling effect in monolayers of TMOs (FeO, NiO and CoO). **In the planar structure of TMOs, transition metal (TM) and oxygen (O) atoms lie on the same plane and this structure has an initial phase of monolayer (100). The buckled structure refers to the non planar structure in which (TM) atoms (Co, Ni and Fe), as well as O atoms, deviate from the initial plane by more than 0.0010 Å. This deviation of the atomic position is called the buckle**

height. In the present research work, there are three types of structures are no buckle, low buckle and high buckle which are considered on the basis of buckle height from 0.000 Å, 0.010 Å to 0.1000 Å, respectively.

Research in GGA has confirmed that the buckle structures are highly stable as compared to the planar structure of TMOs. Structural and electronic properties of buckle monolayer of TMOs (FeO, NiO and CoO) have been studied with GGA approach. Spin orbital coupling with GGA calculations investigate the impact of spin contributions in buckle monolayers. Spin up and spin down states were determined to explore the magnetic properties in order to investigate the ferromagnetic phase and anti-ferromagnetic phase in buckle monolayer of TMOs (FeO, NiO and CoO) [4, 5, 9, 26]. The changes in the magnetic properties of TMOs material from bulk (anti-ferromagnetic phase) to monolayer (ferromagnetic phase) were investigated in these compounds. The authors have restricted this study to monolayer of FeO, NiO and CoO, hence monolayer of TMOs refers to these three materials unless stated otherwise.

2 Computational Details and Structural Aspects

Self-consistent (DFT) calculations are used to study monolayers of TMOs (Fe, Ni, Co) employing the *QUANTUM ESPRESSO* software package. For structural optimization and electronic structures, the authors have used pseudopotential method as implemented in Plane Wave Self-Consistent Field (PWSCF) program [27]. Generalized Gradient Approximation (GGA) in the form of the Perdew–Burke–Ernzerhof (PBE) functional is used to determine exchange and correlation interaction [28]. For the relaxation structure calculation, the stress error tolerance was set to 0.1 GPa and the force tolerance was set to 1×10^{-2} eV $^{-1}$. So, the process of structural optimization is repeated until the convergence criterion was less than 10^{-2} eV for total energy and tolerance force less than 0.01 eV/Å. A large vacuum layer of over 15 Å is employed to avoid interactions between interlayers. The Brillouin Zone (BZ) is sampled by adopting $8 \times 8 \times 1$ Monk Horst–Pack k-points, the plane wave energy cut-off was set to 55 Ry for all calculations and 350 Ry adopted for charge density Fourier expansion. To investigate an accurate electronic band structure, the sampling of the Brillouin zone (BZ) includes a fine $18 \times 18 \times 1$ Monk Horst-Pack k-point grid for all structures studied, a similar fine grid was used to produce accurate band structure [6, 8]. The converged output results carried out from Quantum espresso then executed in wien2k, to describe the electronic structure properties [29].

3 Results and Discussions

3.1 Structural Properties

TMOs (FeO, CoO and NiO) are closely related to the typical cubic structure as NaCl rock salt structure [4, 5]. In this work, the authors have studied the monolayers of TMOs along the (100) plane. **Monolayer oxides (100) have a one molecule thick layer of TMOs and the typical thickness is around 1–10 Å. Transition metal oxide surfaces can be generated by cutting the crystal along any crystal plane such as (100), (110), (111) in case of cubic lattice and the (0001), (10–10) and (11–20) crystal planes for a hexagonal lattice. In this research work, the authors have considered (100) plane orientation of transition metal oxides surfaces, which are simple to obtain as a cut perpendicular to the (100) crystal direction results two equivalent rock salt (100) surfaces as illustrated in Fig. 1a, b. The computational efforts are focused on the buckle monolayers of TMOs. Three buckle structural monolayers, shown in Fig. 1c–h, have been investigated: Fig. 1c, d a planar or no buckle monolayer (100) of TMOs; Fig. 1e, f a low buckle monolayer (100) of TMOs; Fig.1g, h a high buckle monolayer (100) of TMOs**. Monolayer structures were set up with the lattice parameters obtained, 8 × 8 × 1 Monk Horst-Pack *k*-point grid and a large vacuum layer over 15 Å is employed to avoid interactions between interlayers [6, 8]. For all the 3 structures, the structural geometry was optimized using GGA-PBE approach. To investigate the structural geometry optimization, energy as a function of volume (E–V) curves for planar monolayer (100), buckle monolayer

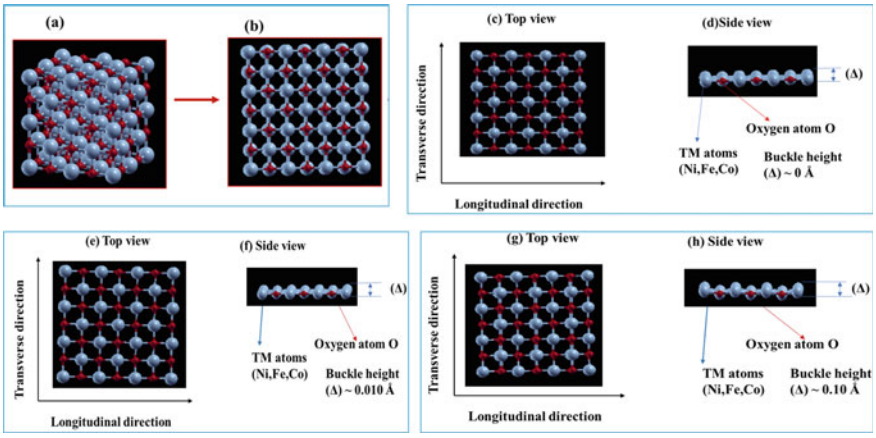

Fig. 1 **a** Bulk crystal structure of TMOs, where the Gray atoms are TM (Fe, Ni, Co) atoms, while the red atoms are oxygen or O atoms **b** Atomic structure of (100) plane of TMOs. Top, as well as side view of planar monolayer (100) structure of TMOs, are explained in (**c**) and (**d**). Top, as well as side view of the low buckle monolayer (100) of TMOs, are illustrated in (**e**) and (**f**). High buckle monolayer (100) of TMOs (NiO, CoO and FeO) structure, the top view as well as side view are shown in (**g**) and (**h**)

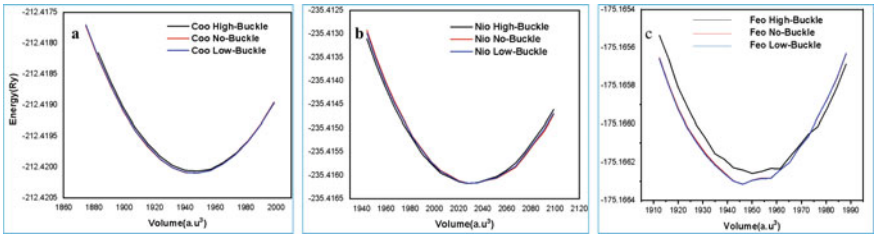

Fig. 2 The optimized energy as a function of volume (E–V) for curves for different relaxed structures of **a** CoO (100), **b** NiO (100) and **c** FeO (100) monolayers

(100) structures of NiO, CoO and FeO were obtained. Initially, the authors deformed the atomic position using vc-relax calculation. Further the optimization of fully relax structures, cell parameters were varied and the values thus obtained were fitted to Mur-naghain's equation of state [30]. The optimized energy as a function of volume (E–V) curves for planar monolayer, buckle monolayer structures for NiO, CoO and FeO are mentioned in Fig. 2a–c.

When relaxing the monolayer structures, the authors found that the low buckle, high buckle structure and low buckle relaxed structure of monolayer CoO (100), NiO (100) and FeO (100) are comparatively stable than the other configurations. **Full relaxation of the low buckle relaxed structure of monolayer of CoO where Co and O atoms deviated from initial phase to around 0.0125 and 0.0082 Å and obtained the top, as well as side view of low buckle monolayer (100) of TMOs structures, are mentioned in Fig. 1c, d. NiO high buckle relax structure where Ni and O oxygen atoms deviated around 0.1044 and 0.00134 Å from initial phase and the longitudinal (side view), as well as transverse (top view) directions of the high buckle monolayer (100) TMOs, are explained in Fig. 1e–h. In FeO low buckle monolayer structure the buckle height was found 0.01271 Å and 0.007176 Å of TM and O oxygen atoms, respectively and top as well as side view of low buckle monolayer (100) TMOs structures are mentioned in Fig. 1c–h.** Optimized the relax lattice parameter '$a = b$' is 3.5423 Å of low buckle monolayer of CoO (100), which was 1.2% less than the lattice constant of planar bulk CoO (experimental value 4.263 Å) [31]. Calculated the bond's length of Co–O, Ni–O and Fe–O are 2.04897 Å, 2.0788 Å and 2.04526 Å, respectively. Our calculated results for the monolayer structure were quite similar to previous reports on bulk structure [4–6, 8]. All these results are mentioned in Table 1. The authors found that non planar monolayer structures are more stable than planar monolayer structures.

Table 1 Comparison of the physical properties of buckle monolayer (100) of TMOs (FeO, NiO and CoO): lattice constant ($a = b$), bond length TM-O(d), Band gap (Δ) using GGA method within experimental results of TMOs

2D monolayer Transition metal oxides	Lattice constant (Å)		Bond length d (Å)	Band gap Δ (eV)	
	Cal.	Exp. (bulk)	Cal.	Cal.	Exp. (absorption) for (Bulk)
Low Buckle FeO (100)	$a = b$ 3.5517	4.3345 [37]	2.04526	Metallic	2.4 [36]
High Buckle NiO (100)	$a = b$ 3.5925(3.95) [a]	4.177 [37]	2.0788(1.97)[a]	Metallic	4.0 [35]
Low Buckle CoO (100)	$a = b$ 3.5423	4.263 [31]	2.04897	Metallic	2.8 [35]

[a] Ref. from [8] the numbers inside brackets are the GGA+U results for NiO (100) monolayers

3.2 *Electronic Properties of Monolayer (100) of TMOs (FeO, NiO and CoO)*

3.2.1 Band Structure

Optimized relaxed lattice constants were used to investigate the full description of the electronic properties of monolayers of TMOs. Electronic structure calculation was obtained using GGA-PBE functions. The band structures were calculated along the high symmetry k-points with the path "M-Gg-X-M".

Obtained electronic band structures of buckle monolayer (100) of TMOs (FeO, CoO and NiO) are illustrated in Fig. 3a–c. **In this research, the authors found the Valence Band (VB) of *p*orbitals and Conduction Band (CB) of 3*d*orbitals have mixing state at the same high symmetric gamma (Γ) points. This indicates phase**

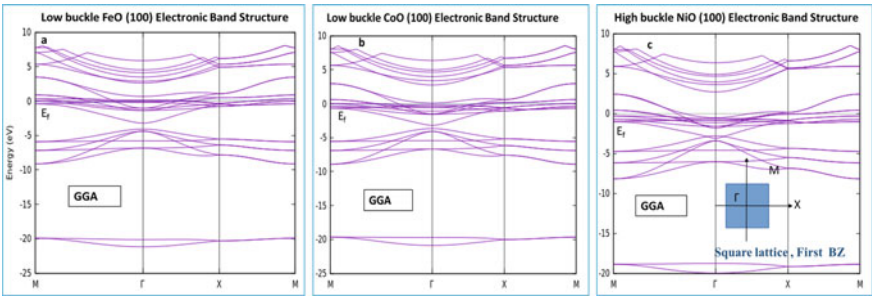

Fig. 3 Electronic band structure for **a** buckle FeO (100), **b** buckle CoO (100) and **c** buckle NiO (100) monolayers. The Fermi energy (E_f) levels are set to 0 and are represented by dotted lines in plots for the electronic band structures

transition in these compounds. It is clearly observed in electronic band dispersion Fig. 3a–c that the 3*d*orbitals of TM are partially filled at the Fermi level thus indicating a metallic phase in the buckle monolayer (100) of TMOs (FeO, NiO and CoO). Therefore, GAA has failed to completely break the degeneracy of the 3*d* orbital at the Fermi level [4, 5]. Outer 3*d* orbitals in TMOs materials play a very significant role in changing the electronic properties of the material due to which TMOs show a wide range of band gap ranging from 2 (MnO) to 4.0 eV (NiO) [4, 5, 9–11].

3.2.2 Density of States (DOS) and Partial Density of States (PDOS)

To further understand the contribution of atoms near the Fermi level in electronic band dispersion, the Total Density of States (DOS) and Partial Density of States (PDOS) of buckle monolayers (100) of TMOs were taken into account and results thus obtained are shown in Figs. 4a–c and 5a, b. From Fig. 4a–c it is quite clear that the Fermi level lies in the overlapping valence band (VB) and conduction band (CB).

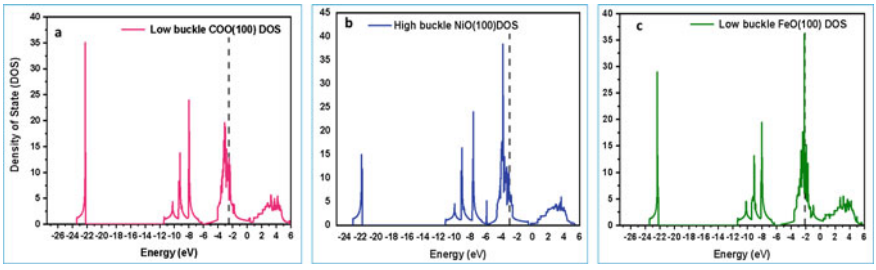

Fig. 4 Total Density of States (DOS) for **a** low buckle CoO (100) monolayer, **b** high buckle NiO (100) monolayer and **c** low buckle FeO (100) Monolayer. The Fermi energy levels are represented by dotted lines (colour lines) in plots for Density of States

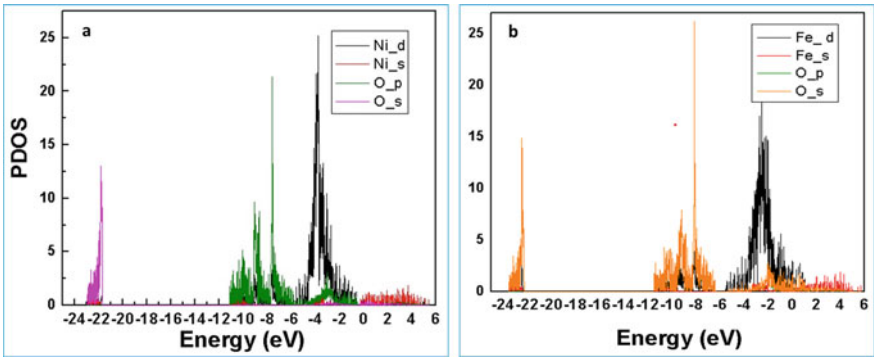

Fig. 5 Partial Density of State (PDOS) of the buckle monolayer **a** NiO (100) **b** FeO (100)

The Fermi energy levels obtained using GGA calculations are represented by dotted lines in Fig. 4a–c with different colour bars for Density of States.

Figure 4a–c shows the orbital contribution in electronic band structure; Four regions are observed indicating the atomic orbital contribution to the electronic structure depending on their respective intensities. In order to understand this further, the Partial DOS have been plotted for these four regions in Fig. 5a and b. First region: a strong peak observed around –22 eV is attributed to oxygen 2*s* states contribution, Second region: peaks around −10 to −8 eV are mainly due to contribution from the oxygen 2*p* states with a small contribution of TM (Fe, Ni, Co) 3*d* states, Third region: the strong peaks observed just below the Fermi level around −4 to −2 eV are attributed mainly due to TM (Fe, Ni, Co) 3*d* states with a small contribution from the oxygen 2*p* states and finally Fourth region: the peaks above the Fermi level in the conduction bands are found mainly due to the partially unoccupied TM (Fe, Ni, Co) 3*d* states with very little hybridisation of the oxygen 2*p* states. From Fig. 5a, b, it is observed that *d* orbital states of TM (Fe, Ni, Co) atoms are partially filled and 3*d*–2*p* orbitals overlapping is also present in these monolayers. Here GGA method was used to calculate the electronic properties of monolayers (100) of TMOs, which predicted a metallic behaviour of the materials however this prediction/result is inconsistent with experimental results [5, 6], which show insulating nature. Thus, one can see that the GGA calculation failed to obtain the correct electronic properties of buckle monolayer of TMOs materials, this inconsistency was also observed for bulk TMOs [5, 16, 17]. **The possible reason for the failure of GGA in predicting the electronic properties for buckle monolayers of TMOs could be due to the strongly correlated electrons, metal–insulator phase transition and exchange coupling in 3*d* orbital. When electron Coulomb repulsion (U) is less than the bandwidth (W) these compound materials show metallic behaviour. Charge transfer character was found in two-states; 3*d*(Fe)–2*p*(O)–4*s*(Fe) and 3*d* (Fe)–2*p*(O)–3*d* (Fe), however, GGA predict an overestimated value of the charge transfer leading to a result inconsistent with experimental result** [5, 6]. **This clearly shows that GGA was not able to remove the strong coupling that existed between 3*d* orbitals. Previous works** [4, 5] **have shown that GGA approximation failed to completely break the degeneracy of the 3*d* orbital at the Fermi level which result in delocalization of the electrons and reduction of bandgap in TMOs mainly in FeO, MnO, CoO and NiO, furthermore Morsey et al. also had shown that GGA approximation is inapplicable for strongly correlated electrons even in bulk materials** [13]. **Crystal field approximation confirmed that five-fold degenerated orbital level split mainly into the e_g orbital and the t_{2g} orbitals** [16]**. The e_g orbitals and the t_{2g} 3*d* orbitals have twofold and threefold degeneracy, respectively**. It is clearly seen in Fig. 5a, b, the TM 3*d* and O 2*p* orbital densities overlap and are prone to exhibit metallic behavior. The results obtained in the present work for buckle monolayer of FeO (100), CoO (100) and NiO (100) using GGA show that buckle structure is a stable state, this result is consistent with previous studies for buckle monolayer of NiO using LDA+U method [6].

3.3 Magnetic Properties

To obtain the magnetization phase (ferromagnetic—FM and anti-ferromagnetic—AFM) in no buckle, low buckle and high buckle monolayer structures, GGA with Spin Orbital Coupling (SOC) method was used. To estimate spin contribution, the authors have plotted the total Density of States (DOS) and Partial Density of States (PDOS) for buckle FeO (100), NiO (100) and buckle CoO (100) monolayer as a function of energy mentioned in Fig. 6a–c, respectively. From Fig. 6a–c, one can see that in monolayer of TMOs, the contribution to the magnetic properties is largely due to 3*d* orbital rather than the *s* and *p* orbitals. The calculated results for buckle monolayer CoO (100) are quite different from the buckle monolayer FeO (100) and buckle monolayer NiO (100), as shown in Fig. 6a–c. **Further, to understand the spin behaviour and orbital interaction in monolayer buckle CoO (100), plotted the contribution of spin configuration for different orbitals, as illustrated in Fig. 7a–c**.

It is observed that strong interaction is present in buckle monolayer CoO (100) as compared to buckle monolayer NiO and FeO results. Besides the FM ordering, where all spins are parallel along the [100] direction of the buckle monolayer crystal

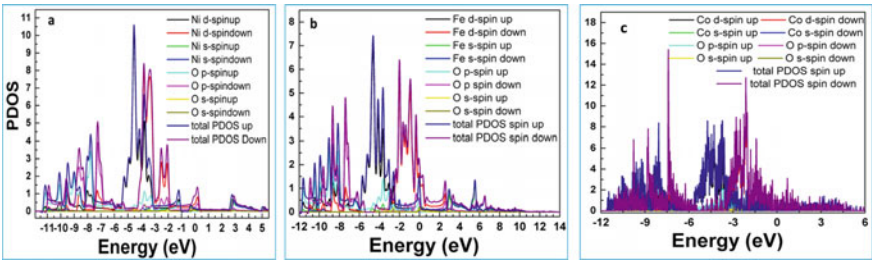

Fig. 6 Total Density of State (DOS) and Partial Density of States (PDOS) of the **a** buckle monolayer NiO (100) and **b** buckle monolayer FeO (100)

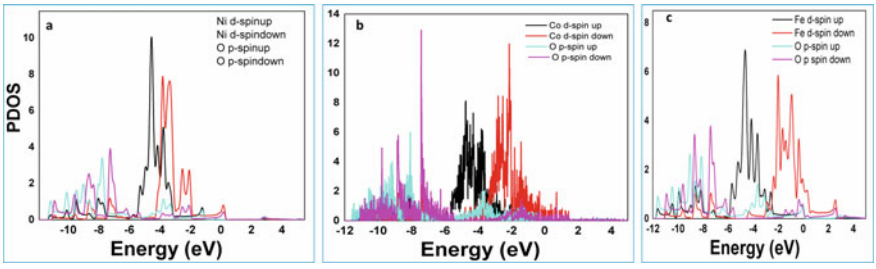

Fig. 7 **a** Partial Density of State (PDOS) of the buckle monolayer CoO (100). Splitting of Partial Density of State of different orbital for spin contribution of buckle monolayer (**b**-) CoO (100). **b** Here colour line shows different spin contributions from majority d orbital of Co and minority p orbitals of O and calculated results from GGA approximation

structure, since the partially occupied 3*d* shells are strongly localized for transition metal ions (Fe, Ni, CO). The authors found that the FeO, NiO and CoO have low buckle, high buckle and low buckle structures respectively as observed in previous section (Sect. 3.1) and they all have FM configuration. Thus, for monolayer magnetization configuration of these three materials were found to be ferromagnetic which is contrary to their bulk state where it exhibits anti-ferromagnetic behaviour [4, 5, 32–34]. **The calculated values of total magnetic moments of buckle monolayer (100) of TMOs (FeO, CoO, NiO) by GGA approach are mentioned in Table 2**. The 2D-XO (monolayer FeO, NiO and CoO) are computed to be buckle in this research with magnetic moments state. The magnetic super exchange interaction in manganite depends on the TM-O-TM bond angle [33, 34]. The FM states are obtained in this research due to disturbance of TM-O-TM bond angle in buckle structure. In bulk structure, inversion symmetry is present since spin up and spin down has equal contribution resulting in zero magnetization [38–40]. In this research, the authors have investigated another stable magnetic phase (FM) with minimum ground energy. The magnetic properties of TMOs material change from bulk (anti-ferromagnetic phase) to monolayer (ferromagnetic phase). These buckle monolayer structures can play a remarkable role in fabrication of nanosheets, spintronics and other applications including catalysis, sensors, piezoelectric devices valley electronics.

Summary

Structural, electronic and magnetization properties of Monolayer Transition Metal Oxides (MTMOs) were investigated using the first principles method and promising magnetic properties were observed. It was found that the planar structure of monolayer of TMOs (FeO, NiO and CoO) is unstable whereas the buckle structure is stable when a buckling height is less than 1 Å. Buckle structures of FeO, CoO and NiO monolayers have shown metallic behaviour in ground state as confirmed by GGA-PBE functions. Further, the authors investigated the magnetic properties of buckle monolayer of TMOs (100) (FeO, CoO and NiO) and obtained the stable states with Ferromagnetic phase which exhibit different magnetic (ferromagnetic) properties as

Table 2 Comparative results for total and partial magnetic moments in different structures (Bulk and monolayer) within different magnetic states (AFM and FM) of FeO (100), NiO (100) and CoO (100) using GGA and other calculations

2D monolayer Transition metal oxides	Magnetic moments (μ_B)			
	Cal. μ™ (GGA)	Exp. (planar) (μ^{TM1})	Other Cal. (μ™)	Exp. (Bulk) (tot. μ™)
Low Buckle FeO (100)	3.55	4.2 [41], 3.32 [37]	3.76 [16]	0.0 [4, 5]
High Buckle NiO (100)	1.515(2.0) [a]	1.7–1.9 [42, 43]	1.75 [16]	0.0 [8]
Low Buckle CoO (100)	2.545	3.8–3.98 [44]	2.78 [16]	0.0 [4, 5]

[a] From [8] for NiO (100) FM state LDA+U method

compared to their bulk structure. In summary, the present study reveals that these monolayers of TMOs have potential applications in the area of spintronics, thin films, nano-heterostructure, thermo-electronics and catalysts.

Acknowledgements The authors would like to thank IIT Delhi for providing computational facility.

References

1. Novoselov KS, Geim AK, Morozov SV et al (2004) Electric field effect in atomically thin carbon films. Science 306(5696):666–669
2. Cheng J, Wang C, Zou X, Liao L (2019) Recent advances in optoelectronic devices based on 2D materials and their heterostructures. Adv Opt Mater 7(1):1800441
3. Khan K, Tareen AK, Muhammad A et al (2020) Recent developments in emerging two-dimensional materials and their applications. J Mater Chem C 8(2):387–440
4. Zaanen J, Sawatzky GA, Allen JW (1985) Band gaps and electronic structure of transition-metal compounds. Phys Rev Lett 55(4):418–421
5. Mott NF (1990) On metal-insulator transitions. J Solid State Chem 88(1):5–7
6. Zhang YG, He HY et al (2012) Structural features and electronic properties of MgO nanosheets and nanobelts. J Phys C 116(43):23130–23135
7. Rao CNR (1974) Transition metal oxides: crystal chemistry, phase transition and related aspects. DC, Washington
8. Shayeganfar F, Vasu KS, Nair RR et al (2017) Monolayer alkali and transition-metal monoxides MgO, CaO, MnO, and NiO. Phys Rev B 95(14):144109–144119
9. Imada M, Fujimori A et al (1998) Metal-insulator transitions. Rev Mod Phys 70(4):1039–1263
10. Tokura, Nagaosa N (2005) Orbital physics in transition-metal oxides. Science 288(5465):462–468
11. Dagotto E et al (2005) Complexity in strongly correlated electronic systems. Science 309(5732):257–262
12. Austin IG, Mott NF (1970) Metallic and non-metallic behaviour in transition metal oxides. Science 168(3927):71–77
13. Mosey N, Liao P, Carter E (2008) Rotationally invariant ab initio evaluation of Coulomb and exchange parameters for DFT+U calculations. J Chem Phys 129(1):014103
14. Cohen RE, Mazin II, Isaak DG (1997) Magnetic collapse in transition metal oxides at high pressure: implications for the earth. Science 275(5300):654–657
15. Leonov I, Shorikov et al (2020) Emergence of quantum critical charge and spin-state fluctuations near the pressure-induced Mott transition in MnO, FeO, CoO, and NiO. Phys Rev B101(24):245144–245210
16. Trimarchi G, Wang Z et al (2017) Polymorphous band structure model of gapping in the antiferromagnetic and paramagnetic phases of the Mott insulators MnO, FeO, CoO, and NiO. Phys Rev B 97(3):035107–035117
17. Duo L, Finazzi M, Ciccacci F (eds) (2010) Magnetic properties of antiferromagnetic oxide materials. Wiley-VCH, Weinheim
18. Kuhlenbeck H, Freund H-J (1997) Structure and electronic properties of ultrathin oxide films on metallic substrates. In: King DA, Woodruff DP (eds) The chemical physics of solid surfaces. Elsevier, pp 340–374
19. Liu Q, Chen Q, Zhang Q, Xiao Y et al (2018) In situ electrochromic efficiency of a nickel oxide thin film: origin of electrochemical process and electrochromic degradation. J Mater Chem C 6(3):646–653

20. Dabrowski M, Nakano T, Burn DM, Frisk A et al (2020) Coherent transfer of spin angular momentum by evanescent spin waves within antiferromagnetic NiO. Phys Rev Lett 124(21):217201–217207
21. Irwin MD, Buchholz DB et al (2008) p-Type semiconducting nickel oxide as an efficiency-enhancing anode interfacial layer in polymer bulk-heterojunction solar cells. Proc Natl Acad Sci USA 105(8):2783–2787
22. Gopalakrishnan SG, Senftle TP et al (2018) Novel solar cell materials: insights from first-principles. J Phys Chem 122(48):27107–27126
23. Poulain R, Klein A, Proost J et al (2018) Electrocatalytic properties of (100)-, (110)-, and (111)-oriented NiO thin films toward the oxygen evolution reaction. J Phys Chem C 122(39):22252–22263
24. Gong S, Wang A, Wang Y et al (2020) Hetero-structured Ni/NiO nano-catalysts for ozone decomposition. ACS Appl Nano Mater 3(1):597–607
25. Poizot P, Laruelle S, Grugeon S et al (2000) Nano-sized transition-metal oxides as negative-electrode materials for lithium-ion batteries. Nature 407(6803):496–499
26. Anderson PW (1950) Anti-ferromagnetism. Theory of super exchange interaction. Phys Rev 79(2):350–356
27. Giannozzi P, Baroni S et al (2009) QUANTUM ESPRESSO: a modular and open-source software project for quantum simulations of materials. J Phys Condens Matter 21(39):395502
28. Perdew JP, Burke K et al (1996) Generalized gradient approximation made simple. Phys Rev Lett 77(18):3865–3868
29. Blaha P, Schwarz K, Madsen GKH et al (2001) WIEN2K, an augmented plane wave plus local orbitals program for calculating crystal properties, 2nd edn. Vienna University of Technology, Vienna, Austria
30. Murnaghan FD (1944) Proc Natl Acad Sci USA 30:244
31. Sasaki S, Fujino K, Takéuchi Y (1979) X-ray determination of electron-density distributions in oxides, MgO, MnO, CoO, and NiO, and atomic scattering factors of their constituent atoms. Proc Japan Acad Ser B Phys Biol Sci 55(2):43–48
32. Cococcioni M, de Gironcoli S (2005) Linear response approach to the calculation of the effective interaction parameters in the LDA+U method. Phys Rev B 71(3):035105–035121
33. Hwang HY, Cheong S-W et al (1995) Lattice effects on the magnetoresistance in doped $LaMnO_3$. Phys Rev Lett 75(5):914–917
34. Zubko P, Gariglio S, Gabay M et al (2011) Interface physics in complex oxide heterostructures. Annu Rev Condens Matter Phys 2(1):141–165
35. Pratt GW, Coelho et al (1959) Optical absorption of CoO and MnO above and below the Neel Temperature. Phys Rev 116(2):281–286
36. Bowen HK, Adler D et al (1975) Electrical and optical properties of FeO. J Solid State Chem 12(3–4):355–359
37. Tran F, Blaha P, Schwarz K, Novak P (2006) Hybrid exchange-correlation energy functionals for strongly correlated electrons: applications to transition-metal monoxides. Phys Rev B 74(15):155108–155218
38. Roth WL (1958) Magnetic structures of MnO, FeO, CoO, and NiO. Phys Rev 110(6):1333–1341
39. Braicovich L, Ciccacci F et al (1992) Ultraviolet inverse photoemission from iron monoxide and self-interaction-corrected local-spin-density calculation. Phys Rev B 46(19):12165–12174
40. Pasternak MP, Taylor RD, Jeanloz R, Li X, Nguyen JH, McCammon CA (1997) Phys Rev Lett 79:046
41. Battle PD, Cheetham AK (1979) J Phys C 12:337
42. Alperin HA (1962) J Phys Soc Jpn Suppl B 17:12; Fender BEF, Jacobson AJ, Wedgwood FA (1968) Covalency parameters in MnO, α-MnS, and NiO. J Chem Phys 48:990
43. Cheetham AK, Hope DAO (1983) Magnetic ordering and exchange effects in the antiferromagnetic solid solutions $MnxNi1-xO$. Phys Rev B 27:6964
44. Schrön A, Rödl C, Bechstedt F (2012) Phys Rev B 86:115134

Electrocaloric Effect in PZT Thick Film for the Cooling Device Applications

Vandana, Reema Gupta, R. P. Tandon, Monika Tomar, and Vinay Gupta

Abstract Electrocaloric effect of sol gel deposited thick film of PZT has been investigated in the present work. The film is successfully deposited on Nickel substrate with an optimized annealing temperature of 650 °C. Single phase PZT thick film has been obtained on nickel substrate at 650 °C annealing temperature. The ferroelectric hysteresis loops were measured at 1 kHz frequency in the temperature range of 310 K–430 K respectively. At an external applied electric field of 250 kV/cm, maximum reversible adiabatic temperature change, $\Delta T = 1.50$ K was calculated at 430 K. The electrocaloric responsivities in terms of change in entropy and change in temperature are also determined for the optimized PZT thick film at an applied electric field of 250 kV/cm and found to be 0.06×10^{-6} K · m/V and 0.04×10^{-6} J · m/(kg · K · V).

Keywords PZT · Ferroelectric · Electrocaloric · Leakage current density

1 Introduction

The change in polarization by the polar materials during the applied external electric field under adiabatic conditions is known as electrocaloric effect (ECE). The adiabatic temperature change (ΔT) is exhibited by the polar materials due to change in polarization [1, 2]. The coupling in electrical and thermal properties of the material takes place due to the ECE effect [2]. It forms the basis for the next-generation refrigeration and power technologies that are highly efficient. In recent few years, new solid state cooling technologies such as refrigeration based on ECE are developing at a large scale. Solid state cooling devices have various fields of applications for example temperature regulation in electronic devices and also in on-chip cooling devices [1, 3]. Theoretical analysis infers that the cooling devices which are

Vandana (✉) · R. Gupta · R. P. Tandon · V. Gupta (✉)
Department of Physics and Astrophysics, University of Delhi, Delhi 110007, India

M. Tomar
Department of Physics, Miranda House, University of Delhi, Delhi 110007, India

S. B. Krupanidhi et al. (eds.), *Advanced Functional Materials and Devices*, Springer Proceedings in Materials 14, https://doi.org/10.1007/978-981-16-5971-3_8

performed on ECE have higher energy conversion efficiency than of vapour compressors [4]. The ECE effect also presents the advantage that less complex components and control are required than other technologies due to the application of external electric fields [4, 5]. Under the application of external electric field, this effect is a significant way for the cooling device applications in the technological fields such as regulation in temperature for electronic devices and sensors and on-chip cooling. The cooling device such as refrigeration which is working on the principle of electrocaloric phenomenon is cost effective and exhibit environmental friendly nature. As a result of this, it is the most alternative approach to the already existing vapour compression in the reports [14]. For the development of efficient cooling devices, the ECE material must possess high temperature and entropy changes as a function of electric field [5]. Amongst the polar materials, the ferroelectric materials are the prominent candidates because of the fact that the application of the electric field induces a large change in polarization in the ferroelectric materials which is suitable for the large ECE effect [6]. Ferroelectric cooling devices which are working on the principle of ECE effect are highly efficient, cheap and can be easily miniaturised in comparison to the other conventional solid state refrigeration technologies [5]. The following equations are used to determine the ΔT and ΔS caused by an applied electric field E varying from E_1 to E_2:

$$\Delta S = \frac{1}{\rho} \int_{E1}^{E2} \left(\frac{\partial P}{\partial T} \right) \mathrm{d}E \tag{1}$$

$$\Delta T = -\frac{1}{\rho} \int_{E1}^{E2} \frac{T}{C} \left(\frac{\partial P}{\partial T} \right) \mathrm{d}E \tag{2}$$

where, C_p is specific heat capacity, polarization is denoted by P and ρ is the density of the material [4, 5]. Electrocaloric properties of ferroelectric materials have been investigated in the present study for cooling device applications. Literature reports that many ferroelectric polymers, ceramics, thick and thin films show weak ECE [7]. Relatively small electrocaloric effect (ECE) is observed in ferroelectrics generally over the past few decades. Sanlialp et al. [15] reported maximum temperature change (ΔT) of 0.33 K for the BZT-BCT ferroelectric ceramic. The reported value was too small for further practical application in the cooling devices. Kandula et al. (2018) reported (ΔT) values of 0.95 K in the NBNT-BT ceramic [16]. However, the recent discovery of a giant electrocaloric effect in some ferroelectric materials provided significant momentum in the revival of the research of the ECE in ferroelectric materials. There exist a number of ferroelectric materials such as Barium Titanate ($BaTiO_3$), Lithium Niobate ($LiNbO_3$), Lead Zirconium Titatanate (PZT) and so on which are exploited for electrocaloric properties in literature [1]. Amongst these ferroelectric materials, the most eminent material is lead zirconium titanate

(PZT) which is a widely used ferroelectric candidate. This is because of its efficient properties such as high spontaneous polarization, high curie temperature, high dielectric constant, superior ECE coefficient, good thermal stability and high electromechanical coupling coefficient [7, 8]. A large electrocaloric effect achieved in the PZT films by Kesim et al. [9] opened a new interest in the electrocaloric effect of PZT. However, recently there is an increasing interest in utilizing PZT based thick films for miniaturized ferroelectric devices. This is because of the fact that thick film plays an intermediate role between thin film and ceramics. PZT thick films are exploited for electrocaloric study in the present work. This is because of the fact that in comparison to the films, bulk ceramic cannot withstand high operating electric field resulting in small values of electrocaloric efficiency. Also nowadays, technology is approaching towards the miniaturaization of device but bulk ceramics are not suitable with microelectronic devices. Although higher breakdown electric field is possessed by the thick film, therefore, can be easily integrated with semiconductor technology. Therefore, Due to high breakdown field possessed by the thick films can meet the requirements of applications in cooling devices. In this direction, PZT thick films are investigated and further exploited for electrocaloric properties.

2 Experimental Section

2.1 Preparation of PZT Slurry

Preparation of thick film of PZT is displayed in the flow chart as shown in Fig. 1. Modified sol gel technique is adopted in the present work for the synthesise of PZT solution which is used for the preparation of PZT slurry. The following precursors such as Zirconium tetrapropoxide $Zr(C_3H_7O)_4$, lead acetate trihydrate $Pb(CH_3COO)_2$, and Titanium isopropoxide $Ti((CH_3)_2CHO)_4$ are used to prepare the PZT sol. These precursors are mixed in the 2-methoxyethanol which acts as a solvent. The complete synthesis process for the preparation of PZT sol is reported in

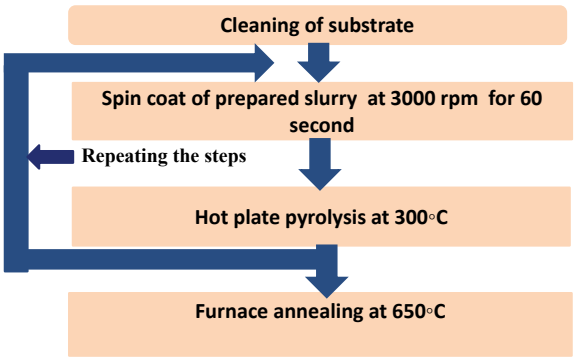

Fig. 1 Flow chart for the PZT thick film fabrication

our prelimilinary work [11]. Simultaneously, PZT powder is procured commercially which act as a particle source. Ball milling technique has been utilized to reduce the size of particles using a closed container with Zirconia balls. During milling, excess lead oxide is added in order to prevent lead loss. Powder was collected after milling for 12 h. Ultrasonication has been used to disperse PZT powder into the PZT solution for PZT thick film deposition.

2.2 Preparation of Thick Film of PZT

In the present study, spin coating technique is used for the preparation of thick film of PZT on the substrate of Nickel. Nickel offers small lattice mismatch with PZT as well as acts as bottom electrode for further characterization in metal-ferroelectric-metal (MFM) configuration. Ni substrates (M/s SHOP-AD INC., Massachusetts) are thoroughly cleaned using Trichloroethylene (TCE), acetone followed by isopropylalchol (IPA) before the preparation of PZT film. On the substrate of Nickel, PZT thick film is successfully deposited at optimized annealing temperature of 650 °C using the fabricated slurry shown in Fig. 1. The obtained slurry and the corresponding sol is alternatively deposited on Nickel substrate using a spin coater at 3000 rpm. The deposited film is pyrolysed at a temperature of 300 °C after each layer deposition. Optimium thickness (1.93 μm) is achieved using repeating the process. Finally, the as deposited PZT film is annealed at 650 °C to achieve perovskite single phase. Structural characterization of annealed thick film is analyzed using High resolution X-ray diffraction (XRD) (Make: Rigaku, Model: Ultima IV) technique having characteristics wavelength of 1.5406 Å (Cu kα_1) radiation at room temperature. On the top of PZT film, gold electrodes with diameter of 600 μm and thickness 40 nm were deposited through a shadow mask using thermal evaporation unit (Make: HHV) for the electrical and ferroelectric measurements. The electrical properties were measured using Keithley 4200 semiconductor characterization unit. at room temperature. P-E Hystersis loop tracer (Make: Radiant) is used to study the electrocaloric properties.

3 Results and Discussion

3.1 XRD

Single phase perovskite structure of the PZT thick film deposited on Nickel substrate and annealed at 650 °C for 1 h is revealed from the X-Ray diffraction pattern as shown in Fig. 2. No secondary phase of PZT is detected from the XRD pattern (Fig. 2). PZT film exhibits long range crystalline order which is concluded from the sharp and well defined diffraction peaks. It is observed from Fig. 2 that there are two major diffraction peaks at $2\theta = 44.54°$ and 51.81° corresponding to (111) and

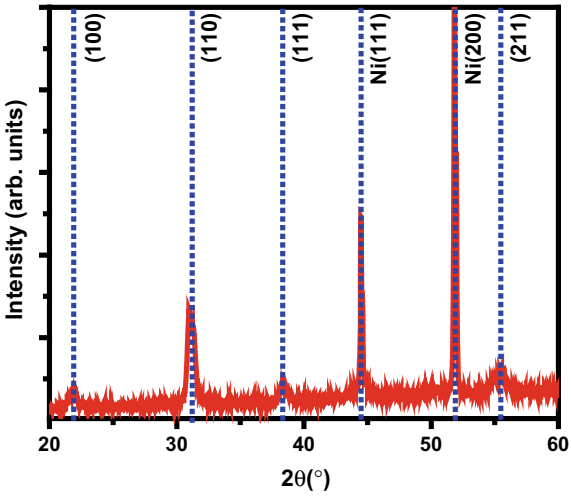

Fig. 2 XRD spectra of thick film of PZT deposited on substrate of Nickel with annealing temperature of 650 °C

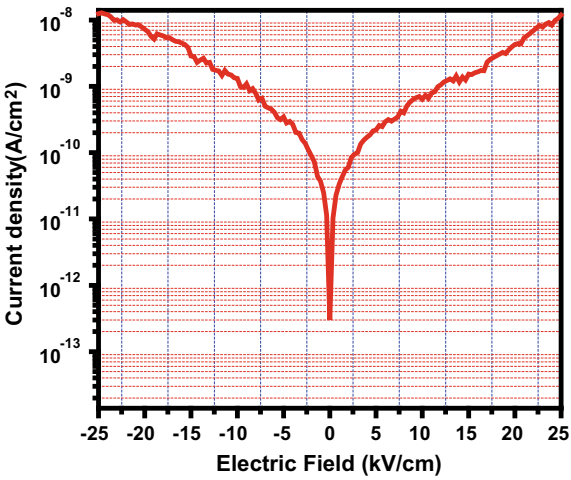

Fig. 3 Variation of current density as a function of electric field for the PZT film deposited using modified sol gel technique

(200) diffraction planes of Nickel substrate [10]. The crystallographic planes (100), (110), (111) and (211) at 21.89°, 31.09°, 38.34° and 55.34° corresponding to PZT are observed and are shown in Fig. 2 [11]. The crystallite size and lattice parameter are determined along the dominant (110) diffraction plane of PZT and are found to be crystallite size = 27 nm and a = 4.05 Å. The obtained values are in accordance with the reported literature [11].

Leakage current density

Figure 3 shows the leakage current density behaviour of the PZT thick film with optimized annealing temperature of 650 °C. Metal-Ferroelectric-Metal (MFM) configuration is adopted to study the leakage behaviour with the variation in external electric field from –25 kV/cm to 25 kV/cm respectively. With increase in the applied electric field, leakage current density is gradually increased as observed from Fig. 3. The following factors such as presence of defects, improper grain boundaries which act as conduction channels in the ferroelectric materials affect the leakage current density [7]. The leakage current density is determined for the PZT film at a particular electric field (25 kV/cm) and found to be 1.22×10^{-8} A/cm^2. The determined leakage current density is low due to proper fine grain boundaries and good crystallinity of deposited thick film. Similar results are also inferred from the XRD pattern as shown in Fig. 2. Low leakage current density proposes practical application of ferroelectric PZT film.

3.2 Temperature Dependent P–E Measurement

The temperature dependent ferroelectric properties of the PZT film annealed at 650 °C temperature are studied using Precision Analyser (Radiant Technologies) at a fixed frequency 1 kHz with variation in the electric field from −250 to 250 kV/cm. The hysteresis loops are also obtained in the temperature range from 310 to 430 K at an interval of 24 K as shown in Fig. 4. Remnant polarization, Maximum polarization at different temperatures are determined from Fig. 4 and tabulated in Table 1. P-E loops are not saturated as observed from Fig. 4. This is because of the presence of a higher leakage current. Cation and oxygen vacancies that exhibit space charges

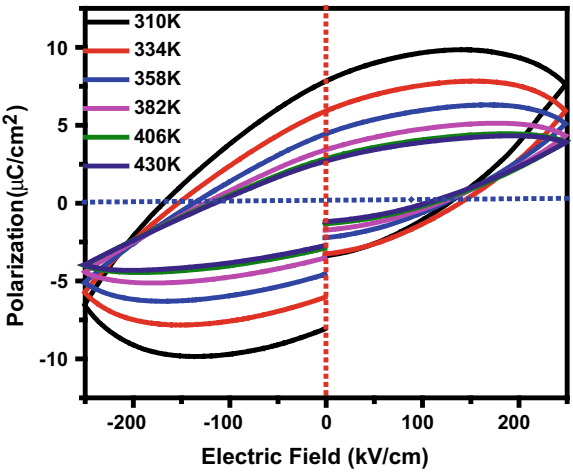

Fig. 4 Temperature dependent P–E hysteresis loop of grown PZT thick film at a particular frequency of 1 kHz

Table 1 Maximum polarization, Remanant polarization and ECE parameters estimated for the PZT thick film grown on Nickel substrate

Temperature (K)	Maximum polarization ($\mu C/cm^2$)	Remnant polarization ($\mu C/cm^2$)	ΔT (K) at 250 kV/cm	ΔS (JK^{-1} kg^{-1}) at 250 kV/cm
310	8.03	7.73	0.80	0.87
334	6.01	5.89	0.89	0.94
358	5.03	4.58	1.00	1.00
382	4.35	3.43	1.21	1.03
406	3.85	3.01	1.30	1.11
430	3.80	2.58	1.50	1.15

contribute to the leaky loop as observed from Fig. 4. The presence of these space charges inhibits the switching of polarization under high applied electric field [17].

It is observed that well defined hysteresis loops are formed indicating ferroelectric nature of PZT film deposited on Nickel substrate. With increase in the temperature, energy barrier is reduced resulting in decreasing the tendency to hold the poled state. As a result of this, the coercive field and remnant polarization are decreased [5].

3.3 Electrocaloric Study

Upper branch of the P–E hysteresis loops ($E > 0$) has been used to extract the temperature dependent polarization at various electric fields for the electrocaloric measurements (Fig. 4). The fourth order polynomial fitting to the $P(T)E$ data has been used to extract the polarization as a function of temperature, $P(T)$ [4, 5]. Figure 5a, b

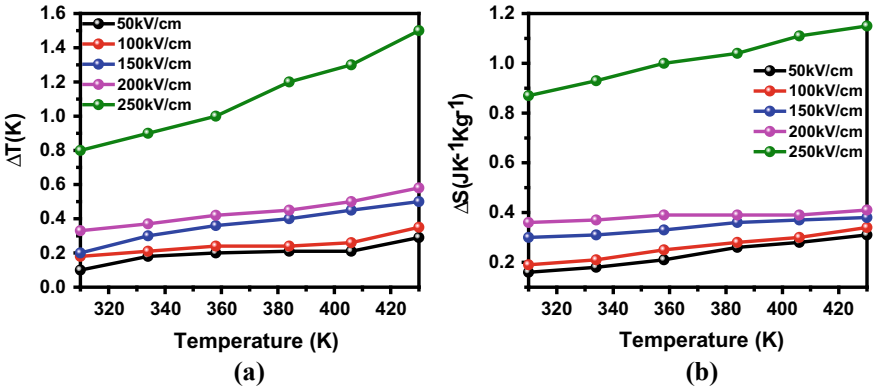

Fig. 5 **a** $\Delta T(K)$ and **b** ΔS(J K^{-1} kg^{-1}) versus temperature variation for the grown PZT film at different applied electric fields

show the electrocaloric parameters ΔT and ΔS values for PZT thick film with respect to temperature calculated at different electric fields. It is observed that both the ΔT and ΔS values are increased with increase in the applied electric field from 50 to 250 kV/cm at each temperature in the given temperature range as shown in Fig. 5. The maximum ΔT & ΔS values are estimated to be 1.50 K and 1.15 J Kg^{-1} K^{-1} at 250 kV/cm respectively. The electrocaloric responsivities ($\Delta T/\Delta E$) and ($\Delta S/\Delta E$) are also determined for the optimized PZT thick film at an applied electric field of 250 kV/cm and found to be 0.06 $\times$ 10^{-6} K $\cdot$ m/V and 0.04 $\times$ 10^{-6} J $\cdot$ m/(kg $\cdot$ K $\cdot$ V) respectively. The values are slightly larger in comparison to the thick PZT films reported in the literature [5]. This is because of the fact that proper growth of grains leads to larger polarizations, thus leading to larger ECE values.

4 Conclusion

1.93 μm thick single phase film of PZT has been successfully grown on the Nickel substrate at an optimized annealing temperature of 650 °C using modified sol gel deposition technique. The leakage current density is determined and found to be 1.22 $\times$ 10^{-8} A/cm^2 which is appreciably low for further applications of PZT film. The ferroelectric hysteresis loops of the film were measured at a frequency of 1 kHz within the temperature range of 310–430 K. The temperature change of $\Delta T = 1.50$ K and change in entropy $\Delta S = 1.15$ JKg^{-1} K^{-1} achieved at 430 K on the application of 250 kV/cm. The electrocaloric temperature change and entropy change responsivities are also determined for the optimized PZT thick film at an applied electric field of 250 kV/cm and found to be 0.06 $\times$ 10^{-6} K.m/V and 0.04 $\times$ 10^{-6} J·m/(kg·K·V).

Acknowledgements Authors are highly thankful to University of Delhi and DST for technical and financial support. One of the author, Vandana is thankful to CSIR for the research fellowship.

References

1. Li X, Lu S, Chen X, Gu H, Qiana X, Zhang QM (2013) Pyroelectric and electrocaloric materials. J Mater Chem C 23. https://doi.org/10.1039/c2tc00283c
2. Sebald G, Guyomar D, Agbossou A (2009) On thermoelectric and pyroelectric energy harvesting. Smart Mater Struct 18:125006. https://doi.org/10.1088/0964-1726/18/12/125006
3. Bowen CR, Taylor J, LeBoulbar E, Zabek D, Chauhanc A, Vaish R (2014) Pyroelectric materials and devices for energy harvesting applications. Energy Environ Sci 7:3836–3856. https://doi.org/10.1039/c4ee01759e
4. Asbani B, El Marssi M, Dellis JL, Lahmar A, Gagou Y, Mezzane D, Amjoud M, Alimoussa A, Kutnjak Z, Pirc R, Rožič B (2020) Electrocaloric response in lanthanummodified lead zirconate titanate ceramic. J Appl Phys 127:224101. https://doi.org/10.1063/5.0005038
5. Lu B, Li P, Tang Z, Yao Y, Gao X, Kleemann W, Lu S, Large Electrocaloric effect in Relaxor ferroelectric and Antiferroelectric lanthanum doped lead Zirconate Titanate ceramics. Sci Rep 7:45335. https://doi.org/10.1038/srep45335

6. Zhao C, Wang Z, Zhu W, Yao X, Liu W (2002) PZT thick films fabrication using a sol-gel based 0–3 composite processing. Int J Mod Phys B 16:242–248
7. Pu Z (2008) Enhanced electrical properties of Pb(Zr0.80Ti0.20)O3 thick films prepared by a modified sol-gel technique. Surf Coatings Technol 202:2068–2071
8. Zhao C, Wang Z, Zhu W, Tan O, Hng H (2004) Microstructure and properties of PZT53/47 thick films derived from sols with submicron-sized PZT particle. Ceram Int 30(7):1925–1927
9. Kesim MT, Zhang J, Alpay SP, Martin LW (2014) Enhanced electrocaloric and pyroelectric response from ferroelectric multilayers. Appl Phys Lett 105:052901. https://doi.org/10.1063/1.4892455
10. Shamim A, Ahmad Z, Mahmood S, Ali U, Mahmood T, Ahmad Nizami Z (2008) Large scale synthesis and characterization of Ni nanoparticles by solution reaction method. Bull Mater Sci
11. Gupta R, Tomar M, Rammohan S, Katiyar RS, Gupta V (2016) Multiferroic cantilever for power generation using dual functionality. Appl Phys Lett 109:193901
12. Kalem V, Ibrahim, Timuc M (2011) Dielectric and piezoelectric properties of PZT ceramics doped with strontium and lanthanum. Ceram Int 37:1265–1275. 0272-8842/$36.00
13. Souni M, Kuhnke M, Piorra A, Solterbeck CH (2005) Pyroelectric and piezoelectric properties of thick PZT films produced by a new sol-gel route. J Eur Ceram Soc 25(12):2499–2503
14. Neese B, Chu B, Guo Lu S, Wang Y, Furman E, Zhang QM (2008) Large electrocaloric effect in ferroelectric polymers near room temperature. Science 321:821
15. Sanlialp M, Shvartsman V, Acosta M, Lupascu C (2016) Electrocaloric effect in Ba(Zr, Ti)$_O$3–(Ba, Ca)T$_i$O3 ceramics measured directly. J Am Ceram Soc 99:4022–4030
16. Kandula R, Banerjee K, Santosh Kumar Raavi S, Asthana S, Enhanced electrocaloric effect and energy storage density of Nd-substituted 0.92NBT-0.08BT lead free ceramic (2018) Phys Status Solid A 215:1700915
17. Vineetha P, Jose R, Venkata Saravanan K (2019) Effect of ZnO on (ferroelectric) fatigue retention and thermal stability of ferroelectric properties in lead free (K0.5Na0.5)(Nb0.7Ta0.3)O3 ceramics (2019) RSC Adv 9:34888

Multifunctional Properties of Non-mulberry Silk Fibroin and Gelatin Blend Solutions: Rheological Study

Priti, Radhika Batra, and Roli Purwar

Abstract In this work, we have studied the influence of blending *Antheraea mylitta* silk fibroin solution (concentration 10% w/v) with solution of gelatin (concentration 20% w/v) by using 99% pure formic acid as a solvent. Various blends with desired ratios namely G0S10, G8S2, G7S3, G5S5, and G10S0 were prepared and studied for their viscoelastic behavior. The time dependent analysis with respect to change in viscosity which is also termed as constant shear rate viscosity study was performed for all the blend solutions. Behavior of the pure and blend solutions in the applied range of shear rates viz., 0.01–500 s^{-1} were also studied. Under dynamic rheological tests, amplitude sweep and frequency sweep were executed. In viscosity test results, a decrease in viscosity was observed in blends of gelatin and silk fibroin as compared to pure silk fibroin solution. Shear thinning behavior was observed in all the blend solutions in the applied shear range. Through amplitude sweep analysis of the blend solutions further, frequency sweep study was carried out by applying a definite percent strain. It can be confirmed through these rheological studies by changing the operating parameters like shear rate, angular frequency, and blend ratios, etc., the properties of blend solutions can be tuned according to the desired end use applications such as medical, textile, tissue engineering, and packaging, etc.

Keywords Non-mulberry · Silk fibroin · Rheology · Blend · Gelatin

1 Introduction

The polymer solutions having the capacity to alter their properties in the solution state itself can be utilized to design materials with specific characteristics and rheological studies are one of the widely accepted methods to observe such alterations. The process parameters to be used for material creation can be fine-tuned through rheological analysis of polymer solutions beforehand.

Priti · R. Batra · R. Purwar (✉)
Department of Applied Chemistry, Delhi Technological University, Shahbad Daulatpur, Bawana Road, Delhi 110042, India

S. B. Krupanidhi et al. (eds.), *Advanced Functional Materials and Devices*, Springer Proceedings in Materials 14, https://doi.org/10.1007/978-981-16-5971-3_9

Silk fibroin which is a natural protein fiber obtained from silkworms is categorized into two mains viz. mulberry (*Bombyx mori*) and non-mulberry (*A. mylitta*, *A. assamensis*, *P. ricini*, etc.). Non-mulberry (wild silk) silk is much more difficult to process than mulberry silk because of its poor solubility in the available conventional solvents. However, it has the arginine-glycine-aspartate (RGD) amino acid sequence which favors cell attachment and proliferation and is useful from the prospects of biomedical applications [3]. After several attempts by researchers, solvents like ionic liquids were found to dissolve non-mulberry silk fibroin [8]. While dissolution, hydrogen bonds in non-mulberry silk are broken down which disrupts their structural arrangements and results in changes in their physiological properties. To regain and improve their physiological properties like mechanical strength, flexibility, biodegradability, etc., other polymers like chitosan, elastin, PVA, etc. are used to blend with silk fibroin. Most of the studies carried out by research groups on silk fibroin blends focus upon the physiological properties of end products generated from them [1, 2, 6]. However, the properties of blend solutions which can impact the final product properties have not been emphasized much. A hand full of reports are available on rheological studies of silk fibroin blend solutions, and majorly mulberry silk is the variety used for the study [10, 11].

Gelatin obtained by partial hydrolysis of collagen is derived from animal tissues such as skin, muscles, and bones. As gelatin is biocompatible, biodegradable, water soluble, non-immunogenic, and inexpensive [5], it is one of the feasible options to blend with non-mulberry silk fibroin. Through the blending process of these two polymers, an improved class of material with superior qualities than both pure polymers alone can be obtained. Rheological analysis of the silk fibroin/gelatin blend solutions can provide great insights on the feasibility of their blending before giving them a material form. In the current research paper, steady shear rheological tests were conducted to check the rheological behavior of pure gelatin, pure silk fibroin, and their blend solutions. The obtained curves provide the relation between shear viscosity and the shear rate of solutions. Under dynamic rheological tests, dynamic parameters like storage modulus (G') and loss modulus (G'') of pure polymeric solutions and their blend solutions were measured. Additionally, time dependent shear viscosity of pure as well as blend solutions were determined at constant shear rates viz., 1, 50, and 100 s^{-1}. All these tests were carried out to explore the solution properties of pure silk fibroin, pure gelatin, and their blend solutions.

Table 1 Sample codes used for silk fibroin and gelatin blend solutions in formic acid

S. No.	Pure gelatin in formic acid (20% w/v)	Pure silk fibroin in formic acid (10% w/v)	Sample code
1	100	0	G10S0
2	50	50	G5S5
3	70	30	G7S3
4	80	20	G8S2
5	0	100	G0S10

2 Experimental

2.1 Materials

Non-mulberry silk of grade Antheraea mylitta silkworm cocoons were obtained from Central Silk Board, Son Bhadra, UP, India. The ionic liquid BMIMAc (1-butyl-3-methylimidazolium acetate) was purchased from Sigma Aldrich. Gelatin bacteriological (average M.W. 20,000 g mol^{-1}) and Slide-A-Lyzer dialysis flask (20 K MWCO, 250 mL) were obtained from Thermo Scientific, India. Formic acid with 98% purity was bought from Loba Chemie Pvt. Ltd., India. Milli-Q water was used for dialysis process of silk fibroin ionic solution.

2.2 Sample Preparation of Antheraea Mylitta *Silk Fibroin and Gelatin Blend Solutions*

Initially *Antheraea mylitta* silkworm cocoons were degummed to removed sericin component. The obtained degummed silk fibers were used to make solution in BMIMAc ionic solution. The dialysis of this silk fibroin ionic liquid solution was done against mili Q water for a week. This aqueous silk fibroin solution was dried at temperature of 100 °C to get completely dry silk fibers. Stock solution of this dried silk powder (10% w/v) and gelatin (20% w/v) were prepared in formic acid to make various blend solutions. Desired blend solutions were prepared by mixing these stock solutions of pure silk fibroin and gelatin in specific ratios (w/w) as abbreviated in Table 1.

2.3 Measurements

The rheological properties of all the prepared blend solutions were measured at 25 °C using Modular Compact Rheometer (MCR 302) by Anton Paar. A concentric

parallel plate of 40 mm diameter geometry (PP40) with a 0.70 mm gap were used to carry out all the tests. Under steady shear rheology tests, viscosities of all the blend solutions were measured with respect to variable shear rate range from 0.01 to 500 s^{-1} and at different constant shear rates viz. 1, 50, and 100 s^{-1} with respect to time. Under dynamic shear rheological tests frequency sweep test was performed in the frequency range from 0.1 to 100 rad s^{-1} at different strain levels for different solutions. The respective strain value was determined by individual amplitude sweep test data.

3 Results and Discussion

3.1 Steady Shear Rheological Studies of Silk Fibroin and Gelatin Blend Solutions

The steady shear rheological studies of silk fibroin/gelatin blend solutions were examined at 25 °C, as shown in Fig. 1. Pure silk fibroin solution (G0S10) showed

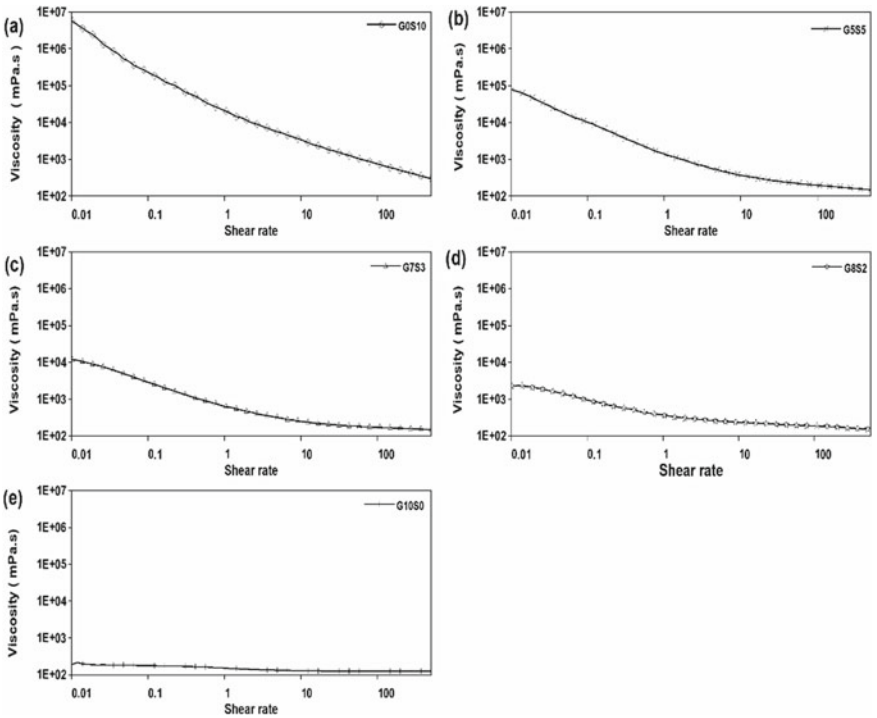

Fig. 1 Steady shear rheological curves of silk fibroin and gelatin blend solutions

the highest and G10S0 solution the least viscosity in the applied range of shear rates viz. 0.01–500 s^{-1}. Upon blending these two pure solutions, viscosities of blend solutions were lying in between which depends upon the polymeric component added. The blend solution with the least silk fibroin content (G8S2) possessed the least viscosity compared to the rest two blend solutions (G7S3, G5S5) with lower gelatin content. Moreover, the viscosity of pure silk fibroin solution was observed dramatically decreasing with an increase in applied shear rate range from 0.01 to 500 s^{-1} while in the case of pure gelatin solution this effect was not prominent. As expected, all the blended solutions showed a similar shear thinning trend of viscosity which was intermediate to the pure polymeric solutions. In shear thinning, either alignment of molecular chains is increased or due to high shear rate molecular chains are uncoiled. Similar shear thinning results were found by Singh in mulberry silk fibroin solution in formic acid which was reported in previous literature [9].

3.2 Constant Shear Rheological Studies of Silk Fibroin and Gelatin Blend Solutions

To study the time dependent behavior of solution viscosities at different shear rates 150,100 s^{-1}, the blend solutions were tested. The viscosities were measured with respect to time at a particular constant shear rate for each sample (Fig. 2). The experiment results can directly provide the values of viscosities at respective shear rates. Pure silk fibroin solution G0S10 has the highest viscosity at all the applied shear rates amongst all the blend solutions while pure gelatin solution G10S0 has the least. As expected, upon blending respective viscosities were falling in between that of pure components. Zhang and Pan also reported similar results in aqueous solutions of mulberry silk and PVA blend [11].

3.3 Frequency Sweep Studies of Silk Fibroin and Gelatin Blend Solutions

In frequency sweep studies, the applied frequency range was from 0.1 to 100 rad/s and the obtained % shear strains of particular blends (G0S10 = 1%, G5S5 = 1%, G7 S3 = 10%, S2G8 = 10% and S0G10 = 10% shear strain) from amplitude sweep results were kept constant. For analysis, storage modulus G' and loss modulus G'' were plotted against angular frequency as shown in Fig. 3. Figure 3a, it was observed that for pure silk fibroin G0S10, G' is dominant throughout the whole angular frequency range which represents viscoelastic solid type behavior. Mu et al. have reported higher storage modulus at the higher frequency and higher loss modulus at low frequency in silk dope [7]. Figure 3e, in the case of pure gelatin G10S0, G'' was dominant throughout the whole angular frequency range implies viscous fluid-like behavior.

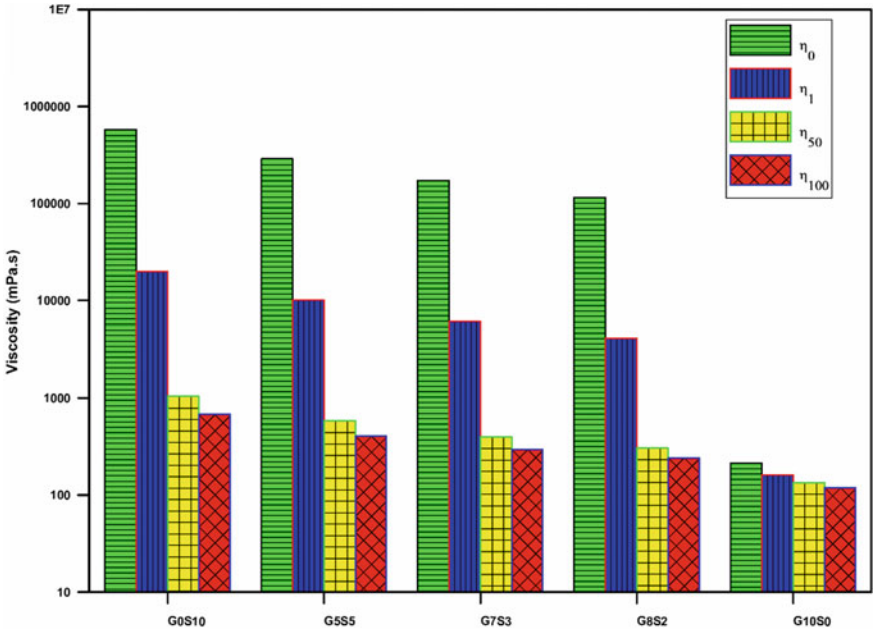

Fig. 2 Constant shear rheological curves of silk fibroin and gelatin blend solutions

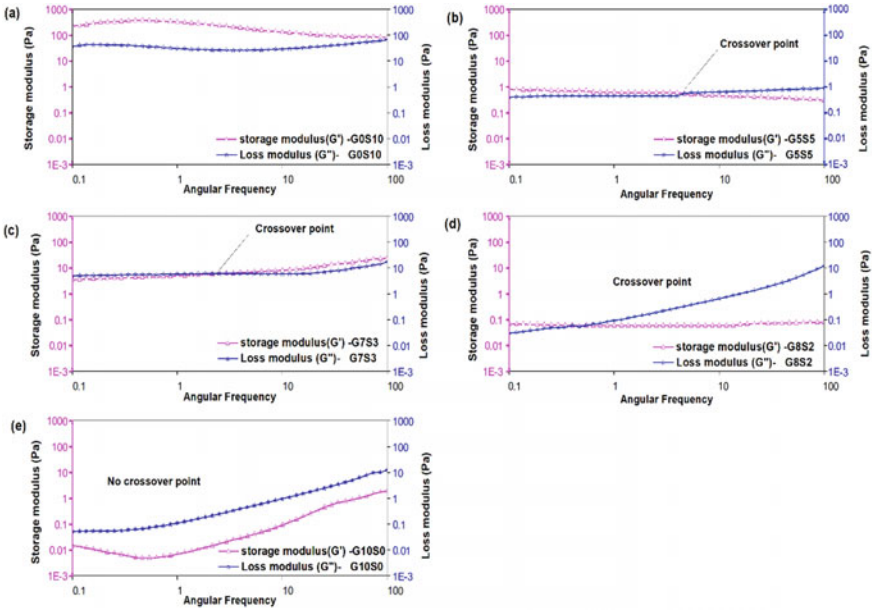

Fig. 3 Frequency sweep data of silk fibroin and gelatin blend solutions

Table 2 Sample code

Sample code	At low frequency		Crossover point	At high frequency	
	G′	G″	Angular frequency in rad/s	G′	G″
G10S0	0.004	0.028	No crossover	0.97	3.75
G8S2	0.085	0.03	8.04	1.28	6.02
G7S3	1.29	2.41	2.37	16.21	9.11
G5S5	5.51	2.61	1.44	17.60	25.51
G0S10	120.89	48.72	No crossover	186.28	26.29

Upon blending, alteration to the viscoelastic behavior of solutions was observed. It was observed that for G5S5 (Fig. 3b) and G8S2 (Fig. 3d), at high frequency, G″ is dominant showing viscoelastic fluid-like behavior while at a lower frequency, after a crossover point G′ is dominant which indicates viscoelastic solid-like behavior. However, a different position of crossover point was observed in both solutions. Surprisingly, in the case of G7S3 solution (Fig. 3c), conflicting viscoelastic behavior was observed than the other two blend solutions, which might be due to intermolecular interactions of silk fibroin and gelatin hence detailed study is required for further clarity.

Overall the blend solutions of silk fibroin with gelatin in formic acid behave both ways like viscoelastic solid as wells as fluid at different frequencies. Similar results were observed by Kaewprasit et al. in previous literature in angular frequency dependent viscoelastic behavior of pure *B. mori* silk fibroin solution in alcohol solvent [4]. The values of G′ and G″ at low and high frequency, as well as crossover point of all solutions, were summarized in Table 2.

4 Conclusion

Steady shear and dynamic shear rheological studies of pure silk fibroin, pure gelatin, and their blends were carried out. Pure silk fibroin solution (G0S10) showed the highest zero shear viscosity means viscosity at rest while pure gelatin solution (G10S0) reflected the least viscosity. As expected, the viscosity of all the blend solutions was found to lay in between these pure solutions. All five solutions showed shear thinning behavior. Based on the results obtained from amplitude sweep data, frequency sweep results showed pure silk fibroin solution behaves like viscose solid, and pure gelatin solution presents viscose fluid type behavior. Upon blending these two solutions it altered the behavior of blend solutions to be viscoelastic at different frequency ranges. Overall, the ability to alter the viscoelastic properties by controlling the conditions at the solution level can be beneficial to create materials with tailorable properties.

References

1. Bhattacharjee P, Naskar D, Kim HW, Maiti TK, Bhattacharya D, Kundu SC (2015) Non-mulberry silk fibroin grafted PCL nanofibrous scaffold: promising ECM for bone tissue engineering. Eur Polym J 71:490–509. https://doi.org/10.1016/j.eurpolymj.2015.08.025
2. Chouhan D, Chakraborty B, Nandi SK, Mandal BB (2016) Role of non-mulberry silk fibroin in deposition and regulation of extracellular matrix towards accelerated wound healing
3. Jasmine S, Mandal BB (2014) Types and properties of non-mulberry silk biomaterials for tissue engineering applications. Woodhead Publishing Limited
4. Kaewprasit K, Kobayashi T, Damrongsakkul S (2018) Thai silk fibroin gelation process enhancing by monohydric and polyhydric alcohols. Int J Biol Macromol 118:1726–1735. https://doi.org/10.1016/j.ijbiomac.2018.07.017
5. Ki CS, Baek DH, Gang KD, Lee KH, Um IC, Park YH (2005) Characterization of gelatin nanofiber prepared from gelatin-formic acid solution. Polymer (Guildf) 46(14):5094–5102. https://doi.org/10.1016/j.polymer.2005.04.040
6. Kundu SC, Nandi SK, Bhattacharya D, Maiti TK, Naskar D, Bhattacharjee P, Das P (2016) Potential of non-mulberry silk protein fibroin blended and grafted poly(Є-caprolactone) nanofibrous matrices for in vivo bone regeneration. Colloids Surf B Biointerf 143:431–439. https://doi.org/10.1016/j.colsurfb.2016.03.058
7. Mu X, Fitzpatrick V, Kaplan DL (2020) From silk spinning to 3D printing: polymer manufacturing using directed hierarchical molecular assembly. 1901552:1–17. https://doi.org/10.1002/adhm.201901552
8. Silva SS, Gomes JM, Vale AC, Lu S, Reis RL, Kundu SC (2020) Green pathway for processing non-mulberry Antheraea Pernyi silk fibroin/chitin-based sponges: biophysical and biochemical characterization. Front Mater 7(May). https://doi.org/10.3389/fmats.2020.00135
9. Singh BN, Panda NN, Mund R, Pramanik K (2016) Carboxymethyl cellulose enables silk fibroin nanofibrous scaffold with enhanced biomimetic potential for bone tissue engineering application. Carbohydr Polym 151:335–347. https://doi.org/10.1016/j.carbpol.2016.05.088
10. Yao Y, Mukuze KS, Zhang Y, Wang H (2014) Rheological behavior of cellulose/silk fibroin blend solutions with ionic liquid as solvent. Cellulose 21(1):675–684. https://doi.org/10.1007/s10570-013-0117-y
11. Zhang X, Pan Z (2020) Rheological behavior of regenerated silk fibroin/polyvinyl alcohol blended solutions in steady and dynamic state and the effect of temperature. J Mater Sci 55(31):15350–15363. https://doi.org/10.1007/s10853-020-05086-4

Monopole Condensation and Dynamical Chiral Symmetry Breaking in Dual QCD Formulation

Garima Punetha

Abstract In the non-perturbative regime of $SU(3)$ dual QCD, the phenomena of monopole condensation and dynamical chiral symmetry breaking (DCSB) have been studied, and a non-trivial solution to the dynamical breakdown of chiral symmetry has been obtained from QCD's Schwinger–Dyson equations (SDEs). The dynamically generated quark mass-function represents the fundamental expression to demonstrate DCSB and has been found to be directly proportional to the strong coupling constant and glueball masses. The DCSB appears to be strong for large values of coupling constant and vector glueball mass and therefore ensures QCD-monopole condensation responsible for the color confinement.

1 Introduction

In the dual-superconductor model of the color confinement [1–4], the condensation of monopoles expels electric field from the vacuum into confining flux tubes. In connection, the dependence of color confinement with DCSB also seems to be natural [5, 6] and arises from $SU(3)$ lattice gauge theory [7]. In general, DCSB has been considered to emerge from the topological structure of the non-trivial vacuum. The DCSB leads to the emergence of bound states between quarks and monopoles and the generation of the non-zero quark condensate. Inspite of the considerable studies related to DCSB [8–11], the detailed examination has not been established. The investigation associated with DCSB has been problematic due to the distinctly non-perturbative nature of QCD. The correlation between quark confinement with DCSB has also been suggested in terms of QCD-monopoles. The dynamical chiral symmetry is broken dynamically in the confined phase, whereas, with raising temperature/chemical potential, it gets restored [12–14]. The lattice simulation has also been proven to be a dynamic method attaining the outcome consistent with the experimental findings [15]. However, in order to resolve the exploration of the mechanism of DCSB from the theoretical point of view, the Schwinger–Dyson approach has been

G. Punetha (✉)
Department of Physics, Government Post Graduate College, Berinag, Pithoragarh 262531, India

S. B. Krupanidhi et al. (eds.), *Advanced Functional Materials and Devices*, Springer Proceedings in Materials 14, https://doi.org/10.1007/978-981-16-5971-3_10

proposed in the present paper. Within the gauge-invariant framework of $SU(3)$ dual QCD formalism [16], the solutions to the SDEs have been extracted which enables us to the study the behavior of the quark mass-function.

The present paper have been mainly organized as follows. In Sect. 2, a symmetry preserving framework of $SU(3)$ dual QCD formulation has been discussed including the color isocharges and the topological charges. In Sect. 3, the phenomenon of DCSB has been studied using SDEs.

2 SU(3) Dual QCD Formulation

The theoretical description of QCD [16–25] within a symmetry preserving framework has been discussed. The homotomy $\Pi_2(G/H) \rightarrow \Pi_2(SU(3)/U(1) \otimes U^{'}(1))$ produces the topological charges, obtaining the following form,

$$\hat{m}^{'} = \sqrt{3}\hat{m} * \hat{m}. \tag{1}$$

Choosing $\hat{m}$ to be always λ_3-like, in which the product symmetry $\hat{m}^{'}$ automatically becomes λ_8-like. The generalized field strength may then be written as,

$$\mathbf{G}_{\mu\nu} = (F_{\mu\nu} + B^{(d)}_{\mu\nu})\hat{m} + (F^{'}_{\mu\nu} + B^{'(d)}_{\mu\nu})\hat{m}^{'}, \tag{2}$$

where $F_{\mu\nu} = \partial_\mu A_\nu - \partial_\nu A_\mu$, $F^{'}_{\mu\nu} = \partial_\mu A^{'}_\nu - \partial_\nu A^{'}_\mu$, $B^{(d)}_{\mu\nu} = \partial_\mu B_\nu - \partial_\nu B_\mu = g^{-1}(\hat{m} \times \partial_\mu \hat{m})$, $B^{'(d)}_{\mu\nu} = \partial_\mu B^{'(d)}_\nu - \partial_\nu B^{'(d)}_\mu = g^{-1}(\hat{m}^{'} \times \partial_\mu \hat{m}^{'})$. Using the following parametrization,

$$U = \exp\left[-\beta^{'}(-\frac{1}{2}t_3 + \frac{1}{2\sqrt{3}}t_8)\right] \times e^{-\alpha t_n} \exp\left[-(\beta - \frac{1}{2}\beta^{'})t_3 e^{-\alpha t_2}\right], \tag{3}$$

where $\beta = n\varphi$, $\beta^{'} = n^{'}\varphi$ and t_i $(i = 1, 2, 3, \ldots 8)$ are the adjoint representations of the $SU(3)$ generators, the magnetic vector $\hat{m}$ may be explicitly written as,

$$\hat{m} = \begin{pmatrix} \sin\alpha \cos\frac{1}{2}\alpha \cos[(\beta - \beta^{'})] \\ \sin\alpha \cos\frac{1}{2}\alpha \sin[(\beta - \beta^{'})] \\ \frac{1}{4}\cos\alpha(3 + \cos\alpha) \\ \sin\alpha \sin\frac{1}{2}\alpha \cos(\beta) \\ \sin\alpha \sin\frac{1}{2}\alpha \sin(\beta) \\ \frac{-1}{2}\sin\alpha \cos\alpha \cos(\beta^{'}) \\ \frac{-1}{2}\sin\alpha \cos\alpha \sin(\beta^{'}) \\ \frac{1}{4}\sqrt{3}\cos\alpha(1 - \cos\alpha) \end{pmatrix}. \tag{4}$$

The corresponding field strength then takes the following form given below,

$$\mathbf{G}_{\mu\nu} \xrightarrow{U} -\frac{1}{g}\Bigg[\sin\alpha\Bigg((\partial_\mu\alpha\partial_\nu\beta - \partial_\nu\alpha\partial_\mu\beta) - \frac{1}{2}(\partial_\mu\alpha\partial_\nu\beta^{'} - \partial_\nu\alpha\partial_\mu\beta^{'})\Bigg)\hat{m} + \frac{1}{2}\sqrt{3}\sin\alpha(\partial_\mu\alpha\partial_\nu\beta^{'} - \partial_\nu\alpha\partial_\mu\beta^{'})\hat{m}^{'}\Bigg]. \tag{5}$$

The quenched Lagrangian for the $SU(3)$ dual QCD is constructed by introducing the regular dual magnetic potential and complex scalar fields expressed in the following form,

$$\mathcal{L}_{SU(3)} = -\frac{1}{4}F_{\mu\nu}^{'2} - \frac{1}{4}B_{\mu\nu}^{2} - \frac{1}{4}B_{\mu\nu}^{'2} + |(\partial_\mu + i\frac{4\pi}{g}B_\mu^{(d)})\phi|^2 + |(\partial_\mu + i\frac{4\pi}{g\sqrt{(3)}}B_\mu^{'(d)})\phi^{'}|^2 - V(\phi,\phi^{'}), \tag{6}$$

where $V(\phi,\phi^{'})$ is the quadratic potential for inducing the magnetic condensation of QCD vacuum is naturally desired and is given below,

$$V(\phi,\phi^{'}) = \frac{48\pi^2}{g^4}\lambda(\phi^*\phi - \phi_0^2)^2 + \frac{432\pi^2}{g^4}\lambda^{'}(\phi^*\phi^{'} - \phi_0^{'2})^2. \tag{7}$$

Under the cylindrical symmetry the field equations reduces,

$$\frac{\mathrm{d}}{\mathrm{d}\rho}\Bigg[\frac{1}{\rho}\frac{\mathrm{d}}{\mathrm{d}\rho}\Big(\rho B(\rho)\Big)\Bigg] - \sqrt{\frac{16\pi}{\alpha_s}}\Bigg(\frac{n}{\rho} + \sqrt{\frac{4\pi}{\alpha_s}}B(\rho)\Bigg)\chi^2(\rho) = 0, \tag{8}$$

$$\frac{1}{\rho}\frac{\mathrm{d}}{\mathrm{d}\rho}\Bigg(\rho\frac{\mathrm{d}\chi(\rho)}{d\rho}\Bigg) - \Bigg[\Bigg(\frac{n}{\rho} + \sqrt{\frac{4\pi}{\alpha_s}}B(\rho)\Bigg)^2 + \frac{6\lambda}{\alpha_s^2}\Big(\chi^2 - \phi_0^2\Big)\Bigg]\chi(\rho) = 0, \tag{9}$$

$$\frac{\mathrm{d}}{\mathrm{d}\rho}\Bigg[\frac{1}{\rho}\frac{\mathrm{d}}{\mathrm{d}\rho}\Big(\rho B^{'}(\rho)\Big)\Bigg] - \sqrt{\frac{48\pi}{\alpha_s}}\Bigg(\frac{n^{'}}{\rho} + \sqrt{\frac{12\pi}{\alpha_s}}B^{'}(\rho)\Bigg)\chi^{'2}(\rho) = 0, \tag{10}$$

$$\frac{1}{\rho}\frac{\mathrm{d}}{\mathrm{d}\rho}\Bigg(\rho\frac{\mathrm{d}\chi^{'}}{\mathrm{d}\rho}\Bigg) - \Bigg[\Bigg(\frac{n^{'}}{\rho} + \sqrt{\frac{12\pi}{\alpha_s}}B^{'}(\rho^{'})\Bigg)^2 + \frac{54\lambda^{'}}{\alpha_s^2}\Big(\chi^{'2} - \phi_0^{'2}\Big)\Bigg]\chi^{'}(\rho) = 0. \tag{11}$$

Table 1 Masses $\bar{m}_\phi$ and $\bar{m}_B$ in $SU(3)$ dual QCD vacuum

λ	α_s	$\bar{m}_\phi$	$\bar{m}_B$	$\lambda^{(d)}_{\rm QCD}$	$\xi^{(d)}_{\rm QCD}$	$\kappa^{(d)}_{\rm QCD}$
		(GeV)	(GeV)	($\rm GeV^{-1}$)	($\rm GeV^{-1}$)	
$\frac{1}{4}$	0.25	1.21	1.74	0.57	0.83	0.69
$\frac{1}{2}$	0.24	1.68	1.63	0.61	0.59	0.99
1	0.23	2.16	1.53	0.65	0.46	1.42
2	0.22	2.89	1.42	0.70	0.34	2.05

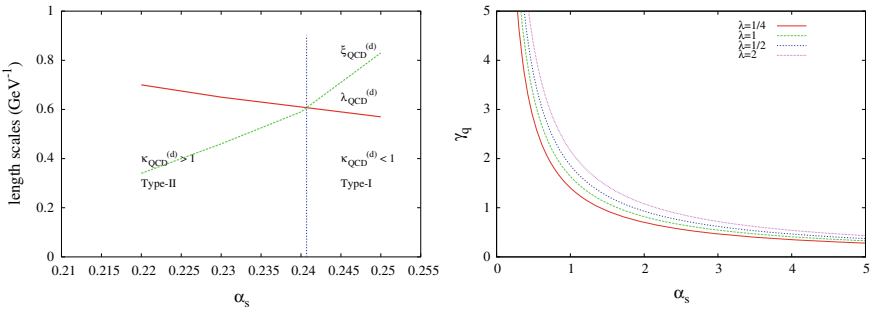

Fig. 1 **a** Variation in length scales as functions of strong coupling constant and **b** γ_q with strong coupling constant for different values of λ in $SU(3)$ dual QCD vaccum

The corresponding string tension of the resulting flux tube configuration takes the following form,

$$
\begin{aligned}
k_q = 2\pi \int_0^\infty \rho d\rho \Bigg[& \frac{n^2 g^2}{32\pi^2\rho^2}\left(\frac{dF}{d\rho}\right)^2 \\
& + \frac{n^2}{\rho^2}F^2(\rho)\chi^2(\rho) + \left(\frac{d\chi}{d\rho}\right)^2 + 3\lambda\alpha_s^{-2}(\chi^2-\phi_0^2)^2\Bigg] \\
& + 2\pi \int_0^\infty \rho d\rho \Bigg[\frac{n'^2 g^2}{96\pi^2\rho^2}\left(\frac{dG}{d\rho}\right)^2 + \frac{n'^2}{\rho^2}G^2(\rho)\chi'^2(\rho) + \left(\frac{d\chi'}{d\rho}\right)^2 \\
& + 27\lambda' \alpha_s^{-2}(\chi'^2-\phi_0'^2)^2\Bigg].
\end{aligned}
\tag{12}
$$

Incorporating the following property of color reflection invariance, the resulting string tension (k_q) of the $SU(3)$ dual QCD flux tube is given as, $k_q = \frac{1}{2\pi\alpha'} = \frac{\alpha_s}{8\pi}\gamma_q \bar{m}_B^2$, where α' is the Regge slope parameter, $\bar{m}_B$ is the vector glueball mass, and γ_q is the dimensional parameter. Using Eq. (13), the scalar ($\bar{m}_\phi$) and vector glueball mass ($\bar{m}_B$) are computed Table 1 [26].

The graphical plot of the length scales, penetration depth ($\lambda^{(d)}_{QCD}$), and coherence length ($\xi^{(d)}_{QCD}$) with α_s has been shown in Fig. 1a. Moreover, Fig. 1b demonstrates the variation in γ_q as a functions of α_s for a fixed λ which eventually indicates the decreasing trend of γ_q with increasing α_s.

3 Dynamical Chiral Symmetry Breaking in $SU(3)$ Dual QCD Formalism

DCSB is one of the most significant non-perturbative phenomena of inter-quark dynamics and evidently has a close relevance to the process of color confinement in the infrared sector of $SU(3)$ dual QCD vacuum. Since we are interested in the dynamically generated quark masses, we start with the case of exact chiral symmetry and solve the quark SDEs in the chiral limit. The SDE for quark propagator is obtained as,

$$S^{-1}(p) = Z_2(i\gamma.p + m_b) + Z_1 \int \frac{d^4q}{(2\pi)^4} g^2 \gamma^\mu \frac{\lambda^a}{2} S(q) \Gamma^{vb} \times D^{ab}_{\mu\nu}(p-q). \quad (13)$$

The quark propagator and the gluon propagator [27, 28] have been given as,

$$S^{-1}(p) = i\gamma.pA(p^2) - M(p^2), \;\; D^{ab}_{\mu\nu}(q) = \delta^{ab}(\delta_{\mu\nu} - \frac{q_\mu q_\nu}{q^2})\beta\delta^4(q), \quad (14)$$

where β is an adjustable parameter. Solving SDEs for the $SU(3)$ QCD system, two coupled integral equation for $A(p^2)$ and $M(p^2)$ have been constructed in the following form,

$$[A(p^2) - 1]p^2 = \frac{4}{3} g^2 \beta \int \frac{d^4q}{(2\pi)^4} \frac{A(q^2)}{q^2 A^2(q^2) + B^2(q^2)} \left[pq + \frac{q(p-q)(p-q)p}{(p-q)^2} \right], \quad (15)$$

$$M(p^2) = 4g^2\beta \int \frac{d^4q}{(2\pi)^4} \delta^4(p-q) \frac{B(q^2)}{q^2 A^2(q^2) + B^2(q^2)}. \quad (16)$$

The solution to the above-mentioned coupled integral equations has also been studied in [29, 30] illustrating the validity of DCSB in the infrared region of $SU(3)$ dual QCD and have been expressed in terms of momentum dependent quark mass-function in the following form,

$$M(p^2)_{SU(3)} = \sqrt{\frac{2\bar{m}_B^2 \alpha_s}{\pi} - \frac{4p^2}{9}} \quad p^2 < \frac{9}{4}\left(\frac{2\bar{m}_B^2 \alpha_s}{\pi}\right),$$

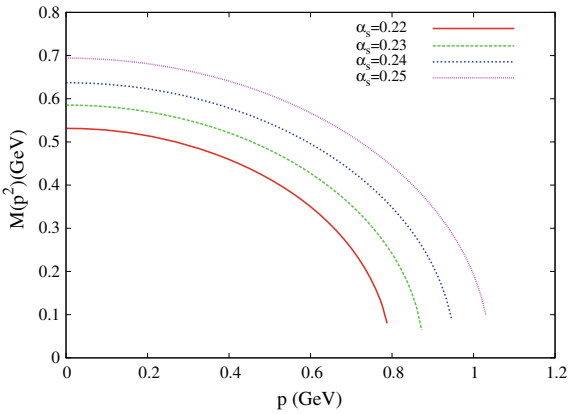

Fig. 2 Variation in quark mass-function with momentum scale in $SU(3)$ dual QCD vacuum at different strong coupling constant

$$M(p^2)_{SU(3)} = 0 \quad p^2 > \frac{9}{4}\left(\frac{2\bar{m}_B^2\alpha_s}{\pi}\right), \tag{17}$$

for any nonzero and positive value of α_s. The dynamically generated quark-mass function $(M(p^2)_{SU(3)})$ is directly proportional to α_s and $\bar{m}_B$ for low energy region indicating more enhancement of the DCSB in $SU(3)$ dual QCD vacuum and is shown in Fig. 2. Moreover, for $p = 0$ the above equation reduces to $M^2(0)_{SU(3)} = \frac{2\bar{m}_B^2\alpha_s}{\pi}$ demonstrating the constituent quark-mass in the confining region of $SU(3)$ dual QCD vacuum consisting of $\bar{m}_B$ and α_s, which increases as $\bar{m}_B$ increases demonstrating the magnetic symmetry breaking, monopole condensation, and color confinement.

4 Results and Conclusions

Confinement and DCSB have been proven as the most important non-perturbative phenomena in low energy QCD generally accepted to originate from the topological structure of the non-trivial QCD vacuum. One of the striking aspects of the $SU(3)$ dual QCD formalism is the fact that one obtains the confinement of color by breaking the magnetic symmetry dynamically.The monopole condensation of the $SU(3)$ dual QCD vacuum leads to the masses and length scales and further investigated in terms of the Ginzburg–Landau parameter in order to examine the nature of the vacuum. The DCSB has been studied using SDEs and investigated analytically with a non-trivial dependence on the quark mass-function on momenta. Its solution has been obtained in terms of the momentum-dependent quark mass-function which have been shown to dependent upon the vector glueball mass and strong coupling constant.

Acknowledgements Garima Punetha is grateful to the Uttarakhand State Council for Science and Technology (UCOST), Dehradun (India) for the financial assistance in terms of the research project for the study.

References

1. Nambu Y (1974) Phys Rev D 10:4262
2. 't Hooft G (1976) Proc Eur Phys Soc 1975 (ed A Zichichi, Ed. Comp. Bologna)
3. Mandelstam S (1976) Phys Rep 23:245
4. Dalla BM, Fritzsch P, Korzec T, Ramos A, Sint S, Sommer R (2016) Phys Rev Lett 117:182001
5. Nambu Y, Jona-Lasinio G (1961) Phys Rev 122:345
6. Maris P et al (2003) Eur Phys J A 18:231
7. Suganuma H et al (2017) J Phys G Nucl Part Phys 44:124001
8. Gongyo S, Iritani T, Suganuma H (2012) Phys Rev D 86:034510
9. Iritani T, Suganuma H (2014) Prog Theor Exp Phys 033B03
10. DiGiacomo A, Hasegawa M (2015) Phys Rev D 91:054512
11. Lang CB, Schrock M (2011) Phys Rev D 84:087704
12. Doi TM, Redlich K, Sasaki C, Suganuma H (2015) Phys Rev D 92:094004
13. Lo PM, Friman B, Kaczmarek O, Redlich K, Sasaki C (2013) Phys Rev D 88:014506
14. Dominguez CA, Loewe M, Zhang Y (2012) Phys Rev D 86:034030
15. Dalla Brida M (2018) Eur Phys J C 78:372
16. Punetha G, Chandola HC (2019) EPJ Web Conf 201:09009
17. Cho YM (1980) Phys Rev D 21:1080
18. Cho YM (1981) Phys Rev D 23:2415
19. Cundy N, Cho YM, Lee W, Leem J (2014) Phys Lett B 729:192
20. Cundy N, Cho YM, Lee W, Leem J (2015) Nucl Phys B 895:64
21. Chandola HC, Punetha G, Dehnen H (2016) Nucl Phys A 945:226
22. Punetha G, Chandola HC (2016) EPL 116:11001
23. Punetha G, Chandola HC (2018) EPJ Web Conf 117:09009
24. Punetha G, Chandola HC (2019) Acta Phys Polonica Ser B 50(9):1483
25. Punetha G, Chandola HC (2020) Rom J Phys 201:09009
26. Cho YM (1981) Phys Rev Lett 46:302
27. Munczek HJ, Nemirovsky AM (1983) Phys Rev D 28:181
28. Mckay DW, Munczek HJ (1997) Phys Rev D 55:2455
29. Tandy PC (1997) Prog Part Nucl Phys 39:117
30. Kumar A, Parthasarathy R (2004) Phys Lett B 595:373
31. Shushpanov IA, Smilga AV (1997) Phys Lett B 402:351

Effect of Sonication of GO in Acetone for the Fabrication of RGO Powder and Thin Film

Akanksha Motla, Anjali Sharma Kaushik, Monika Tomar, and Vinay Gupta

Abstract Graphene Oxide (GO) is known to be an insulating material because of the presence of saturated sp^3 hybridized bonds. Thus, the need of Reduced Graphene Oxide (RGO) arises so as to recover the conductivity of the material, by the restoration of sp^2 hybridized bonds. In the present work, modified Hummers method has been used for the synthesis of GO followed by rapid thermal annealing for the formation of RGO at 850 °C in ambient environment for both sonicated and un-sonicated GO powder samples. FTIR spectroscopy, Raman spectroscopy, and XRD were used to confirm the formation of RGO from GO. Further, the effect of sonication on GO was studied in detail using these characterization techniques both in powder and thin film forms. These analyses show various functional groups being eliminated and thus restoring the pi conjugated network in RGO. XRD results confirm the reduction of GO by rapid thermal annealing. Raman spectra show 2D band formation in addition to G to D band progression, showing the disorder and tangential bands. Thus, this facilitates the use of graphene and other graphene-based materials for larger applications.

1 Introduction

Graphene is known to be one of the thinnest 2D materials, a single layer one atom thick carbon sheet, which is sp^2 hybridized. It has honeycomb lattice structure implying carbon atoms bonding to each other in a repeating pattern of hexagons. Since its discovery in 2004, it has attracted enormous research, because of its outstanding properties of large surface area, high electrical conductivity and it also acts as an eminently good optical transparent material [1–3]. This allows graphene to be used

A. Motla (✉) · V. Gupta (✉)
Department of Physics and Astrophysics, University of Delhi, Delhi 110007, India

A. Sharma Kaushik
Department of Physics, ARSD College, University of Delhi, Delhi 110021, India

M. Tomar
Miranda House, University of Delhi, Delhi 110007, India

S. B. Krupanidhi et al. (eds.), *Advanced Functional Materials and Devices*, Springer Proceedings in Materials 14, https://doi.org/10.1007/978-981-16-5971-3_11

as a potential material for numerous applications such as sensors, photo detectors [4–6]. The rolled graphene known as carbon nanotubes has major application in biomedicines [7]. Now, the use of graphene is not trivial, as its production is relatively hard and expensive [8]. Thus, graphene derivatives are used or other similar materials instead of graphene. Another graphene-based material, Graphene Oxide (GO), is very well explored in various applications. A strong oxidation of graphite results in Graphene Oxide (GO), a single atom thick carbon sheet having abundant oxygen containing functional groups. The production of GO from graphite involves oxidation in large amount resulting in large interlayer spacing and functionalization of graphite basal planes. The method of production is relatively cheap, as it is easy to process because of its dispersibilty in water and many other solvents. GO is reported to have poor conductivity, and it is thus, termed as an insulator because of the presence of sp^3 hybridized bonds [9, 10]. The synthesis of GO has been reported by several methods like Hummers, modified Hummers, Brodie, Hofmann and Staudenmaeir [11–13]. Several other variations in the same methods are also reported for the improved synthesis of GO. To overcome the issue of poor conductivity of GO, the reduction of Graphene Oxide is needed.

The chemical, electro-chemical or thermal reduction of Graphene Oxide (GO) results in Reduced Graphene Oxide (RGO). RGO is also an atomically thin carbon sheet. The reduction process involves its own merits and de-merits which consists of reducing the oxygen containing groups present in GO [14]. The end production of each reduction process is same and the aim in all of the above reduction processes is to reduce the oxygen containing groups and also to repair and reduce the defects produced in GO. This results in an increase in the conductivity of the material. The conductivity and the transmittance properties of GO and RGO films can be tuned by tuning the thickness of the deposited films and also by the degree of oxygen reduction [14, 15].

Thus, in the present work efforts have been made to explore GO and RGO synthesis via modified Hummer's method and to study the effect of sonication in acetone and rapid thermal annealing (for 30 s at 850 ºC) on properties of RGO with various characterization techniques like X-ray Diffraction (XRD), Raman spectroscopy, Fourier Transform Infrared (FTIR) spectroscopy.

2 Experimental

2.1 Synthesis of Graphene Oxide (GO) Powder and Reduced Graphene Oxide (RGO) Powder

Vigorous oxidation of natural graphite powder was performed at a temperature of 293 K using concentrated sulphuric acid (H_2SO_4), sodium nitrite ($NaNO_3$), and potassium permanganate ($KMnO_4$). This whole suspension in an ice bath setup was stirred for around 1 h. The process was similar to Hummer's method with minor

alterations. This suspension was then permitted to warm up at room temperature naturally, and then DI water was added to the suspension, after which 30% of H_2O_2 was added and a color change to brown was observed, resulting in the formation of GO. The precipitate was then collected on a filter paper and was washed and centrifuged several times for 72 h with alcohol and warm water so as to get a pH value of 7. Finally, the powder was collected and dried at 60 °C overnight. Half of the powder was then ultra-sonicated at room temperature in acetone for 6 h. Reduced Graphene Oxide (RGO) for both sonicated and un-sonicated GO was obtained by rapid thermal annealing at 850 °C in ambient environment. The four different powders of un-sonicated (U) and sonicated (S) GO and RGO are named as S-GO, U-GO, S-RGO, U-RGO. Thin films of S-GO and U-GO powder were also grown on glass and Silicon (Si) substrates using drop cast method. 0.1 gm of S-GO and U-GO powders were dissolved in 3 ml of acetone and, 500 μL of both solutions were used to drop caste over the glass and Si substrates using micropipette.

2.2 Characterization

X-ray diffraction of RGO and GO both sonicated and un-sonicated powders was performed using wavelength of Cu-K_α radiations of 1.54 Å with tube voltage of 40 kV and tube current of 40 mA in the range of 5–80º, with a scan speed of 3°/min and step size of 2°. Raman spectroscopy results of the same sample powders and respective thin films were obtained using Renishaw Laser Raman Spectrometer of 542 nm laser with a power of 50 mW. Fourier Transform Infrared (FTIR) spectroscopy, Nicolet iS50 was used to investigate the various functional groups of the formed GO and RGO both sonicated and un-sonicated, in the form of pellets.

3 Results and Discussion

X-Ray Diffraction spectra of GO, RGO sonicated, and un-sonicated powder samples are shown in Fig. 1. A blatant peak at $2\theta = 11.45°$, could be observed for S-GO powder, implies the crystal phase orientation of (001) plane, corresponding to an interlayer distance of 0.78 nm, drawn by Bragg equation. The rapid thermal treatment made this dominant peak disappear and a shift in peak was observed centered around $2\theta = 25.16°$ which implies to an interlayer spacing of about 0.34 nm in both S-RGO and U-RGO. The reduction in interlayer distance corresponds to removal of oxide functional groups at carbon basal plane. Thus, the distance between consecutive carbon layers decreased. The broad peak, at $2\theta = 25.16°$, in case of S-RGO and U-RGO diffraction pattern, implies the crystal phase orientation of (002) plane, showing the randomness in arrangement of atoms [9, 10, 16, 17].

Figure 2 shows the Fourier Transform Infrared (FTIR) spectroscopy of U-GO, U-RGO, and S-RGO samples. FTIR spectra confirm the presence of various functional

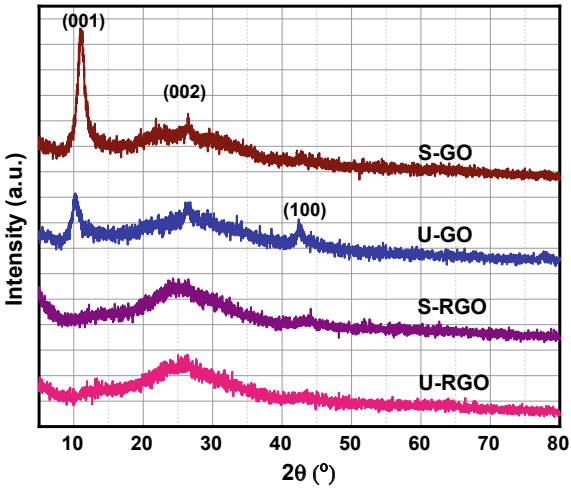

Fig. 1 XRD patterns of GO and RGO sonicated and un-sonicated powders

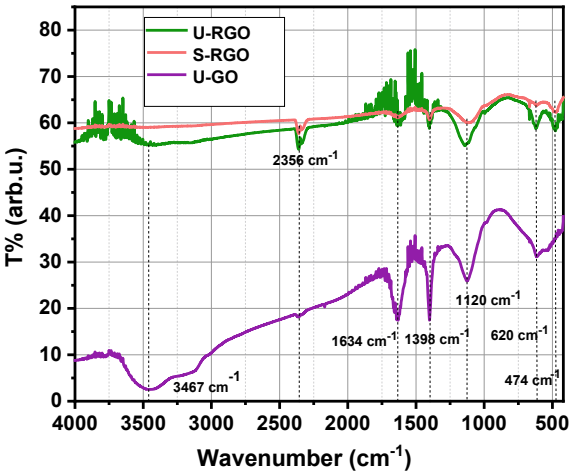

Fig. 2 FTIR spectroscopy of U-GO and S-RGO and U-RGO samples

groups before and after reduction of U-GO. The intense broad peak at 3467 cm^{-1} in U-GO sample, confirms the presence of hydroxyl group (O–H bond), which appeared to vanish after rapid thermal annealing treatment in U-RGO. Presence of –COOH group appearance in U-GO was confirmed at 1634 cm^{-1}. The epoxy group (C–O–C stretching) appearing 1398 and 1120 cm^{-1}. All these peaks conclude that U-GO was synthesized successfully. And all these peaks significantly reduced after reduction of U-GO, to form S-RGO and U-RGO, due to removal of oxygen containing functional groups. The appearance of peak at 2356 cm^{-1} in S-RGO and U-RGO samples corresponds to CO_2. Thus, it can be concluded that the reduction was good enough in S-RGO for the removal of carboxyl, epoxy and hydroxyl groups to a great extent, as compared to U-RGO sample [1, 18, 19].

Figure 3a, b shows the Raman spectra of S-GO and U-GO thin films on glass and silicon substrates and S-RGO U-RGO powders, respectively. The degree of defects produced was compared for both types RGO and GO formed using Raman spectra. In all the samples, D and G bands are observed at 1353 cm^{-1} and 1604 cm^{-1}. The peak intensities of the D and G bands indicate the amount of defects and order of carbon bonding present. Raman spectroscopy turns out to be a sensitive characterization technique, to study the presence of sp^2 hybridized carbon bonds. The intensities of peaks corresponding to D and G bands are named as I_D and I_G, respectively. The I_D/I_G ratio was found to be 0.78 in both S-GO and U-GO samples and 0.81 and 0.90 in S-RGO and U-RGO samples, respectively. The same I_D/I_G ratio as observed for the S-GO nd U-GO samples clearly indicates that the effect of sonication on GO is negligible. The observed increase in the intensity ratio for RGO samples shows

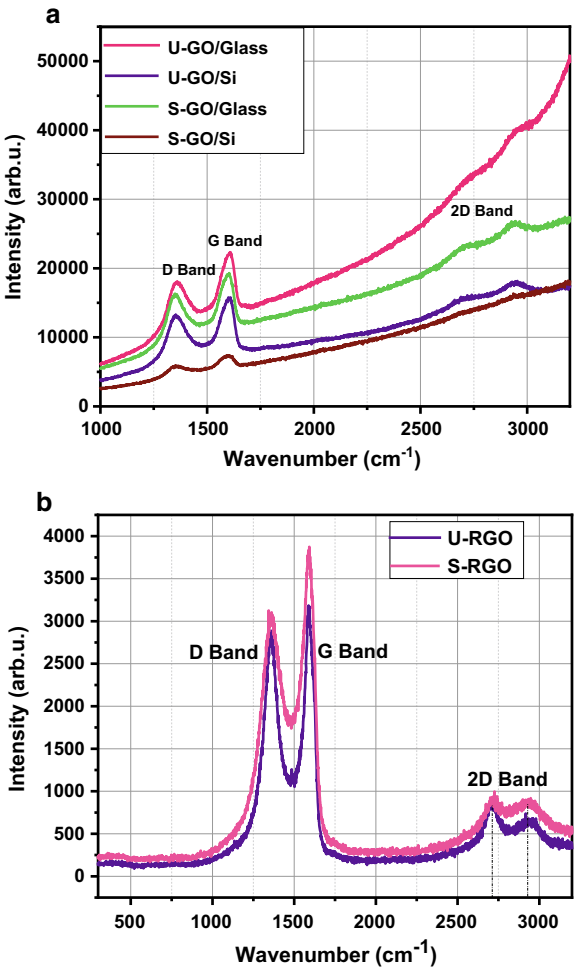

Fig. 3 **a** Raman spectra for GO films on glass and silicon wafer **b** Raman Spectra for sonicated and un-sonicated RGO samples

better formation of RGO samples as compared to GO samples. Thus, the increase in the I_D/I_G ratio attributes to the removal of oxygen containing functional groups in the RGO samples, prepared with rapid treatment. This further implies to the decrease in the sp^2 domain size formed in S-RGO and U-RGO. Also, the presence of 2D band as shown in Fig. 3a implies the formation of multilayer GO [10]. The shift observed in the 2D band location in Fig. 3b may be attributed to the presence of oxygen containing functional groups in RGO samples [11, 16, 20].

In the present work, the annealing time and the low annealing temperature, results in reducing the disorders, defects, removal of functional groups and restoration of pi conjugated network to a great extent. The results obtained are better when compared to other literatures [10, 16, 21].

4 Conclusion

GO and RGO were synthesized successfully using popular Hummer's method with slight modifications and displayed their unique characteristics. The effect of sonication in acetone shows the effect of reduced defects and removal of functional groups as studied from FTIR and Raman spectroscopy, further confirms the restoration of the pi conjugated network in RGO. Reduction of GO via rapid thermal annealing helped in achieving much smaller sp^2 domain size in S-RGO and U-RGO when compared to U-GO and S-GO samples. The various characterization techniques confirmed the formation of RGO from GO by rapid thermal annealing process for 30 s, at 850ºC. These results could now open up other possibilities to reduce the defect and domain size for larger applications.

Acknowledgement The authors are thankful to Defense Research and Development Organization (DRDO), India for providing financial support and University of Delhi for providing basic research characterization facilities. One of the authors, AM, is thankful to Council of Scientific and Industrial Research- Human Resource Development Group (CSIR-HRDG), India for providing the Junior Research Fellowship.

References

1. Wang H, Hu YH (2013) Electrolyte-induced precipitation of graphene oxide in its aqueous solution. J Colloid Interface Sci 391(1):21–27. https://doi.org/10.1016/j.jcis.2012.09.056
2. Ferrari AC et al (2006) "Raman spectrum of graphene and graphene layers," Phys Rev Lett 97(18). https://doi.org/10.1103/PhysRevLett.97.187401
3. Nair RR et al (2008) "Fine structure constant defines visual transparency of graphene," Science (80) 320(5881), 1308. https://doi.org/10.1126/science.1156965
4. Gahoi A et al (2011) Intrinsic Response of Graphene Vapor Sensors. Solid State Electron 6(5):179–184
5. Ang PK, Chen W, Wee ATS, Kian PL (2008) Solution-gated epitaxial graphene as pH sensor. J Am Chem Soc 130(44):14392–14393. https://doi.org/10.1021/ja805090z

6. Gautam AK, Faraz M, Khare N (2020) Enhanced thermoelectric properties of MoS2 with the incorporation of reduced graphene oxide (RGO). J Alloys Compd 838:155673. https://doi.org/10.1016/j.jallcom.2020.155673
7. Fisher C, Rider AE, Jun Han Z, Kumar S, Levchenko I, Ostrikov K (2012) "Applications and nanotoxicity of carbon nanotubes and graphene in biomedicine," J Nanomater 2012. https://doi.org/10.1155/2012/315185
8. Bhuyan MSA, Uddin MN, Islam MM, Bipasha FA, Hossain SS (2016) Synthesis of graphene. Int Nano Lett 6(2):65–83. https://doi.org/10.1007/s40089-015-0176-1
9. Ghorbani M, Abdizadeh H, Golobostanfard MR (2015) Reduction of graphene oxide via modified hydrothermal method. Procedia Mater Sci 11(2009):326–330. https://doi.org/10.1016/j.mspro.2015.11.104
10. Hidayah NMS et al (2017) "Comparison on graphite, grapheme oxide and reduced graphene oxide: synthesis and characterization," AIP Conf Proc 1892. https://doi.org/10.1063/1.5005764
11. Ghorbani M, Abdizadeh H, Golobostanfard MR (2015) "Reduction of graphene oxide via modified hydrothermal method," Procedia Mater Sci 11(January 2016):326–330. https://doi.org/10.1016/j.mspro.2015.11.104
12. Feicht P et al (2019) Brodie's or hummers' method: oxidation conditions determine the structure of graphene oxide. Chem A Eur J 25(38):8955–8959. https://doi.org/10.1002/chem.201901499
13. Poh HL, Šaněk F, Ambrosi A, Zhao G, Sofer Z, Pumera M (2012) Graphenes prepared by staudenmaier, Hofmann and Hummers methods with consequent thermal exfoliation exhibit very different electrochemical properties. Nanoscale 4(11):3515–3522. https://doi.org/10.1039/c2nr30490b
14. Sundaram RS (2014) Chemically derived graphene
15. Ning J et al (2014) A fast room-temperature strategy for direct reduction of graphene oxide films towards flexible transparent conductive films. J Mater Chem A 2(28):10969–10973. https://doi.org/10.1039/c4ta00527a
16. Zheng Y, Wang A, Lin H, Fu L, Cai W (2015) A sensitive electrochemical sensor for direct phoxim detection based on an electrodeposited reduced graphene oxide-gold nanocomposite. RSC Adv 5(20):15425–15430. https://doi.org/10.1039/c4ra15872e
17. Garlow JA, Barrett LK, Wu L, Kisslinger K, Zhu Y (2015) Pulecio JF (2016) "Large-area growth of turbostratic graphene on Ni(111) via physical vapor deposition." Sci Rep 6:1–11. https://doi.org/10.1038/srep19804
18. Yeo LP et al (2019) Electrophoretic deposition of reduced graphene oxide thin films for reduction of cross-sectional heat diffusion in glass windows. J Sci Adv Mater Devices 4(2):252–259. https://doi.org/10.1016/j.jsamd.2019.04.002
19. Bhardwaj SK, Yadav P, Ghosh S, Basu T, Mahapatro AK (2016) Biosensing test-bed using electrochemically deposited reduced graphene oxide. ACS Appl Mater Interfaces 8(37):24350–24360. https://doi.org/10.1021/acsami.6b04562
20. Bîru EI, Iovu H (2018) Graphene nanocomposites studied by raman spectroscopy. Raman Spectrosc. https://doi.org/10.5772/intechopen.73487
21. Phan DT, Chung GS (2015) Effects of rapid thermal annealing on humidity sensor based ongraphene oxide thin films. Sens Actuators B Chem. https://doi.org/10.1016/j.snb.2015.06.055

Recombination Zone Inside Transistor Channel in an Alq3/Pentacene Organic Light-Emitting Transistor

Suleshma Katiyar and Jyotika Jogi

Abstract In the present work, a tris-(8-hydroxyquinolinato) aluminum (Alq3)/Pentacene organic light emitting transistor (OLET), forming laterally arranged heterostructure is studied in an attempt to position recombination zone inside the transistor channel, in order to avoid quenching. The organic layer of pentacene provides good field-effect properties and a p-type or hole transporting behavior, while Alq3 layer provides electron transporting behavior and exhibits electroluminescent (EL) characteristics. An inbuilt p–n junction is formed away from electrodes, in the channel, due to the device geometry. The device is simulated in ATLAS 2-D (2 dimensional) device simulation tool in bottom contact, bottom gate configuration to study the output and emissive characteristics of the device. An ambipolar behavior is observed in the device output characteristics and the device shows emissive behavior under the ambipolar regime, as observed from Langevin recombination rate. The recombination rate is observed to be tunable with the applied bias and the recombination position is controlled by drain voltage. At high drain voltage, recombination position is observed to be at the hetero-interface of the two layers, away from source and drain electrodes.

Keywords Alq3 · Heterostructure · Organic light-emitting transistor · Pentacene · 2-D simulation

1 Introduction

Advances in application of organic semiconductor materials in opto-electronics have led to the development of an organic light emitting transistor (OLET) also known as organic light emitting field-effect transistor (OLEFET). It is a multi-functional device which combines the emissive properties of the OLED and the field-effect and switching properties of an OFET, enabling its usage in display technology and injection lasers [1]. Apart from its multi-functional nature, OLET can also be used

S. Katiyar · J. Jogi (✉)
Microelectronics Research Laboratory, Department of Electronic Science, A.R.S.D College, University of Delhi, South Campus, New Delhi 110021, India

S. B. Krupanidhi et al. (eds.), *Advanced Functional Materials and Devices*, Springer Proceedings in Materials 14, https://doi.org/10.1007/978-981-16-5971-3_12

to investigate optical and charge transport properties of organic semiconductors. Depending upon the charge carrier mobilities inherent to semiconductor, choice of contacts, and device architecture, OLETs show either unipolar or ambipolar operation. Exciton quenching and photon loss at the metal electrodes have been major drawbacks of organic light-emitting diodes (OLEDs), which are overcome in OLETs by their various device structures [2]. In OLETs, the gate terminal controls the electroluminescence by controlling the amount of induced charge carriers, a feature typically not available in OLEDs. The first single layer OLET based on tetracene had shown light emission in unipolar mode, as the electrons had to tunnel through the symmetric gold drain electrode and the emission zone was positioned next to drain electrode [3]. Further improvements in single layer OLETs suggested the use of asymmetric contacts leading to light emission in ambipolar mode [4–6]. In single layer ambipolar OLETs, though the exciton-metal quenching can be avoided by controlling the recombination zone position at suitable bias conditions, however, exciton-charge quenching cannot be avoided since accumulated charge carriers and excitons lie in the same plane [2]. Therefore, various research groups have proposed a number of bilayer and multilayer OLETs [2, 7–14]. In bilayer OLETs, charge carrier accumulation and transport are separated from the position of light emission, thus minimizing exciton losses. In particular, bilayer OLETs seem to be promising since they provide a way for optimizing the field-effect and emissive properties by optimizing the two layers [8, 15, 16].

It has been demonstrated previously that the simulation of Alq3/pentacene bilayer OLET with asymmetric contact could show emission characteristics [15]. However, the recombination zone was observed to be positioned at Alq3/pentacene interface in the vicinity of drain electrode. It is desirable that the recombination zone is positioned in the channel region away from source or drain electrodes, in order to avoid quenching. Also, if recombination happens away from dielectric, leakage phenomena due to dielectric polarization can be avoided [10]. Therefore, in this work, an OLET consisting of organic semiconductor heterostructure based on an electron transporting and emissive material, Alq3 and a hole transporting and field-effect material, pentacene is realized in bottom contact bottom gate architecture which results in the recombination zone being positioned inside the transistor channel, away from metal electrodes.

2 Device Structure and Model

A laterally arranged [16] Alq3/pentacene heterostructure is proposed as shown in Fig. 1. The device has bottom gate, bottom contact structure to achieve direct injection of charge carriers into active layers from the respective electrodes, with channel length and width of the device being 8 μm and 20 mm, respectively. The Alq3 and pentacene material layers are asymmetric in terms of their thickness, to form inbuilt p-n heterojunction. For 1–3 μm device length, pentacene material has a thickness of 50 nm, whereas for 3–7 μm, device length, the thickness is 10 nm. For Alq3 material,

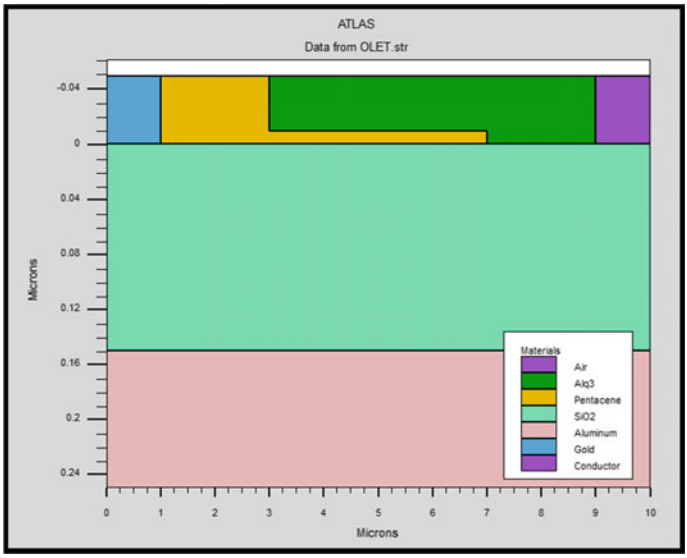

Fig. 1 Simulated OLET device containing laterally arranged Alq3/pentacene heterostructure

from 3 μm to 7 μm device length, the thickness is 40 nm, whereas for 7–9 μm device length, the thickness is 50 nm. Aluminum acts as metal contacts for gate, in order to apply biasing voltage at gate and has a thickness of 100 nm. The SiO2 gate oxide layer has a thickness of 150 nm. It is gate dielectric material having infinite resistivity, such that there is no carrier transport through this oxide layer under biasing condition. It acts as an insulating layer between conducting semiconductor and gate electrode contact, in order to separate them. Oxide layer also acts as parallel plate capacitor with one plate being the gate electrode and other being the semiconductor layer. It therefore, possesses gate capacitance which controls drain current. Gate oxide reduces leakage current when voltage is applied to gate metal contact. If the leakage current is sufficiently high, it can cause dielectric breakdown. Oxide layer has to be sufficiently thick, as the amount of current flowing in the device is inversely proportional to the gate oxide thickness. Decrease in oxide thickness can lead to charge carrier tunneling from gate electrode, which act as majority carriers in the oxide and lead to device failure as gate electrode loses its control.

The device also has asymmetric electrodes. The source electrode is made of gold (Au) (work function of 5.1 eV), while the drain electrode material is Lithium Fluoride/aluminum (LiF/Al) (work function of 2.9 eV), leading to an easy electron injection in the Lowest unoccupied molecular orbital (LUMO) of Alq3 [17]. Both of them are 1 μm long and 50 nm thick. The band gap and electron affinity of pentacene are 2.2 eV and 2.8 eV, respectively, [18], and that of Alq3 is 2.5 eV and 3.2 eV [19], respectively, as shown in band diagram in Fig. 2. Figure 2 is the band diagram of the Alq3 and pentacene materials with respect to source and drain electrodes which explains the working of the device qualitatively. The asymmetric contacts provide

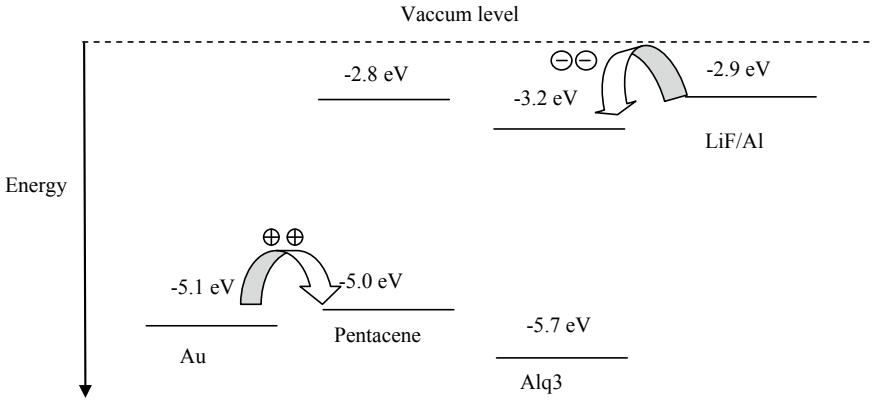

Fig. 2 Band diagram

favorable condition for injection of holes and electrons directly into pentacene and Alq3 layers, respectively, under gate and drain bias. As gold source electrode aligns with the HOMO level (analogous to valence band) of the pentacene, it favors easy hole injection since there is negligible or no injection barrier. The barrier for electron injection is high since LUMO (analogous to conduction band) is at 2.8 eV below the vacuum level. Thus, pentacene behaves as a p-type material with holes as its majority carriers. Similarly, drain electrode having work function of 2.9 eV is above the LUMO level of Alq3 which is at 3.2 eV with respect to vacuum level, favors easy electron injection, since electrons are stable at lower lying energies. These injected carriers are then transported in their respective channels and meet in the channel at the hetero-interface of the two organic layers where they recombine and decay radiatively to emit light.

In the ATLAS 2-D device simulation, simulation revolves around the length (x-direction) and thickness (y-direction) of the device. The third dimension is by default set as 1 μm. ATLAS 2-D device simulator from Silvaco is a numerical simulator that helps in understanding the device physics. It consists of organic display module, which can perform analysis of organic material-based active display devices such as organic field-effect transistors (OFETs) and organic light-emitting diodes (OLEDs). The three terminal OLET is therefore simulated using this software, employing Poole–Frenkel electric field dependent Mobility model (PFMOB), bimolecular Langevin recombination model (LANGEVIN) and singlet excitons (SINGLET) to account for transport, recombination mechanism and radiative rate of luminescence inside the organic semiconductor material [20].

3 Results and Discussion

The proposed Alq3/pentacene OLET structure has an inbuilt p–n junction within the channel [21], so that the chances of recombination inside channel, away from electrodes are greatly enhanced. Figures 3, 4, 5 and 6 show simulated recombination zone for Alq3/ pentacene lateral heterojunction structure at constant gate voltage of −20 V and varying drain bias.

It can be observed that for $V_{ds} = -10$ V, weak recombination occurs and the recombination zone is close to drain electrode in the Alq3 material, suggesting very low electron injection from drain. In order to operate, the organic light-emitting transistor (OLET) in hole accumulation mode, a negative gate to source voltage (V_{gs}) is applied to the gate electrode. The source terminal is grounded ($V_s = 0$), which implies that the source is more positive than the gate and thus injects holes into pentacene active layer. An electric field is also created across the dielectric which causes accumulation of these injected holes at pentacene/oxide interface. Thus, injected holes from source electrode into the pentacene material, travel toward Alq3 material after facing a barrier of 0.7 eV to recombine with the available injected electrons. For $V_{ds} = -20$ V, the recombination zone shifts away from the drain, indicating an increased number of injected electrons from the drain and its accumulation at Alq3/SiO2 interface. As V_{ds} is increased to −30 V (i.e.,$|V_{ds}|>|V_{gs}|$), there is an increment in the

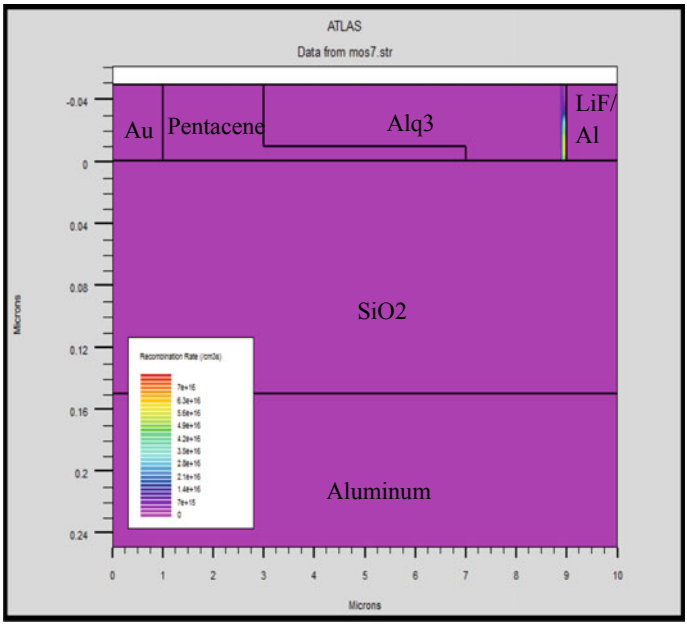

Fig. 3 Simulated recombination zone of laterally arranged Alq3/pentacene heterostructure OLET at $V_{gs} = -20$ V and $V_{ds} = -10$ V

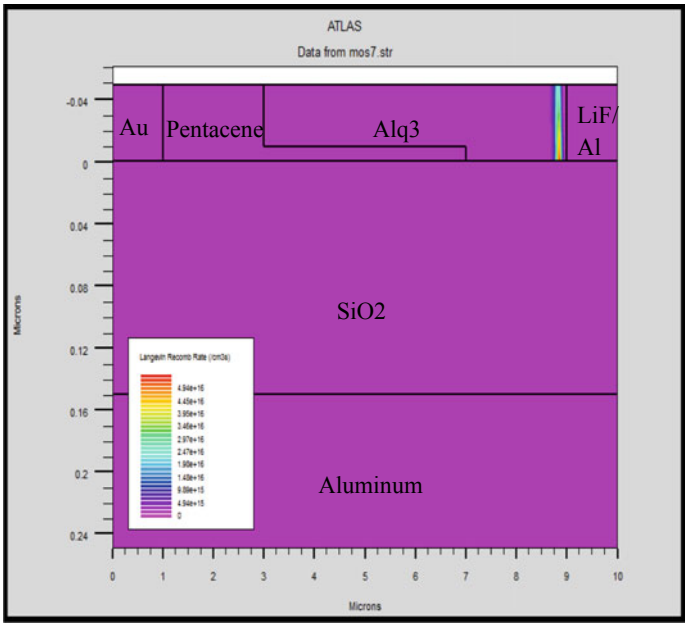

Fig. 4 Simulated recombination zone of laterally arranged Alq3/pentacene heterostructure OLET at $V_{gs} = -20$ V and $V_{ds} = -20$ V

recombination rate and also the point of recombination is shifted to Alq3/pentacene interface, due to rapid increase in the length of electron accumulation, suggesting that the electron injection has crossed threshold voltage. For higher drain voltage value of −60 V, recombination zone does not move further which may be due to the fact that the length of the electron accumulation region has reached its maximum at Alq3/SiO2 interface. The recombination rate is, however, still observed to have an increased value, which indicates that the electroluminescence can be tuned with changing bias conditions.

Figure 7 presents the output characteristics in the hole accumulation mode, i.e., for negative gate and drain voltage. For negative applied gate bias, holes are injected from gold (Au) source into the pentacene layer which accumulates at Pentacene/SiO2 interface. Thus, for $|V_{ds}|<|V_{gs}|$ typical p-channel characteristics are observed in saturation. For $|V_{ds}|>|V_{gs}|$ an abrupt increase in drain current is observed, which is a characteristic of ambipolar behavior of OFETs [12]. This is due to electron injection from drain electrode. It can be noted that for higher gate voltages, electron injection reduces and shifts to higher drain voltage value, indicating that the device now operates in the hole transport regime. However, low order hole current is observed, which is due to high contact resistance in bottom contact structure [22] and also due to the barrier of 0.7 eV at hetero-interface of Alq3 and pentacene for holes to cross over to the channel region. From the recombination results and output characteristics, it

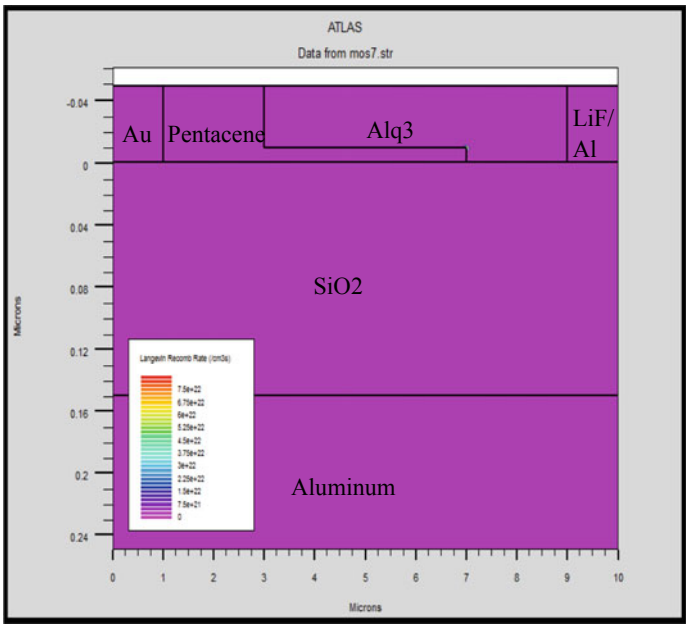

Fig. 5 Simulated recombination zone of laterally arranged Alq3/pentacene heterostructure OLET at $V_{gs} = -20$ V and $V_{ds} = -30$ V

can be concluded that for light emission to occur ambipolar characteristics are an essential requirement, which depends on non-saturating drain current.

4 Conclusion

An Alq3/pentacene-based laterally arranged heterostructure OLET is presented with the position of the recombination zone inside the channel shifted away from source and drain electrodes. A comprehensive ATLAS-2D simulation provides a tool to predict and optimize the performance of the proposed novel device before the actual device fabrication. It was observed that the recombination zone in the simulated laterally arranged Alq3/pentacene heterostructure OLET has shifted towards the center of the channel away from source and drain electrodes, as well as away from SiO2 interface when operated in the ambipolar regime. The proposed Alq3/pentacene OLET structure helps minimize the exciton and photon loss at the electrodes, thus improving the device characteristics.

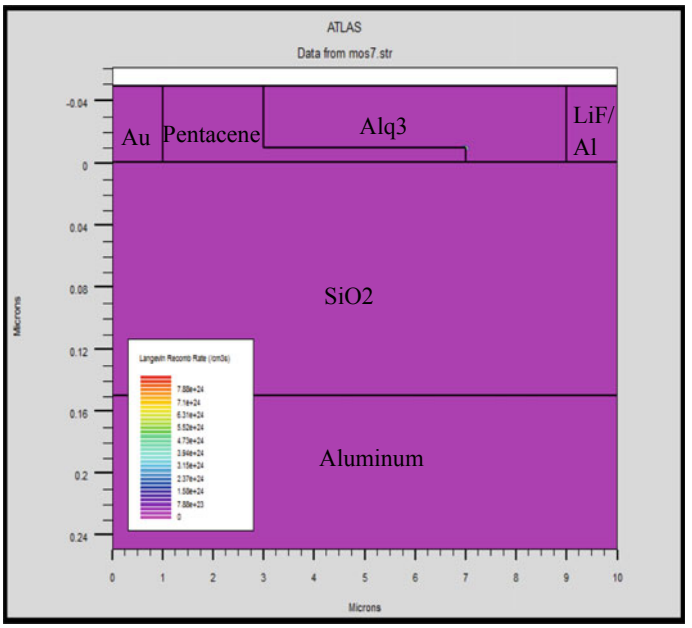

Fig. 6 Simulated recombination zone of laterally arranged Alq3/pentacene heterostructure OLET at $V_{gs} = -20$ V and $V_{ds} = -60$ V

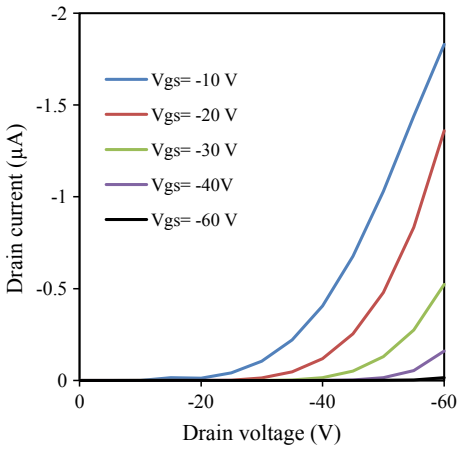

Fig. 7 Simulated output characteristics of laterally arranged Alq3/pentacene heterostructure OLET

Acknowledgements Suleshma Katiyar acknowledges University Grants Commission, Government of India (3734/(NET-DEC2018) for providing financial assistance for this research work.

References

1. Chaudhry MU, Muhieddine K, Wawrzinek R et al (2020) Organic light-emitting transistors: advances and perspectives. Adv Funct Mater 30(20):1905282
2. Capelli R, Toffanin S, Generali G et al (2010) Organic light-emitting transistors with an efficiency that outperforms the equivalent light-emitting diodes. Nat Mater 9(6):496–503
3. Hepp A, Heil H, Weise W et al (2003) Light-emitting field-effect transistor based on a tetracene thin film. Phys Rev Lett 91(15):157406
4. Swensen JS, Soci C, Heeger AJ (2005) Light emission from an ambipolar semiconducting polymer field-effect transistor. Appl Phys Lett 87(25):253511
5. Zaumseil J, Friend RH, Sirringhaus H (2006) Spatial control of the recombination zone in an ambipolar light-emitting organic transistor. Nat Mater 5(1):69–74
6. Schidleja M, Melzer C, von Seggern H (2009) Electroluminescence from a pentacene based ambipolar organic field-effect transistor. Appl Phys Lett 94(12):94
7. Prosa M, Benvenuti E, Pasini M et al (2018) Organic light-emitting transistors with simultaneous enhancement of optical power and external quantum efficiency via conjugated polar polymer interlayers. ACS Appl Mater Interfaces 10(30):25580–25588
8. Cui S, Hu Y, Lou Z et al (2015) Light emitting field-effect transistors with vertical heterojunctions based on pentacene and tris-(8-hydroxyquinolinato) aluminum. Org Electron 22:51–55
9. Di CA, Yu G, Liu YQ et al (2007) Organic light-emitting transistors containing a laterally arranged heterojunction. Adv Function Mater 17(9):1567–1573
10. Maiorano V, Bramanti A, Carallo S et al (2010) Organic light emitting field effect transistors based on an ambipolar p-i-n layered structure. Appl Phys Lett 96(13):64
11. Dinelli F, Capelli R, Loi MA et al (2006) High-mobility ambipolar transport in organic light-emitting transistors. Adv Mater 8(11):1416–1420
12. Rost C, Karg S, Riess W et al (2004) Light-emitting ambipolar organic heterostructure field-effect transistor. Synth Met 146(3):237–241
13. Kajii H, Tanaka H, Kusumoto Y et al (2015) In-plane light emission of organic light-emitting transistors with bilayer structure using ambipolar semiconducting polymers. Org Electron 16:26–33
14. Verma R, Yadav V, Kaur K et al (2016) A vertically stacked phosphorescent multilayer organic light emitting transistor. RSC Adv 6(93):90873–90877
15. Katiyar S et al (2020) Simulation of pentacene/Alq3 bilayer OLET to analyze the effect of Alq3 layer thickness and asymmetric contacts on device performance. International conference on electrical and electronics engineering (ICE3), Gorakhpur, February 2020, IEEE, pp 184–189
16. Zhang C, Chen P, Hu W (2016) Organic light-emitting transistors: materials, device configurations, and operations. Small 12(10):1252–1294
17. Gassmann A, Melzer C, von Seggern H (2009) The Li_3PO_4/Al bilayer: An efficient cathode for organic light emitting devices. J Appl Phys 105(8):084513
18. Gupta D, Katiyar M, Gupta D (2009) An analysis of the difference in behavior of top and bottom contact organic thin film transistors using device simulation. Org Electron 10(5):775–784
19. Meng M, Song W, Kim YH et al (2012) White organic light-emitting diodes with different order of RGB-emitting layers. Mol Cryst Liq Cryst 569(1):125–142
20. Manual AUS (2010) Device simulation software, Version 5.16. 3. R Silvaco Int., Santa Clara, CA
21. De Vusser S, Schols S, Steudel S et al (2006) Light-emitting organic field-effect transistor using an organic heterostructure within the transistor channel. Appl Phys Lett 89(22):223504
22. Street RA, Salleo A (2002) Contact effects in polymer transistors. Appl Phys Lett 81(15):2887–2889

Optical Constants of BiI_3 Polycrystalline Thin Films with Potential Applications in X-ray Detectors and Photovoltaic Cell

Alka Garg, Monika Tomar, and Vinay Gupta

Abstract Structural and optical properties as a function of film thickness have been studied for the thermally evaporated bismuth triiodide films. The thickness of investigated films ranges from 1 to 2 microns. According to XRD pattern, films are preferably oriented along c-axis of hexagonal structure normal to the glass substrate. Both the crystallite size and lattice strains have been determined using Williamson and Hall method. The optical constants and refractive index have been determined using envelope method. The optical transmittance data indicates an allowed direct interband transition near the absorption edge with an optical energy gap that decreases continuously from 1.89 eV to 1.85 eV. Both the optical constants and energy gap show thickness dependence that can be explained in terms structure parameters, Crystallite size and lattice strain.

1 Introduction

Bismuth iodide is a wide bandgap semiconductor material with potential for room temperature gamma-ray detection and photovoltaic applications [1]. It has high absorption coefficient in the visible region of the electromagnetic radiation spectrum and its optical bandgap is appropriate for sensing high energy radiations like X-rays and gamma rays, etc., [2]. Since the optical properties are closely related to the structure of films, therefore, there is a constant interest to compute the complete set of optical parameters by a simple method to get the valuable information about the structure of films [3]. Envelope method developed by Swanepoel [4] based on the idea of Manifacier et al. [5] is the basis for determining the optical parameters

A. Garg (✉)
Department of Physics, Gargi College, University of Delhi, Delhi, India
e-mail: alka.garg@gargi.du.ac.in

M. Tomar
Physics Department, Miranda House, University of Delhi, Delhi, India

V. Gupta
Department of Physics and Astrophysics, University of Delhi, Delhi 110007, India

S. B. Krupanidhi et al. (eds.), *Advanced Functional Materials and Devices*, Springer Proceedings in Materials 14, https://doi.org/10.1007/978-981-16-5971-3_13

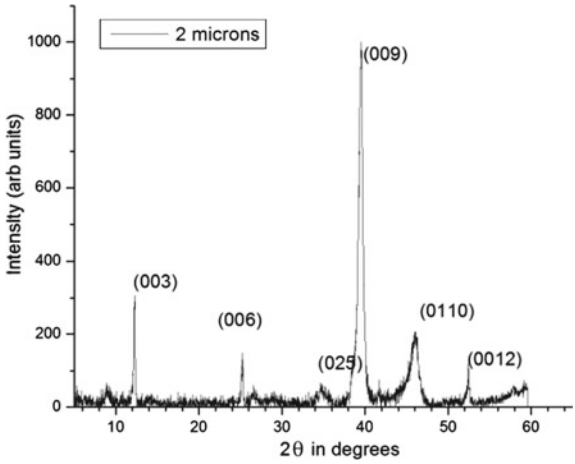

Fig. 1 XRD diffractogram of the BiI_3 thin film

of films. To apply this method, the transmission optical spectra of the film must show oscilllations as shown in Fig. 1. These oscillations are caused by the interference phenomena occurring due the relative difference between substrate and film refractive indices and thicknesses. It is important to note that presence of oscillations on the optical spectra is strongly related to the geometrical properties of the film and suggests a homogenous smooth surface with uniform thickness [6]. Interference effects are completely destroyed for non-uniform films [7] so the existence of oscillations in the optical spectra for the relatively thick films is the primary indicator for assessing the quality of film formation. Swanepoel's method is quite effective in calculating the complete set of optical parameters of film through in the medium and weak absorption region by creating upper and lower envelope of transmittance spectra. Practical usability of this method is limited to relatively thick films as in thin films the oscillations are spaced out to the extent that drawing envelope over the oscillations becomes difficult as interpolation between extremes becomes difficult and it may result into limited accuracy. In this paper, a complete set of optical parameters are determined for the bismuth triiodide films for the first time.

2 Experimental

Powder of compound bismuth triiodide having purity 99.99% from Aldrich chemical was procured to synthesize thin films of bismuth triiodide in a vacuum of about 10^{-6} Torr, to avoid any inclusion of impurities, using evaporation coating set up [8]. Thin films of thickness 1 micrometer and 2 micrometer were deposited on cleaned glass substrate kept at room temperature by evaporating powder kept in the molybednem boat. The deposition rate was maintained to be constant at 5–6 mm/s. Thickness of the deposited films was controlled by quartz crystal monitor. Thickness and uniformity

of the film were also checked and measured through surface profiler (DEKTEK 150). Structure analysis of the as deposited films was carried out using X-ray Diffraction (Bruker D8 XRD) with CuKα radiations having wavelength λ= 0.15418 nm. Optical transmission spectra of the as deposited BiI_3 thin films were obtained as a function of wavelength in the range of 190–900nm using UV-VIS-NIR spectrometer (Perkin elemer, lamda35).

3 Result and Discussion

3.1 XRD Evaluation

Thin films as -grown on glass substrate are found to be uniform and adhered strongly to the glass surface. Figure 1 shows the XRD patterns of thin films of two thicknesses films are polycrystalline and having hexagonal structure with diffraction peaks at $2\theta =$ 12.29^0, 25.241^0, 38.440^0, $39.46.167^0$, 52.422^0 corresponding to (003), (006), (025), (009), (0110), (0012) planes, respectively, as per PCPDF WIN card number 76-1742. Also, it is observed that both peak intensity and crystallite size increases with increase in film thickness [9]. It can be concluded that as the growth rate of depositing film is less therefore grains of BiI_3, while evaporating, get sufficient time to align themselves in the preferred direction of growth. Due to which the enhancement in the peak intensity takes place and accumulation of grains in a particular preferred orientation leads to increase in the average size of crystallites. Williamson method proposed by Williamson and Hall was used for to calculate grain size and strains of BiI_3 films grown on glass substrate [10]. The Following relation can be used to enumerate the information about crystallite size and the strains present in the thin films [11].

$$\beta Cos\theta = \frac{\lambda}{D} + 4\varepsilon(Sin\theta)$$

where D, ε and λ are the crystallite size, strain, and the wavelength of X-ray used, respectively. Crystallite size and microstrains present in the film were determined by plotting $\beta\cos\theta$ against $\sin\theta$ shown in Fig. 2, Results are tabulated (Table 1) which shows that strain is less for thicker film. Through calculations also it is observed that crystallite size increases with increase in film thickness. This increase in crystallite size is due to the increase in peak intensity which leads to decrease in FWHM and thus crystallinity of film increases for thick film.

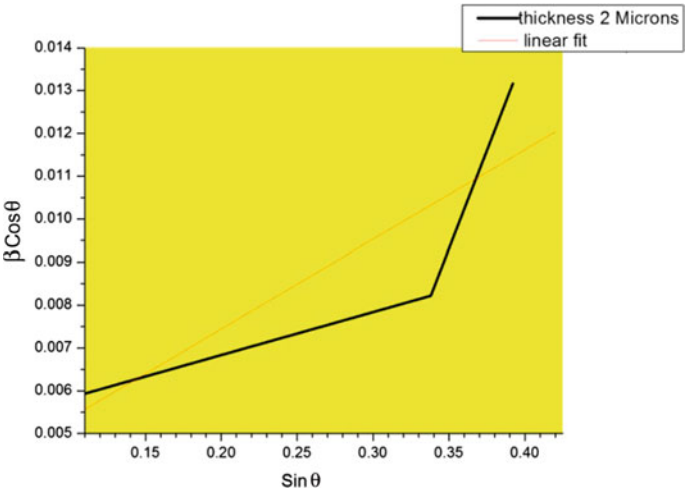

Fig. 2 Showing the plot of $\beta Cos\theta$ versus $Sin\theta$

Table 1 Showing the values of Grain size and strain as calculated using Williamsons-Hall method

S.no	Thickness (microns)	Grain size (nm) (W and Hall method)	Strain	Grain size (Scherrer's method)
1	2	18 nm	0.005136	16 nm
2	1	10 nm	0.008220	~10 nm

3.2 Optical Characteristics

Optical constants of c-axis oriented films have been studied. Figure 3 depicts the transmittance spectra of the thin films in the spectral range of 190–1100 nm. Transmission of the wavelengths lying in the spectral range of 650–1100 nm is found to be very high (around 80%) for films. and optical spectra show a sharp absorption edge at around 650 nm. The presence of well-defined interference pattern indicates that films are uniform grown on the substrate and also free from any inhomogeneity which is also well explained by sharp reflections in the XRD pattern. Transmittance Specrtra show a steep fall near the absorption edge which could be due to direct type of transition. Sharp absorption edge corresponding to forbidden energy bandgap confirms the semiconducting properties of the thin films of bismuth triiodide [12]. Usually for polycrystalline semiconducting thin films direct transitions are valid [13]. Therefore, the value of optical band was estimated from the linear portion of the tauc's plot () by plotting $(\alpha h\upsilon)^2$ against $h\upsilon$. Optical bandgap (shown in Fig. 4) was calculated to be in the range of 1.85–1.89 eV which is close to the reported values of bandgaps at room temperature [14]. During the growth of thick films, sufficient numbers of atoms are deposited on the films in the proper orientation with each other such that film homogeneity increases and localized states or trapped levels or the defect decreases.

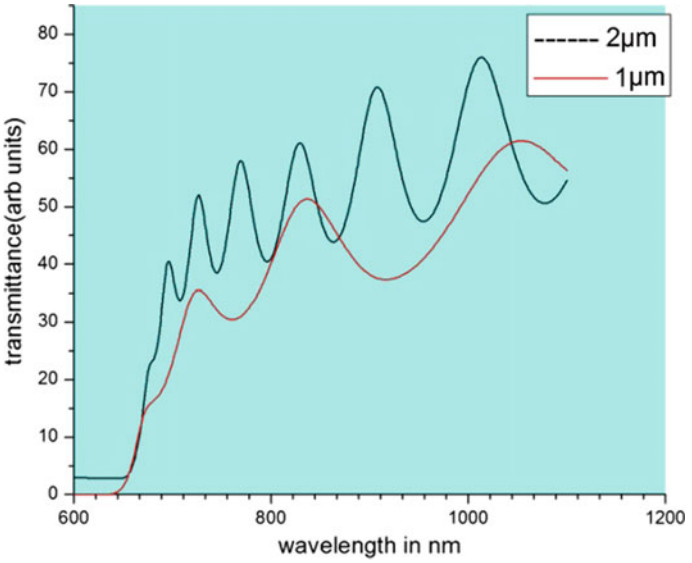

Fig. 3 Transmission spectra of BiI_3 films on glass substrate

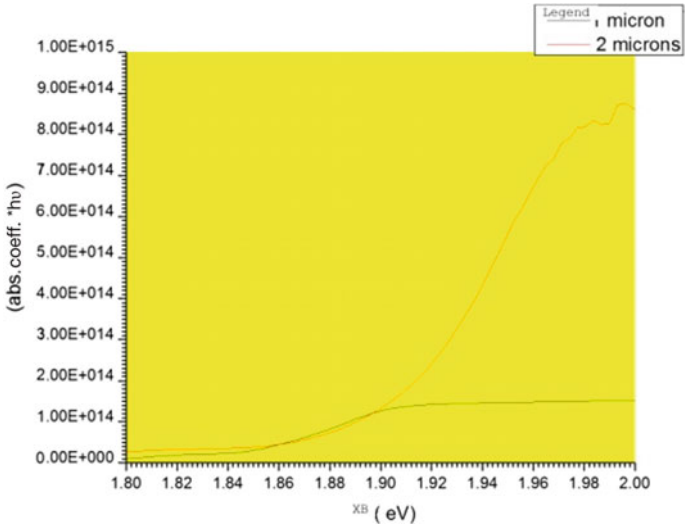

Fig. 4 Variation of absorption coefficient versus hυ for BiI_3 films with different thickness

Hence, the crystallinity of the higher film thickness is improved. It could lead to increase in optical bandgap.

Table 2 Showing the values of optical constants for Thin films of various thickness

S.no	Thickness (μ m)	Bandgap (eV)	Absorption coefficient	Refractive index				
				695 nm	725 nm	830 nm	908 nm	1013 nm
1	2	1.89	$7.35X10^6$	2.8376	2.7656	2.4226	2.5960	2.0585
2	1	1.85	$6.19X10^6$	–	2.6302	2.6811	–	2.4576

3.3 Refractive Index

Refractive index is one of the important optical constant which is considered as a finger print of the material and provides important functionalities for the fabrication industry. It is determined by analyzing the transmittance spectra of the film as per the approach suggested by Swanepoel [4]. The following formula is used to estimate the value of refractive at a particular wavelength:

$$n = \left[N + \left(N - S^{*}S\right)^{1/2}\right]^{1/2}$$

where $N = 2^{*}S\left(T_{max} - T_{min}/T^{*}_{max}T_{coin}\right) + (S^{*}S + 1)/2$.

And T_{max} and T_{min} are the transmittance maximum and the corresponding minimum at a certain wavelength λ. On the other hand, the necessary values of the refractive index of the substrate are obtained from the transmittance spectrum of the substrate T_s using the well-known equation:

$$S = 1/T_5 + (1/T_s - 1)^{1/2}$$

The values of the refractive index n for BiI_3 polycrystalline thin films are calculated and Tabulated in Table 2 using equation and are plotted against the wavelength (Fig. 5). Refractive index shows dispersion with wavelength above the fundamental absorption edge at 650 nm. It can be concluded from the data that refractive index is higher for the film having higher thickness. Since this film also has comparatively larger bandgap which is explained on basis of depositing sufficient number of atoms in proper orientation such that film density and homogeneity of the film increases. It is reported that refractive index is higher for the dense films as compared to porous films, as at wavelength far from the absorption edge speed of electromagnetic wave would be reduced in denser medium.

4 Conclusion

XRD analysis confirms the growth of stoichiometric thin films of BiI_3 with preferred (009) orientation with c-axis normal to the substrate. Films are polycrystalline and crystallites of bismuth triiodide have hexagonal structure. Average crystallite size of

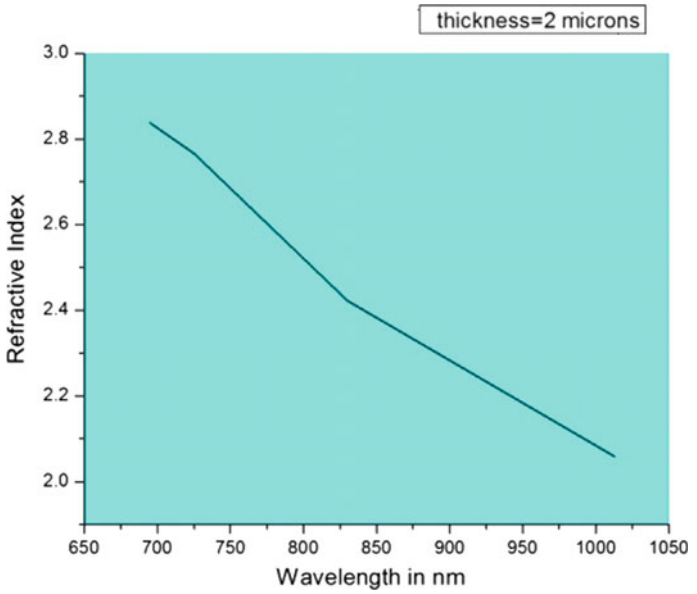

Fig. 5 Variation of refractive index with wavelength for BiI_3 film of thickness 2 microns

film having thickness 2 microns is found to be of the order of 18 nm which matches well with the calculation by Scherrer's method and microstrain present in the films is around 0.001536. It was found out that crystallite size increases with increase in thickness of the film. The microstrain shows a decrease on increasing the thickness as the lattice defects are pronounced at small thicknesses. The possible optical transition in these films is found to be allowed direct transition with bandgap in the range 1.85–1.89 eV. It was concluded that bandgap increases with the increase in thickness which may be attributed to the increase in crystallite size. Films showed reasonable number of oscillations in the transmittance spectra. As per the envelope method suggested by Swanepoel, the value of refractive index is higher for film of greater thickness at wavelength 725 nm and film show dispersion, i.e., refractive index is decreasing with increase in wavelength. Overall it can be concluded that thickness change is a good choice to control the optical properties of the BiI_3 films. So apart from its ability to detect high energy radiations, it can be tuned to synthesize layered photovoltaic cell.

References

1. Owen A, Peacock A (2004) Compound semiconductor in radiation detectors. Nucl Ins Methods A53:18–37
2. Garg A, Tomar M, Gupta V (2014) Structural optical and electrical properties of thin films of BiI_3. Adv Sci Lett 20:1442–1445

3. Shabaan ER, Afify N, Taher AEl, (2009) Effect of film thickness on microstructure parameters and optical constants. J Alloys Compds 482:400–404
4. Swanepoel R (1983) J Phys Sci Instrument 16:1214
5. Manifacier JC, Gaslot J, Fillard JP (1976) A simple method for the determination of the optical constants n, K and thickness of a weekly absorbing thin film. J Phys E: Sci Instrum 9:1002
6. Sharma A, Tomar M, Gupta V (2011) SnO2 thin film sensor with enhanced response for NO2 gas at lower temperatures. Sensors Actuators B 156:743–752
7. Marquez E, Bernal AM, Gonzalez JM, Prieto R, Ledesma A, Jimenez R, Martil L (1999) optical constant calculations of non uniform thin films of chalcogenide glassy alloy in the sub band gap region. Material Chem Phys 60(3):231–239
8. Garg A, Tomar M, Gupta V Synthesis and characterisation of thin films of bismuth triiodide for semiconductor radiation detector. Conference paper open Access. 2014. https://doi.org/10.1155/2014/37046.
9. Tyagi P, Vedeshwer AG (2007) Grain size dependent band gap of CdI2 films. Bull Mater Sci 24:297
10. Williamson GK, Hall WH (1953) Acta Metall 22
11. Klug HP, Alexander L (1974) Xray diffraction procedure for polycrystalline and Amorphous Materials, 2nd ed. Wiley, Newyork
12. Nowak M Thin solid films 266:255
13. Wang T, Daiber B, Frost JM, Mann AM, Garnett EC, Walsh A, Ehrler B Indirect to direct bandgap transition in methylammonium lead halide perovskite. Energy Environ Sci 10:509–515
14. Brandt RE, Kurelin RC, Hoye RLZ, Poindexter JR, Wilson MWB, Sulekar S (2015) Investigations of bismuth triiodide for photovoltaic applications. J Phys Chem Lett 6:4297–4302

Structural, Microstructural and Electrochemical Properties of Carbonaceous Nanocomposite for Supercapacitor Applications

Shweta Tanwar, Nirbhay Singh, and A. L. Sharma

Abstract In this paper, we prepared CCT nanocomposite comprising of Co_3O_4, carbon black and TiO_2 via microwave-assisted sol–gel technique. The composite is designed as electrode material for supercapacitor application. We have synthesised two samples namely CT and CCT where CT is optimised composite of carbon black and TiO_2 nanoparticle, and CCT is composite of Co_3O_4, carbon black and TiO_2, respectively. The prepared electrode material has been characterised by X-ray diffraction, field emission scanning electron microscopy, cyclic voltammetry (CV), galvanostatic charging-discharging (GCD) and electrochemical impedances spectroscopy (EIS). The structural and microstructural characterisation of the material confirms the formation of the crystal structure and nanocomposite. The CCT material shows better specific capacitances of 250 F g^{-1} at a rate of ten millivolts per second which is advanced than that of CT composite. The CCT sample exhibits energy density (E_d) of 46 W h kg^{-1} at corresponding power density (P_d) of value around two thousand watt per kilogram. The analysed result reveals that the prepared CCT nanocomposite can be considered as potential electrode material for supercapacitor applications.

1 Introduction

The major issue of human society across the world is the energy crisis. The major challenges in front of energy crisis are depleted fossil fuel, environment impact (like pollution, greenhouse effect, etc.) and rapid growth of population [1]. To address the aforementioned issues, the renewable energy resources (such as wind, solar and thermal energy) are emerging very fast. These renewable energy resources are devoted for production of energy only. The produced energy from these renewable

S. Tanwar · N. Singh · A. L. Sharma (✉)
Department of Physics, Central University of Punjab, Bathinda, Punjab 151401, India
e-mail: alsharma@cup.edu.in

N. Singh
BabaSaheb Bhimrao Ambedakar University Lucknow, Lucknow, Uttar Pradesh 226025, India

S. B. Krupanidhi et al. (eds.), *Advanced Functional Materials and Devices*, Springer Proceedings in Materials 14, https://doi.org/10.1007/978-981-16-5971-3_14

resources cannot be utilised on requirement basis rather continuous basis. In order to utilisation of produced energy on requirement basis, the safest way out is supercapacitor and batteries [2]. But in between two, supercapacitors are getting more attention as it delivers energy at higher rates. Supercapacitor is basically comprising of electrode, current collector and electrolyte as its prime components. Among three prime components, electrodes are playing key role in deciding of overall performance of the supercapacitor. It improves specific capacitances, operating potential window, energy density and power density [3]. Based on the ways of material charge storage processes, supercapacitors are categorised as electric double layer capacitor (EDLC) and pseudocapacitor. The EDLC capacitor store charge via depositing ions at the electrode–electrolyte interface while pseudocapacitor accumulates charges with the help of redox (faradaic) reaction on the surface of the active material. The hybrid capacitors are found to be interesting as it exhibits mechanism of both EDLC and pseudocapacitor [4].

The literature review has indicated that composite formation of nanomaterials is a good way to enhanced the performance of the electrode especially improvement in the energy density value of the material [5]. In this paper, we used carbonaceous nanocomposite namely CT and CCT through analysis of XRD, FESEM and electrochemical analyser. The XRD and FESEM confirm the formation of crystal structure and nanocomposite formation. The analysed result reveals that the prepared nanocomposite can be considered as potential electrode material for supercapacitor applications.

2 Material and Method

All chemical used to prepare sample are of high grade and are purchased from Sigma Aldrich.

Preparation of CT and CCT nanocomposite

The CT sample is prepared via sol–gel technique. Initially, the commercial purchase carbon black is taken as base and different weight percentage of TiO_2 nanoparticles has been added to the carbon black matrix as schematic steps shown in Fig. 1. The 15 weight percentage of TiO_2 powder in carbon black is found to be optimised sample.

The CCT sample is synthesised using microwave assisted sol–gel technique. Firstly, Co_3O_4 nanoparticles has been prepared via microwave where cobalt nitrate hexahydrate dissolved in 35 ml DDW. Thereby prepared precursor solution subjected to microwave treatment for 15 min at 180 °C temperature, respectively. Thus, obtained Co_3O_4 nanoparticles (15%) doped into above-optimised CT sample by utilising sol–gel technique following steps as depicted in Fig. 1.

Electrode preparation for electrochemical measurements

The electrode for carrying out electrochemical measurements is prepared by mixing synthesised material, carbon black and polyvinyldene (PVDF) in 80:10:10

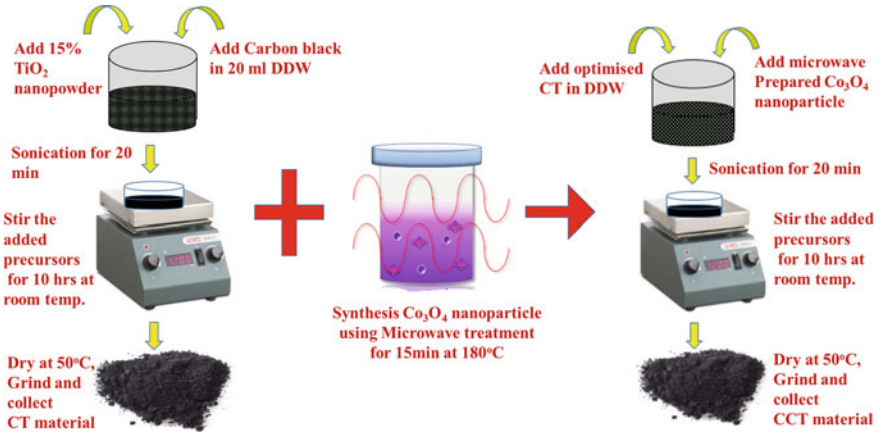

Fig. 1 Schematic diagram of procedure followed to synthesis of final CCT samples

ratio, respectively. A uniform slurry of above composition is formed by using *N*-Methyl-2-Pyrrolidone (NMP) solvent, which is pasted (~2 mg) over nickel foam (used as current collector). The 6M sodium hydroxide is used as electrolyte. The Whatman paper is treated as separator. All electrochemical measurements like cyclic voltammetry, galvanostatic charging-discharging and electrochemical impedance spectroscopy are performed in two-electrode cell assembly, i.e. *Ni foam||6M NaOH||Ni foam* using electrochemical workstation (Model: 760; USA).

3 Result and Discussion

The crystal structure of the prepared CT and CCT samples studied using X-ray diffraction. Figure 2a represents XRD graph of CT and CCT material. It shows that peaks at 24° for (200) and 43° for (100) plane corresponds to carbon black [6], diffraction peaks related to TiO_2 anatase phase found to be located at 25°, 37°, 47°, 54°, 62° which are conforming to (110), (004), (200), (105) and (204) planes, respectively [7]. The peaks at 27°, 37°, 48°, 54°, 62° for (220), (311), (422), (440) planes features the presences of cubic phase of Co_3O_4 nanoparticle. The overlap of some peaks confirms the formation of the nanocomposite of cobalt oxide, TiO_2 and carbon black. The indication of low crystallinity in the XRD spectra of nanocomposite relates to low lattice energy. Hence, supports the improved electrochemical results.

The FESEM micrograph of the CT and CCT sample are depicted in Fig. 2b, c, respectively. The images are taken to analyse the morphological characteristics of the synthesised samples. It indicates the uniform and unique composite formation which is in synchronise with XRD results. The present of pores in the composite formed predicted to help in electrolyte ions transport for fast charge-discharging process. Hence, it will aid in improvement of electrochemical performances.

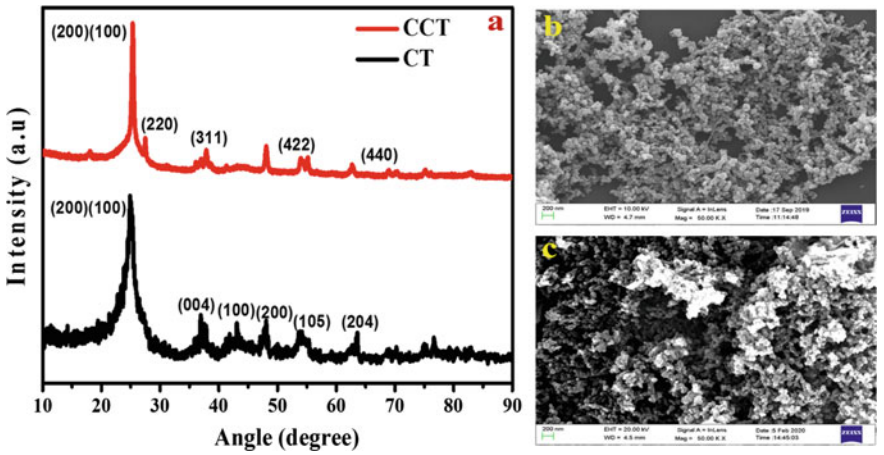

Fig. 2 **a** XRD plot for CT and CCT samples and FESEM image of **b** CT, **c** CCT nanocomposites, respectively

The electrochemical properties of the CT and CCT material studied by performing electrochemical analysis in two-electrode system. Figure 3a, b represents the CV curve of CT and CCT electrodes. It is concluded from the CV plots that CCT sample comprise of higher specific capacitance than CT sample. Unlike CT sample, the disappearance of redox peaks in CCT material indicates more EDLC behaviour and less pseudocapacitive behaviour of the material [8]. The specific capacitance for the electrode material is evaluated using equation $C_{sp} = \frac{\int I(V)dv}{m\upsilon\Delta V}$, where m, υ, V are mass of the active material, scan rate and potential window, respectively. The deviation of specific capacitance with various scan rate (ten to hundred millivolt per second) demonstrated in Fig. 3c shows better electrochemical results for CCT than CT material. This notified difference among both sample is might be due to synergistic effect between the active materials. It is observed that specific capacitance decreases as scan rate increases, it is because of the limitation of the diffusion of electrolyte ions into the electrode material for charge storage as scan rate increases [9]. Figure 3d, e represents the GCD curve of both CT and CCT sample at different current densities. It is seen that CCT sample exhibits larger discharge time than CT. The capacitance (C_s) of the electrode material is found from galvanostatic charging-discharging curve by equation $C_s = \frac{i\Delta t}{m\Delta V}$, where I, t, m, V are constant discharge current, discharge time, mass of the active material loaded over current collector and potential window for discharge. The calculated specific capacitance for CT and CCT sample at current density of 0.2 A g^{-1} is 158 and 187 F g^{-1}, respectively. Figure 3f represents the variation of specific capacitance at different current densities ranging from 0.2 to 1 A g^{-1}. The C_s value reduces with the growth of current density value because of the fact of dropping of electrolyte ions permeation inside the active material in order to fulfil the target of maximum charge storage.

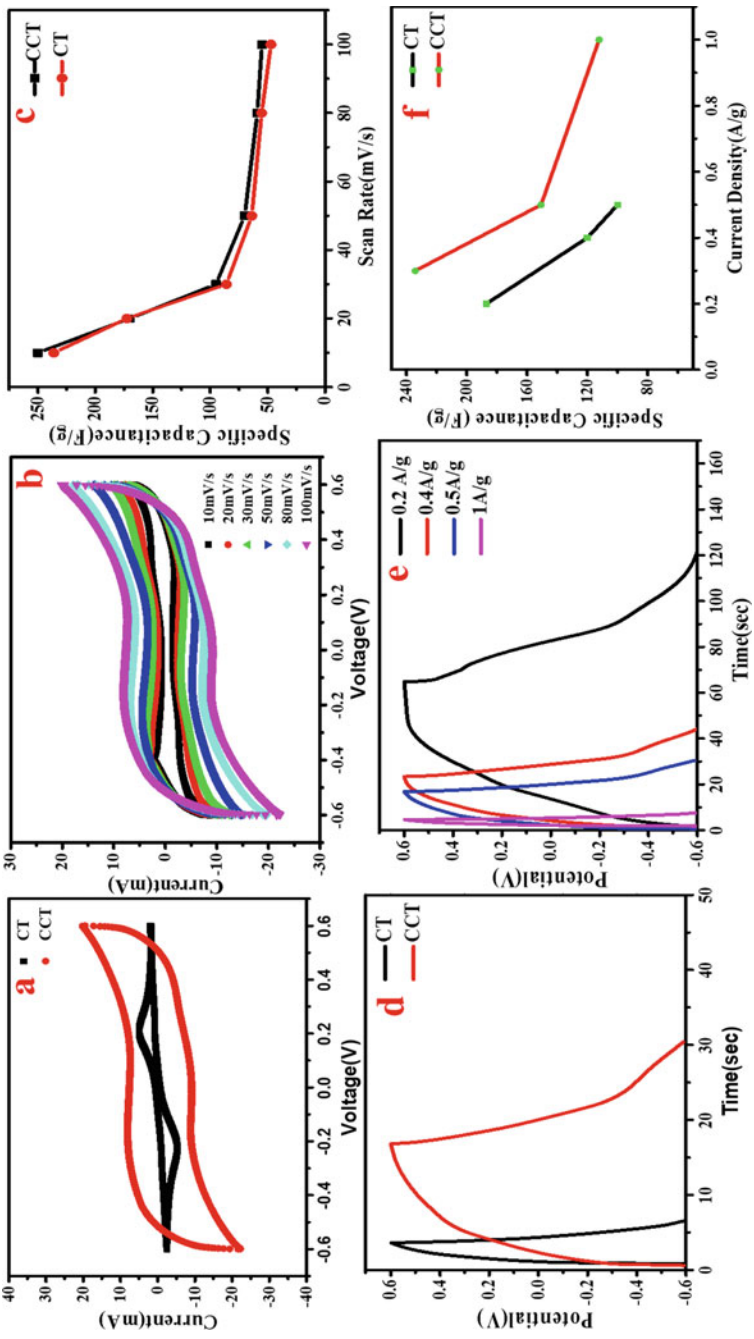

Fig. 3 Cyclic voltammogram of **a** CT and CCT at scan rate of 100 mV s^{-1}, **b** CCT material at various scan rate 10–100 mV s^{-1}, **c** specific capacitance versus scan rate for CT and CCT, **d** galvanostatic charge–discharge plot for CT and CCT at constant current density of 0.4 A g^{-1}, **e** GCD curves at current densities 0.2–1 A g^{-1}, **f** variation of specific capacitance as function of current density

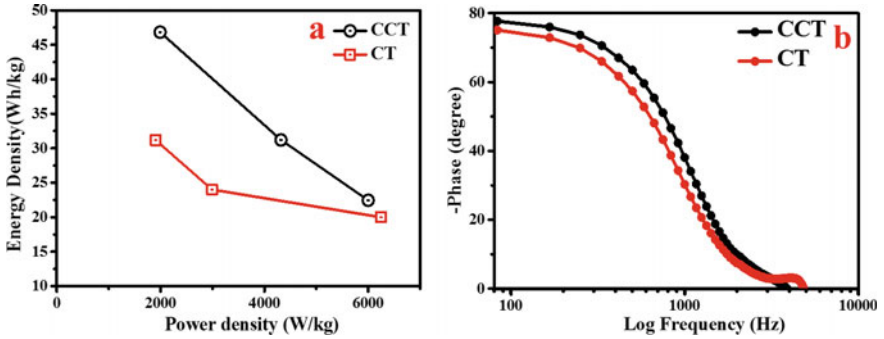

Fig. 4 **a** Ragone plot for CT and CCT samples, **b** phase angle as function of frequency in 6M NaOH electrolyte

Table 1 Calculated resistances, specific capacitance, energy density and power density of CT and CCT electrode, respectively

Sample	Resistance (Ω)		CV	GCD		
	R_b	R_{ct}	C_s (F g^{-1})	C_s (F g^{-1})	E_d (Wh kg^{-1})	P_d (W kg^{-1})
CT	5	3	237	158	46	2162
CCT	3	1	250	187	31	1992

The plot of energy density versus power density called as Ragone plot for CT and CCT electrode material is depicted in Fig. 4a. The CCT material showcases better electrochemical results as given in Table 1. The variation of phase as function of frequency is shown in Fig. 4b. The phase angle of −78 and −75 for CCT and CT samples, respectively, indicate enhanced capacitive behaviour of the prepared electrode material [10].

The Nyquist plot for CCT and CT sample are represented in Fig. 5. It comprises of three regions: semicircle at high frequency relating to electrical resistance between electrode and electrolyte, a slanting line at slope of 45° in mid-frequency region. Nearly parallel straight line to imaginary impedance axis at very low frequency refereeing to EDLC charge storage mechanism [11]. The intercept of real impedance axis and diameter of semi-circular arc aid to determine the bulk (R_b) and charge transfer resistance (R_{ct}) of the CT and CCT material that are determined to be R_b (5 and 3 Ω) and R_{ct} (3 and 1 Ω), respectively. The reduction of R_b and R_{ct} for CCT compared to CT material infers to the high electrolyte ion diffusion and more storage of charges at electrode material surface.

The inset plot in Fig. 5 comprise of fitted data and equivalent circuit fitted using Z_{simp} Win software. The fitted data exactly matches with the experimental data. Thus, the electrochemical analysis via CV, GCD and EIS plotting supports the idea of considering CCT electrode material as potential candidate for supercapacitor application.

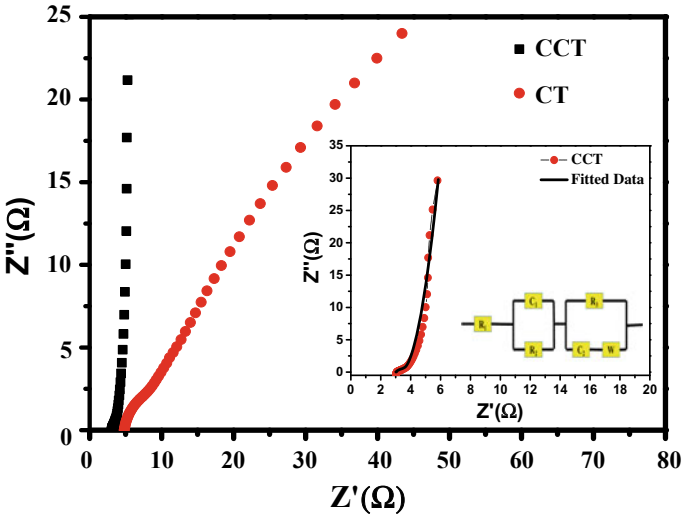

Fig. 5 Nyquist plot for both CT and CCT nanocomposite. Inset shows the fitted and equivalent circuit for CCT electrode

Acknowledgements Shweta Tanwar is thankful to UGC for providing fellowship and CUPB for carrying out experimental results.

References

1. Sirengo K, Jande YAC, Kibona TE, Hilonga A, Muiva C, King'ondu CK (2019) Fish bladder-based activated carbon/Co_3O_4/TiO_2 composite electrodes for supercapacitors. Mater Chem Phys 232:49–56
2. Çakıroğlu B, Özacar M (2018) A self-powered photoelectrochemical glucose biosensor based on supercapacitor Co_3O_4-CNT hybrid on TiO_2. Biosens Bioelectron 119:34–41
3. Chen TY, Lin LY, Geng DS, Lee PY (2021) Systematic synthesis of ZIF-67 derived Co_3O_4 and N-doped carbon composite for supercapacitors via successive oxidation and carbonization. Electrochim Acta 137986
4. Usman M, Adnan M, Ahsan MT, Javed S, Butt MS, Akram MA (2021) In situ synthesis of a polyaniline/Fe–Ni codoped Co_3O_4 composite for the electrode material of supercapacitors with improved cyclic stability. ACS Omega 6(2):1190–1196
5. Naushad M, Ahamad T, Ubaidullah M, Ahmed J, Ghafar AA, Al-Sheetan KM, Arunachalam P (2021) Nitrogen-doped carbon quantum dots (N-CQDs)/Co_3O_4 nanocomposite for high performance supercapacitor. J King Saud Univ Sci 33(1):101252
6. Reddy NR, Kumari MM, Shankar MV, Reddy KR, Joo SW, Aminabhavi TM (2021) Photocatalytic hydrogen production from dye contaminated water and electrochemical supercapacitors using carbon nanohorns and TiO_2 nanoflower heterogeneous catalysts. J Environ Manag 277:111433
7. Sanchez-Sanchez A, Izquierdo MT, Mathieu S, Ghanbaja J, Celzard A, Fierro V (2020) Structure and electrochemical properties of carbon nanostructures derived from nickel (II) and iron (II) phthalocyanines. J Adv Res 22:85–97

8. Kazemi SH, Hosseinzadeh B, Kazemi H, Kiani MA, Hajati S (2018) Facile synthesis of mixed metal–organic frameworks: electrode materials for supercapacitors with excellent areal capacitance and operational stability. ACS Appl Mater Interfaces 10(27):23063–23073
9. Zhou D, Lin H, Zhang F, Niu H, Cui L, Wang Q, Qu F (2015) Freestanding MnO_2 nanoflakes/porous carbon nanofibers for high-performance flexible supercapacitor electrodes. Electrochim Acta 161:427–435
10. Karthik N, Edison TNJI, Sethuraman MG, Lee YR (2017) Sonochemical fabrication of petal array-like copper/nickel oxide composite foam as a pseudocapacitive material for energy storage. Appl Surf Sci 396:1245–1250
11. Zhao W, Zhu Y, Zhang L, Xie Y, Ye X (2019) Facile synthesis of three-dimensional porous carbon for high-performance supercapacitors. J Alloy Compd 787:1–8

Schwarzschild Metric from Arbitrary Choice of Function

Umang Kumar and S. D. Pathak

Abstract We investigate and construct a metric by assuming arbitrary function of position and time and obtain the solution of Einstein field equations. We show that the solution is independent of choice of the arbitrary function and only depends on the symmetry conditions taken into account.

1 Introduction

Schwarzschild metric is one of the most trivial solutions of Einstein field equations arrived at by Schwarzschild [1] which describes the gravitational field around a spherically symmetric, non-rotating, and uncharged mass.

Schwarzschild solution's significance in general relativity comes from the fact that it explains the general features of Einstein's field equations elegantly in a single equation of the Schwarzschild line element which enables us to extract physics from an otherwise obscure set of mathematical equations. Due to the nonlinear nature of Einstein field equations and a lack of easy to approach visualization, it is not easy to understand what these equations represent or are trying to convey. J. C. Baez and E. F. Bunn have discussed the meaning of Einstein's field equations [2] and is a good starting place. We will first try to explore the simpler and easy to understand physical aspects of the Schwarzschild metric and then go on to derive it using the Minkowski line element by considering an arbitrary ansatz.

The Schwarzschild line element is given by,

$$\mathrm{d}s^2 = \left(1 - \frac{p}{r}\right)\mathrm{d}t^2 - \left(1 - \frac{p}{r}\right)^{-1}\mathrm{d}r^2 - r^2(\mathrm{d}\theta^2 + \sin^2\theta\,\mathrm{d}\phi^2) \tag{1}$$

U. Kumar (✉) · S. D. Pathak
Department of Physics, Lovely Professional University, Phagwara, Punjab 144411, India

S. B. Krupanidhi et al. (eds.), *Advanced Functional Materials and Devices*, Springer Proceedings in Materials 14, https://doi.org/10.1007/978-981-16-5971-3_15

[3–7] and its metric form can be visualized as,

$$\begin{pmatrix} \left(1-\frac{p}{r}\right) & 0 & 0 & 0 \\ 0 & -\left(1-\frac{p}{r}\right)^{-1} & 0 & 0 \\ 0 & 0 & -r^2 & 0 \\ 0 & 0 & 0 & -r^2\sin^2(\theta) \end{pmatrix}$$

where $p = \dfrac{2GM}{c^2}$ also known as the Schwarzschild radius.

There are other forms of Schwarzschild metric in different coordinate systems like Eddington–Finkelstein, Kerr–Schild, and others. C. Heinicke and F. H. Hehl have presented all the forms of the Schwarzschild metric in different coordinates in a tabular form [8].

As stated above, the Schwarzschild metric gives the static space-time outside a non-rotating, uncharged and spherically symmetric body of mass M with radius r. The Schwarzschild metric gives the Newtonian solution in the limit where $\frac{r}{M}$ is very large. It might even be possible to obtain the Schwarzschild metric from pre-relativistic considerations [9–11]. Extracting more information from this metric requires us to consider the singularity of this metric which is presented in the next section.

1.1 Schwarzschild Singularity

The Schwarzschild metric has the following singularities:

- $r = 0$. This singularity occurs in Newtonian theory of gravity as well.
- $r = \left(\dfrac{2GM}{c^2}\right)$. This value of r is known as the Schwarzschild radius [6]. At this value of r, the coefficient of $\mathrm{d}t^2$ becomes 0 and the coefficient of $\mathrm{d}r^2$ becomes infinite. This singularity is removable through coordinate transformations [12].

This exact form of Schwarzschild radius can be obtained from Newtonian gravity as well by equating the escape velocity to the speed of light c. Newtonian escape velocity is given by,

$$v_e = \sqrt{\frac{2GM}{r}} \tag{2}$$

Replacing v_e by c and rearranging the terms, we obtain the exact same form of the Schwarzschild radius. This tells us even more about the general nature of the metric and how it is compatible with the Newtonian gravity.

The equating of c as escape velocity has a physical significance, and in that we assume there exists a body of mass M having some radius r for which the escape velocity is comparable to the speed of light [13] which would mean that even light

would not be able to escape the gravitational effect of this body. This special body is known as a black hole [14] and presents itself as a singular point in the Schwarzschild metric.

Schwarzschild radius can be calculated for any massive body as we will see by calculating the Schwarzschild radius of the Earth.

$$r = \frac{2GM}{c^2} \tag{3}$$

$$r = 8.85 \times 10^{-3}\text{m}$$

Thus, the Schwarzschild radius of the Earth is about 8.85 mm as compared to the Schwarzschild radius of the Sun which is about 2.95 km [6].

In the further sections, we explore the prevalent derivations of the Schwarzschild metric and compare the solutions thus obtained with our proposed ansatz.

2 Schwarzschild Metric from Different Initial Functions

The derivation of Schwarzschild metric starts with a spherical polar form of the Minkowski metric and introducing functions in that metric which follow some properties that our required solution should exhibit. The line element used for the derivation of the Schwarzschild metric in its most general form [15] can be given as

$$\mathrm{d}s^2 = A\mathrm{d}t^2 - B\mathrm{d}r^2 - Cr^2\mathrm{d}\theta^2 - Dr^2\sin^2(\theta)\mathrm{d}\phi^2 \tag{4}$$

The functions A, B, C, D are the functions we inserted and to be determined by our solution. We can limit them by considering certain properties of our solution:

- The solution is spherically symmetric; hence, the functions should not depend upon θ and ϕ. Also the angular part of the metric can be put as 1 without compromising on generality.
- The solution we are finding is a vacuum solution that limits the Einstein field equations [16] to the form

$$G_{ik} = R_{ik} - \frac{1}{2}g_{ik}R = 0 \tag{5}$$

We proceed to take different forms of the functions presented above of which only A and B are left for consideration.

2.1 Functions of r only

Here, we take $A = \omega(r)$ and $B = \psi(r)$ which depend only on the radial distance r and are independent of time. Putting values of A and B in (4) and taking $C = D = 1$, we get

$$ds^2 = \omega(r)dt^2 - \psi(r)dr^2 - r^2 d\theta^2 - r^2 \sin^2(\theta) d\phi^2 \tag{6}$$

Metric :

$$\begin{pmatrix} \omega & 0 & 0 & 0 \\ 0 & -\psi & 0 & 0 \\ 0 & 0 & -r^2 & 0 \\ 0 & 0 & 0 & -r^2 \sin^2(\theta) \end{pmatrix}$$

Here, the prime on a symbol means differentiation with respect to r.
The nonzero Christoffel symbols can be found out using the relation,

$$\Gamma^i{}_{jk} = \frac{1}{2} g^{il} \left[\frac{\partial g_{lj}}{\partial x^k} + \frac{\partial g_{lk}}{\partial x^j} - \frac{\partial g_{jk}}{\partial x^l} \right] \tag{7}$$

Solving the Einstein field equations for vacuum, we get the following equations:

$$-\frac{1}{r^2\psi} + \frac{1}{r^2} + \frac{\psi'}{r\psi^2} = 0 \tag{8}$$

$$-\frac{\psi}{r^2} + \frac{1}{r^2} + \frac{\omega'}{r\omega} = 0 \tag{9}$$

$$\frac{r\omega''}{\omega} - \frac{r\omega'\psi'}{2\omega\psi} - \frac{r\omega'^2}{2\omega^2} + \frac{\omega'}{\omega} - \frac{\psi'}{\psi} = 0 \tag{10}$$

$$\sin^2\theta \left[\frac{r\omega''}{\omega} - \frac{r\omega'\psi'}{2\omega\psi} - \frac{r\omega'^2}{2\omega^2} + \frac{\omega'}{\omega} - \frac{\psi'}{\psi} \right] = 0 \tag{11}$$

As (10) and (11) are equivalent, we use Eqs. (8) and (9) for our solution. Equation (8) is easily integrated to give:

$$\psi = \frac{1}{1 - \frac{\kappa}{r}} \tag{12}$$

Now using the value of ψ from (12), we substitute it in Eq. (9) and integrate, which gives:

$$\omega = 1 - \frac{\kappa}{r} \tag{13}$$

Now, κ (integration constant) can be expressed in terms of the mass of the body, and by requiring that at large distances Newton's Law should hold [7], and we can write $\kappa = p = \frac{2GM}{c^2}$. Using the values thus obtained, we can rewrite Eq. (6) as:

$$ds^2 = \left(1 - \frac{p}{r}\right) dt^2 - \left(1 - \frac{p}{r}\right)^{-1} dr^2 - r^2(d\theta^2 + \sin^2\theta d\phi^2)$$

which is the required Schwarzschild metric.

2.2 Functions of r and t to the Power n

The ansatz most generally present in literature to derive the Schwarzschild metric is $A = e^{\omega(r,t)}$ and $B = e^{\psi(r,t)}$, given by Landau [7] and many others in their books [3–5, 17]. Now, we explore our proposed form of the ansatz which extends the generality by raising the functions themselves to power n. The functions now become $A = \omega^n$ and $B = \psi^n$ where ω and ψ are functions of both time and r.

We get the line element as:

$$ds^2 = \omega^n(r,t)dt^2 - \psi^n(r,t)dr^2 - r^2 d\theta^2 - r^2 \sin^2(\theta) d\phi^2 \tag{14}$$

Metric:

$$\begin{pmatrix} \omega^n & 0 & 0 & 0 \\ 0 & -\psi^n & 0 & 0 \\ 0 & 0 & -r^2 & 0 \\ 0 & 0 & 0 & -r^2\sin^2(\theta) \end{pmatrix}$$

Listing the nonzero Christoffel symbols:

$$\Gamma^0_{00} = \frac{n\dot{\omega}}{2\omega} \quad \Gamma^0_{01} = \Gamma^0_{10} = \frac{n\omega'}{2\omega} \quad \Gamma^0_{11} = \frac{1}{2}n\dot{\psi}\psi^{n-1}\omega^{-n}$$

$$\Gamma^1_{00} = \frac{1}{2}n\omega'\psi^{-n}\omega^{n-1} \quad \Gamma^1_{01} = \Gamma^1_{10} = \frac{n\dot{\psi}}{2\psi} \quad \Gamma^1_{11} = \frac{n\psi'}{2\psi}$$

$$\Gamma^1_{22} = -r\psi^{-n} \quad \Gamma^1_{33} = -r\sin^2(\theta)\psi^{-n}$$

$$\Gamma^2_{12} = \Gamma^2_{21} = \frac{1}{r} \quad \Gamma^2_{33} = -\sin(\theta)\cos(\theta)$$

$$\Gamma^3_{13} = \Gamma^3_{31} = \frac{1}{r} \quad \Gamma^3_{23} = \Gamma^3_{32} = \cot(\theta)$$

Again solving the Einstein field equations for vacuum, we obtain the following equations:

$$-\frac{\psi^{-n}}{r^2}+\frac{n\psi'\psi^{-n-1}}{r}+\frac{1}{r^2}=0 \tag{15}$$

$$\frac{n\dot{\psi}}{r\psi}=0 \tag{16}$$

$$-\frac{\psi^{n}}{r^2}+\frac{n\omega'}{r\omega}+\frac{1}{r^2}=0 \tag{17}$$

$$\begin{aligned}&-\frac{n^2r^2\psi'\omega'\psi^{-n-1}}{4\omega}+\frac{n^2r^2\dot{\psi}\dot{\omega}\omega^{-n-1}}{4\psi}-\frac{n^2r^2\dot{\psi}^2\omega^{-n}}{4\psi^2}+\\&\frac{n^2r^2\omega'^2\psi^{-n}}{4\omega^2}+\frac{nr^2\dot{\psi}^2\omega^{-n}}{2\psi^2}-\frac{nr^2\ddot{\psi}\omega^{-n}}{2\psi}+\frac{nr^2\omega''\psi^{-n}}{2\omega}\\&-\frac{nr^2\omega'^2\psi^{-n}}{2\omega^2}-\frac{1}{2}nr\psi'\psi^{-n-1}+\frac{nr\omega'\psi^{-n}}{2\omega}=0\end{aligned} \tag{18}$$

$$\begin{aligned}\sin^2\theta\Bigg[&-\frac{n^2r^2\psi'\omega'\psi^{-n-1}}{4\omega}+\frac{n^2r^2\dot{\psi}\dot{\omega}\omega^{-n-1}}{4\psi}-\frac{n^2r^2\dot{\psi}^2\omega^{-n}}{4\psi^2}\\&+\frac{n^2r^2\omega'^2\psi^{-n}}{4\omega^2}+\frac{nr^2\dot{\psi}^2\omega^{-n}}{2\psi^2}-\frac{nr^2\ddot{\psi}\omega^{-n}}{2\psi}+\frac{nr^2\omega''\psi^{-n}}{2\omega}\\&-\frac{nr^2\omega'^2\psi^{-n}}{2\omega^2}-\frac{1}{2}nr\psi'\psi^{-n-1}+\frac{nr\omega'\psi^{-n}}{2\omega}\Bigg]=0\end{aligned} \tag{19}$$

Equation (16) gives the time independence of ψ and Eqs. (18) and (19) are equivalent, and thus, we use Eqs. (15) and (17) to derive our solution. Integrating (15), we get:

$$\psi^n=\left(1-\frac{\kappa}{r}\right)^{-1} \tag{20}$$

Substituting (20) in (17) and then integrating, we obtain:

$$\omega^n=1-\frac{\kappa}{r} \tag{21}$$

Again using $\kappa = p$ and rewriting Eq. (14),

$$ds^2 = \left(1 - \frac{p}{r}\right) dt^2 - \left(1 - \frac{p}{r}\right)^{-1} dr^2 - r^2(d\theta^2 + \sin^2\theta d\phi^2)$$

we get the Schwarzschild metric.

The tensor components and Christoffel symbols presented above can become tedious to solve manually and have a greater possibility of having errors; it is advisable to use the widely accepted open source computer algebra systems like Sage Math or Maxima [18] or commercial applications like Mathematica.

3 Conclusion

We took the general form of the Minkowski metric and then assumed different ansatz which accounts for the symmetry conditions of the Schwarzschild solution and used these metrics to solve the Einstein's field equations for the vacuum solution and finally arrived at the Schwarzschild metric. We conclude that the Schwarzschild solution is independent of choice of arbitrary ansatz. The solution of field equations remains unaffected for a metric obtained by taking any arbitrary function of position.

References

1. Schwarzschild K, Antoci S, Loinger A (1999) On the gravitational field of a mass point according to Einstein's Theory. arXiv:physics/9905030 [physics.hist-ph]
2. Baez John C, Bunn Emory F (2005) The meaning of Einstein's equation. Am J Phys 73(7):644–652
3. Narlikar JV (2010) An introduction to relativity. Cambridge University Press, Cambridge. 978-0-521-17877-8
4. Narlikar JV (1993) Introduction to cosmology. Cambridge University Press, Cambridge. 978-0-521-42352-6
5. Chandrasekhar S (2009) The mathematical theory of black holes. Oxford University Press, Oxford. 978-0-19-886313-7
6. Hartle JB (2014) Gravity: an introduction to Einstein's general relativity. Pearson, Harlow, Essex. 978-93-325-3508-4
7. Landau LD, Lifshitz EM (1975) Classical theory of fields. Course of theoretical physics, vol 2. Butterworth-Heinemann Press, New York. ISBN:978-81-8147-787-3
8. Heinicke C, Hehl FW (2015) Schwarzschild and Kerr solutions of Einstein's field equation: an introduction. Int J Mod Phys D 24(2):1530006 (78)
9. Czerniawski J (2006) The possibility of a simple derivation of the Schwarzschild metric. arXiv:gr-qc/0611104
10. Pössel M (2020) Deriving the Schwarzschild solution from a local Newtonian limit. arXiv:2009.03738 [physics.ed-ph]
11. Kassner K (2017) Dust ball physics and the Schwarzschild metric. Am J Phys 85(8):619–627
12. Gsponer A (2004) More on the early interpretation of the Schwarzschild solution. Indep Sci Res Inst Phys 0408100. ISRI-2004-09
13. Visser M (2005) Heuristic approach to the Schwarzschild geometry. Int J Mod Phys D 14(12):2051–2067

14. Logunov AA, Mestvirishvili MA (1989) The relativistic theory of gravitation. Mir Publishers, Moscow. 978-5030009056
15. Sacks William M, Ball John A (1986) Simple derivations of the Schwarzschild metric. Am J Phys 36(3):240–245
16. Rindler W (2006) Relativity: special, general, and cosmological. Oxford University Press, Oxford. 978-0-19-856732-5
17. Adler R et al (1975) Introduction to general relativity. McGraw-Hill, New York. 978-0-07-000423-8
18. Birkandan T, Güzelgün C, Şirin E, Uslu MC (2018) Symbolic and numerical analysis in general relativity with open source computer algebra systems. Gen Relativ Gravit 51:4

High-Pressure Structural Phase Transition of Alkali Hydride Compounds: An Ab Initio Study

Agnibha Das Majumdar and Neha Munjal

Abstract The present work is contributed basically to the topic on the investigation of structural properties of alkali hydride compounds XH (X=K, Rb, Cs) using the first principle total energy calculations within linear combination of atomics orbital method. The work is basically built up using density functional theory or DFT with the coordination of CRYSTAL coding. The hybrid scheme B3LYP is used for making the Kohn–Sham Hamiltonian. We are taking the compounds XH (X=K, Rb, Cs) and investigated that there is occurrence of phase transition from B1 to B2. And with the help of the Birch–Murnaghan formula, the investigation of the important parameter of structural property that is the bulk modulus has been calculated**.**

Keywords Density functional theory · B3LYP · Alkali hydride · Structural properties · Frist principle study

1 Introduction

The group of lithium, sodium, potassium, rubidium, caesium and francium atoms are basically acknowledged as alkali metals, as those atoms has shown alkali properties. Now if a chemical reaction can occur at about 673 K between those alkali compounds and the dry hydrogen, it will form the crystalline alkali hydrides. Those alkali hydrides do not have any colours and are having high melting point along with the good ionic bonds. As the alkali metal and hydrogen bond become feeble because of increasing nature in the size of alkali metal atoms down to the group from K to Cs, then as a result it shows the decreasing stability from K to Cs also [11]. Alkali hydrides attain the attention as a technologically important material for its application in nuclear and chemical industries. So, these hydride materials are being treated by both the experimental and the theoretical observations. The experimental studies show that at the normal conditions, the alkali hydride compounds show the rock salt (RS) structure, but at a conditional range of pressure, the alkali hydride

A. D. Majumdar · N. Munjal (✉)
Lovely Faculty of Science and Technology, School of Chemical Engineering and Physical Sciences, Lovely Professional University, Phagwara, Punjab 144411, India
e-mail: neha.18869@lpu.co.in

S. B. Krupanidhi et al. (eds.), *Advanced Functional Materials and Devices*, Springer Proceedings in Materials 14, https://doi.org/10.1007/978-981-16-5971-3_16

materials show phase transition from sodium chloride phase to caesium chloride phase [8]. Investigation of the structural as well as mechanical attributes of the alkali metal hydride compounds LiH, NaH, KH, RbH and CsH has been done, and it was investigated with the help of first principle calculations. The generalized gradient approximation (GGA) method is used with the combination of density functional theory for this calculation. The obtained results for the calculations by first principle calculations are compared also with the alkaline earth metal (BeH_2, CaH_2, MgH_2, BaH_2 and SrH_2) hydride. In this work, a method of principle component analysis (PCA) is also discussed [17]. The approach of FP-LAPW method for calculating the electronic structure, optimization of volume, bulk modulus, elastic constant and frequencies of the transversal optical vibration has been utilized for the different alkali metal hydride compounds. Along with this, they have also illustrated several selected experimental results, not only that but also talked about different theoretical approaches, respectively, used in purpose of various alkali hydride properties [14]. The structural stability and elastic constants of alkali hydrides (LiH, KH, NaH) can be calculated by using the FP-LAPW method which is first principle approach. To explain the exchange correlation functional, the GGA can be used [2]. The stability and electron structure has been calculated through the FLAPW method within the GGA for the lithium aluminium hydride ($LiAlH_4$), which is useful for the hydrogen storage. As a result of this work, the electronic structure shows the non-equivalent bond of H and Al in $[AlH_4]^-$ [16]. When alkali hydride crystallizes in rock salt structure, it has coordination no. 6, and when it crystallizes in CsCl structure, it has coordination no. 8 [5]. The alkali radii increase the structural transition pressure from B1 to B2 phase [7]. It can be considered as hydrogen is a very basic chemical element, which can be easily available in a huge quantity in the whole atmosphere. It can easily be combined with maximum no. of element of the periodic table and can make the stable binary compounds. Metal hydrides are good enough in applications also, like as storage of hydrogen, as an agent uses in reducing process, as a catalyst, and also as in synthetic transformations. Now alkali hydrides are that kind of solids which have high melting property [5]. The Vienna ab initio stimulation package of first principle calculations is to determine the physical properties, electronic properties and mechanical attributes of alkali hydride MH, where M stands for lithium, rubidium, sodium, potassium and caesium. In structural parameter lattice constant, bulk modulus and density of state are also determined. In this work, at a condition of high pressure, the structural phase transition from rock salt phase to CsCl phase has been predicted. For correlation and exchange potential, LDA and GGA both have been done. For calculating the fundamental properties through density functional theory, the coding which is using is VASP code. As a result of this work, LiH is considered to be the stiffest compound among the all the alkali hydride compounds [15]. In more application point of view, hydrides are reliable materials for the rechargeable batteries, cells, optical switches, sensors and also for heat storage. In case of purification of hydrogen and in nuclear energy industries, hydrides are too useful. Alkali metals are also the important compounds because alkali metals are efficient to obtain very large amount of energy in case of fusion. So these alkali metals hydrides have also some importance as it helps to understand the hydrogen properties in terms of

storage enhancement. Not only the dense population of hydrogen atoms, but also the metal hydrides with lightweight are very much suitable for transport industries [17]. All those above study has been carried out with the help of computational study. Computational studies have its own importance in the field of material science. This approach is also known as first principle studies. First principle studies have been carried out on the concept of DFT study. Density functional theory is a quantum simulation process dealing with N number of atoms. And it is often used in the field of physics and chemistry. For many body condensed system, or any many body atomic system, this method is efficiently used for calculating the different physical attributes like band gap, lattice parameter, bulk modulus, etc. The concept of density functional theory for the many body has been first introduced by two renowned scientists Professor Walter Kohn and John A Pople. Professor Kohn and Professor Pople are from University of California and North Western University, respectively. They both have received the noble prize from the Royal Swedish academy of science in the year of 1998. Above-mentioned works have been utilized with different methods. In this paper, LCAO method has been taken into focus. Many researchers have used this method efficiently. This is efficiently used for the semiconductor method. A review article has been published on the different methods of the computational studies on the density functional theory approach. In this review article, authors have differentiated about the different DFT approaches such as CASTEP, LCAO and FP-LAPW [3].

2 Computational Method

In the present work, the first principles linear combination of atomic orbitals (LCAO) method is used to determine the structural attributes of alkali hydride compounds, that is XH, where X stands for K, Rb and Cs. This method has been proved to be efficient in many cases [12, 13, 19]. The Kohn–Sham Hamiltonian equation under the density functional theory was resolved for calculating the energy values in CRYSTAL [4] code. The CRYSTAL programme explains about the calculations of the electronic as well as the structural properties of any systems which are periodic in the basis of several theories like Hertree–Fock theory, density functional theory and several hybrid approximations. This code can be expressed to fulfil the investigations about the chemical and physical properties of crystalline solids, the polymers, the molecules, the nano-tubes, etc. It can also calculate the vibrational, magnetic, piezoelectric, elastic, dielectric and photo-elastic properties of any type of compounds. Many excellent results for many compound have been obtained by this coding.

The Gaussian basis set function for K, Rb, Cs and H has been built from the CRYSTAL software (www.tcm.phy.cam.ac.uk). Kohn–Sham equation for the Hamiltonian function has been utilized while applying the hybrid scheme B3LYP. Calculation of the structural attributes of the concerned materials had been done with the optimization of the energies along with the reference volume values of the unit cells. Then calculated parameters were compared with previous results. The tolerance has

considered at 84 k points and used with adequate tolerance, and 55% mixing has been done for the self-consistency within the ten cycles.

In this work, presented figures are having dotted line as well as fitted line. The dotted lines present the energies calculated with the software, and the fitted lines present the energies calculated from the Brich–Murnaghan equation. The Brich–Murnaghan equation presents mathematically with expression.

$$E(V) = E_0 + \frac{9V_0B_0}{16}\left\{\left[\left(\frac{V_0}{V}\right)^{\frac{2}{3}} - 1\right]^3 B_0'\left[\left(\frac{V_0}{V}\right)^{\frac{2}{3}} - 1\right]^2\left[6 - 4\left(\frac{V_0}{V}\right)^{\frac{2}{3}}\right]\right\}$$

Here, $E(V)$ present energy associated with the volume of unit cell, E_0 represent the minimum energy, V_0 present corresponding volume of the E_0, and B_0 and B'_0 stand for bulk modulus and pressure derivative of bulk modulus, respectively.

3 Result and Discussion

The structural attributes of the alkali metal compound XH in NaCl phase as well as in CsCl phase have been examined. The energy vs. unit cell volume loop for the alkali metal hydrides has been shown for both the phases (Figs. 1, 2, 3, 4, 5 and 6).

Present results are consistent with previous investigations (Table 1). For calculating that particular value of pressure at which that structural phase transition from rock salt phase to CsCl occurs, the concept of the Gibbs free energy has been used. The conditional temperature is put at 0 k, so that Gibbs free energy decreases the amount of enthalpy, which is $H = \Delta E + \mathrm{PV}$. So, at which point two lines have crossed each other, the corresponding pressure is the one at which the structural transition occurs. So, for KH, it is 5.1 GPa. As well as for RbH and CsH, this has occurred

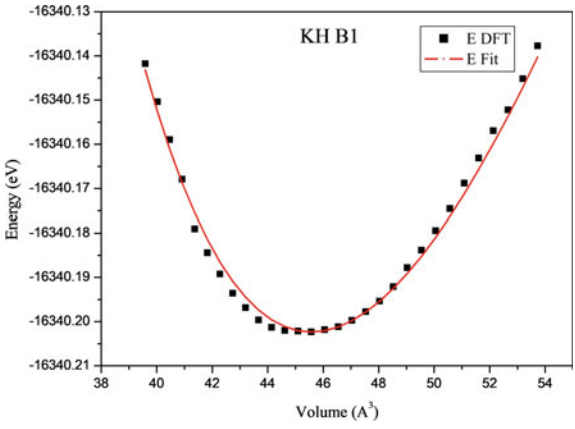

Fig. 1 Energy versus volume curve

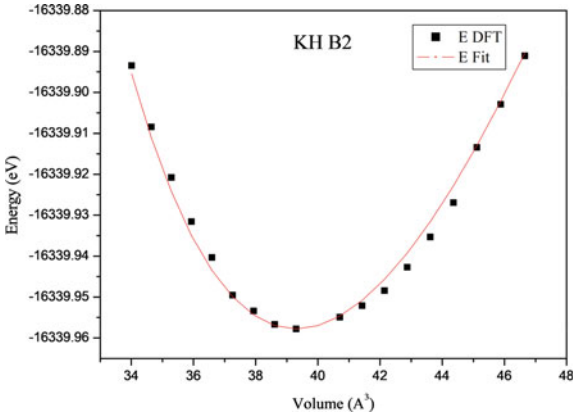

Fig. 2 Energy versus volume curve

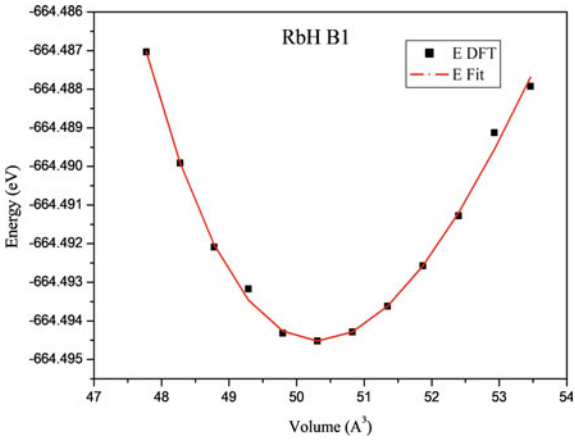

Fig. 3 Energy versus volume curve

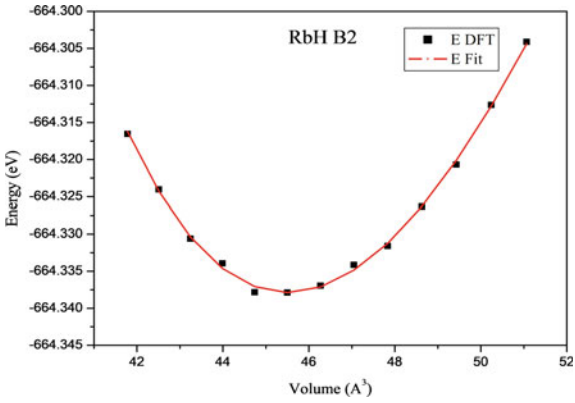

Fig. 4 Energy versus volume curve

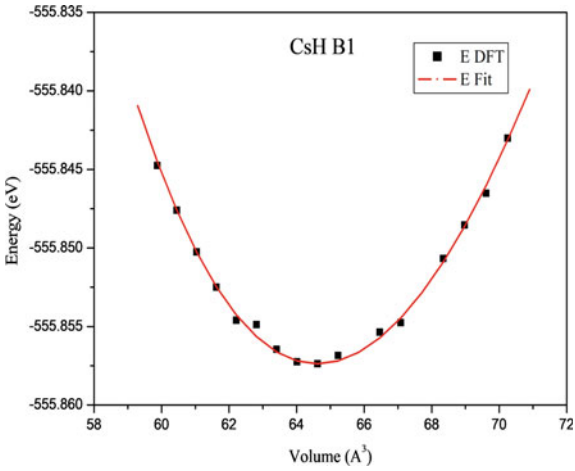

Fig. 5 Energy versus volume curve

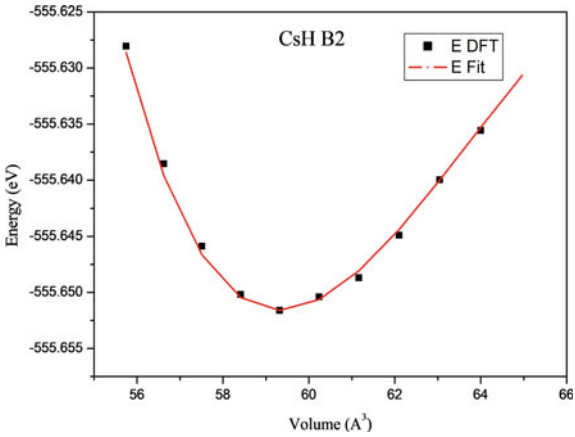

Fig. 6 Energy versus volume curve

at 3.66 GPa and 2.5 GPa, respectively (Table 2). Present results are consistent with previous data (Figs. 7, 8, 9 and 10).

4 Conclusion

In summary, the ab initio calculations are performed using LCAO method in combination with GGA to determine the different structural attributes of alkali hydride compounds. The change in total energy versus volume is defined in above figures and also had shown the variation in lattice constants of XH (X=K, Rb and Cs) as atomic radii as function. The lattice constant increases with the increasing value of atomic radius of alkali compounds, i.e. K, Rb, and Cs. Also the compounds XH

Table 1 Current and exist values of lattice constants (a) and bulk modulus (B_0) for the alkali hydrides

Compounds	KH	KH	RbH	RbH	CsH	CsH
	(*B*1)	(*B*2)	(*B*1)	(*B*2)	(*B*1)	(*B*2)
Lattice parameter (Å)						
Present work	5.67	3.4	5.86	3.59	6.37	3.9
Experimental work	5.7 [18]	–	6.037 [20]	–	6.376 [20]	–
Others calculations	5.721 [15]	3.520 [15]	6.199 [25]	3.81 [15]	6.344 [15]	3.84 [15]
	5.701 [21]	3.41 [9]	6.064 [6]	3.62 [9]	6.407 [21]	3.863 [9]
Bulk modulus (GPa)						
Present work	18.5	21.5	14.91	19.5	10.54	23.98
Experimental work	15.6 ± 1.5 [7]	28.5 ± 1.5 [7]	10.0 ± 1.0 [7]	18.4 ± 1.1 [7]	8.0 ± 0.7 [7]	22.3 ± 1.5 [7]
Others calculations	17.3 [1], 16 [15]	20 [15]	14.7 [1], 14.1[15]	14.9 [15], 13.64 [10]	11.9 [1], 12 [15]	14 [15], 11.5 [10]

Table 2 Presented previously calculated phase transition (in GPa) from RS to CsCl for the alkali hydride compounds

Compounds	KH	RbH	CsH
Present work	5.1	3.66	2.5
Experimental work	4 [7]	2.2 3.1 [7]	1.2 [7]
Others work	5.11 [10], 3.5 [15]	3.50 [10], 3 [15]	2.45 [10], 2.1 [15]

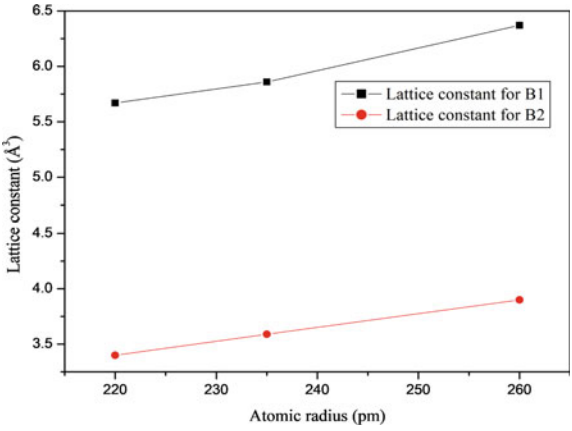

Fig. 7 Plot of the variation of atomic radii of alkali metals with the lattice constant

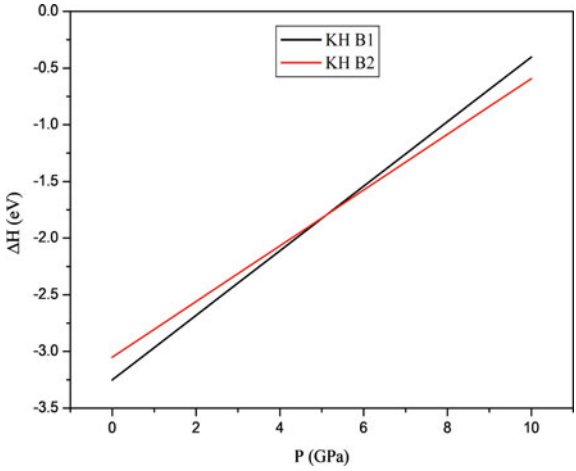

Fig. 8 Plot of the enthalpy versus pressure for KH

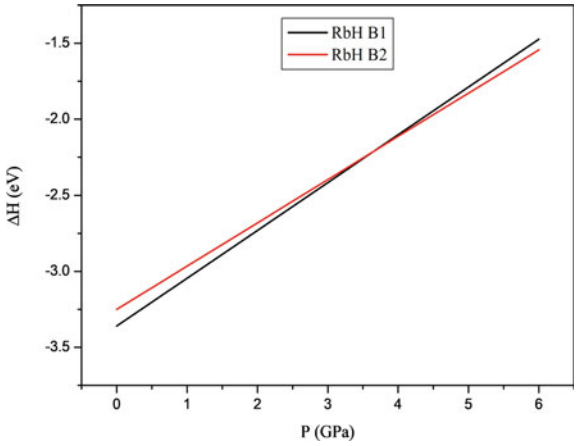

Fig. 9 Plot of the enthalpy versus pressure for RbH

show the structural transition from B1 to B2 structure at very high pressure, which are 5.1 GPa, 2.66 GPa and 2.5 GPa, respectively.

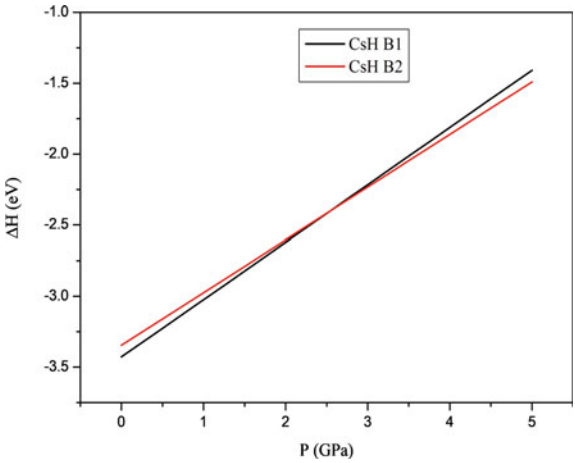

Fig. 10 Plot of the enthalpy versus pressure for CsH

References

1. Barrera GD et al (2005) LDA or GGA? A combined experimental inelastic neutron scattering and ab initio lattice dynamics study of alkali metal hydrides. Chem Phys 317(2–3):119–129
2. Banger S, Nayak V, Verma UP (2016) A first-principle approach to study the structural and elastic properties of alkali hydrides. In: AIP conference proceedings 1731. 1. AIP Publishing LLC
3. Burke K, Wagner L (2014) ABC of ground-state DFT. University Lecture
4. Dovesi R, Saunders VR, Roetti C, Orlando R, Zicovich-Wilson CM, Pascale F, Civalleri B, Doll K, Harrison NM, Bush IJ (2006) Ph D'Arco; M Llunell, CRYSTAL06 user's manual. University of Torino, Torino
5. Fohlmeister L, Stasch A (2015) Alkali metal hydride complexes: well-defined molecular species of saline hydrides. Aust J Chem 68(8):1190–1201
6. Gulebaglan SE et al (2015) First-principles study on electronic, optic, elastic, dynamic and thermodynamic properties of RbH compound. Int J Simul Multidisc Des Opt 6(A6)
7. Hochheimer HD et al (1985) High pressure X-ray investigation of the alkali hydrides NaH, KH, RbH, and CsH. Z Phys Chem 143:139–144
8. Jaradat R et al (2017) High-pressure structural phase transition and electronic properties of the alkali hydrides compounds XH (X= Li, Na). Phase Transit 90(9):914–927
9. Jaradat R et al (2018) Elastic and thermodynamic properties of alkali hydrides XH (X= K, Rb and Cs). Chin J Phys 56(3):830–843
10. Jaradat R et al (2018) Insight into the structural, electronic, elastic and optical properties of the alkali hydride compounds, XH (X= Rb and Cs). AIP Adv 8(4):045017
11. Liu Y, Merinov BV, Goddard WA (2016) Origin of low sodium capacity in graphite and generally weak substrate binding of Na and Mg among alkali and alkaline earth metals. Proc Natl Acad Sci 113(14):3735–3739
12. Majumdar AD et al (2020) Investigation of structural and electronic properties of BaX (X= S, Se, and Te): A DFT study. Advances materials science engineering. Springer, Singapore, pp 281–289
13. Munjal N et al (2020) Structural properties of scandium chalcogenides via first principle calculations. J Phys Conf Ser 1531.1. IOP Publishing
14. Novaković N et al (2007) First principle calculations of alkali hydride electronic structures. J. Phys Cond Mat 19(40):406211

15. Priyanga G, Sudha et al (2014) Structural, electronic and elastic properties of alkali hydrides (MH: M= Li, Na, K, Rb, Cs): Ab initio study. Comp Mat Sci 84:206–216
16. Song Y, Singh R, Guo ZX (2006) A first-principles study of the electronic structure and stability of a lithium aluminum hydride for hydrogen storage. J Phys Chem B 110(13):6906–6910
17. Settouti N, Aourag H (2016) Structural and mechanical properties of alkali hydrides investigated by the first-principles calculations and principal component analysis. Solid State Sci 58:30–36
18. Villars P, Calvert LD (1985) Pearson's handbook of crystallographic data for intermediate phases. American Society of Metals, Cleveland
19. Walia SS et al (2020) Theoretical investigation of structural properties of ternary alloy CuBrxI1-x through first principle method. J Phys Conf Ser 1531.1. IOP Publishing
20. Zintl E, Harder A (1931) Uber Alkali hydride. Z Phys Chem Abt 14:265
21. Zhang J et al (2007) Phonon and elastic instabilities in rock salt alkali hydrides under pressure: first-principles study. Phys Rev B 75(10):104115

Expansion of Free Energy in the Field of Magnetized Quark–Gluon Plasma

Yogesh Kumar, Poonam Jain, Sanjeev Kumar, R. K. Meena, and M. S. Khan

Abstract We determine the total free energy of a system of magnetized quark–gluon plasma (QGP). The system is found to be highly affected at nonzero magnetic field. In order to see free energy evolution, we developed a theoretical model based on the quasi-particles generated due to interactions of fundamental particles in highly dense and hot medium of QGP. The dependence of temperature and chemical potential in the quark mass with nonzero magnetic field provide useful results to describe the free energy expansion. The outputs are useful to generate finite size of QGP droplet and also advantageous for calculating the equation of state (EoS) in huge magnetic field environment. Thus, our model is applicable in various sectors such as cosmology, astrophysics, and heavy-ion collisions to describe the dynamics of QGP. The current findings try to confirm the order of phase transition and help to understand the phase diagram of QCD.

1 Introduction

An extremely hot and moderately dense matter of complex quark–gluon plasma (QGP) in a huge external magnetic field has developed a great interest in the various region of temperature and/or densities. These regions are important to unfold the interest in the field of cosmology [1], astrophysics [2–5], and in non-central collisions of heavy-ion [6].

Y. Kumar (✉) · R. K. Meena · M. S. Khan
Department of Physics, Deshbandhu College, University of Delhi, Kalkaji, New Delhi 110019, India
e-mail: ykumar@db.du.ac.in

P. Jain
Department of Physics, Sri Aurobindo College, University of Delhi, Malviya Nagar, New Delhi 110017, India

S. Kumar
Department of Physics, Motilal Nehru College, University of Delhi, Benito Juarez Marg, New Delhi 110021, India

S. B. Krupanidhi et al. (eds.), *Advanced Functional Materials and Devices*, Springer Proceedings in Materials 14, https://doi.org/10.1007/978-981-16-5971-3_17

The setup of ultra-relativistic heavy ions which is accelerated at speed too close to the speed of light generates an immense electric current, and due to this, extremely intense magnetic field of $10^{19} - 10^{20}$ G produces in marginal collisions with some finite impact parameter [7–13]. Such strong magnetic field survives for a little span of time [14]. Several authors [15–20] noticed that the QGP temperature comes down with the effect of magnetic field. The main role of such an intense magnetic field is to probe a new state of matter created in these experiments. One of the unique signature is the formation of QGP droplet which help to predict the order of phase transition.

So far physicists believe that QGP was the main part of the Universe which appeared just after big bang. Several models have been introduced to describe the properties of QGP. Among various models, a MIT bag model has been used extensively. An outstanding work with the bag model was done by many authors [21–24] under the consideration of zero chemical potential μ and it was considered for the relevance of cosmological quark hadron phase transition. Although MIT bag model was very successful in exploring the phase structure of QGP, there were some disagreement pointed out by the Peshier et al. [25, 26]. In addition to this, there were some potential models used to express the thermodynamic properties of quark–gluon plasma [27–31].

In our model, the parametrization factors and temperature are the essential parameters which describe the physical picture of QGP fireball formation by calculating the total free energy. It indicates the critical dimension of QGP droplets when changing the stage from a phase of quark–gluon to a confined phase of hadrons. However, the order of transition can be arranged as either Ist order/IInd order/crossover phase transition. The lattice QCD results show that the transition into the QGP phase is a smooth crossover [32] at zero or small value of chemical potential and high temperature, whereas the first-order phase transition is assumed at high chemical potential [33, 34]. Inspite of having lattice QCD data, the confirmation of the order of phase transition is still unclear even in these experiments. However, the phenomenological studies are the only appropriate and significant tool to depict the nature of phase transition. Moreover, free energy evolution of QGP and entropy behavior suggested the order of phase transition which categories transition as a first order or crossover. Ramanathan et al. have pointed out that the transition into QGP phase has a type of weakly first-order one [35] at zero chemical potential. In addition to this, there are some reports in which phase transitions depend on the number and mass of quark flavors [36].

Thus, above studies motivate us to investigate how the QGP system works under the influence of magnetic field environment. This magnetized field occur when heavy ions beam smash with each other in opposite direction with the help of giant accelerators situated at BNL and CERN.

The main structure of our paper is as follows: Sect. 2 elucidates a brief overview of model. Then, Sect. 3 explicate total free energy of QGP. Section 4 elaborates our main output in the form of results, followed by the conclusion in our Sect. 5.

2 A Brief Overview of Model

The expansion of free energy in the magnetized field can be the useful signature for the detection and formation of QGP. The work on quasi-particle model has received remarkable attention to deal with the properties of QGP. In quasi-particle treatment, it is important to take care the range of temperature as it works fine near or above the critical temperature. Thus, the mass of these quasi-particles are considered to be temperature dependent [25, 26, 37, 38]. Initially, dynamical quark mass have been used in our previous work. Further we replaced the dynamical quark mass with specific value of quark mass [39, 40]. Under the effect of magnetic contribution, it is important to perceive that how these thermodynamic properties change in such environment. So, we used our previous work in the same environment by taking into the consideration of strong magnetic effects at LHC and RHIC. The finite quark mass depends on both chemical potential μ and temperature T. We extensively use this quark mass as [41–45]:

$$m_q^2(T,\mu) = \gamma_q \frac{N}{\ln(1+\frac{k^2}{\Lambda^2})}\left(T^2+\frac{\mu^2}{\pi^2}\right) \tag{1}$$

Here μ is the chemical potential, and we set our calculations for both zero and nonzero values of chemical potential. The other parameters involved in given Eq. 1 are well defined in Ref. [38, 39, 41].

3 Free Energy Evolution of Quark–Gluon Plasma

The calculation of free energy based on quark's and gluon's density of state are defined by many authors [46–48]. In this work, free energy is again modified using earlier work [41] in the environment of huge magnetic field. We define free energy for quarks, F_q with finite quark mass and in the strong magnetic field environment. It is defined as:

$$F_q = \mp T g_q \int \mathrm{d}k\rho(k)\ln(1\pm \mathrm{e}^{-(E-\mu)/T}) \,, \tag{2}$$

Here, $\rho(k)$ is quark's density of states. Similarly, gluon's free energy, F_g is referred as [41]. Rest parameters can be used from Ref. [41]. The pions free energy and interface energy are specified in Ref. [35, 41].

Since we believe that a constant magnetic field produced at RHIC and LHC along z-axis, the energy eigen value is used as [49, 50]:

$$E = \left[k^2 + m_q^2 + eB(2n+s+1)\right]^{1/2} \,, \tag{3}$$

We refer [50, 51] for specifying the parameters related to above equation. Finally, we use the single particle energy eigen value as:

$$E = \left[k^2 + m_q^2 + 2B\right]^{1/2}, \tag{4}$$

Now total free energy F_{total} is calculated involving free energy term for quark, gluon, pion, and interface term in the environment of huge magnetic field, and it is specified as,

$$F_{\text{total}} = F_q + F_{\text{gluon}} + F_\pi + F_{\text{interface}}. \tag{5}$$

Above Eq. 5 is the total free energy of QGP which is very much advantageous to express the dynamic of QGP in the presence of magnetic field considering the zero and finite value of chemical potential.

4 Results

The results are presented for free energy evolution in a strong magnetic field environment. At RHIC and LHC, these huge magnetic effects are quite remarkable owing to the fact that the free energy evolution are applicable in non-central collisions of heavy ion. This model furnish a meaningful role in order to observe QGP droplet formation and also help to predict the nature of phase transition. Results are as follows:

In Fig. 1, the total free energy versus droplet radius is shown for various range of temperature, i.e., $T = 150 - 250$ MeV at fix value of magnetic field $B = 0.2$ GeV^2 for zero chemical potential. We found that the size of QGP droplet enhanced much as compared to our earlier reports [35, 38, 41]. The large barrier height of droplets and smooth cut at the phase boundary indicate very strong stability of QGP droplet. On critical observation, a stable QGP droplet appeared around 10.3 fm in the presence of magnetic field, while in earlier work, it is around 9 fm with the lack of magnetic effects [35, 38, 41]. In these results, the parametrization factors also play an important role in the formation of QGP droplet. The choice of these parameters are well taken into the account to form finite size of QGP droplet. With the suitable choice of parameters, we have a realistic picture of stable QGP droplet represented by bunching of curves as shown by arrowhead. This indicate that our model results are improved and enhanced in the presence of magnetic field. Therefore, we can not ignore the effects of magnetic field produced in these experiments, and thus, these effects are useful to deal with the properties of QGP.

In Fig. 2, although we found almost the same pattern as in Fig. 1, here we observe that the barrier height and QGP droplet size goes on decreasing with increasing temperature at $B = 0.2$ GeV^2 on introducing the chemical potential $\mu = 50$ MeV. By introducing the chemical potential value, overall energy of the system changes that affect the size of QGP droplet and also suppressed the barrier height. It is very

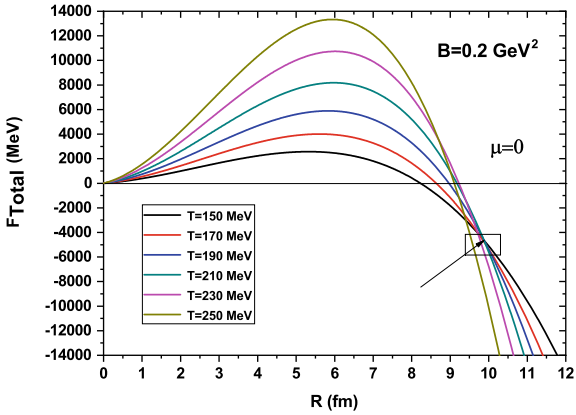

Fig. 1 Free energy with respect to size of droplets is shown by varying temperature at $B = 0.2$ GeV^2 and $\mu = 0$ MeV

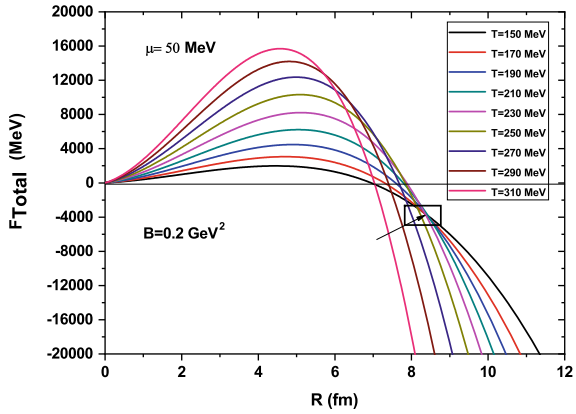

Fig. 2 Free energy with respect to size of droplets is shown by varying temperature at $B = 0.2$ GeV^2 and $\mu = 50$ MeV

difficult to propose the exact reason behind this behavior. Future experiments may give some clue to understand this issue.

Further in Fig. 3, we supply the chemical potential $\mu = 100$ MeV at same value of magnetic field $B = 0.2$ GeV^2, this again reduce the size as well as barrier height of QGP droplet. It means that the size as well as barrier height of QGP droplet decreases as we increase the chemical potential for same range of temperature. It is interesting to see the behavior of QGP droplet formation by considering magnetic field with and without chemical potential. This information provides an opportunity to explore the QCD phase diagram and also suggest about the order of phase transition.

The overall model results with finite quark mass by considering magnetic field indicate that there is a first-order phase transition at zero chemical potential and a weak first-order phase transition suggest at finite value of chemical potential although it is still uncertain to forecast the nature of phase transition. The current results suggested that transition is of first order.

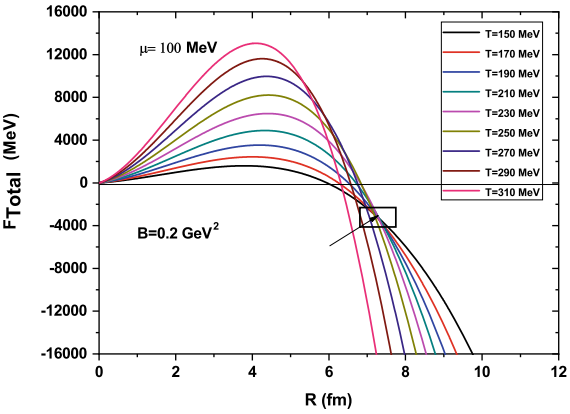

Fig. 3 Free energy with respect to size of droplets is shown by varying temperature at $B = 0.2$ GeV^2 and $\mu = 100$ MeV

5 Conclusion

We conclude that the finite quark mass value with strong magnetic fields affect the free energy evolution of QGP. A stable and enhanced QGP droplet produced successfully in a strong magnetic field environment with suitable parametrization factors. Finally, the results are useful in order to describe the QCD phase diagram. A quasi-particle model shows an improved results with the effect of magnetic field and agrees well with the experimental results in order to predict the order of phase transition. Our results are enhanced as compared to earlier results. Overall results are treated as an important signature of quark–gluon plasma.

References

1. Grasso D, Rubinstein HR (2001) Phys Rept 348:163
2. Duncan RC, Thompson C (1992) Astrophys J 392:L9
3. Bordbar GH, Peyvand A (2011) Res Astron Astrophys 11:851
4. Bordbar GH, Poostforush A, Zamani A (2011) Astrophys 54:309
5. Chakrabarty S, Bandyopadhyay D, Pal S (1997) Phys Rev Lett 78:2898
6. Kharzeev D, Landsteiner K, Schmitt A, Yee HU (2013) Lect Notes Phys 871:1
7. Guo X, Liao J, Wang E (2020) Sci Rep 10:2196
8. Gursoy U, Kharzeev D, Rajagopal K (2014) Nucl Phys A 931:986
9. Tuchin K (2013) Adv High E Phys 2013:490495
10. Fraga ES, Mizher AJ (2008) Phys Rev D 78:025016
11. Mizher AJ, Fraga ES (2009) Nucl Phys A 831:91
12. Kharzeev DE, Warringa HJ (2009) Phys Rev D 80:034028
13. Mizher AJ, Chernodub MN, Fraga ES (2010) Phys Rev D 82:105016
14. Skokov V, Illarionov AY, Toneev V (2009) Int J Mod Phys A 24:5925
15. Bali GS et al (2012) J. High E Phys 02:044
16. Agasian NO, Fedorov SM (2008) Phys Lett B 663:445
17. Endrodi G (2015) J High E Phys 07:173
18. Ayala A, Loewe M, Zamora R (2015) Phys Rev D 91:016002

19. Ayala A, Dominguez CA, Hernandez LA, Loewe M, Zamora R (2015) Phys Rev D 92:096011
20. Ayala A, Loewe M, Zamora R (2016) J Phys Conf Ser 720:012026
21. Mardor I, Svetitsky B (1991) Phys Rev D 44:878
22. Shuryak EV (1980) Phys Rep 61:71
23. Cleymans J, Gavai RV, Suhonen E (1986) Phys Rep 130:217
24. Gangopadhyay MR, Mathews GJ, Olson JP (2020) J Phys Commun 4:025004
25. Peshier A, Kampfer B, Pavlenko OP, Soff G (1994) Phys Lett B 337:235
26. Peshier A, Kampfer B, Pavlenko OP, Soff G (1996) Phys Rev D 54:2399
27. Prasanth JP, Koothottil S, Bannur VM (2020) Phys A 558:124921
28. Udayanandan KM, Sethumadhavan P, Bannur VM (2007) Phys Rev C 76:044908
29. Nilima I, Agotiya VK (2018) Adv High E Phys 2018:8965413
30. Shukla P, Mohanty AK (2001) Phys Rev C 64:054910
31. Csernai LP, Kapusta JI, Osnes E (2003) Phys Rev D 67:045003
32. Aoki Y, Endrodi G, Fodor Z, Katz SD, Szabo KK (2006) Nature 443:675
33. Ejiri S (2008) Phys Rev D 78:074507
34. Bowman ES, Kapusta JI (2009) Phys Rev C 79:015202
35. Ramanathan R, Gupta KK, Jha AK, Singh SS (2007) Pram J Phys 68:757
36. Tawfik A, Harko T, arXiv: 1108.5697v2
37. Bannur VM (2007) Eur Phys J C 50:629
38. Kumar Y, Singh SS (2013) ISRN High E Phys 156747
39. Kumar Y, Singh SS (2012) Can J Phys 90:955
40. Jain P, Kumar Y (2014) J Mod Phys 5:686
41. Kumar Y (2016) J Phys Conf Ser 668:012110
42. Kumar Y, Goel A, Jain P (2015) J Phys Conf Ser 636:012018
43. Kumar Y (2014), POS: Conf Proc 071
44. Kumar Y, Jain P (2015) Int J Mod Phys A 30(33):1550196
45. Sethy PK, Kumar Y, Singh SS (2020) J Sci Res 12(2):215
46. Neergaad G, Madsen J (1999) Phys Rev D 60:05404
47. Christiansen MB, Madsen J (1997) J Phys G 23:2039
48. Elze HT, Greiner W (1986) Phys Lett B 179:385
49. Landau LD, Lifshitz EM (1965) Statistical mechanics. Pergamon Press, New York
50. Endrodi G (2013) J High E Phys. 04:023
51. Kumar Y (2019) JPS Conf Proc 26:024028

Nitrides as Alternative Materials for Plasmonics

Hira Joshi

Abstract Noble metal-based nanostructures exhibit plasmonic resonance in the visible region. Search is for plasmonic materials active in other regions of electromagnetic spectrum. Alternative materials such as nitrides, carbides and semiconductors play an important role in nanophotonics as optical properties in these materials can be tuned to study plasmonic response. Also alternative materials to noble metals should have multiple properties like low optical losses, thermal and chemical stability, cost effective, easy to fabricate and also must have CMOS compatibility. Alternative materials such as transition metal nitrides fulfil these conditions up to a certain extent. In this work, optical properties of nitrides as alternative materials to noble metals are studied theoretically and compared with noble metals such as Au and Ag. Nitrides are having real part of permittivity less negative as compared to noble metals and both real and imaginary parts are extending up to infrared region. It is shown by comparison that nitrides such as TiN and ZrN are having absorption spectrum extending up to infrared region thereby making them suitable materials in the construction of devices. TiN and ZrN nanostructures show their potential for plasmonic performance in a wider spectral range than those made of Au or Ag and can act as next-generation materials for refractory plasmonics.

Keywords Plasmonics · Nitrides · TiN · ZrN

1 Introduction

Plasmonics is study of light interaction at nanoscale and has wide range of applications as in bio and chemical sensing [1], SERS [2], photovoltaics [3, 4], optical storage of information [5] and in nanoantenna [6]. Plasmonic materials are chosen according to their performance in localised surface plasmons resonance (LSPR) in different regions. Gold and silver are the most popular materials used for plasmonics [7] in visible range but due to certain drawbacks of these noble metals such as optical

H. Joshi (✉)
Department of Physics, Gargi College, University of Delhi, Delhi, India

S. B. Krupanidhi et al. (eds.), *Advanced Functional Materials and Devices*, Springer Proceedings in Materials 14, https://doi.org/10.1007/978-981-16-5971-3_18

loss and integration challenge, unable to cover entire range of electromagnetic spectrum. Search is for alternative materials which can overcome different losses suffered by the conventional metals in plasmonics. Nitrides are used as alternative materials as these are refractory materials, have high electron conductivity, mobility, high melting points and also CMOS compatibility. These properties make nitrides as good candidates in optical sensors, heat-assisted recording magnetic (HAMR) [8–12]. As both the imaginary part (loss) and the real part of the permittivity are critical factors to consider when developing alternative plasmonic materials, It is shown by comparing permittivities of Au, Ag, TiN and ZrN that nitrides are best plasmonics in infrared region. In this paper, optical efficiencies such as extinction coefficient of Au, Ag, TiN and ZrN are compared and suggested that both nitrides are very good alternative plasmonic materials. In near-infrared region, TiN efficiency values are larger than Au, and it can be used for bio-imaging applications [13–24].

Here, we have studied optical properties such as extinction coefficient theoretically using Mie's formalism for nitrides (TiN and ZrN) and compared with gold and silver. It is found that nitrides can be good candidates for plasmonics in NIR and visible range for plasmonics and applied devices.

2 Discussion and Conclusion

Extinction coefficient which is combination of absorption and scattering coefficient is calculated for spherical nanoparticles using Mie's formalism [25] for spherical nanoparticles in the limiting case of static state regime within the dipolar approximation. Dielectric function which plays an important role in optical response is taken from Palik [26] for TiN and ZrN but for Au and Ag from Baber [27].

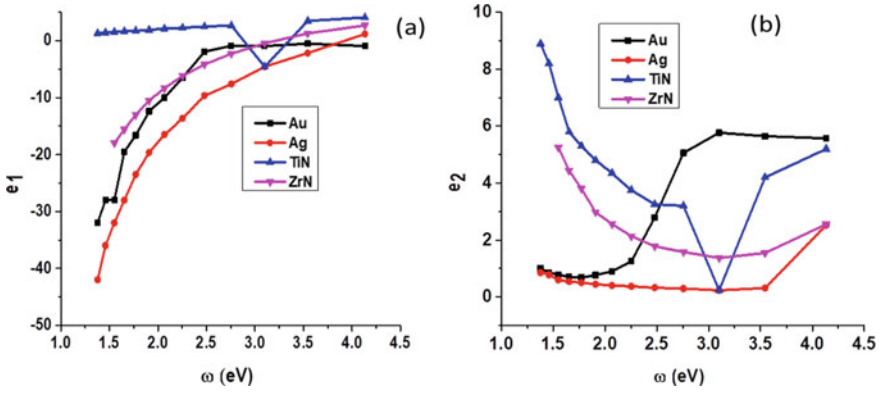

Fig. 1 **a** Variation of real part of permittivity for different materials. **b** Variation of imaginary part of permittivity for different materials

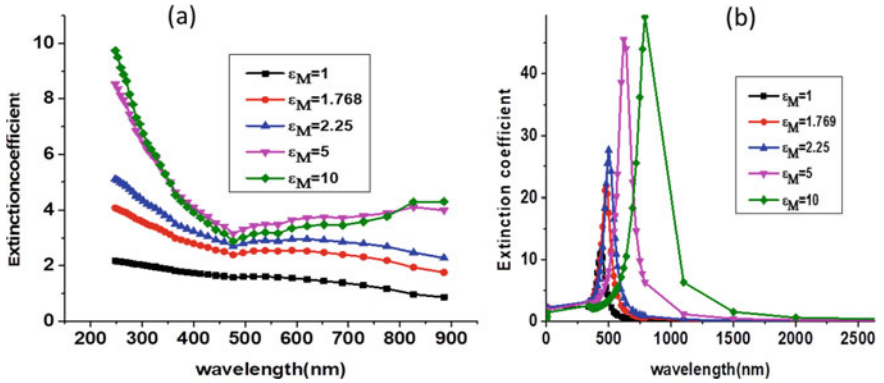

Fig. 2 **a** Variation of extinction spectrum in the presence of different external media in TiN. **b** Variation of extinction spectrum in the presence of different external media in ZrN

Figure 1 is showing comparison of real and imaginary parts of dielectric functions for Au, Ag, TiN and ZrN. Real part of dielectric function of these materials is compared in figure (a). Real part of Au and Ag is showing large negative values in the frequency less than 2.5 eV as compared to TiN and ZrN also confirming condition for plasmonic material that real part should be less negative. TiN is much better choice as compared to ZrN. Figure 1b shows comparison of imaginary part of dielectric function of Au, Ag, TiN and ZrN. It shows decrease in TiN and ZrN, having a minimum which is well defined in case of TiN.

Figure 2 is showing variation of extinction coefficient with wavelength for different external medium dielectric constant for spherical nanoparticle of size10nm in Fig (a) for TiN and Fig (b) for ZrN. In case of TiN, absorption spectrum is not so well defined as in case of ZrN. For both materials, the trend is same, i.e., resonant peak is red shifted as refractive index of external matrix is increased for a fixed size of nanoparticle. Extinction coefficient is calculated using Mie's formalism when dielectric constants are taken from Palik [26].

Fig. 3 compared extinction coefficients of Au, Ag, TiN and ZrN when dielectric constants are taken for Au, Ag [27] and TiN, ZrN [26]. Size of nanoparticle is 10 nm, and external matrix is having dielectric constant as 1.769. Resonant wavelength for Au matches with both nitrides which is 500 nm, but maximum value is higher for ZrN. Resonant wavelength for Ag is 377 nm. Extinction amplitude is maximum for Ag (10) and for ZrN (1.8). This figure shows that absorption spectrum of Au and Ag is limited up to 600 nm and 450 nm, respectively, thereby confirming the use of Au and Ag in UV–visible region only. But in TiN and ZrN, absorption spectrum is in entire range from 300 to 900 nm. From this comparison, it is clear that nitrides (TiN and ZrN) can be utilised for IR (infrared) region also and that TiN nanoparticles (NPs) can support LSPRs in the blue part of the spectrum. Therefore, it can be concluded that TiN and ZrN nanostructures show their potential for plasmonic performance in a wider spectral range than those made of Au or Ag.

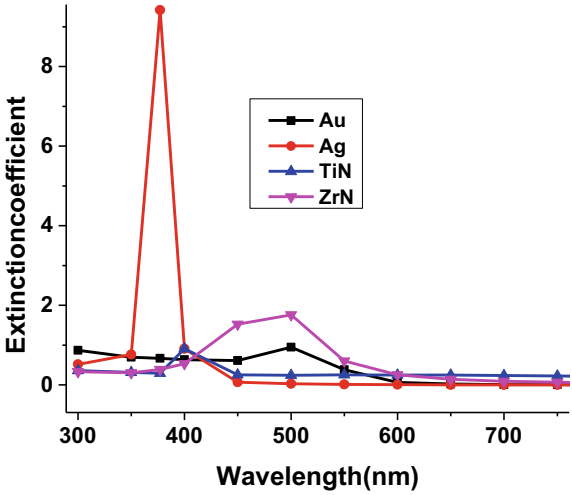

Fig. 3 Comparison of extinction spectrum of different materials when size of spherical nanoparticle is 10 nm and placed in external medium of dielectric constant 1.769

3 Conclusion

It is shown in this paper that nitrides (ZrN and TiN) can be alternative materials for plasmonics in infrared region as noble metals such as Au and Ag are not working in this region. As the real part of dielectric function in nitrides are less negative thereby making these materials suitable for plasmonics. Nitrides can be utilised in the construction of devices working in this region of spectrum. Also by increasing the concentration of nitrogen in nitrides can improve their plasmonic performance. It can be concluded that TiN and ZrN nanostructures show their potential for plasmonic performance in a wider spectral range than those made of Au or Ag. Nitrides also offer many fabrication and integration advantages over conventional materials such as gold and silver. Ceramic nanoparticles such as TiN and ZrN are also promising next-generation photonic materials.

References

1. Sturaro M, Della G et al (2016) Degenerately doped metal oxide nanocrystal as plasmonic and chemoresistive gas sensors. Acs Appl Mater Interfaces 8(44):30440–30448
2. Zhang R, Dong Y et al (2013) Chemical mapping of a single molecule by plasmon-enhanced Raman scattering. Nature 498: 82–86
3. Guo Y, Molesky S et al (2014) Thermal excitation of plasmons for nearfield thermophotovoltaics. Appl Phys Lett 105(7):073903
4. Pelayo García De Arquer, F, Mihi A, Konstantatos G (2015) Molecular interfaces for plasmonic hot electron photovoltaics. Nanoscale 7:2281–2288
5. Wan D, Chen HL, Tseng SC, Wang LA, Chen YP (2010) One-shot deep-UV–pulsed laser-induced photomodification of hollow metal nanoparticles for high density data storage on flexible substrates. ACS Nano 4:165–173

6. Hentschel M et al (2012) Quantitative modelling of third harmonic emission spectrum of plasmonic nanoantenna. Nano Lett 12(7):3778–3782
7. Derkachova A, Kolwas K (2013) Simple analytic tool for spectral control of dipole plasmon resonance frequency for gold and silver nanoparticles. Photon Lett Poland 5:69–71
8. Chernyshev AP (2009) Effect of nanoparticle size on the onset temperature of surface melting. Mater Lett 63:1525–1527
9. Losurdo M, Suvorova A, Rubanov S, Hingerl K, Brown AS (2016) Thermally stable coexistence of liquid and solid phases in gallium nanoparticles. Nat Mater 15:955–1006
10. Wu PC, Kim TH, Brown AS, Losurdo M, Bruno G, Everitt HO (2007) Real time plasmon resonance tuning of liquid nanoparticles by in situ spectroscopic ellipsometry. Appl Phys Lett 90:103119
11. Gutiérrez Y, Giangregorio MM, Brown AS, Moreno F, Losurdo M (2019) Understanding electromagnetic interaction and electron transfer in Ga nanoparticle-graphene-metal substrate sandwich systems. Appl Sci 9:4085–4090
12. Matula RA (1979) Electrical resistivity of copper, gold palladium and silver. J Phys Chem 8:1147–1298
13. Koutsokeras LE, Matenoglou GM, Patsalas P (2013) Structure, electronic properties and electron energy loss spectra of transition metal nitride films. Thin Solid Films 528:49–52
14. Naik GV, Shalev VM, Boltasseva A (2013) Alternative plasmonic materials: beyond gold and silver. Adv Mater 25(24):3284–3294
15. Boltasseva A, Atwater HA (2011) Low-loss plasmonic metamaterials. Science 331:290–291
16. Gbordzoe S, Kotoka R, Craven E, Kumar D, Wu F, Narayan J (2014) Effect of substrate temperature on the microstructural properties of titanium nitride nanowires grown by pulsed laser deposition. J Appl Phys 116:064310
17. Gutierrez Y et al (2020) Plasmonics beyond noble metals: Exploiting phase and compositional changes for manipulating plasmonic performance. J Appl Phys 128: 080901-18
18. Naik GV et al (2012) Titanium nitride as a plasmonic material for visible and near-infrared wavelengths. Opt Mater Expr 2(4):478–489
19. Guler U et al (2015) Nanoparticle plasmonics: going practical with transition metal nitrides. Mater Today 18(4):227–237
20. Parsalas et al (2018) Conductive nitrides: growth, optical and electronic properties and their perspectives in photonics and plasmonics. Mat Sci Eng R 123:1–55
21. Guler U et al (2012) Performance analysis of Nitride alternative plasmonic materials for localised surface plasmon applications. Appl Phys B 107(2):285–291
22. Boltasseva, Shalev VM (2015) All that glitters need not be gold. Science 347(6228):1308–1310
23. Patsalas P, Logothetidis S (2001) Optical, electronic, and transport properties of nanocrystalline titanium nitride thin films. J Appl Phys 90:4725–4734
24. Guo W-P et al (2019) Titanium nitride epitaxial films as plasmonic material platform: alternative to gold. ACS Photon 6(8):1848–1854
25. Mie G (1908) Ann Phys 25(3):377–445
26. Palik ED (1998) Handbook of optical constants of solids. Academic Press, San Diego
27. Baber S, Weaver JH (2015) Optical constants of Cu, Ag. Au revisited. Appl Opt 54(3):477–487

Preparation of Elemental Thin Foils for Exploring Collision-Induced Atomic Processes

Ch Vikar Ahmad, Ruchika Gupta, Kajol Chakraborty, G. R. Umapathy, and Punita Verma

Abstract Thin foils of Au, Pb and Bi of different thicknesses were prepared via physical vapor deposition to be used as targets in ion–atom collision experiments. The quality of the fabricated foils was assessed by different characterization techniques. The α-energy loss method was used to measure the thicknesses of the foils, Rutherford backscattering was used to measure both thickness and purity of the foils, and scanning electron microscopy was used to study the surface morphology of the foils. Herein, details on the fabrication techniques along with the thickness measurements and characterization results are reported. These investigations formed a crucial part of a study wherein the effect of target thickness on heavy-ion-induced X-ray production cross sections was explored.

Keywords Thin-film targets · Atomic collisions · Rutherford backscattering · X-rays

1 Introduction

X-rays are an indispensable tool for studying the ion–atom collision-induced atomic processes. The collision-induced X-ray production cross sections are influenced by various factors, such as nuclear screening and changes in the fluorescence yields. However, most of the studies performed so far have investigated the cross sections without considering the influence of target thickness, except a few [1, 2]. The cross sections reported to date have been calculated by assuming their independence from target parameters. Thus, for understanding the inner-shell vacancy processes via

C. V. Ahmad · R. Gupta · K. Chakraborty
Department of Physics and Astrophysics, University of Delhi, New Delhi, New Delhi 110007, India

C. V. Ahmad · R. Gupta · K. Chakraborty · P. Verma (✉)
Department of Physics, Kalindi College, New Delhi, New Delhi 110008, India
e-mail: punitaverma@kalindi.du.ac.in

G. R. Umapathy
Inter-University Accelerator Center, New Delhi, New Delhi 110067, India

S. B. Krupanidhi et al. (eds.), *Advanced Functional Materials and Devices*, Springer Proceedings in Materials 14, https://doi.org/10.1007/978-981-16-5971-3_19

collision-induced X-rays, it is crucial to first comprehend the effects of target thickness on the X-ray cross sections. Such studies are especially important for investigating heavy-ion–heavy-atom collisions in which both the target and projectile electrons are affected by each other's nuclear perturbations, thus influencing the emitted X-rays [3–6].

Depending on the nature of investigations, various factors need to be considered while deciding the material and thickness of the target foils to be fabricated for an ion–atom collision experiment. Among them, the following three requirements are crucial to obtain sufficiently clean data, especially in a heavy-ion–heavy-atom collision experiment: (i) Difference between the atomic number of the target (Z_1) and that of the projectile (Z_2) should be large to avoid overlapping of the emitted X-rays as both collision partners emit X-rays during the collision; (ii) the foils should not have any structural damage, such as pinholes and wrinkles; and (iii) the foils should have high stability, with good tensile strength so that they remain intact during the characterization and various stages of the ion–atom collision experiments, which are generally 3–10 days long.

2 Preparation of Thin Foils

The thin targets ($\sim$10–500 μg/cm^2) undergo radiation damage both during the characterizations and collision experiments (with heavy ions). In addition, they should have a high tensile strength so that they do not undergo damage while moving them in-between chambers for the different characterizations and finally the collision experiments (the characterization techniques, i.e., alpha particle energy loss method, Rutherford backscattering spectrometry (RBS) and scanning electron microscopy (SEM) were performed in different vacuum chambers). These factors tend to limit the stability of self-supporting thin foils, especially when the foil thicknesses are of the order of a few nanometers. Consequently, a suitable supporting material characterized by a high tensile strength, durability and small X-ray absorption coefficient is required such that the energy loss of the projectile is minimum in the supporting material, and its characteristic X-rays do not interfere with those of the collision partners during the heavy-ion–heavy-atom collision experiments. These requirements are fulfilled by C, which is used as the supporting material in most cases. It possesses good chemical stability and a very high melting point. Additionally, very thin foils of C ($\sim$5 μg/cm^2) can be easily prepared, as compared to the other elements of the periodic table, via the physical deposition processes.

In this study, thin metallic foils were fabricated by electron gun evaporation inside an ultra-high vacuum (UHV) evaporation unit at the target laboratory of Inter-University Accelerator Centre (IUAC), New Delhi [7]. The evaporation unit consists of a chamber equipped with a scroll pump for attaining a roughing vacuum of the order of $\sim 10^{-2}$ Torr, and a turbomolecular pump for attaining a base pressure of $\sim 10^{-7}$ Torr. The chamber houses a 6 kW electron gun and includes a six-pocket crucible for holding different materials (source) for the film fabrication (Fig. 1).

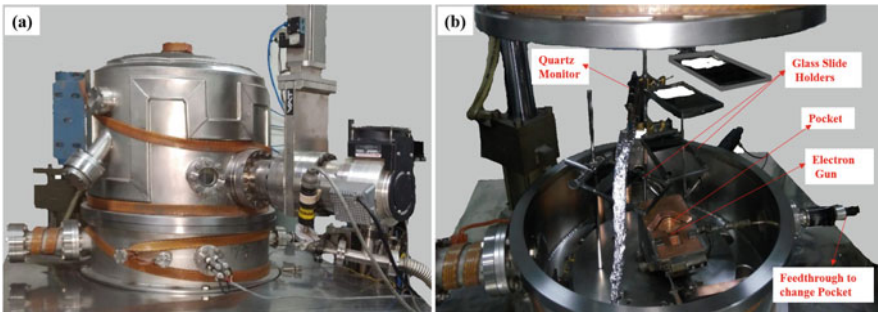

Fig. 1 **a** UHV chamber. **b** Inside the UHV deposition chamber showing the slide arrangement at different heights

The target thin foils were prepared by the following three steps:
Step I: Ultra-clean glass slides were used as the substrates. These slides were placed at the predetermined source–substrate distances. The material to be evaporated, called the source, was placed in the crucible.
Step II: Pellets of the releasing agent and backing support (C) were kept in different pockets of the crucible for evaporation. We used $BaCl_2$ as the releasing agent. The metals were used in different forms, such as in the form of shots for Pb.
Step III: Initially, the electron gun voltage was increased slowly to enable evaporation and subsequent deposition of the releasing agent on the glass substrates. Next, the voltage was further increased to facilitate C deposition followed by the deposition of the target material to a desired thickness.
The film thickness was monitored in real time by using a Au-coated quartz crystal thickness monitor installed inside the UHV chamber. For measuring the thicknesses, the crystal height was adjusted at the same source–substrate distance as that for the deposition material and glass slides. A quartz crystal works on the principle of piezoelectric effect—with increasing mass (Δm) deposition on the face of the crystal, its frequency of oscillation changes continuously, i.e.,

$$f = -\frac{{f_o}^2 \Delta m}{N \rho_q F}, \tag{1}$$

where f_o is the natural frequency of the crystal, f is the change in frequency when there is change in mass Δm, F represents the area of the crystal, N is a constant of frequency, and ρ_q is the density of the quartz crystal. The quartz crystal used in this study had a thickness measuring accuracy of 1Å.

2.1 Releasing Agent and C Backing Deposition

Thin C foils were prepared, as backing, to provide mechanical support to the elemental target foils. C foils were selected as the backing material owing to their high tensile strength and low atomic number of C, thus eliminating the possibility of

recording undesired X-rays during the collision experiment. To prepare the films, first, the deposition chamber was cleaned with ethanol; then ultra-clean glass slides (dimensions: 75 × 25 mm) were kept at a certain measured height (ideally same as the height of the quartz crystal) from the electron gun crucible. The glass slides were either coated or polished with a releasing agent to separate the deposited thin films from the glass slides. Various alkali halides are used as the releasing agents. We used $BaCl_2$ as the releasing agent because of its good thermal stability. Initially, a 38–46 $\mu g/cm^2$ thick layer of $BaCl_2$ was deposited on the slides via electron gun evaporation, followed by evaporating a 15–20 $\mu g/cm^2$ C layer over it. The deposition rate was maintained at approximately 0.1 nm/s. The UHV chamber was then cooled for 5 h prior to venting to remove the *C*-coated slides.

These *C*-coated slides were then annealed under a constant inert gas flow (Ar) environment for ∼1 h to improve the durability and surface homogeneity of the fabricated films [8].

2.2 Thin-Film Deposition of Elemental Targets

The annealed *C*-coated glass slides were again mounted on the slide holders at various heights from the electron gun crucible inside the UHV chamber to achieve simultaneous deposition of multiple thicknesses of the same material in a single deposition. The amount of material deposited on different slides placed at different heights from the source was monitored with a quartz crystal monitor by considering the rate of evaporation to be uniformly constant throughout the chamber [9]. Thus, the amount of material deposited at two heights r_1 and r_2 from the source on the two slides is related as follows:

$$4\pi {r_1}^2 t_1 \rho = 4\pi {r_2}^2 t_2 \rho \tag{2}$$

where t_1 and t_2 are the thicknesses deposited on the slides at r_1 and r_2, respectively; and ρ is density of the material being deposited. The simplified Eq. (2) is written as follows:

$$\frac{t_1}{t_2} = \left(\frac{r_2}{r_1}\right)^2 \tag{3}$$

Equation 3 was used to extract the thicknesses of the films deposited at different heights with respect to the height at which the quartz crystal was installed inside the UHV chamber. The thickness of the films deposited on the slides mounted at a height that is same that of the quartz monitor was easily obtained. As this thickness was known, the thickness of films deposited on the other slides that were placed at different heights from the crucible could be calculated using Eq. (3). The current supply to the electron gun was increased in small steps by carefully monitoring the pressure inside the chamber and rate of deposition of material. The rate of deposition was kept constant ∼0.1nm/s until the desired thickness was achieved. The current

Table 1 Summary of different target thicknesses prepared

Target	Density (ρ) (g/cm^3)	Thickness (μg/cm^2)			C backing
		Quartz	α particle	RBS	
Au_1	1.93×10^1	120	–	135	No
Au_2	1.93×10^1	360	510	508	No
Pb_1	1.13×10^1	35	295	107	Yes
Pb_2	1.13×10^1	150	400	157	Yes
Pb_3	1.13×10^1	340	694	391	Yes
Bi_1	9.80×10^0	120	257	122	Yes
Bi_2	9.80×10^0	293	543	314	Yes
Bi_3	9.80×10^0	431	637	391	Yes

supply was then switched off, and the chamber was cooled for 4–5 h before venting it to remove the thin-film deposited slides.

Next, with the help of scale and graphite cutter, a mark was made in the middle of each thin-film deposited glass slide along its length and three marks at equal distances along its width. The glass slide was then very slowly immersed into warm deionised water in a water bath by dipping it at an angle of $\approx 45°$ with respect to the water surface. The warm deionised water quickly dissolves the releasing agent, and small strips of thin foils (dimension: 12.5×16 mm as marked by the diamond cutter) separate from the slide and start floating on the water surface. Next, specially designed stainless target holders (dimension: 20×25 mm), with a central circular aperture of radius 5 mm, were slowly dipped into the water bath, placed below the floating foils and then carefully picked up. In this process, the thin foils become attached on the holders due to surface tension. These holders with attached foils form the targets for collision experiments. These targets were then stored in vacuum desiccators. Various types of the targets fabricated are summarized in Table 1.

3 Characterization Results and Discussion

Measurement of absolute X-ray cross sections during ion–atom collision studies requires pure elemental targets with minimum contamination because the latter affects the results adversely. Thus, all the fabricated targets were characterized by different techniques, as mentioned below, and the results were compared with each other.

Initially, the thicknesses of the thin foils were confirmed by measuring the energy loss of 5.54 MeV α particles, emitted by ^{241}Am, which is a radioactive source, through the foils. The alpha particle energy loss measurement setup consists of a vacuum chamber with a horizontal movable target ladder, which can accommodate four targets at a time with one blank space. The emitted α particles were allowed to

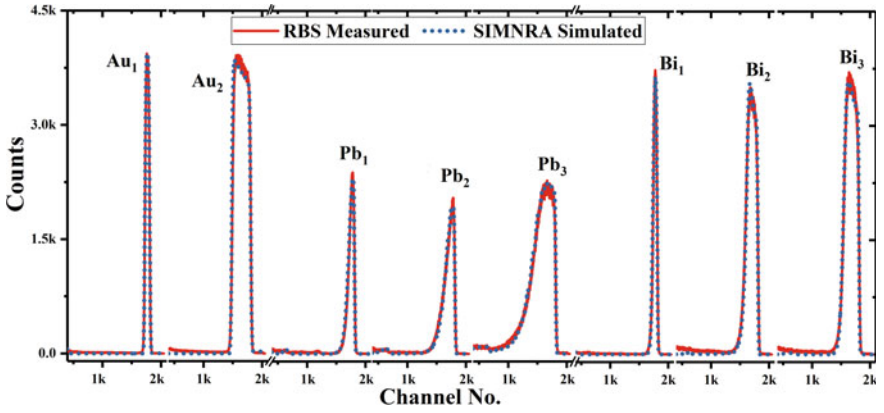

Fig. 2 RBS plot for F different thicknesses of Au (Au_1 and Au_2), Pb (Pb_1, Pb_2 and Pb_3) and Bi (Bi_1, Bi_2 and Bi_3) along with SIMNRA simulation

pass through the blank space first, followed by the foils individually and were detected by a surface barrier detector (SBD) kept at 0° with respect to the source. The alpha particles, impinging on the foils, loose some of their energy and are subsequently detected by the SBD, thereby yielding a particle spectrum. The difference between the channel numbers of the peak corresponding to the blank space and that of the individual foils is converted to the energy loss of the α particles following a simple procedure. In this procedure, this difference in channel numbers is compared with the calculated amount of energy lost by the incident particle per cm of the target thickness. The amount of energy lost by the incident particle per cm of the target thickness is calculated by using the stopping range of ions in matter (SRIM) software [10], thereby yielding the thicknesses of the foils.

As can be seen from Table 1, the thicknesses measured by the α particle energy loss method do not show good agreement with those obtained from the quartz monitor. Thus, RBS was employed to further investigate this discrepancy. No contamination of other elements were found in the Au_1 and Au_2 foils; additionally, the foil thicknesses measured by the α particle energy loss method are similar to those obtained from the RBS. In contrast, the Pb_3 foils were found to have some O content. As the α particle energy loss method does not account for the oxide density and accurate C layer thickness, RBS is a more reliable method because it provides information about the thickness as well as composition of the foils. For accurate measurement of the thickness and elemental composition of the fabricated thin foils, we performed RBS analysis of the foils using the 5SDH-2 tandem accelerator in the RBS laboratory of the IUAC [11]. In this setup, the foils were bombarded by a 2 MeV $^4He^{2}+$ beam inside a vacuum chamber, and the backscattered particles are detected by a silicon SSBD, mounted inside the chamber at an angle of 160° with respect to the beam direction.

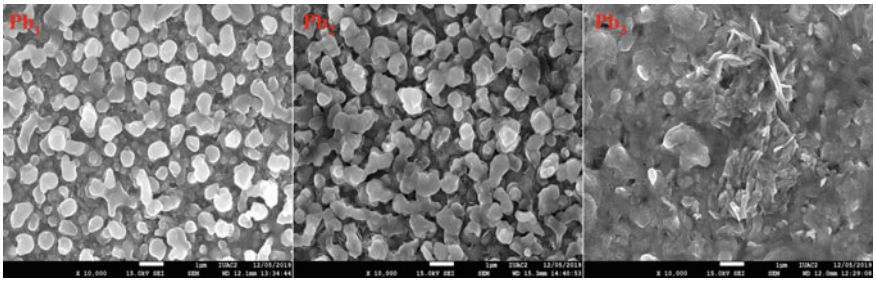

Fig. 3 SEM images for different thicknesses of the Pb foils (Pb_1, Pb_2, and Pb_3) corresponding to RBS plots in Fig. 2

The obtained data reduction was carried out using RUMP [12] and SIMNRA [13] software, which provide the composition and thickness of the foils. The fitted RBS spectra of the different foils are shown in Fig. 2. The resulting thicknesses of the different foils are tabulated in the fifth column of Table 1. In the RBS spectrum of the Pb_3 foil, the observed extended tail of the peak in the low-energy region was further examined using field emission scanning electron microscopy (FE-SEM). As evident from Fig. 3, the surface morphology of the Pb foils appears rough and semiporous in nature. The surface roughness values were included into the RBS simulations to obtain results that match the experimentally obtained spectra.

From the SEM images in Fig. 3, the grain size in Pb_1 is observed to be $\sim$1 μm, and the grain distribution is uniform. The Pb_2 foil has an overlying grain size 1.5–2 μm with non-uniform grain distribution. The Pb_3 foil is very thick and has large clusters; consequently, the corresponding RBS spectra are expected to be very rough. Similarly, the Bi foils having oxidation tendency were found to have O content on the surface of foils. These factors can explain the mismatch between the thicknesses measured by the α particle energy loss method and those by the RBS method.

The differences in the Pb foil thicknesses measured by the three techniques can be explained by the following reasons: (1) Oxidation changes the foil density; (2) the foils had *C* backing layer, whose accurate thickness was not known and (3) surface roughness. As described before, the foils were deposited by the current-controlled electron gun evaporation method. Thus, there is a definite probability that the local melt temperature may be low at the lower thicknesses ($<$100μ g/cm^2) and too high above 500 μg/cm^2 so that the deposition is more in this case. This is the reason for the observed differences between the thicknesses measured by the quartz monitor and those measured by the other two technique. For the thicknesses in the range of 100–500 μg/cm^2, both quartz crystal and RBS show similar results.

Contrarily, the RBS technique gives accurate thickness and information on the elemental composition of the foils. The SEM images complement the RBS spectra and help us to obtain a better understanding of the RBS spectra. Based on both the SEM images and RBS spectra of the foils, we can state that the energy loss of a penetrating charged particle ($^4He^2+$ in case of RBS and electrons in case of SEM) in clustered grains or porous materials may occur due to plural or multiple scattering of the traversing particle with more straggling and variations.

4 Conclusion

Pure and stable thin metallic foils of Au, Pb and Bi metals were successfully fabricated using the ultra-high vacuum evaporation technique. This technique was found to be an efficient foil fabrication method for foils having thicknesses in the range of 20–500 $\mu g/cm^2$. Among the various applied characterization techniques (i.e., α particle energy loss method, RBS and SEM), RBS yielded accurate thickness and information on the elemental composition of the foils. Thus, RBS is a highly effective ion beam-based tool to monitor foil thickness and determine its elemental composition. The quality of the data obtained in the ion-induced collision experiments validated the purity of these foils and affirmed the importance of using pure and uniform thin foils in such experiments.

Acknowledgements One of the authors (C. V. Ahmad) acknowledges the Ministry of Tribal Affairs, Govt. of India, for providing financial assistance in the form of National Fellowship for Tribal Students. The authors duly acknowledge the target laboratory, RBS laboratory, data support laboratory and LEIB facility of IUAC for their support. The SEM characterization was performed at the FE-SEM facility (IUAC), established under a geochronology project [MoES/P.O.(Seismic)8(09)-Geochron/2012] funded by the Govt. of India.

References

1. Brandt W et al (1973) Phys Rev Lett 30(9):358–361
2. Verma P et al (2005) Nucl Instrum Methods Phys Res B 235(1–4):309–314
3. Burgdörfer J (1992) Nucl Instrum Methods Phys Res B 67(1–4):1–10
4. Verma P et al (2006) Nucl Instrum Methods Phys Res B 245(1):56–60
5. Verma P et al (2006) Radiat Phys Chem 75(11):2014–2018
6. Verma P et al (2017) J Phys Conf Ser 875(10):092029
7. https://www.iuac.res.in/index.php/target-lab
8. Jaklovsky J (2013) Springer Science & Business Media
9. Holland L, Steckelmacher W (1952) Vacuum 2(4):346–364
10. Ziegler JF et al (2010) Nucl Instrum Methods Phys Res B 268(11–12):1818–1823
11. Umapathy GR (2016) DAE-BRNS symposium, 1038
12. Doolite LR (1985) Nucl Instrum Methods Phys Res B 344
13. Mayer M (1999) AIP Conf Proc 475:541–544

Insight into Structural and Electrical Properties of Potassium and Lithium Substituted Non-stoichiometric Sodium Bismuth Titanate ($Na_{0.54}Bi_{0.46}TiO_{3-\delta}$)

Pragati Singh, Raghvendra Pandey, and Prabhakar Singh

Abstract Sodium bismuth titanate ($Na_{0.5}Bi_{0.5}TiO_3$) has been reported as a fast oxide ion conductor. Sodium rich non-stoichiometric $Na_{0.54}Bi_{0.46}TiO_{3-\delta}$ has also been reported to have good oxide ion conductivity. Here, we report the influence of Potassium (K) and Lithium (Li) doping on the *A*-site (i.e. Na site) of the $Na_{0.54}Bi_{0.46}TiO_{3-\delta}$ system. XRD results revealed the formation of perovskite rhombohedral phase having R3c space group. SEM study showed the existence of dense morphology in the sintered samples. TGA technique is performed to estimate the oxygen deficiency in the investigated system. Impedance results suggested an increase in the bulk conductivity by doping of potassium; however, a decrease in the conductivity was observed for Li-doping on *A*-site. A correlation between the structural and electrical properties have been established to explain the conductivity behaviour. Further, three-dimensional oxide ion diffusion mechanism was also studied using the bond valance energy (BVE) technique.

Keywords NBT · Impedance spectroscopy · Conductivity · SOFCs · Oxide ion migration

1 Introduction

Solid oxide fuel cells (SOFCs) are electrochemical energy conversion devices that produce electricity through the oxidation of fuel. It consists solid electrolyte material as one of the components, which should be fast oxygen ion conductor. The research is going on to increase the conductivity of oxygen ion conductors at the reduced operating temperature. Various electrolyte materials such as Yttria stabilized ZrO_2

P. Singh · P. Singh (✉)
Department of Physics, Indian Institute of Technology (BHU) Varanasi, Varanasi 221005, India
e-mail: psingh.app@iitbhu.ac.in

R. Pandey (✉)
Department of Physics, ARSD College, University of Delhi, New Delhi 110021, India
e-mail: raghvendra@arsd.du.ac.in

S. B. Krupanidhi et al. (eds.), *Advanced Functional Materials and Devices*, Springer Proceedings in Materials 14, https://doi.org/10.1007/978-981-16-5971-3_20

(YSZ), Sm doped CeO_2 (SDC), Sr-and Mg-doped $LaGaO_3$ (LSGM), doped molybdate (LAMOX), Apatite structured electrolytes possess high oxygen ion conductivity of the order of ~9.74×10^{-4} S/cm, 2.5×10^{-4} S/cm, 0.03 S/cm, 0.06 S/cm and 0.01 S/cm, respectively in the intermediate temperature (IT-SOFC) range, i.e., 550–700 °C [1]. Sodium bismuth titanate ($Na_{0.5}Bi_{0.5}TiO_3$; hereafter abbreviated as NBT), a well-known ferroelectric material [2], simultaneously attracted research community as one of the oxide ion conductors for SOFC applications [3, 4]. It has a very good oxide ion conductivity with transference number $t_{ion} > 0.9$. The research community still argues with the structure of NBT at room temperature, whether it has rhombohedral (R3c) or monoclinic structure (Cc) [5]. However, in the temperature regime of IT-SOFC, i.e., 550–700 °C, the NBT switches to a non-ferroelectric—cubic structure, which is the more preferable structure for solid electrolytes [5]. Interestingly, the sample should be highly dense for both ferroelectric and electrolyte applications. Thus at the microstructure level, both applications require the similar feature. However, for SOFC-electrolyte materials, the sample should be a good ionic conductor. This fact is contrary to the choice of ferroelectric materials.

In electrolyte materials for SOFCs, oxide ion conduction occurred through ion-conducting channels formation [6]. These ion channels can be predicted theoretically and experimentally [6]. According to Li et al., even a low level of *A*-site nonstoichiometry (<1%) in NBT imparts a change in the conductivity, with more than 3 order of magnitude than that of the bulk conductivity. It has been reported that NBT with Na/Bi ratio > 1 are conducting in nature with activation energy ~0.44 eV, and compositions with Na/Bi ratio < 1 are insulating in nature with high activation energy ~1.6 eV [7–9]. The oxide ion conductivity has been found to be further enhanced via Bi deficiency and Mg-doping at the B site, which is ascribed to the oxygen vacancy concentration, weak Bi-O bond strength and highly polarizable Bi^{+3} cation [3]. The oxide ion conductivity in NBT occurs through the migration of ions along the edges of TiO_6 octahedra. During the migration, oxygen ions pass through the critical triangle defined by two *A*-site and one *B*-site cations. Several attempts have been made to explain the origin of high conductivity, phase formation and anion migration using the first principle DFT calculation. This study also suggests that the energy barrier is also dependent on cation properties. Therefore, an appropriate dopant is required to lower the migration energy barrier for the fast movement or diffusion of oxide ions. In earlier studies, several dopants such as Fe^{+3}, Mg^{+2} on *B*-site, Li^{+1}, Ca^{+2}, Sr^{+2} and Ba^{+2} on *A*-site and influence of excess sodium on NBT system has been investigated [8–12]. Experimentally highest enhancement in the ionic conductivity was observed for the Mg-dopant. The enhancement in the conductivity was by half order of magnitude. However, the solubility limit of Mg^{+2} on the Ti site is very low. He et *al*. have predicted that replacing 4% of K^+ on Bi-site leads to higher conductivity than Mg-doped composition, and this enhancement is attributed to the disordered A site lattice [12]. Theoretical *ab* initio calculations also suggest that the acceptor dopant on the *B*-site increases the oxygen migration barrier by binding with the oxygen vacancies. These studies also suggest that the acceptor doping on the *A*-site of the NBT is probably more effective method to hold down the binding with the

oxygen vacancies, which results in enhancement of ionic conductivity. The disordered A site lattice acquires different local atomistic configuration to accommodate the electrostatic and strain field of the dopants, which improves the phase stability and undesirable binding with the B site atom. Recently Rahul et *al.* have reported that among all the studied dopants, excess sodium, $Na_{0.54}Bi_{0.46}TiO_{3-\delta,}$ is found to be the most suitable dopant as it improves the conductivity almost three times than that of the $Na_{0.5}Bi_{0.49}Ti_{0.96}Mg_{0.04}O_{2.965}$ [13].

In the present study, we report the influence of K^+ and Li^+ substitution on the *A*-site of $Na_{0.54}Bi_{0.46}TiO_{3-\delta}$ in which the dopant replaces the Na^+ ion without the creation of any excess oxygen vacancies as the ionic charge is the same as the host ion. We have also studied the oxide ion migration path using the bond valance method. In addition, the chemical stability of NBT and its derivative compounds is also examined in the reducing atmosphere.

2 Experimental

Polycrystalline samples of $Na_{0.54-x}M_xBi_{0.46}TiO_{3-\delta}$ (M = K, Li and x = 0.00, 0.02, and 0.04) were synthesized by the solid-state synthesis method. Raw materials of Na_2CO_3 (99.5%, Rankem), Li_2CO_3(99%, Molychem), TiO_2 (99.8%, Alfa Aesar), Bi_2O_3 (99%, Alfa Aesar), and K_2CO_3 (98%. Merk) were weighed in stoichiometric ratio and mixed thoroughly in a mortar and pestle using acetone as mixing media. The well-mixed powders were then calcined at 820 °C for 2 h in air. The resultant powders were then mixed with 2% of Polyvinyl alcohol as a binder and compacted into pellets by applying a pressure of 5 MPa. The cylindrical pellets were then sintered for 2 h at 1050 °C in air.

The phase formation and purity of the synthesized compositions were studied using Rigaku Miniflex desktop X-ray Diffractometer (XRD) with CuK_α radiation (λ = 1.5405 Å) in the range $2\theta \sim 20–70°$. The microstructures and morphology of the samples were observed by scanning electron microscopy (EVO—Scanning Electron Microscope MA15/18). The Thermograemetric measurement of the sintered samples was done using TG-DSC (Mettler Toledo, Germany) thermal analyzer at the heating rate of 10 °C/min in nitrogen atmosphere. The band gap of the synthesized compositions was measured using JASCO V-770 spectrometer. The impedance spectroscopy was performed using Wayne Kerr LCR meter (6500 P Series) over the frequency range from 20 Hz to 1 MHz at different temperatures in the temperature range 500–700 °C at the step of 5 °C. Prior to impedance measurement, Pt paste was coated on the sample surface and fired at 700 °C for 30 min. To investigate the migration barrier, crystal distortion and oxide ion diffusion path in the crystal structure, we have done Bond valance based energy calculations using the softVB program for a test O^{2-} ion. The Rietveld refined parameters were used for the BV Calculations, and the spatial resolution was set to 0.1 Å. The samples synthesized and the acronyms are listed in the Table 1. The crystal structure and bond valence energy landscape

Table 1 Compositions with their acronyms

Composition	Acronyms
$Na_{0.54}Bi_{0.46}TiO_{3-\delta}$	N00
$Na_{0.52}K_{0.02}Bi_{0.46}TiO_{3-\delta}$	K02
$Na_{0.50}K_{0.04}Bi_{0.46}TiO_{3-\delta}$	K04
$Na_{0.52}Li_{0.02}Bi_{0.46}TiO_{3-\delta}$	L02
$Na_{0.50}Li_{0.04}Bi_{0.46}TiO_{3-\delta}$	L04

(BVEL) were drawn with the VESTA software. The migration barrier for oxide ion were determined using BE landscape.

3 Results

3.1 Structural Analysis

X-ray diffraction patterns of the investigated compositions are shown in Fig. 1. XRD profile admits the formation of rhombohedral symmetry with the ABO_3 perovskite phase in all the compositions. No any extra peaks are observed within the resolution limit of the XRD. For more structural clarification, Rietveld refinement was performed using Full Prof Suite Package. Figure 2a shows the Rietveld refinement of the samples. The R-factors and the atomic position coordinates obtained after

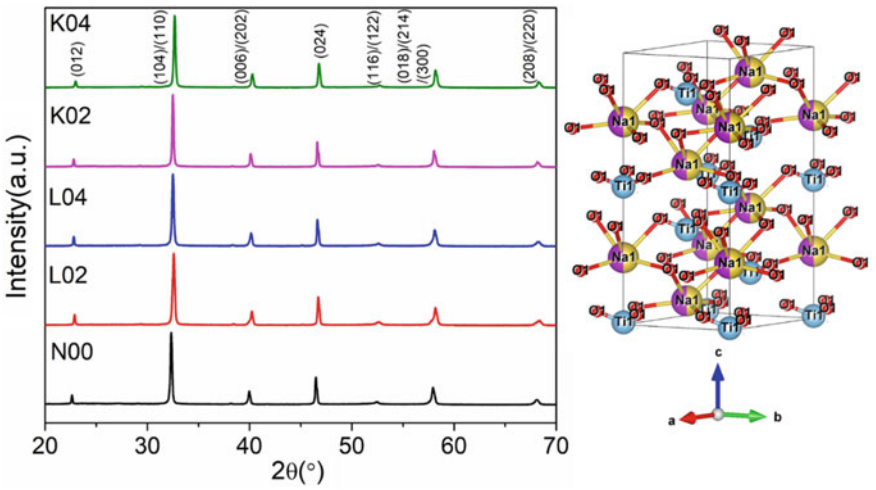

Fig. 1 (a) X-ray diffraction pattern of investigated composition (b) Representative crystal structure K/Li doped $Na_{0.54}Bi_{0.46}TiO_{3-\delta}$

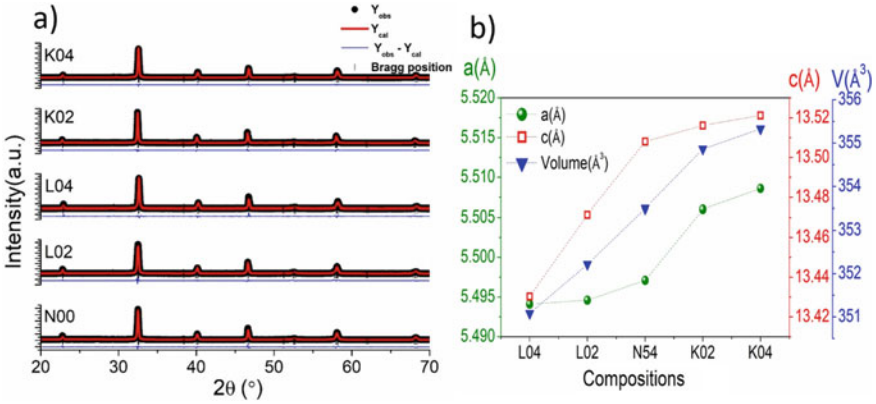

Fig. 2 **a** Rietveld refinement fit patterns of the N00, L02, L04, K02, and K04 systems. Y_{obs}, Y_{cal}, Y_{obs}, Y_{cal} and Bragg positions represent the experimentally observed intensity, calculated intensity and the difference of experimental and calculated intensities and Bragg's positions, respectively **b** Variation of lattice constant and volume as a function of composition

refinement are listed in Table 2. Figure 2b depicts the variation of the lattice parameters and volume. From this figure, it is observed that Li doped compositions have smaller cell volume, while for K doped, composition volume increases as compared to NBT. It seems to be justifiable as K cation ($r_K^{1+} = 1.38$) are large in size, and Li ($r_{Li}^{1+} = 0.76$) are small in size, as compared to the A site host Na ($r_{Na}^{1+} = 1.02$) [14].

Figure 3 depicts the tolerance factor and the free volume of the studied compositions. Usually, in the perovskite, larger volume and lower distortion favour the ionic conduction. To correlate the structure with the conduction properties, volume and tolerance factor is calculated. The degree of distortion (i.e. tolerance factor) of any perovskite structure is given by $t = \frac{r_A + r_o}{\sqrt{2}(r_B + r_o)}$ where r_o is the ionic radii of oxygen ion, r_A and r_B are the radii of cation occupying A and B site respectively. It is perceived that the tolerance factor increases linearly with the increment of K^+-content and decreases for Li^+-content. Thus the structure tends towards more symmetric (cubic) phase with K^+-doping.

Additionally, the specific free volume is also found to increase for K^+ doping and decreases for the Li^+ doping. The specific free volume V_{SF} is given by $V_{SF} = \frac{V - \sum V_{ion}}{V}$, where V is the volume of the unit cell, and $\sum V_{ion}$ is the volume of ions in the unit cell. Thus, the dopant with larger ionic radii exhibits larger tolerance factor and high free volume.

3.2 Ion Migration Study

To inspect the oxide ion conduction in the compositions, we investigated the bond valance energy landscapes (BVELs) for a test oxide ion O^{2-}. The BVE of the test

Table 2 Rietveld refinement parameters for N00, L02, L04, K02 and K04 system at room temperature

Sample	Atoms	Position			R-factor			Lattice parameters (Å)
		x	y	z	χ^2	Bragg R-factor	R_f-factor	
N00	Na	0	0	0.24663	4.64	3.77	2.92	a = b = 5.4971 c = 13.5080
	Bi	0	0	0.24663				
	Ti	0	0	0.00859				
	O	0.17267	0.26762	0.04909				
K02	Na K	0 0	0 0	0.25009 0.25009	3.34	2.27	1.91	a = b = 5.5060 c = 13.5161
	Bi	0	0	0.25009				
	Ti	0	0	0.00883				
	O	0.17121	0.27647	0.05330				
K04	Na K	0 0	0 0	0.25816 0.25816	6.60	6.15	3.88	a = b = 5.5086 c = 13.5212
	Bi	0	0	0.25816				
	Ti	0	0	0.01118				
	O	0.16997	0.27738	0.08545				
L02	Na Li	0 0	0 0	0.24624 0.24624	13.1	4.55	3.87	a = b = 5.4946 c = 13.4714
	Bi	0	0	0.24624				
	Ti	0	0	0.00945				
	O	0.16884	0.26126	0.04972				
L04	Na Li	0 0	0 0	0.24593 0.24593	8.74	2.69	1.81	a = b = 5.4941 c = 13.4303
	Bi	0	0	0.24593				
	Ti	0	0	0.01106				
	O	0.17478	0.26520	0.04904				

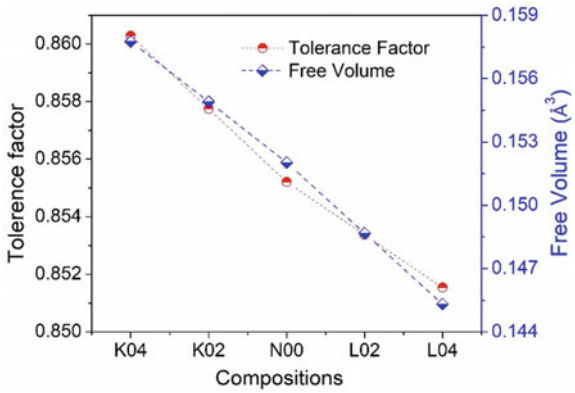

Fig. 3 Variation of tolerance factor and free volume with compositions

anion was calculated using the position coordinates and lattice parameters obtained from the Rietveld refinement. Continuous yellow iso-surface means low energy barrier for migration, and detached iso-surface represents the high energy barrier for migration [6].

The BVEs landscape for connected and extraneous iso-surface for all the studied composition projected in the b-c plane are displayed in Fig. 4a–f. The path along all the three *a, b* and *c* axis have the same migration energy. So the conduction in all the compositions was found to three dimensional. The migration energy barrier for any system is defined as the energy difference between the energy maxima and local minima [15, 16]. The migration barrier for oxide ion migration is 1.4 eV for N00 and is found to increase significantly with the K^+ and Li^+ doping. Usually, in the perovskite materials, the area of the critical triangle is decisive for the migration of the oxide ion, as the ion is assumed to migrate through the opening. The migration path follows the edges of TiO_6 octahedra via -O1-O1- pathway and through the interstices and saddle points.

The increase in the migration barrier for doped compositions suggests that the oxide ions encounter a more significant migration barrier for diffusion. The oxygen vacancies also have the tendency to be trapped by the dopant defects such as K^+ and Li^+ owing to strong electrostatic and elastic interaction, to form local defect complexes of low mobility. The electrostatic interaction is expected to be higher in the doped samples as the size mismatch between the host and dopant is more. The defect cluster creates local compressive strain within the lattice, which reduces the bottleneck size. It is previously reported using Molecular dynamics simulation and static lattice that both these parameters strongly influence the migration barrier for oxide ion in $LaGaO_3$ perovskite [17].

3.3 Microstructural Studies

SEM micrographs of the investigated compositions are depicted in Fig. 5. All the samples exhibit polycrystalline nature and dense morphology of grains with well-defined grain and grain boundary. All the samples appear to be in pure phase; however, K04 shows the formation of some rod-like structure. The average grain size (AGS) of all the compositions has been determined using *Image J* software and is depicted in the inset. AGS of all the samples lies between 0.5 and 3 μm. The average grain size increases with the smaller dopant size and decreases for the larger radii of the dopant. Along with the change in the grain size, change in morphology is also observed from hexagonal (for N00) to polygonal for Li^+ and K^+-doped samples.

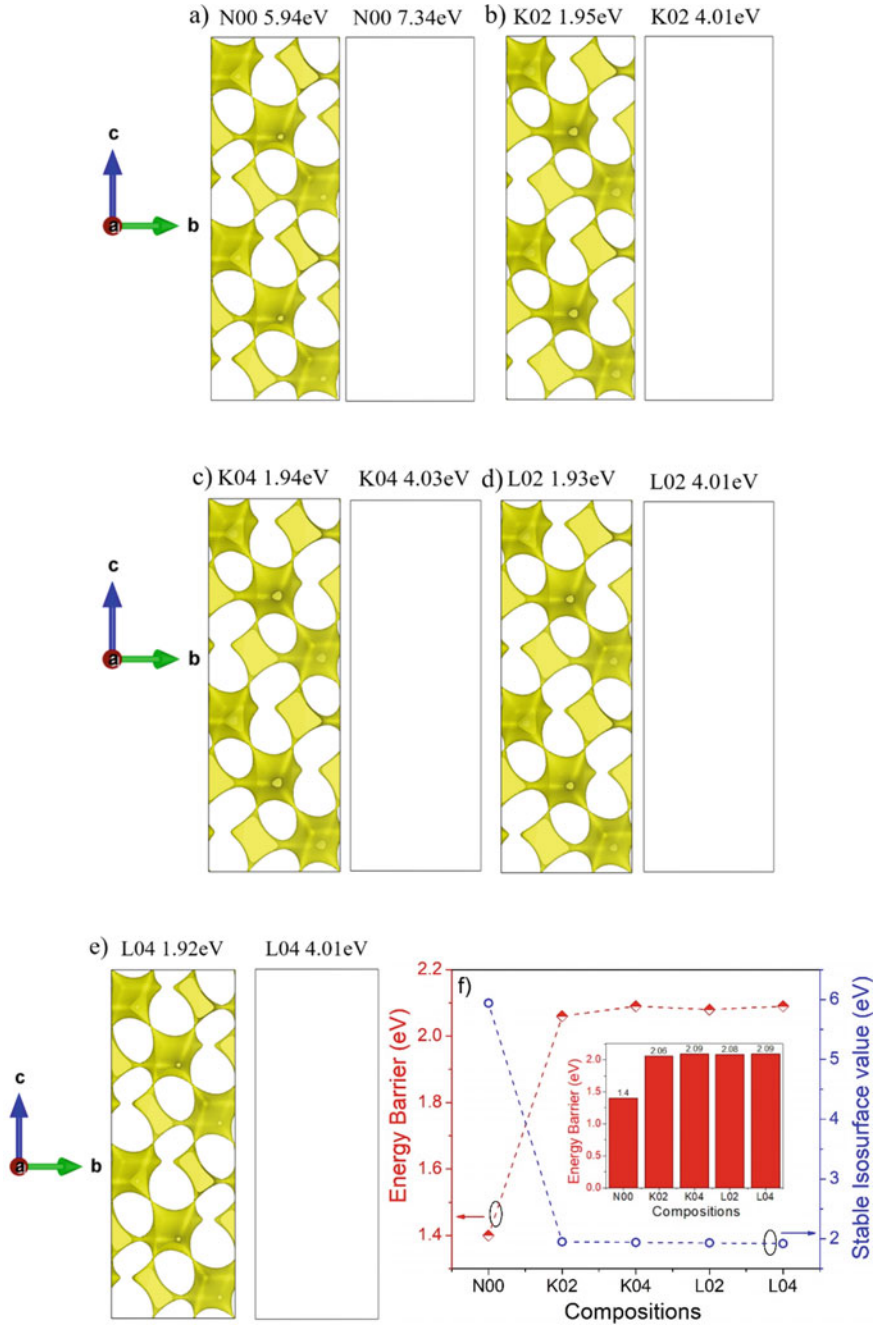

Fig. 4 **a**–**e** BVEL pathways of all the studied compositions viewed along *a*-axis. Connection of yellow surface represents the presence of possible oxide ion diffusion path and absence of iso-surface represents an energy barrier for migration. **f** Energy barrier and stable Iso-surface energy value with composition

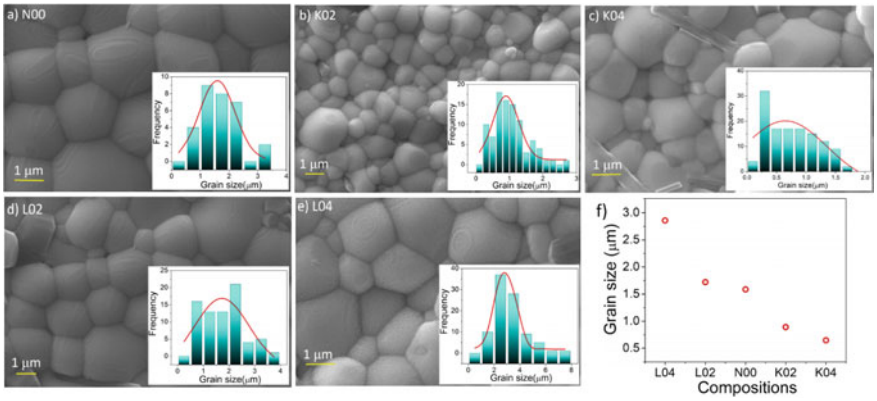

Fig. 5 **a**–**e** SEM micrographs. Inset in the figure shows the respective grain size histograms for the individual samples **f** Grain size variation of $Na_{0.54-x}M_xBi_{0.46}TiO_{3-\delta}$ (M = K, Li and x = 0.00, 0.02, and 0.04) ceramics

3.4 UV–Vis Analysis

The band gap of the investigated compositions were calculated using the Tauc's relation, as given by $\alpha hf = A(h_f\text{-}E_g)^n$. Here, h_f is the energy of the photon, α is the absorption coefficient, E_g is the band gap of the material, and n peculiarize the type of transition. Variation of Tauc's plot is shown in Fig. 6, and the estimated band gap are recorded in Table 3. The band gap of N00 is comparable to that described in the literature [18]. The band gap decreases for 2% of K^+/Li^+ doping. For instance, band gap becomes 3.038 and 3.047 for 2% K^+ and Li^+ doping, respectively. At the same time, it increases to 3.098 and 3.140 for 4% doping of K^+ and Li^+, respectively. This

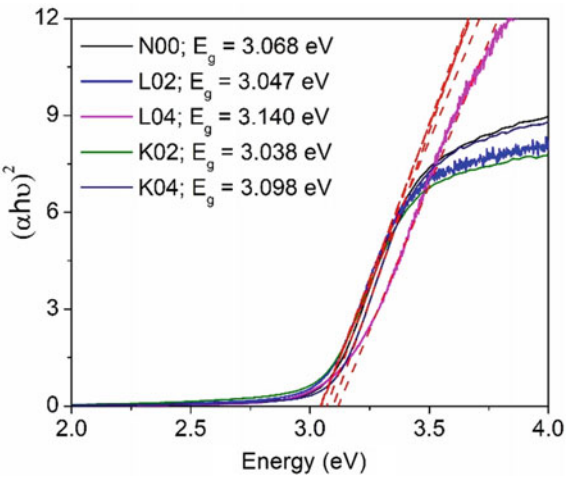

Fig. 6 Band gap estimation using Tauc's relation using UV–vis spectra

Table 3 Band gap of studied compositions

Composition	Band-gap (eV)
N00	3.068
K02	3.038
K04	3.098
L02	3.047
L04	3.140

Table 4 Oxygen deficiency evaluated from the TGA data in nitrogen atmosphere

Sample	Oxygen deficiency (δ)
N00	−0.0061
L02	−0.0057
L04	−0.0048
K04	−0.0494

increase in the band gap for 4% substitution is attributed to (i) band gap tailing [19] and (ii) Moss-Burstein effect [20, 21]. Further, the lesser value of band gap for K^+ as compared to Li^+ doping may be attributed to weaker K–O bond strength as compared to Li–O (See Table 4).

3.5 Thermogravimetric Analysis (TGA)

The TGA curves of the studied sample in Nitrogen atmospheres are shown in Fig. 7. All the samples are showing a continuous decrease in the mass with temperature, with a kink at ~100 and 300 °C. These kinks are attributed to weight loss owing to H_2O and O_2 [22]. Isovalent doping at the Na^+ site will not produce any defects, and the effect of doping is given by the following relation.

$$A_2CO_3 \xrightarrow{Na_2CO_3} 2A_{Na}(A = K, Li)$$

The deficiency (δ) is calculated in accordance with the relation given by:

$$\delta = \frac{MW}{16}\left(1 - \frac{g_{Na0.54-xMxBi0.46TiO3-\delta}}{g_{Na0.54-xMxBi0.46TiO3}}\right) = \frac{MW}{16}\left(1 - \frac{g}{g_{max}}\right)$$

where δ is anion deficiency, MW is the molecular mass of the perovskite, g is the weight of sample at corresponding temperature and g_{max} is weight at 700 °C [23]. According to the above Kroger-Vink notation, the number of oxygen vacancies should be the same for all the samples, but number of vacancies increases for potassium doping and decreases for lithium doping. The suppressed oxygen vacancies for

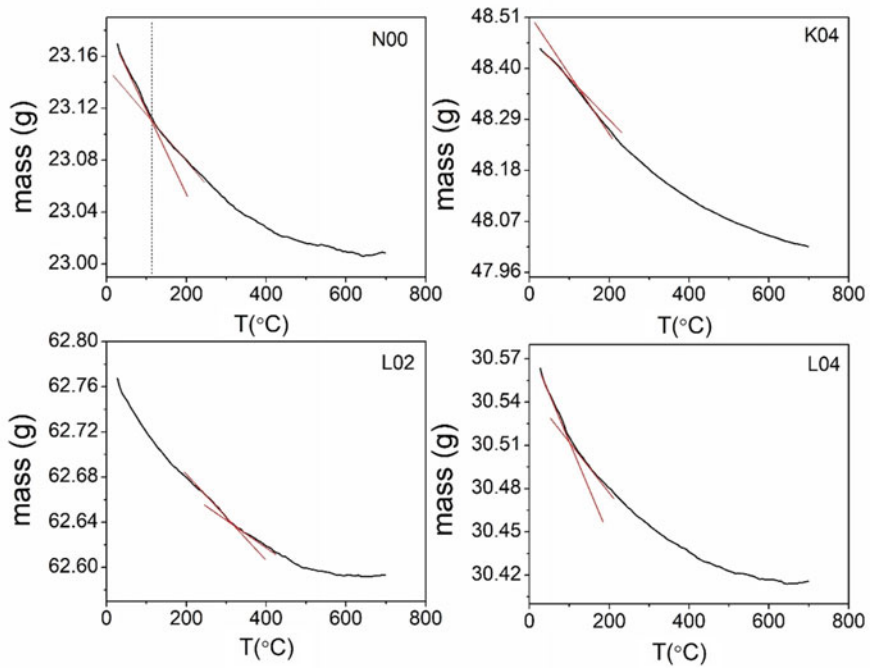

Fig. 7 Thermogravimetric analysis of the studied compositions in nitrogen atmosphere

Li^+ doping suggests trapping of oxygen vacancies as the bond strength of Li^+ is more than Na^+.

3.6 Impedance Analysis

The representative Nyquist plots for all the studied samples at 650 °C are shown in Fig. 8. Typical impedance spectra of a polycrystalline material consist of three arcs. The arc observed at higher frequency is associated with the grain polarization, and the arc at intermediate frequency corresponds to the grain boundary polarization. Bulk resistance increases with the increase in the lithium content and decreases with the potassium content, and there is a shift also observed in their corresponding frequency arcs. Figure 9a depicts the Arrhenius plot of total conductivity in the intermediate temperature range. A change in slope observed in the Arrhenius plot with temperature for all the studied compositions suggests that the conduction mechanism in the higher temperature region is different from the low-temperature region. This change may be due to NBT undergoes phase transition from the tetragonal to cubic (ferroelectric to paraelectric) at the temperature of around 520 °C [2]. It was noticed that the total conductivity increases significantly with K^+-substitution while decreases for

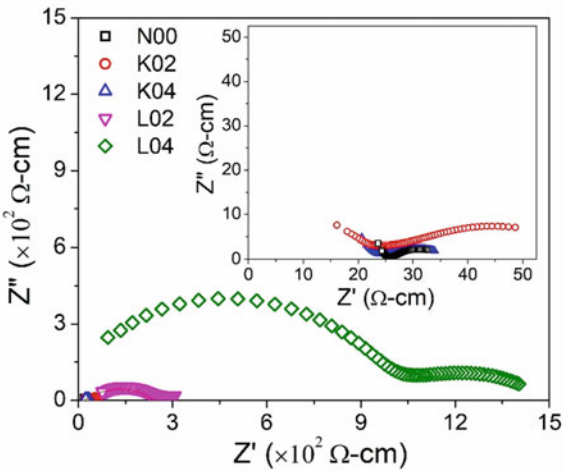

Fig. 8 Representative Nyquist plot showing the variation of impedance for N00, L02, L04, K02 and K04 at 650 °C. Inset shows the enlarged vision of N00, K02, K04

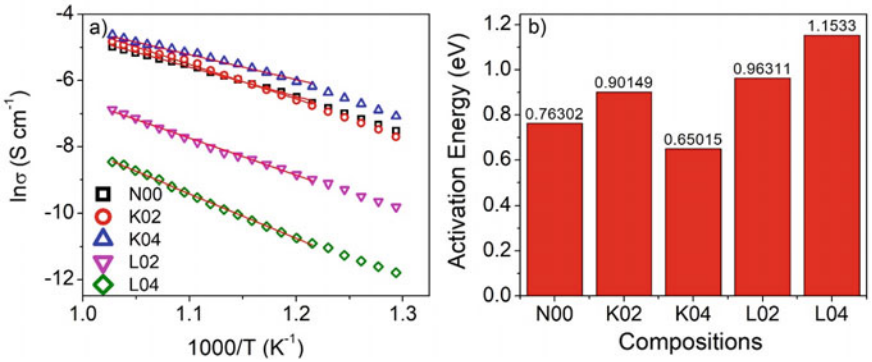

Fig. 9 **a** Arrhenius plot of total conductivity and **b** Activation energy with composition

Li^+ substitution. The activation energy (E_a) is evaluated using the Arrhenius relation [24], and the values obtained are shown in Fig. 9b. The alteration in the value of activation energy suggests change in the migration energy barrier for oxide ion. H. Zhang et al. have recently predicted that the value of activation energy required for the Na^+ migration lies between 2 and 4 eV and activation energy required for Bi^{+3} ion migration lies between 5 and 9 eV. The E_a value in the range of 1.82 eV–0.93 eV is required for the oxide ion migration from the NaO^- layer to TiO_2 layer [25]. So the value of activation energy suggests the oxide ion conductivity in all the samples. The difference in the value of activation energy is accounted to the dopant substitutions. The partial replacement of Na^+ by K^+ significantly increases the bulk conductivity. The enhancement in the conductivity with the increase in the potassium concentration can also be related to higher polarizability strength (3.83 $Å^3$) and lower bond strength of the K–O bond (2.48 eV) as compared to sodium with polarizability strength of

Table 5 Dopant ion polarizability and its strength with oxygen [26]

Dopant ion	Bond energy with oxygen (eV)	Polarizability (Å^3)
Bi^{+3}	3.55	6.12
K^{+1}	2.48	3.83
Li^{+1}	3.53	–
Na^{+1}	2.66	1.80
Ti^{+4}	8.30	2.93

1.80 Å^3 and bond strength of 2.66 eV with oxygen which makes the system more favourable for the conduction.

A transformation from the ionic to resistive behaviour is observed with the Li^+ doping as there is decrease in the conductivity. Moreover, the conductivity declines rapidly with the increase in the Li^+ doping concentration. Shrinkage in the unit cell volume and decrease in the lattice parameters discloses that the mass transport referred by the oxygen vacancies weakens on Li^+ substitution. Therefore oxide ion migration also reduces with the Li^+ substitution. The anomaly between the calculated bond valence energy and the conductivity results is probably because at higher temperature energy barrier height will decrease, as NBT shows the cubic structure, which is more favourable structure for the conduction process (Table 5).

3.7 Degradation Study

In earlier report, the stability issue of NBT was addressed in reducing atmosphere [27], where NBT gets totally reduced and convert to some other phase when kept in propane-2-ol for 48 h. However, when the non-stoichiometric NBT and its potassium and lithium doped derivatives were kept in propane-2-ol for 48 h, and they don't show any traces of impurity phases. The comparative XRD pattern of fresh and reduced samples are shown in Fig. 10. It indicates the chemical stability of the studied compositions in reducing atmosphere and its suitability as solid electrolyte material for SOFCs.

4 Conclusions

The influence on the structure and electrical properties owing to K^+ and Li^+ substitution on *A*-site (Na-site) of $Na_{0.54}Bi_{0.46}TiO_{3-\delta}$ system is investigated. Dense morphology samples of $Na_{0.54-x}M_xBi_{0.46}TiO_{3-\delta}$ (M = K, Li; x = 0.00, 0.02 and 0.04) were synthesized via SSR route at the sintering temperature of 1050 °C. XRD results of the investigated systems show the existence of pure rhombohedral phase. However, SEM micrographs are showing the presence of some impurity phase in the

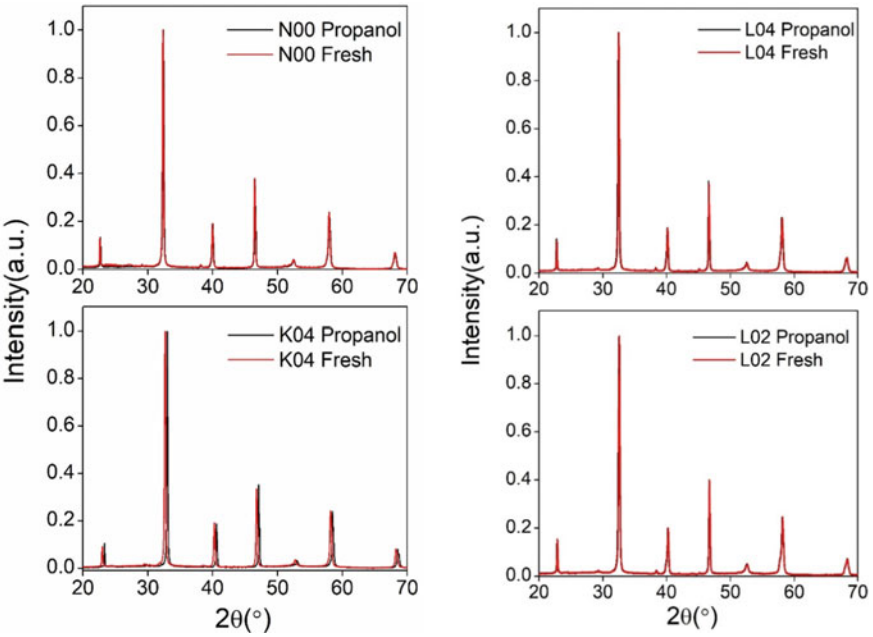

Fig. 10 Comparative XRD of freshly prepared and sample kept in propan-2-ol for 48 h, showing the stability of the sample

$Na_{0.50}K_{0.04}Bi_{0.46}TiO_{3-\delta}$ sample. Impedance results show a deterioration in the bulk conductivity with the increase of lithium concentration, and this decline in the bulk conductivity is attributed to the electrostatic and elastic interaction between Li_{Na} and $V_O^{\cdot\cdot}$ defects. However, the replacement of Na^+ by K^+ significantly increases the bulk conductivity, which may be because of the higher polarizability and weaker bonding strength of K^+ with oxygen as compared to Na^+. TGA and band gap studies have also been carried out in order to correlate and verify the experimental findings. The degradation study performed for all the samples suggests the stability of the sample in the reducing atmosphere and its suitability as a solid electrolyte for electrochemical device applications.

Acknowledgements One of the authors, Pragati Singh, acknowledges the support of SERB for project funding.

References

1. Yang F, Zhang H, Li L, Reaney IM, Sinclair DC (2016) Chem Mater 28:5269
2. Khatua DK, Mehrotra T, Mishra A, Majumdar B, Senyshyn A, Ranjan R (2017) Acta Mater

3. Bi N, Li M, Pietrowski MJ, De Souza RA, Zhang H, Reaney IM, Cook SN, Kilner JA, Sinclair DC (2013) Nat Mater 13:31
4. Yang F, Li M, Li L, Wu P, Pradal-Velázque E, Sinclair DC (2017) J. Mater Chem A 5:21658
5. R. Garg, A. Senyshyn, H. Boysen, and R. Ranjan, J. Phys. Condens. Matter **20**, 0 (2008)
6. Adams S (2006) Solid State Ionics 177:1625
7. Koch L, Steiner S, Meyer KC, Seo IT, Albe K, Frömling T (2017) J Mater Chem C 5:8958
8. Meyer KC, Albe K (2017) J Mater Chem A 5:4368
9. Li M, Zhang H, Cook SN, Li L, Kilner JA, Reaney IM, Sinclair DC (2015) Chem Mater 27:629
10. Yang F, Wu P, Sinclair DC (2017) Solid State Ionics 299:38
11. Shih DPC, Aguadero A (2018) S. J. Skinner 317:32
12. He X, Mo Y (2015) Phys Chem Chem Phys 17:18035
13. Bhattacharyya R, Das S, Omar S (2018) Acta Mater 159:8
14. Shannon RD (1976) Acta Cryst. A 32
15. Xiao R, Li H, Chen L (2015) Sci Rep 5:1
16. Singh P, Pandey R, Miruszewski T, Dzierzgowski K, Mielewczyk-Gryn A, Singh P (2020) ACS Omega 5:30395
17. Tealdi C, Mustarelli P (2014) Chem Commun 50:14732
18. Franco A, Banerjee P, Romanholo PL (2018) J Alloys Compd 764:122
19. Rajashree C, Balu AR, Nagarethinam VS (2015) Surf Eng 31:316
20. Tansley TI, Foley CP (1986) J App Phys 59:3241
21. Moss TS (1954) Proc Phys Soc Sect B 67:775
22. Singh P, Jha PK, Sinha ASK, Jha PA, Singh P (2020) Solid State Ionics 345
23. Pandey N, Thakur AK (2010) Adv Appl Ceram 109:83
24. England AW, Simmons G, Strangway D (1968) J Geophys Res 73:3219
25. Zhang H, Ramadan AHH, De Souza RA (2018) J Mater Chem A 6:9116
26. Li K, Xue D (2006) J Phys Chem A 110:11332
27. Singh P, Jha PK, Jha PA, Singh P (2019) Int J Hydrogen Energy

Hybrid Mechanism of Supercapacitor and Battery for Building High Performance of Electric Vehicles

Divya Prabha, Abhishek Kumar Gupta, Shivani Gupta, Sarvesh Kumar Gupta, Jyoti Singh, and Rajesh Kumar Yadav

Abstract As per the high requirement of energy storage, the hybrid mechanism of supercapacitors (SCs) and batteries are gradually widespread as an alternative for conventional and traditional batteries. The supercapacitor has enlarged consideration due to its exceptional properties like high power, density, long life cycle, exceptional specific capacitance, rate capability, and virtuous electrochemical reversibility. SC is the link between high-energy storage devices like fuel cells/batteries and high-power energy density devices like a capacitor. There are various types of energy storage devices used for high energy delivery. This article mainly introduces the higher efficiency hybrid mechanism of supercapacitor and battery, fundamentals, applied aspects, materials and the future of research & development.

Keywords Supercapacitor · Electrochemical · Electric Double Layer Capacitor (EDLC) · Energy density

1 Introduction

Due to the increase in petrol and gas prices, we are focusing on electrical sources. Non-renewable resources are very harmful to our environment. Shifting our dependency from non-renewables to renewables requires high energy density and high-power density storage system like efficient secondary batteries, supercapacitor, fuel cells etc. To full fill, the requirement of a higher density energy hybrid system is one of the best choices. Here we have used a supercapacitor and battery hybrid system. The electrochemical double layer also called supercapacitor or ultra-capacitor are power storage devices using the electrostatic double-layer phenomenon. It should be

D. Prabha · A. K. Gupta (✉) · S. Gupta · S. K. Gupta · J. Singh
Nanoionics and Energy Storage Laboratory (NanoESL), Department of Physics and Material Science, Madan Mohan Malviya University of Technology, Uttar Pradesh, Gorakhpur 273010, India

R. K. Yadav
Department of Chemical and Environmental Science, Madan Mohan Malaviya University of Technology, Uttar Pradesh, Gorakhpur 273010, India

S. B. Krupanidhi et al. (eds.), *Advanced Functional Materials and Devices*, Springer Proceedings in Materials 14, https://doi.org/10.1007/978-981-16-5971-3_21

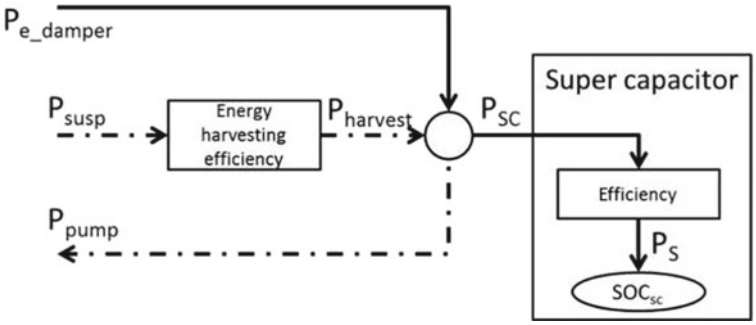

Fig. 1 Hybridization Ref. [7]

our effort to use it at its maximum efficiency [1, 2]. A difference between supercapacitors and batteries is in their energy and power density. Rechargeable batteries possesses sufficiently large energy capacities, while supercapacitors possess high power capabilities. They possess high power density and high cyclability. The first (main) process is by the partition between the electrode and the electrolyte [3, 4].

Electrical vehicle recently has gained attention. So, the demand and use of the battery have witnessed an alarming increase. So, it is more important to improve its efficiency. In this paper, we have discussed the hybrid mechanism of supercapacitor and battery for building a high performance of electric vehicles (Fig. 1). Due to their high-power density characteristics when compared to batteries, double-layer capacitors (DLCs) have proven to be very useful in the hybridization of energy storage [5, 6]. After applying the voltages, the potential difference is generated due to this the attraction force starts to work.

Due to this, charges start to move from one end to another end resulting in the flow of charges or ions current. As the concentration of ions increases, the flow of current and density increases. For improving the delivery energy capability, the hybrid mechanism is the best method to fulfil the higher density energy requirement [2, 8].

2 Basic Principle of Supercapacitor

The capacitor is a storage device, which stores energy in electrostatic form. It is formed by two parallel plates, when we apply a voltage across it, a positive charge at one plate and a negative charge at another plate is generated. Charges accumulate between these plates resulting in an electrostatic field. This is the process by which the capacitor stores energy. Whenever we need energy from this storage device, we must connect load across it. As we connect the load across the plates, it delivers energy in a fast and uncontrollable manner. Here, we used supercapacitors because of need of controlled and maximum power output [9]. For this, The SC is formed by many

methods using different types of dielectric material. As we add dielectric material in between plates of supercapacitor then the storage capacity of the supercapacitor increases. Let charge q is stored on the plate, the applied voltage is v and storage capacity are C then the relation between q, v, and C is

$$C = \frac{\mathrm{d}q}{\mathrm{d}v}$$

$$C = \frac{\frac{\mathrm{d}q}{\mathrm{d}t}}{\frac{\mathrm{d}v}{\mathrm{d}t}} = \frac{i}{V}$$

If we change the dielectric material, then capacitance is changed proportionally. Similarly, if we change the area of plat then it changes as proportional and if we change the distance between the plates the capacitance will change inversely according to the equation below,

$$C = \frac{\in A}{d}$$

3 Circuit Analysis of Supercapacitor

For proper analysis and study of the behaviour of supercapacitors, we need to draw an equivalent circuit diagram of supercapacitors. The representation of the first-order model for a supercapacitor is shown in Fig. 2.

As we can see there are four ideal elements of the circuit as shown in Fig. 2, namely, a capacitance C, a series resistor R_s, a parallel resistor R_p, and a series inductor. Series resistances show the charging and discharging, parallel resistance shows the dielectric resistance loss. Figure 3 shows the Ladder circuit model of a DLC [10].

It can withstand many cycles without deteriorating. It takes a second to fully charge (due to their minimal internal resistance). It can store a lot of energy in a miniature. The energy is released much faster than the battery [11]. A few of the initial uses were motor start-up capacitors for large appliances in tanks and submarines.

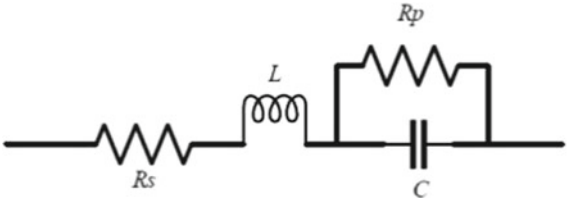

Fig. 2 First-order circuit model of DLCs

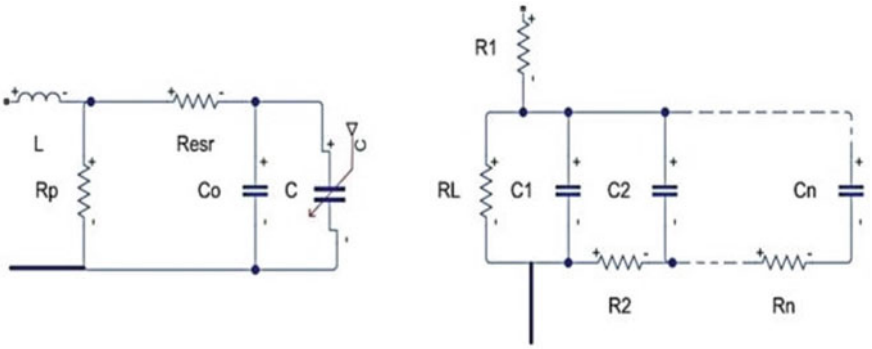

Fig. 3 Ladder circuit model

4 Design and Configuration

The hybrid connection of supercapacitor and battery has a considerable influence on its performance. To enhance performance, the configuration of the supercapacitor and its component plays an important role. The high energy storage capacity of the batteries and high-power densities can have a major impact on EVs [12]. Charles et al. [13] and Ting et al. [14] discussed three types of configuration of the components: (a) SC with battery (b) SC-battery and DC-DC converter (c) SC, battery, DC-DC converter, and freewheeling switches. In SC with battery, there is no converter used in the design. Delivering of power by SC is at a very fast rate. It is uncontrollable. So, it is necessary to supply the energy in a controlled manner using energy management system. For this, we must use a DC-DC converter.

In SC-battery and DC-DC converter, there is a DC-DC converter that manages the flow rate of energy. The best strategy for increasing the performance of hybrid EV is to add a freewheeling diode switch. It allows feeding the reverse leakage current in the circuit [15]. However, in this design size of the hybrid is increased. Due to this, their cost and efficiency have increased.

5 Proposed Circuit Structure of the Hybrid System

The main cause of the low performance of EVs is driving range loss due to the energy and power capacity drop of batteries. It is found that Li-ion batteries suffer from degradation due to the Li plating. The parameters of supercapacitor that depend on the type of electrode materials used in supercapacitors are capacitance and charge storage capability. In this hybrid system, the bidirectional DC-DC converter relates to the battery and supercapacitor parallel. There are two switches connected to control the flow of power to load. As in normal driving, power is supplied by the battery to the motor. But inclination or high torque requirement power is full fill by supercapacitor

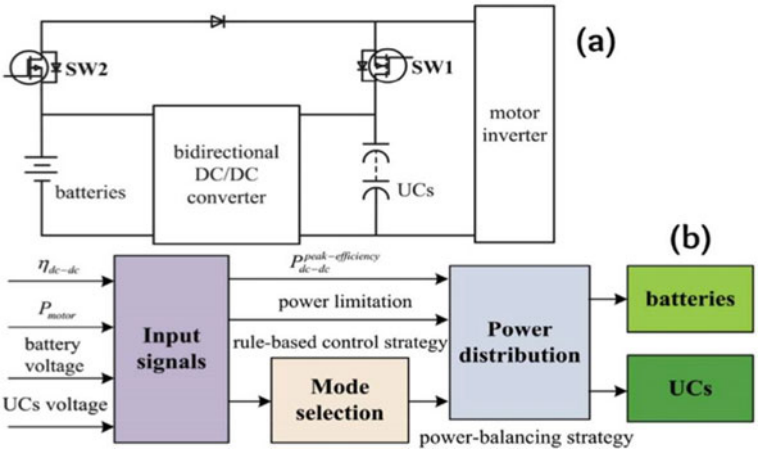

Fig. 4 Proposed circuit model

bank [16]. It delivers the power where peak energy is needed. In this, switching and power management is much needed where the converter is used. As shown in Fig. 4 input voltage is given by battery and supercapacitor to the input signal. It is controlled by mode selection and power limitation. Further, it distributes to load by the load distribution system. There are freewheeling switches used to improve the efficiency of the vehicle. It allows feedback from the inductive power to the battery.

6 Supercapacitor Matlab Simulink

Specification Used in Simulink

R = [0.2901000]; % fixed resistances, [R1 R2 R3].
C = [2.5 1.5 4]; % Fixed capacitances, [C1 C2 C3].
Kv = 0.95; % Voltage-dependent capacitor gain.
R_discharge = inf; % Self-discharge resistance.
N_series = 1; % Number of series cells.
N_parallel = 1; % Number of parallel cells.

The behaviour of supercapacitor charging, and discharging is shown by the MATLAB Simulink (Fig. 5). In the output graph (Fig. 6), the charging current density is high and fast.

As shown in MATLAB Simulink, as voltage is applied across the terminal charging starts. Increasing the voltage increases the charge rate. As the generation of charge increases the charging current rapidly changes as shown in Fig. 7. In supercapacitor high current is required in a controlled manner. For this, we have applied the supply current in pulse form. Due to this efficiency of capacitor charging is increased. The

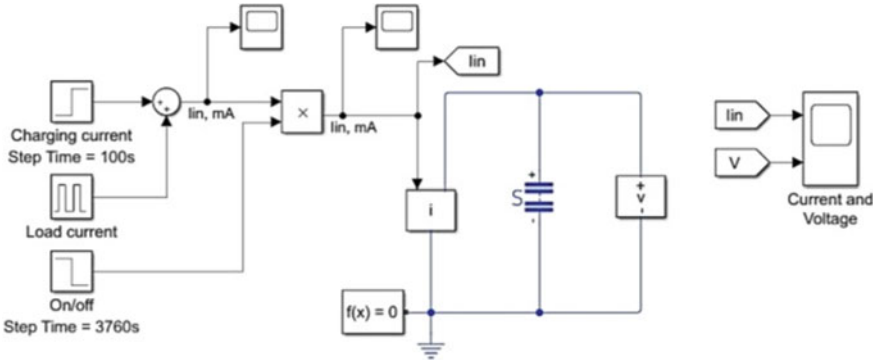

Fig. 5 MATLAB Simulink

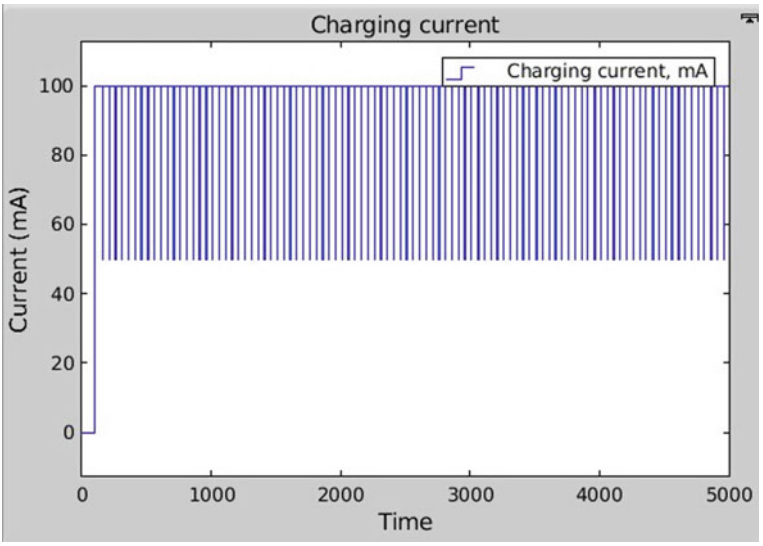

Fig. 6 Charging current

storage of the capacitor must be high. For this, we have inserted the dielectric and sustainable wall of the capacitor.

In normal capacitor charging and discharging exponentially increase and decrease. In the PWM mechanism supercapacitor, switching works ideally off.

In Fig. 8, the charging current of the supercapacitor is shown. As we can see the current density of charging is high at the higher voltage. This happens due to high storage capacity dielectric material likes activated carbon, carbon nanotube, graphene, etc. It is important to discharge slowly for any capacitor as per our requirement. This is not possible due to high charge flow and a combination of plate surface-induced ions. In supercapacitor, the main target is focused on to charging currents

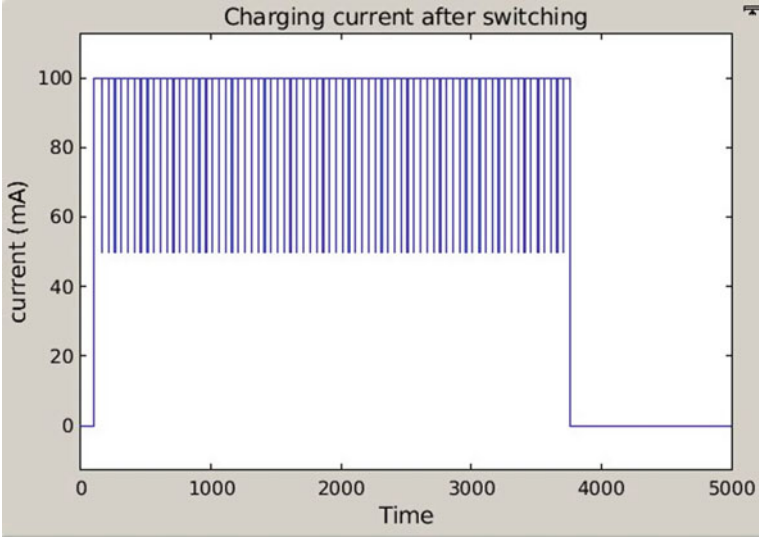

Fig. 7 charging current after switching

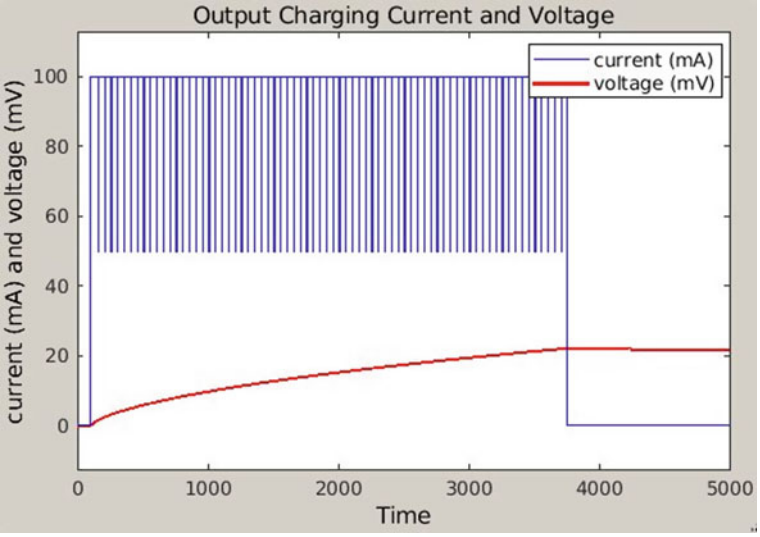

Fig. 8 Output charging current and voltage

should be high and discharging current to be low as controlled by the user. These different materials are used for slow charge combinations.

Figure 9 shows the discharging of a supercapacitor in a controlled manner.

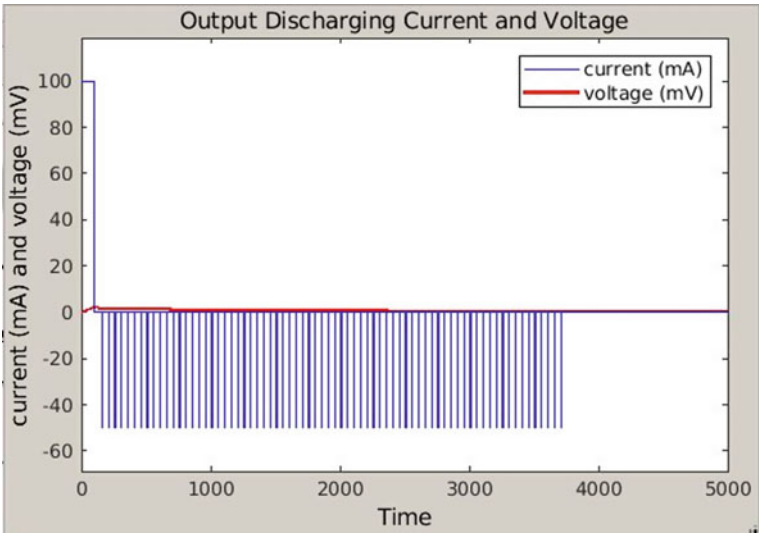

Fig. 9 Discharging current

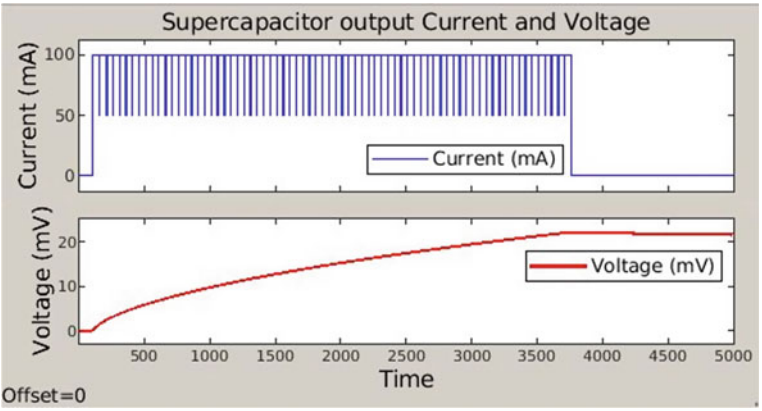

Fig. 10 Discharging output current and voltage

After applied load discharging current start to flow rapidly after few second its value come in a controlled manner (Fig. 10).

7 Conclusion

In this paper the vital role played by hybrid system for resolving the existing environmental issue is discussed. Hybrid hybrid vehicles comprise an internal combustion

engine and electric powered battery. Here, we discussed the proposed use of supercapacitor with electric vehicles and also proposed a new mechanism for improving the performance of the system. The result is verified using the MATLAB Simulink. It works on the use of peak energy requirements with a supercapacitor and battery for normal driving.

Acknowledgements Authors would like to gratefully acknowledge the assistance provided by TEQIP-III, Madan Mohan Malaviya University of Technology, Gorakhpur, India in the form of research initiation grant (No.-RIG/975/2018). Helpful discussion with my colleagues is also acknowledged.

References

1. Yoshida I, Tanahashi Y, Takeuchi, Nishino A (1987) IEEE Trans Comp Hybrids Manuf Technol 11:100–102
2. Chau KT, Wong YS (2002) Energy Convers Manage 43:1953–1968
3. Emadi A, Lee YJ, Rajashekara K (2008) IEEE Trans Industr Electron 55:2237–2245
4. Yan-Su WANG and Cheng-yang Wang (2010) New Carbon Mater 25:376–381
5. Okamura M (2001) Nikkan Kogyo Newspaper Corp. 1:25–31
6. Usman Sammani Sani and Ibrahim Haruna Shanon (2015) AKGEC International J Techn 6:2
7. Zhang Q, Deng W (2016) Energies 9:341
8. Wu ZS, Zheng Y, Zheng S, Wang S, Sun C, Parvez K, Ikeda T, Bao X, Mullen K, Feng X (2017) Adv Mater 29:1602960
9. Karden E, Ploumen S, Fricke B, Miller T, Snyder K (2007) J Power Sources 168:2–11
10. Gee AM, Dunn RW (2010) Proc 45th Int Univ Power Eng Conf (UPEC), 1–6
11. Hassan M, Reddy KR, Haque E, Faisal SN, Ghasemi S, Minett AI, Gomes VG (2014) Composites science and technology 98:1–8.
12. Sharma P, Bhatti TS (2010) Energy conversion and management 51:2901–2912
13. Kaigri C, Xia X (2015) Energy Procedia. 105:2145–2150
14. Zhu T, Gu Y, He T, Zhang ZL (2010) In proceeding of the 8th ACM Conference on Embeded Networked Sensors Systems 1:239–252
15. Kollimalla SK, Mishra MK, Narasamma NL (2014) IEEE Transactions on Sustainable Energy 5:1137–1144
16. Sathish Kumar R, Sathish Kumar K, Mishra MK (2012) Proc Annu IEEE India Conf (INDICON) 1:1078–1083

A Review on Different Techniques for Analysis for Uranium as a Ground Water Contaminant

Reena Rani, Neha Munjal, and Uma Kamboj

Abstract Water is most essential element on the surface of earth. There is no possibility of life on earth without water. Contaminants present in the water destroys its importance make it a cause of many diseases. Contamination of groundwater due to uranium in different part of worlds is as a result of natural organic industrial activities, fertilizers in agriculture and mining. All the people in the world mainly depends upon safe groundwater for use of drinking. In south-western region of Punjab, India the situation is critical due to chemical contaminants in water and limited study had done on source of chemical contaminants, ground water quality. Intake of groundwater contaminated with uranium can cause nephrotoxicity, genotoxicity and development effect. Uranium mainly affects kidney tubular cells, bone effect and different form of cancer can be caused. There is chemical and radioactive effect on human due to Uranium. Present review paper give information about sources of groundwater contamination with uranium, different techniques for analysis, uranium health risk and also how to remove this problem.

Keywords Uranium · Ground water · Toxicity · Analysis

1 Introduction

Ground water contamination due to natural source or with anthropogenic give rise to major problem in many parts of the world. Due to consumption of groundwater contaminated with uranium many people from all over the world had been affected seriously. In India, Malwa region of Punjab had highly Uranium contaminated groundwater. Food and water contaminated with uranium can cause harmful effect on human health [1–3].

Literature shows the research performed on water of Bathinda district of Punjab using Laser fluorometric technique. Uranium concentration in this region had found 3.72 times the safe limit given by AERB [4]. For analysis of water sample collected

R. Rani · N. Munjal · U. Kamboj (✉)
Department of Physics, School of Chemical Engineering and Physical Sciences, Lovely Professional University, NH-1, Phagwara, Punjab, India

S. B. Krupanidhi et al. (eds.), *Advanced Functional Materials and Devices*, Springer Proceedings in Materials 14, https://doi.org/10.1007/978-981-16-5971-3_22

from four district of Punjab (India), laser fluorometric technique had been used and 0.5–579 μg/L variation was found in concentration of uranium in south west Punjab region [5].

2 Different Techniques of Uranium Detection

2.1 Uranium Removal Technique

For removal of uranium, pump and treat technology such as anion exchange, membrane filtration and absorbent can be used, such as titanium dioxide or iron oxide. Application of coagulation with addition of lime softening and Fe/Al can also be used for removal of uranium [6]. According to WHO 30 μg/L is permissible limit of uranium. Literature shows that in ground water samples of Gurdaspur, Pathankot and Amritsar districts the average values of uranium concentration in pre-monsoon were found to be 4.3 μg L^{-1}, 3.0 μg L^{-1}, 8.6 μg L^{-1} respectively and in post-monsoon 4.9 μg L^{-1}, 3.4 μg L^{-1} and 8.8 μg L^{-1} respectively. Most of samples in this region had been found in the safe limits (30 μg/L) [7]. Present review gives sources of uranium, techniques for analysis and best technique for removal of pollutant.

3 Sources of Uranium

Uranium is most important for nuclear power. Uranium is a natural element found in water and concentration of Uranium varies from one sample to other. There are many chemical and radio logical effects of Uranium. Water having high concentration of Uranium is not safe for drinking. Uranium gets transferred to human body through water plants and food supplements, where maximum contribution is due to water. Main source of Uranium can be natural or geogenic industrial activities, mining and fertilizers in agriculture. Studies show that fertilizer generates low level of Uranium. Anthropogenic shows include miling activities, mining, uranium conversion, uranium fuel fabrication or nuclear weapons production and phosphate fertilizers average uranium 2.6–2.8 mg/kg had found in earth crust [8]. Uranium concentration in earth crust is 2.7 ppm, among igneous rocks, granites are maximum 4.8 ppm, and in sedimentary rocks is 4 ppm [9]. Study had shown that agrochemical process in calcareous soil is favoured source of uranium in ground water [10].

4 Techniques for Analysis

4.1 Fission Track Technique

Research was carried out on the samples from Punjab state. Water sample had been taken from hand pump of 34 villages. For analysis fission track technique has been used. Fleischer and Lovett [11] had given technique to determine uranium concentration and determined by using the following formula

$$C = \frac{TM}{VGNE\phi\sigma} \tag{1}$$

where N is Avogadro Number, ϕ is total thermal neutron fluence rate, T is Total no. of Track, σ is fission cross section, V is volume of Drop, G is the Geometry Factor (assumed unity), and E is the etching efficiency factor for Lexan taken as unity, M is atomic weight of Uranium. 5.41 μg/L–40.39 μg/L was the range of uranium concentration with average of 17.33 μg/L [11]. According to commission on radio logical protection (ICRP1993) has given 1.9 μg/L uranium in the safe limit. According to WHO 15 μg/L is safe limit of Uranium (2004). According to United State environmental protection agency (USCPA) given 30 μg/L as safe limit 2003. Thus uranium concentration was found above the limit given by (ICRP 1993). Table 1 shows the amount of Uranium concentration found in districts of Malwa region. Main reason for high concentration of Uranium is radioactive rich granites of Tusham hills, Bhiwani district of Haryana [12].

4.2 Inductive Coupled Plasma Mass Spectroscopy

Samples are collected from the sources and kept the plastic bottles, washed with soap solution and with distilled water and dried. 10–20 ml groundwater had collected from water source in Barnala district of Punjab. First sample filtered through a 0.45 capsule filter. 0.5 m HNO_3 required for uranium determination. Analysis had done using model 770 Agilent series (ICP-MS) in the model. The multi-element and isotope analysis mass spectrometer with inductively coupled plasma (ICP) was required. Due to uranium there can be chemical risk and radio logical risk.

Radio logical risk assessment was given by

$$\text{ECR} = \text{AC} * R \tag{2}$$

where R is risk factor, ECR is Excess cancer risk; AC is activity concentration of Uranium,

Table 1 Uranium concentration in water in the districts of Malwa region

Sample location		Uranium concentration in water μg/L	Sample location	Uranium concentration in water μg/L
Faridkot	Faridkot	10.43 ± 0.14	Khara	16.32 ± 0.13
	Kot kapura	17.88 ± 0.18	Sadik	13.95 ± 0.16
	Jaiton	19.32 ± 0.19		
Patiala	Kauli	30.4 1 ± 0.24	Rajpura	10.73 ± 0.14
	Patiala	21.4 3 ± 0.20	Samana	14.43 ± 0.16
	Nabha	20.2 1 ± 0.20		
Moga	Baga purana	17.43 ± 0.17	Smalsar	9.45 ± 0.13
	Ajitwala	5.50 ± 0.10	Nihal Singh wala	17.80 ± 0.18
	Moga	19.47 ± 0.20	Burj harike	43.39 ± 0.29
Mansa	Mansa	26.93 ± 0.24	Bareta	16.68 ± 0.17
	Burlada	11.78 ± 0.15		
	Bhiki	14.33 ± 0.16		
Sangrur	Handiaya	14.42 ± 0.16	Dhrnola	21.24 ± 0.20
	Sangrur	9.37 ± 0.13	Malerkotla	8.43 ± 0.12
	Dhuri	19.43 ± 0.19	Jagraon	20.43 ± 0.20
	Sunam	20.13 ± 0.20	Sarhind	30.31 ± 0.24
	Tapa	12.93 ± 0.15	Khanna	6.78 ± 0.14
	Barnala	5.41 ± 0.10	Ludhiana	27.35 ± 0.23
	Bhawanigarh	13.42 ± 0.16	Raikot	11.68 ± 0.15

$$\text{Riskfactor} = r * I \tag{3}$$

R is risk of coefficient of Uranium (1.19 × 10–9), I = 4.05 L/day × 23,250 days. Here assumed life 63.7 years and 4.05 L is daily consumed water.

4.3 Chemical Risk assessment

Chemical risk assessment had been defined in term of life time average daily dose (LADD) of Uranium Intake through drinking water.

$$\text{LADD} = C * \text{IR} * \text{ED} * \frac{\text{EF}}{\text{AT}} * \text{BW} * 365 \tag{4}$$

where IR = water consumption rate, C = concentration of Uranium, ED = life time exposure duration (63.7 years), EF = exposure frequency, AT = average time

(63.7 years), BW = average today weight of the receptor (70 kg).

$$\mathrm{HQ} = \frac{\mathrm{LADD}}{R_f D} \tag{5}$$

HQ is Hazard quotient—it major of the limit of who formed due to uranium intake.

Where $R_f D$ is reflectance dose 4.53 μg/kg/day, LADD = life time average daily dose. Result had shown that uranium found 62.9 1 Ppb (Raja village) 290.60 Ppb (Ramgarh Tubewell) with average value of 127.90 Ppb at 110 sites in this survey. By Atomic energy regulatory board (AERB) safe limit is 60 Ppb. It was absorbed that from results all sample fail in safe limit set by AERB.

From results 1.78 to 8.23 $\times$ 10^{-4} is excess cancer risk but according to AERB maximum level is 1.67 $\times$ 10^{-4}. So result was higher than this limit of AERB. From results variation in LADD and hazards quotient values has observed from 3.64 to 16.81 μ/kg/day and 0.80 to 3.71 respectively [13].

4.4 Uranium Fluorimeter (UAI Quantalase)

Literature had been observed for the use of Uranium Fluorimeter. Twenty samples had collected from borewells, head pumps from Faridkot and Muktsar district of Punjab. In the region of study area for agriculture depends on groundwater. Total dissolved solids, PH, Temperature, dissolved oxygen, electrical conductivity had measured in this area. Acid treated bottles are used for storage and 0.45 μm filter had used for filtration of water samples. For measurement of Uranium fluorimeter (UAI Quantalase) had been used. The standard addition method had used for determination of detection limit. In this method with increment of 5 μg/L, 5–20 μg/L standard uranium solution head text in to water. Best fit equation with Y intercept have used to measure background noise, typical detection limit was 0.2 μg/L.

For high concentration of Uranium stable dilution had done. ICP-MS analytic method have used for validation of Uranium measurement. Result had shown that uranium concentration had found 32-90 μg/L in Muktsar and average value of 43 μg/L was found in this district and 4–171 μg/L in Faridkot and average value of 67 μg/L was found in this district, it is above the permissible limit. 44.44% sample had found contaminated while 81.8% in Faridkot. Up to 30 m death uranium contamination was high due to bicarbonate concentration with death uranium concentration decrease. In water sample no evaporation signature had been found. So irrigation return did not contribute to groundwater recharge on their sites. With high concentration of Uranium alkalinity does not show proportionality. Possible source of Uranium maybe geogenic not anthropogenic activities [14]. mainly fluorimeter is a device which measure parameter of florescence, wavelength of emitted spectrum, its intensity. Used to find out specific substance in a given medium. It uses two beams. One upper beam is passed through the sample and lowerbeam is passed through attenuator

and adjusted to match the power which is off from sample. Both beam are detected by different transducer and converted into electrical signal and which are interpreted by computer. Transducer which detect upper beam is at 90° from the beam [16].

4.5 Laser Fluorimeter (UAI, Quantalase)

Mansa and Bathinda districts were chosen for the research. The average rainfall is 400 to 500 per year. Depth level for water was noted 2.24–20 bgl for district Bathinda and 3.89–12.36 m bgl for district Mansa. In this study 35 samples had collected from head pump, Tubewell, canal and borewells in Feb 2015. Electrical conductivity was found in this area due to Ghaggar River. Well depth was 0.9–111 m bgl. Before taking sample pumping out water for 30 min and acid washed polythene bottles were used for uranium analysis. Laser fluorimeter (UAI, Quantalase) had used for uranium analysis. Result had shown that in this study area uranium concentration varies from 2.3 to 3. 57 μg/L. 34% sample fall in permissible limit that is 30 μg/L and 66% fall in a safe limit. 66% fall in unsafe limit. But according to an AERB (Atomic Energy Research Board 63% of sample fall in safe limit while 37% in unsafe limit.

Highest concentration had found 357 μg/L in the shallow zone in phul village and low concentration had noted in canal command area, which is near to Ghaggar in district Mansa [3].

Mainly uranium found as a result of release from mill tailings, contribution from fly ash, leaching from natural deposits, emission from nuclear industry. Four main districts Mansa, Bathinda, Muktsar and Faridkot had covered in study. Total 56 water sample have collected from canals, tubewells, hand pump and borewells. Before collection for 30 min running of water had done. For uranium measurement laser fluorometer had used and result had shown that 12.2–621 μg/L uranium concentration and maximum 621 μg/L in Mansa district had found [15]. in this technique uranium can be excited by laser in UV region of 300–350 nm. In this method sealed off nitrogen laser emit 371.10 nm pulses which excite the fluorescence of uranyl ions in the solution and emit green luminescence and which are detected by photomultiplier tube [17].

4.6 LED Fluorometerre

Uranium is heaviest radioactive element which occurs naturally. Rural area in India fully depends upon groundwater. Due to hazards due to uranium, interest in study of Uranium has increased. 266 water samples had taken from 6 district of Punjab which is highly contaminated with uranium. Sample had taken from borewells, tubewells and hand pump. After running 5–10 min of water sample had taken in polythene bottles. For determination of Uranium concentration in groundwater sample LED fluorometer, model LF-2a had used. This instrument mainly contain photometer

tube, sample compartment, LED excitation source. Result has shown that uranium concentration lies between 0.48 μg/L and 645. 22 μg/L. At Jatana kainchian village of district Mansa maximum limit 645.22 μg/L had observed and at Attowal village in district Hoshiarpur minimum 0.48 μg/L was observed [2].

4.7 Comparison of Different Techniques

Comparison of different technique for uranium detection in water shows that Track etching technique is more sensitive than others methods and for environmental studies reproductively of this method is also good. For lower concentration of uranium laser fluorimeter cannot give accurate quantitative results, but fission track technique could give [18]. Studies shows that laser fluorimeter method is faster, cost effective and simple as compare to ICP-MS (inductive coupled mass spectroscopy) [19].

5 Conclusion

The review covers the different successful methods and the techniques used for identification of Uranium content in ground water. Comparison of all the methods was done and it was observed that the laser fluorometer is faster.

References

1. Kumar R et al (2020) Source apportionment, chemometric pattern recognition and health risk assessment of groundwater from southwestern Punjab, India. Environmental Geochemistry Heal, 1–23
2. Saini K, Singh P, Bajwa BS (2016) Comparative statistical analysis of carcinogenic and non-carcinogenic effects of uranium in groundwater samples from different regions of Punjab, India. Appl Radiation Isotopes 118:196–202
3. Sharma DA et al (2017) Distribution of uranium in ground waters of Bathinda and Mansa districts of Punjab, India: inferences from an isotope hydrochemical study. J Radioanalytical Nuclear Chemistry 313(3):625–633
4. Singh L, et al (2013) Health risk assessments due to uranium contamination of drinking water in Bathinda region, Punjab state, India. Radioprotection (EDP Sciences) 48(2)
5. Bajwa BS et al (2017) Uranium and other heavy toxic elements distribution in the drinking water samples of SW-Punjab, India. J Radiation Research Appl Sci 10(1):13–19
6. Katsoyiannis IA, Zouboulis AI (2013) Removal of uranium from contaminated drinking water: a mini review of available treatment methods. Desalin Water Treat 51(13–15):2915–2925
7. Sharma T, et al (2019) Uranium distribution in groundwater and assessment of age dependent radiation dose in Amritsar, Gurdaspur and Pathankot districts of Punjab, India. Chemosphere 219: 607–616
8. Liesch T, Hinrichsen S, Goldscheider N (2015) Uranium in groundwater—fertilizers versus geogenic sources. Sci Total Environ 536:981–995

9. Singh KP (2010) Uranium in groundwater in Punjab State, India: Status Paper
10. Alrakabi M et al (2012) Study of uranium contamination of ground water in Punjab state in India using X-ray fluorescence technique. J Radioanal Nucl Chem 294(2):221–227
11. Fleischer RL, Lovett DB (1968) Uranium and boron content of water by particle track etching. Geochim Cosmochim Acta 32(10):1126–1128
12. Mehra R, Singh S, Singh K (2007) Uranium studies in water samples belonging to Malwa region of Punjab, using track etching technique. Radiat Meas 42(3):441–445
13. Virk HS (2019) Uranium Content Anomalies in Groundwater of Barnala District of Malwa Belt of Punjab (India) for the Assessment of Excess Cancer Risk. Research & Reviews: J Oncol Hematol 8(1):19–26p
14. Pant D, et al (2017) Study on uranium contamination in groundwater of Faridkot and Muktsar districts of Punjab using stable isotopes of water. J Radioanalytical Nuclear Chemistry 313(3):635–639
15. Rishi MS, et al (2017) Spatial trends in uranium distribution in groundwaters of Southwest Punjab, India-A hydrochemical perspective. J Radioanalytical Nuclear Chem 311(3):1937–1945
16. Sahu SK, et al (2014) Determination of uranium in ground water using different analytical techniques. No. BARC—2014/E/011. Bhabha Atomic Research Centre
17. Bhangare RC et al (2013) Laser flourimetric analysis of uranium in water from Vishakhapatnam and estimation of health risk. Radiat Prot Environ 36(3):128
18. Guo S-L, et al (1986) Comparison between fission track method and laser-fluorometry and fluorocolorimetry for determination of uranium concentration in natural water. Int J Radiation Appl Instrumentation Part D Nuclear Tracks and Radiation Measurements 12(1–6): 801–804
19. Shenoy N, et al (2012) A comparative analysis of uranium in potable waters using laser fluorimetry and ICPMS techniques. J Radioanalytical Nuclear Chemistry 294(3):413–417

Study of Haff's Law in Binary Granular Gas

Rameez Farooq Shah, SK Wasim Ahamed, and Syed Rashid Ahmad

Abstract The free evolution of a two component or binary granular gas (in dimensions $d = 2, 3$) is studied using large-scale molecular dynamics simulation. To prepare a binary granular gas, we consider half the particles to be of a different mass. The time dependence of temperature of the system as well as the components is studied. The results are compared with the free cooling of a single component granular gas. The results are found to be at variance with Haff's law that single component granular gases obey in the homogeneous cooling state.

1 Introduction

Granular matter is a collection of discrete solid particles or *grains* with dimensions of around 1 μm–1 cm [1]. These materials are found abundantly in the universe in different shapes and sizes ranging from powders and sand to pebbles and nuts. Depending on preparation and how the system is excited, these materials can be thought to behave as solids, liquids, or gases [2, 3]. In general, the contact forces may have a dissipative tangential component as well. As a consequence of these dissipative contact forces, the system continuously loses energy or *cools* with time.

A prototype of a freely evolving granular gas is the free relaxation of energized powder without any external drive. The study of such a system has received considerable attention in recent years [4–14]. From the theoretical standpoint, the initial state of such a system is taken to be one in which the density is homogeneous. The initial velocity distribution is taken to be Maxwell-Boltzmann distribution. At the initial stages of evolution while the system loses energy, the density field remains homogeneous and the system is said to be in the *Homogeneous Cooling State* (HCS). However, at later times, due to the density and velocity field's fluctuations, the system evolves into a bi-continuous morphology consisting of regions of high and low densities, which is usually called as *Inhomogeneous Cooling State* (ICS) [5, 13]. In an experimental set-up, the loss of energy is compensated by driving granular

R. F. Shah · S. W. Ahamed · S. R. Ahmad (✉)
Department of Physics, Jamia Millia Islamia, New Delhi 110025, India
e-mail: srahmad@jmi.ac.in

S. B. Krupanidhi et al. (eds.), *Advanced Functional Materials and Devices*, Springer Proceedings in Materials 14, https://doi.org/10.1007/978-981-16-5971-3_23

materials in standard geometries, e.g., horizontal or vertical vibration [15], pouring in a chute [16, 17], rotating in a drum [18, 19], etc. These experimental settings give rise to various non-equilibrium phenomena.

This paper is organized as follows. In Sect. 2, we presented a brief review of the cooling problem. This section consists of two subsections. Section 2.1 describes the phenomenology of the cooling of granular gases in the HCS where the system continuously looses energy while the density field appears relatively homogeneous. In Sect. 2.2, we briefly described the ICS. In Sect. 3, we presented detailed numerical results from our MD simulations. Finally, in Sect. 4, we concluded this paper with a summary and discussion of our results.

2 Cooling of a Granular Gas

2.1 HCS or Homogeneous Cooling State

For the purpose of reference, we modeled a granular gas as an assembly of identical hard spheres with diameter $\sigma = 1$ and mass $m = 1$. The particles underwent inelastic collisions with a restitution coefficient e where $0 < e < 1$, where $e = 1$ corresponds to the elastic limit. The problem of time dependence of temperature of a system of inelastically interacting hard spheres in a homogeneous distribution was first studied by Half [4].

We considered a collision between particles i and j. The velocities of the particles after collision $\vec{v'}_i$ and $\vec{v'}_j$ were related to the velocities before collision $\vec{v}_i$ and $\vec{v}_j$ by the following rule:

$$\begin{aligned} \vec{v'}_i &= \vec{v}_i - \frac{1+e}{2}[\hat{n} \cdot (\vec{v}_i - \vec{v}_j)]\hat{n}, \\ \vec{v'}_j &= \vec{v}_j + \frac{1+e}{2}[\hat{n} \cdot (\vec{v}_i - \vec{v}_j)]\hat{n}, \end{aligned} \tag{1}$$

where e (< 1) is the coefficient of restitution. Here, $\hat{n}$ the unit vector pointing from j to i at the time of collision; $\hat{n} = \hat{r}_{ij}$, $\vec{r}_{ij} = \vec{r}_i - \vec{r}_j$ The corresponding loss of kinetic energy in this collision is given by

$$\delta E = -\frac{(1-e^2)}{4}\left[\left(\vec{v}_i \cdot \hat{n}\right)^2 + \left(\vec{v}_j \cdot \hat{n}\right)^2 - 2\left(\vec{v}_i \cdot \hat{n}\right)\left(\vec{v}_j \cdot \hat{n}\right)\right] \tag{2}$$

We define the granular temperature as $T = \left\langle \vec{v}^2 \right\rangle / d$, where $\langle \vec{v}^2 \rangle$ is the mean-squared velocity. After averaging overall possible velocity directions in the homogeneous state, the time rate of change of granular temperature is given as

$$\frac{\mathrm{d}T}{\mathrm{d}t} = -\frac{\epsilon\omega(T)T}{d}, \quad \epsilon = 1 - e^2, \tag{3}$$

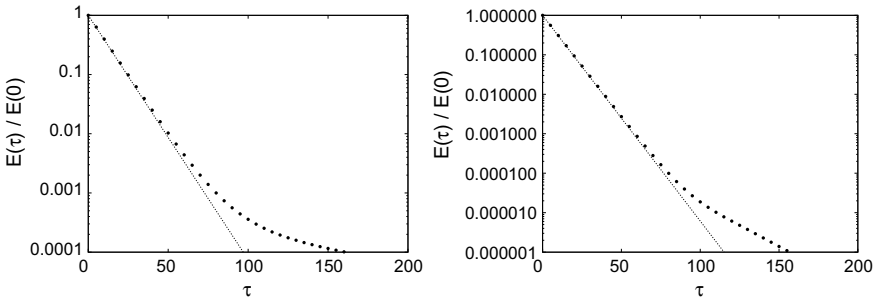

(a) $d = 2$ (b) $d = 3$

Fig. 1 Haff's law for $d = 2, 3$

where $\omega(T)$ represents the frequency of collision at temperature T. We know from kinetic theory of gases, that it is given by [20]:

$$\omega(T) \simeq \frac{2\pi^{(d-1)/2}}{\Gamma(d/2)}\, \chi(n) n T^{1/2}, \tag{4}$$

where $\chi(n)$ represents pair correlation function at contact for hard spheres with density n. With Eqs. (3) and (4), we arrive at the Haff's law for the HCS:

$$T(t) = T_0 \left[1 + \frac{\epsilon \omega(T_0)}{2d}\, t\right]^{-2}, \tag{5}$$

where T_0 is the initial temperature. We define τ as the average number of collisions in time t. This can be calculated as

$$\begin{aligned} \tau(t) &= \int_0^t dt' \omega(t') \\ &= \frac{2d}{\epsilon} \ln\left[1 + \frac{\epsilon \omega(T_0)}{2d} t\right]. \end{aligned} \tag{6}$$

We saw a logarithmic increase in the number of collisions (instead of a linear increase) with time as the system loses energy (Fig. 1). When we write Haff's law in terms of τ, the collision time has the following form:

$$T(\tau) = T_0 \exp\left(-\frac{\epsilon}{d}\, \tau\right). \tag{7}$$

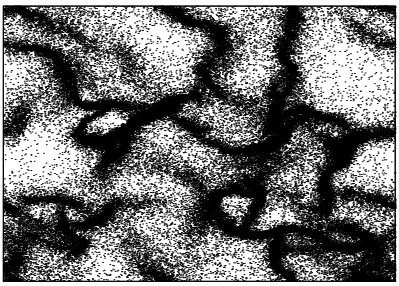

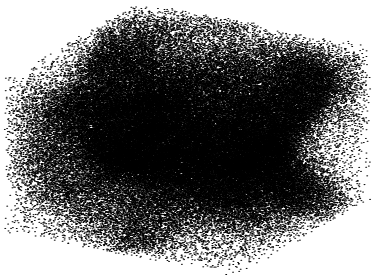

Fig. 2 Evolution snapshots of the density fields in the in homogeneous cooling state of an inelastic granular gas in $d = 2, 3$. These pictures correspond to $\tau = 200$ for a system with particle number $N = 100{,}000$. For restitution coefficients for $d = 2, 3$ are $e = 0.9$ and $e = 0.8$, respectively

2.2 Inhomogeneous Cooling State (ICS)

The density as well as the velocity field in HCS was unstable to fluctuations as mentioned earlier. We showed this in Fig. 2, for the density field. The figure shows the evolution of density field for a 2-d granular gas with $e = 0.9$ and 3-d granular gas with $e = 0.8$.

3 Results from Molecular Dynamics Simulations

In this paper, our primary interest was the time dependence of energy of a granular gas consisting of two different species of particles, i.e, is a binary granular gas. The diameter of particles in both $d = 2, 3$ was the same, i.e, $\sigma = 1$. However, half of the particles in either case was chosen to be $m = 1.0$, whereas the other half of the particles was assigned a different mass. The restitution coefficient chosen was $e = 0.8, 0.9$ and 0.95. Since the mass of the particles was different, the collision rules given by Eq. (1) got modified. The modified equations are given by

$$\begin{aligned}
\vec{v'}_i &= \vec{v}_i - (1+e)\left(\frac{m_j}{m_i+m_j}\right)[\hat{n}\cdot(\vec{v}_i-\vec{v}_j)]\hat{n}, \\
\vec{v'}_j &= \vec{v}_j + (1+e)\left(\frac{m_i}{m_i+m_j}\right)[\hat{n}\cdot(\vec{v}_i-\vec{v}_j)]\hat{n},
\end{aligned} \tag{8}$$

We simulated a system of $N = 100000$ particles using event-driven molecular dynamics method [21, 22]. For $d = 2, 3$, the size of the simulation domain was chosen to be 1000^2 and 100^3, respectively. Periodic boundary condition was applied in all directions. For simplicity, we have taken identical particles having unit diameter σ. Our binary gas consisted of two species of $N/2$ particles each. One of the

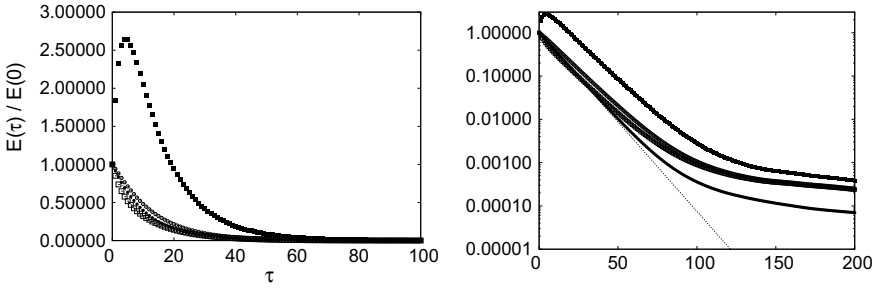

Fig. 3 The graph shows dependence of scaled energy with time in $2d$ on normal scale (left) and log-scale (right). The line corresponds to the Haff's law. The bold circles are drawn for reference and correspond to equal masses. The hollow circle is correspond to the result for $m_a = 1.0$ and $m_b = 0.1$. The other two graphs represented by hollow and solid spheres represent the energy dependence of the two species separately

species had a mass $m_a = 1.0$, whereas the mass of the other species was taken to be $m_b = 0.9, 0.5$ and 0.1. For reference, $m_b = 1.0$ was taken, which essentially corresponds to identical particles where the Haff's law is known to be followed. The system was initialized by randomly distributing particles throughout the simulation domains such that no two particles were allowed to overlap. Velocity components were chosen randomly in such a manner that the total momentum was conserved, $\Sigma_i m_i v_i = 0$. This system was allowed to evolve elastically $e = 1$ using the event-driven molecular dynamics method upto $\tau = 100$. This ensured a homogeneous density distribution with Maxwell-Boltzmann velocity profile which served as the initial condition of our simulation.

In Fig. 3, scaled energy dependence on τ is represented in normal as well as log-scale in $d = 2$. For reference, we have drawn the Haff's law with line. The graph for equal masses which is in good agreement with the Haff's law in HCS has been plotted with bold circles. The hollow circles, which clearly deviate from the Haff's law, represent the results of a system of two unequal masses $m_a = 1.0$ and $m_b = 0.1$. The other two plots are of individual components. It is important to note that the species with $m_b = 0.1$ not only depart from the haff's law, but initially gain energy on an average.

In Fig. 4, scaled energy dependence on τ is represented in normal as well as log-scale in $d = 3$. Here, we have presented results $m_a = 1.0$ and $m_b = 0.5$. Rest of the features of this graph are similar to the case of $d = 2$.

Finally, in Fig. 5, we showed the density plots for $d = 2$ for the two species $m_a = 1.0$ (left) and $m_b = 0.1$ (right) at $\tau = 200$. A comparison between the two clearly shows that the heavier mass has a greater tendency to stick together. At the same time, the density field of the lighter particles is more homogeneous as compared to heavier particles.

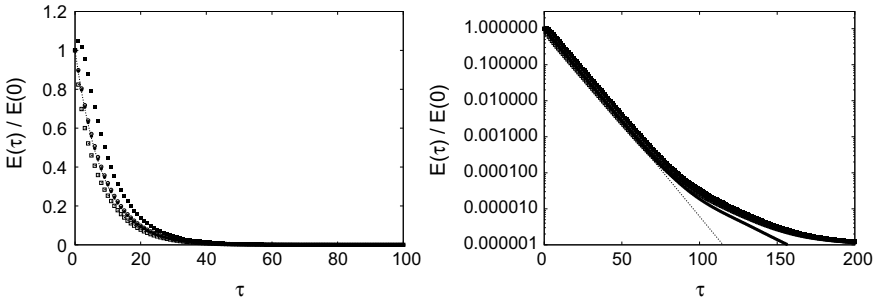

Fig. 4 The graph shows dependence of scaled energy with time in $3d$ on normal scale (left) and log-scale (right). The line corresponds to the Haff's law. The bold circles are drawn for reference and correspond to equal masses. The hollow circle is correspond to the result for $m_a = 1.0$ and $m_b = 0.5$. The other two graphs represented by hollow and solid spheres represent the energy dependence of the two species separately

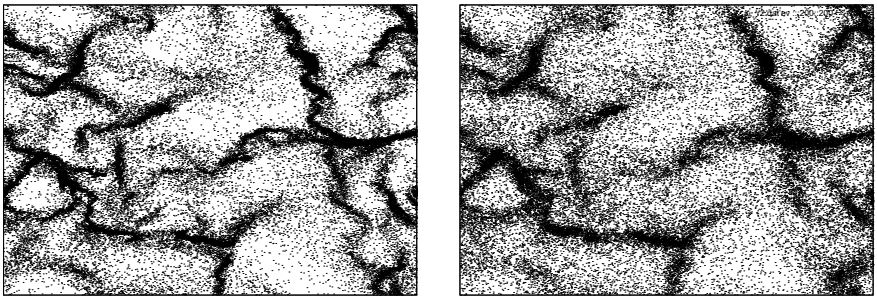

Fig. 5 Density snapshots of $m_a = 1.0$ (left) and $m_b = 0.1$ (right). The heavier particles display a greater propensity to stick together than the lighter particles

4 Summary and Discussion

Using large-scale molecular dynamics, we have simulated a system of a binary granular gas with particles of two species in equal number in $d = 2, 3$. The aim of this paper was to compare the results of energy dependence with time with Haff's cooling law. We saw a departure of energy dependence from Haff's law for the entire system as well as individual species.

Acknowledgements The authors gratefully acknowledge the computational facilities at the Department of Physics, Jamia Millia Islamia, New Delhi.

References

1. de Gennes PG (1999) Granular matter: a tentative view. Rev Mod Phys 71:S374
2. Jaeger HM, Nagel SR, Behringer RP (1996) Granular solids, liquids, and gases. Rev Mod Phys 68:1259
3. Aranson IS, Tsimring LS (2006) Patterns and collective behavior in granular media: theoretical concepts. Rev Mod Phys 78:641
4. Haff PK (1983) Grain flows as a fluid-mechanical phenomenon. J Fluid Mech 134:401
5. Goldhirsch I, Zanetti G (1993) (1993) A molecular dynamical study of granular fluids I: the unforced granular gas in two dimensions. Phys Rev Lett 70:1619
6. McNamara S, Young WR (1992) Kinetics of a one-dimensional granular medium in the quasielastic limit. Phys Fluids A 4:496
7. Brey JJ, Moreno F, Dufty JW (1996) Model kinetic equation for low-density granular flow. Phys Rev E 54:445
8. van Noije TPC, Ernst MH, Brito R, Orza JAG (1997) Mesoscopic theory of granular fluids. Phys Rev Lett 79:411
9. Luding S, Huthmann M, McNamara S, Zippelius A (1998) Homogeneous cooling of rough, dissipative particles: theory and simulations. Phys Rev E 58:3416
10. Baldassarri A, Marconi UM, Puglisi A (2002) Driven granular gases with gravity. Phys Rev E 65:051301
11. Das SK, Puri S (2003) Pattern formation in the inhomogeneous cooling state of granular fluids. Europhys Lett 61:749
12. Nakanishi H (2003) Effects of velocity correlation on early stage of free cooling process of inelastic hard sphere system. Phys Rev E 67:010301(R)
13. Ahmad SR, Puri S (2006) Velocity distributions in a freely evolving granular gas. Europhys Lett 75:56
14. Bodrova A, Dubey AK, Puri S, Brilliantov N (2012) Velocity distribution function and effective restitution coeffcient for a granular gas of viscoelastic particles. Phys Rev Lett 109
15. Melo F, Umbanhowar PB, Swinney HL (1995) Hexagons, kinks, and disorder in oscillated granular layers. Phys Rev Lett 75:3838
16. Peng G, Herrmann HJ (1994) Density waves of granular ow in a pipe using lattice-gas automata. Phys Rev E 49:1769
17. Moriyama O, Kuroiwa N, Matsushita M, Hayakawa H (1998) Phys Rev Lett 80:2833
18. Rajchenbach J (1990) Flow in powders: from discrete avalanches to continuous regime. Phys Rev Lett 65:2221
19. Das Gupta S, Khakhar DV, Bhatia SK (1991) Axial segregation of particles in a horizontal rotating cylinder. Chem Eng Sci 46:1531
20. Chapman S, Cowling TG (1970) The mathematical theory of non-uniform gases. Cambridge University Press, New York
21. Allen MP, Tildesley DJ (1987) Computer simulation of liquids. Oxford University Press, Oxford
22. Rapaport DC (2005) The art of molecular dynamics simulation, 2nd edn. Cambridge University Press, Cambridge

Recent Advances in ZnO Based Electrochemical Ethylene Gas Sensors for Evaluation of Fruit Maturity

Ribu Mathew and Avirup Das

Abstract India is the largest producer of fruits and vegetables in the world. However, a major portion of agro-products is wasted during harvesting, shipping, and storage, i.e., negligence in the food supply chain management (FSCM) system. Globally, one third of food produced is wasted. Importantly, two-third of the wastage of food occurs due to limitations in the supply chain management system. Wastage of perishable agro-products due to negligence in FSCM is a critical issue, especially in the case of agro-products like fruit. Therefore, the early detection and segregation of fruits are critical to reduce agro-product wastage. A typical indicator of maturity and ripening of fruits is the rate of generation and concentration of ethylene gas. Even though, literature encompasses examples of a variety of ethylene gas sensors, ZnO based electrochemical ethylene gas sensors depict numerous advantages compared to other sensor variants. ZnO is an extensively studied wide band gap semiconductor for sensing applications. When used as a sensing layer material it 'senses', ethylene gas by changing its band gap and thereby electrical property. Further, the sensitivity and selectivity of the pristine ZnO vary with shape, substrate, and metal doping. This paper elucidates a review of recent advances in ZnO based electrochemical sensors for ethylene gas detection. The review covers various levels of design abstraction that include material and device. In addition, we summarize the design challenges and future trends in the development of ZnO based electrochemical ethylene gas sensors.

Keywords Ethylene · Gas sensor · Fruit maturity · Food wastage · Real time detection · Portable

R. Mathew (✉)
School of Electrical and Electronics Engineering (SEEE), VIT Bhopal University, Bhopal 466114, India

A. Das
School of Advance Science and Languages (SASL), VIT Bhopal University, Bhopal 466114, India

S. B. Krupanidhi et al. (eds.), *Advanced Functional Materials and Devices*, Springer Proceedings in Materials 14, https://doi.org/10.1007/978-981-16-5971-3_24

1 Introduction

Indian economy is one of the fastest growing economies in the world and one of the major driving forces that contribute to its growth is agro-industries. India's economy is driven by agriculture sector and its associated industries as it employs more than 50% of the Indian workforce and contributes 17–18% of India's GDP. According to a report from food and agricultural organization (FAO) in the year 2014, India is the largest producer of fruits and vegetables in the world. However, a major portion of the crop is wasted in various stages of production, distribution, and consumption or limitation in food supply chain management (FSCM) system. FSCM involves various stages of food processing, starting from crop harvest to end customer supply through phases like processing, packaging, storage, transportation, etc. Food wastage, especially wastage of perishable food like fruits is primarily due to limitations in transportation and storage. Thus, the early evaluation of fruit maturity becomes critical to reduce food wastage during transportation and storage.

Traditionally, the evaluation of fruit maturity is performed based on its properties like texture and firmness, or by means of destructive techniques in which the sample undergoes tampering during an inspection. Although the aforementioned inspection techniques are extensively used, such techniques are inaccurate and require destruction of sample. An alternative solution is to monitor the changes in fruit maturity stages using markers that are generated by fruits during the process of maturity and stages of ripening. A typical indicator of fruit maturity and ripening is the concentration of ethylene gas generated by fruits [1, 2]. Ethylene is a colorless and odorless gaseous phyto-hormone. Ethylene gas can be used as an indicator of fruit maturity as the rate of generation of ethylene gas increases through ripening stages, especially for climacteric fruit species like apple, kiwi, pears, banana, mango, etc. [3, 4]. The concentration of ethylene gas generated by climacteric fruits changes as it undergoes various ripening stages, i.e., unripe, half-ripe, full-ripe, and over-ripe.

The detection of ethylene gas concentration as an indicator of fruit maturity is accomplished by electronics nose (e-nose). An e-nose is a sensing element that converts the ethylene gas concentration into an equivalent electrical signal that gives an indication of fruit maturity under study. Typical sensors have been realized using micro-electro-mechanical system (MEMS) technology to detect various physical [5–12], chemical/biological [13–23] entities. Such sensors depict high sensitivity and performance to cost index due to their high surface-to-volume ratio and possibility of batch fabrication. Other solutions to develop e-nose include gas chromatography (GC) sensor, electrochemical sensor, optical sensor, chemical sensor, organic field effect transistor sensor, to cite a few. Compared to other sensor variants, electrochemical sensors have an edge due to their advantages like low power consumption, scalability, adequate response time, and cost-effectiveness. The premise makes electrochemical sensors an ideal choice for developing portable, cost-effective, low power, and real time monitoring devices for evaluating fruit maturity during storage and transportation. Among electrochemical sensors, chemo-resistive sensor variant with

active ZnO has advantages over other types due to its low power, cost-effectiveness, better scalability, simple fabrication techniques.

In this paper, we review the recent advances in ZnO based chemo-resistive sensors for ethylene gas sensing applications. This review elucidates the types and specifics of the current research in different ethylene gas sensors. More specifically we detail the operation and working of chemo-resistive ethylene gas sensors at various levels of abstraction. We also discuss the various design challenges in developing ethylene gas sensors and the future trend.

2 Classification of Sensors

Ethylene gas sensors can be broadly classified into the following categories depending on its transduction principle:

- Gas chromatography,
- Electrochemical, and
- Optical.

2.1 Gas Chromatography

Gas chromatography (GC) is one of the conventional techniques that have been used for detection of gas molecules. In this technique, the gaseous mixture is separated by passing it in the GC setup. A typical GC setup includes an inlet, GC column, detectors like flame ionization detector (FID), thermal conductivity detector (TCD), flame ionization detector (FID), alkali flame detector (AFD), flame photometric detector (FPD), etc. so that it can interact with analyte. Such systems have advantages such as high sensitivity, high resolution, low sample volume size, possibility of complex mixture investigation, to mention a few. GC is used to separate and investigate compounds that can be vaporized without decomposition. A typical GC system constitutes a mobile phase (carrier gas like nitrogen and helium), and a stationary phase, i.e., a polymer or liquid microscopic layer in a column. For investigation, the sample mixture is passed through the column coated with a stationary phase. GC with mass spectrometer (GC–MS) can be used to identify component's weight with a trade-off of evaluation time. Over the years, standard GC systems have been extensively used in the detection of ethylene gas. For instance, Pereira et al. [24] in 2017 reported a GC based ethylene detection system depicting a limit of detection in the range of 0.41 ± 0.04 ppm in 2.6 min.

Even though, standard GC systems have been extensively used, such devices have limitations due to bulkiness and are cost intensive in nature. An alternative solution is miniaturized GC systems. For more specifics, readers may refer [25–28]. It may be noted that although GC systems have advantages, application of such systems is limited to thermally stable and volatile compound detection.

2.2 Electrochemical

Electrochemical sensors work on the principle of change in electrical properties of an active material like change in conductivity or resistivity, capacitance, etc., upon chemical reaction/binding of ethylene (targeted) molecules. Thus, such systems are a typical example of chemo-electrical systems. Examples of electrochemical sensors include amperometric and electro-catalytic sensors, chemo-resistive sensors, and chemo-capacitive sensors.

An amperometric sensor measures the relative change in current flowing through a sensing electrode upon detection of ethylene gas molecules. Amperometric sensors are based on the redox reaction process induced by the ethylene gas molecules upon interaction with the sensor. A typical amperometric sensor consists of an anode (sensing electrode-gold), a cathode electrode, electrolyte, diffusion barrier layer, and reference electrode. The electrodes are submerged in an electrolyte (electro-catalytic solution). A voltage source is connected to electrodes resulting in a potential difference between electrodes. Upon exposure, targeted ethylene molecules oxidize the anode resulting in electron transfer and thereby change in current equivalent to concentration of molecules. Sensitivity of the sensor is a function of sensing electrode material mainly its surface area and material. Much focus has been on material selection and techniques to improve the sensitivity of such sensors in recent times [29, 30].

In the case of both chemo-resistive and chemo-capacitive sensors, upon exposure to specific targeted molecules like ethylene, there is a change in electrical property of the sensor in proportion to the concentration of target molecules. For instance, in the case of a chemo-resistive sensor when ethylene molecules interact with sensing element, there is a change in nominal resistance of the sensor, whereas, in the case of a chemo-capacitive sensor, there is a relative change in the initial capacitance value. In both chemo-resistive and chemo-capacitive sensors, the sensing materials for detecting ethylene are typically realized with carbon nanotubes, conductive polymers, and/or semiconductor metal oxides like WO_3, SnO_2, MnO_3 to cite a few. In the last decade or so, much focus has been on choosing the sensing material, fabrication process/technology, and optimizing the process parameters for maximizing sensor performance metrics [31–33]. Although such sensors have various advantages, they suffer from issues such as poor selectivity, reliability constraints, susceptibility to external parameters like moisture and temperature.

2.3 Optical

Optical sensors for ethylene gas detection function on the principle of absorption of incident light and its detection. Typically when light is incident, it gets absorbed or scattered. Entities like ethylene gas molecules depict a specific absorption characteristic for a specific wavelength of light (mid-IR). A typical optical sensor includes

an optical source, cell/chamber with targeted gas (ethylene), an optical detector, and associated optics. For detection, the light is incident in the chamber with the targeted gas. The incident light of a certain specific wavelength is absorbed by the ethylene gas molecules. This specific absorption of light allows detection of targeted molecules as absorption strength of ethylene gas provides a measure (quantification) of ethylene molecular concentration.

In general, optical sensors are classified as dispersive and non-dispersive types. In non-dispersive optical sensors, the light source is broadband and multiple narrow band filters are required to detect targeted molecules by a method of subtraction of interface gases. On the other hand, in dispersive broadband sensors, dispersive elements like prisms are used to segregate the incident light wavelengths. Examples of optical sensors include: (i) non-dispersive infrared spectroscopy [34–36], (ii) laser based sensor [37–39], and (iii) Raman spectroscopy [40–42]. Compared to other sensors, optical sensors depict high sensitivity, resolution, better selectivity, and response time. However, optical sensors are typically bulky, consume high power, and are costly.

In addition to the aforementioned detection techniques like gas chromatography, electrochemical and optics based gas sensors, other detection schemes that are reported in the literature include field effect transistor (FET) based sensors [43, 44], gravimetric sensors [45, 46], colorimetric sensors [47], photoluminescence sensor [48, 49], to cite a few.

3 Chemo-Resistive Sensor: Operation Principle and Performance Metrics

A chemo-resistive sensor constitutes a sensing layer that changes its electrical conductivity upon target molecule interaction. An unexposed sensor has a nominal resistance (R_0). As the sensor surface is coated with receptor molecules that have a high affinity towards the targeted ethylene gas molecules, upon exposure there is a change in the electronic configuration on the sensor surface resulting in a change in the nominal resistance (new resistance value: R_1). This change in the electrical resistance of the sensor is proportional to the ethylene gas concentration. The sensor is connected to a signal processing circuitry which converts this change in the nominal resistance of the sensor into an equivalent electrical signal (voltage value). The sensing operation of a typical chemo-resistive sensor is depicted in Fig. 1.

Performance metrics

Performance metrics of an ethylene gas molecule sensor includes the following:

- Sensitivity,
- Selectivity,
- Response time,
- Recovery time, and
- Dynamic range.

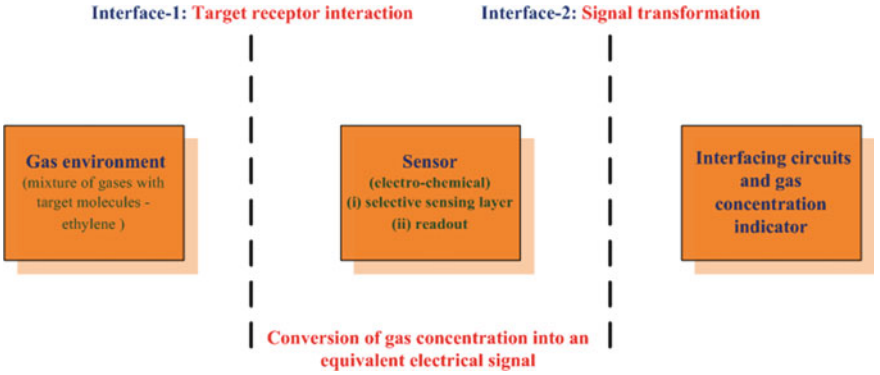

Fig. 1 Operational principle of a typical chemo-resistive sensor with specifics (i) target-receptor interaction interface, (ii) sensor core section, and (iii) signal transformation interface

Table 1 Specifications a typical ethylene gas sensor

Parameters	Value
Detection range (measurand)	10–200 ppm
Sensitivity	1–3 (for 10–200 ppm gas concentration)
Response time	1–2 min
Measurement temp	25–45 °C
Recovery time	2–3 min

Specifications of a typical ethylene gas sensor are summarized in Table 1.

It may be noted that the design of a chemo-resistive ethylene sensor is an interplay between electrical, mechanical, and thermal parameters that impacts the development stages of material selection and geometrical design. Therefore, optimization of the aforementioned performance metrics can be done by rational selection of material set and sensor geometry.

4 Literature Survey

In this section, we summarize the recent developments in the field of ethylene gas sensors over the last decade or so. The sensing property of a ZnO based gas sensor is largely affected by three factors that are as following: (i) temperature, (ii) effect of dopant, and (iii) structural modification.

Operating temperature of the device controls the electron migration, conductivity, and thereby device efficiency. At an elevated temperature, typically the device sensitivity improves due to availability of high energy redox ions capable of overcoming activation energy barrier. However, it also limits the practical applicability of the

device in large scale implementation. Whereas a room temperature (RT) operated gas sensor can become a highly stable low power device suitable for installation in different warehouses and containers. So, for feasible application, a RT operated gas sensor with improved sensing properties is needed.

Gas sensing property of pristine ZnO material can be significantly improved by using dopants, mainly metal. Literature shows different noble metals (Ag), and transition metals (Ni, Cd) that have been used for this purpose. In this section, we summarize the doping effect on the ethylene gas sensing property for ZnO (Table 2).

For instance, Sholehah et al. has shown noble metal (Ag) doped ZnO nanoflakes for ethylene gas sensing. The group reported an improved sensing performance at room temperature. This improvement is due to the phenomenon of surface plasmon resonance (SPR) on the sensor surface. The SPR phenomenon enhances the O_2 absorption process on the surface and eventually helps to achieve fast response and recovery times [52]. This scheme of enhanced performance has been depicted in Fig. 2. Similarly, Li Dianqing et al. used Cd doping in ZnO nano rod [53] for ethylene gas sensing. On the other hand, Shirage et al. has shown gas detection at very low limits (ppm level) with Sr and Ni doped ZnO based gas sensors.

Large surface-to-volume ratio of the nanostructured materials also helps to improve the gas sensing property. In addition, it has been seen that different surface morphology of ZnO nanostructured like (i) nanoflake, (ii) flowerlike, (iii) hemisphere, and (iv) nanorod have shown improved sensitivity, due to their enhanced oxygen adsorption property at the device surface. This high oxygen adsorption property at the surface reduces the resistivity of the device.

In this regard, various researchers have carried out research. For instance, (1) Jun Rao et al. [50] used hollow ZnO structures. Their work reported a fast response time (4 s) and recovery rate (6 s) along with a significant increase (10%) in conductance for 5 ppm ethanol. This is mainly due to the large surface area of the nanomaterials [50], (2) Yi Zeng et al. has used flowerlike ZnO nano rod. Their gas sensor depicted ethanol sensing (~15) property at very low (10 ppm) ethanol level [54], (3) Hui Zhang et al. has reported ZnO hemisphere based gas sensor. It depicted ethanol sensing (80 ppm) [55] at room temperature, (4) Pradipta Samanta et al. has prepared ZnO nanofibre on ITO substrate. Their work reported gas sensing at 15 ppm level [51]. ZnO in the form of nanofiber (1D) [57], nanosheet (2D) [58, 59], and microspheres (3D) [60, 61] have been also reported as sensing elements for detecting gases. For instance, Du et al. [57] reported 1D ZnO nanofiber for sensing acetone with a sensitivity of 125Ra/Rg and a response time of 75 s@100 ppm. Similarly, 2D ZnO nanosheets as the sensing element were reported by Chen et al. [59] that depicted a sensitivity of 0.035Ra/Rg. 3D ZnO microspheres has been reported to detect ethanol and acetone gases. Chen et al. [60] has reported a ZnO microsphere based ethanol gas sensor with a response time and sensitivity of 1 s@2 ppm and 1.66 Ra/Rg respectively at a temperature of 350 °C. Recently, Shi et al. [61] reported an acetone gas sensor with a sensitivity of 36Ra/Rg and a response time of 1 s@ 100 ppm.

Apart from ZnO based nanostructures, there are other materials that have been used for sensing (Table 3). These emerging ethylene gas sensors show impressive room temperature gas sensing properties with excellent response time and sensitivity.

Table 2 ZnO based gas sensors and their sensitivity

Detected gas	Material	Temp	Response	Sensitivity Delta_R/V/I/Ra-Rg	References
Ethanol	ZnO	693 K	2@5 ppm-7 (Ra/Rg) @50 ppm-693 K	5(Ra/Rg)@5–50 ppm	[50]
Methanol	ZnO	250 °C	400–650 (Ohm)@0–15 ppm @250C	250 Ω@15 ppm	[51]
Ethylene	ZnO-Ag (1 mM)	RT	17.2%@29 ppm	74–65 kΩ @0–29 ppm	[52]
Ethanol	ZnO 1D	325 °C	120@400 ppm VOC@350C	–	[53]
Ethanol	ZnO 1D	325 °C	225@400VOC	–	[53]
Ethanol	ZnO	250 °C	<20–154.3@10–100 ppm@12 s response time	134 Ra/Rg	[54]
Ethanol	ZnO	RT	0–28 nA @80 ppm	28 Na	[55]
Methane	ZnO	250 °C	76.6%	–	[56]
Acetone	ZnO 1D (nano fibers)	250 °C	75 s@100 ppm	125 Ra/Rg	[57]
Ethylene	ZnO 2D	200	4 min@29 ppm	17.2 ($\Delta R/Ra$) × 100%	[58]
Ethanol	ZnO 2D (nanosheets)	200	–	0.035 Ra/Rg	[59]
Ethanol	ZnO 3D (microspheres)	350	1 s @ 2 ppm	1.66 Ra/Rg	[60]
Acetone	ZnO 3D (microspheres)	280	1 s @ 100 ppm	36 Ra/Rg	[61]

Note RT depicts room temperature

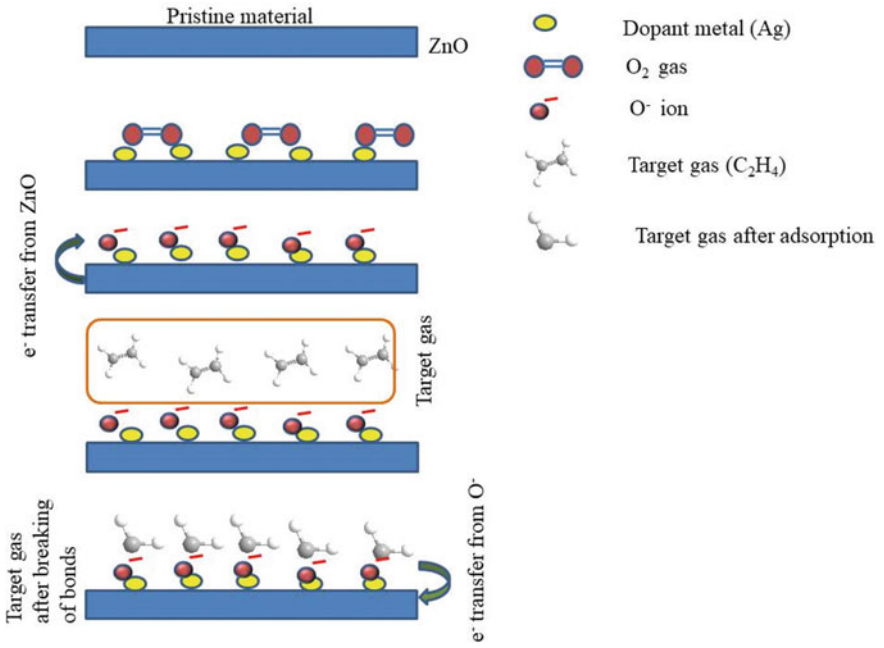

Fig. 2 Metal doped ZnO structure and their gas sensing scheme

5 Design Challenges

Design of electrochemical (chemo-resistive) ethylene gas sensors is challenging as it is a multi-variant complex problem with interdependence between material and geometrical constants. In addition, the performance metrics like sensitivity, selectivity, response time, dynamic range, SNR ratio need to be satisfied. Compared to other sensors like optical, gas chromatographic (GC), chemo-capacitive and chemical techniques, chemo-resistive sensors have advantages such as relatively fast response time, low power consumption, cost-effectiveness, portability along with easiness of handling on-field.

In recent years, much research has been on improving sensitivity, selectivity, detection limit, and response time of such sensors using innovative design strategies at the material and geometrical levels. In addition, to the aforementioned factors, development of chemo-resistive sensors design with low power consumption, high scalability, and portability in a cost-effective manner remains a challenge. However, there are issues that limit the operation of such sensors that include the following: (i) susceptibility to change in physical conditions like temperature and humidity, (ii) relatively low lifetime, (iii) low selectivity, to mention a few. These issues depend on characteristics of sensing layer, fabrication technique, and process parameters.

Table 3 Emerging gas sensors for ethylene

Detected gas	Material	Temp	Response	Sensitivity Delta_R/V/I/Ra-Rg	References
Ethylene	Ionic liquid	RT	100 nA@2000 ppm-300 nA@6000 ppm	0–10 nA@0–10 ppm (normalized)	[57, 62]
Ethylene	8YSZ	550 °C	15-45 mV@50–200 ppm	30 mV	[58, 63]
Ethanol	NiO–SnO	300 °C	25.5@100 ppm	–	[59, 64]
Ethanol	Cu-Graphene	RT	0–50 mV@0–100 ppm	–	[60, 65]
Ethylene oxide	Sm_2O_3-doped SnO_2	200–400 °C	61.9 towards 30 ppm	10^6–10^4 Ω@30 ppm @350 °C	[61, 66]
Ethylene	MWCNT-PEG	RT	0–8@10–100 ppm	–	[62, 67]
Ethylene	120 mM Pd ([$PdCl_2$(PhCN)2]) and 90 mM nitrite (nBu4N[NO_2])-CNT	RT	4@50 ppm	–	[63, 68]
Ethylene	TiO_2-WO_3	250 °C	50@200 ppm	–	[64, 69]
Ethanol	CuO nanoplates	250 °C	–	176@100 ppm	[70]
Ethanol	α-MnO_2 nanoparticles	300 °C	30 s@200 ppm	30.6@200 ppm	[71]
Ethanol	hematite (α-Fe_2O_3)/silver nanoparticles	RT	32 s@20 mgL^{-1}	2.4@20 mgL^{-1}	[72]
Ethanol	Cauliflower-shaped Bi_2O_3–ZnO heterojunction	175 °C	7 s @100 ppm	21.6@100 ppm	[73]

6 Conclusions and Future Trends

In this paper, we review the recent advances in ZnO based electrochemical ethylene gas sensors for evaluation of fruit maturity. Compared to sensing techniques like optical, chemical, chemo-capacitive, and gas chromatography (GC), electrochemical (chemo-resistive) method of ethylene detection holds an edge in terms of its relatively better performance at a lower cost. Development of such sensors is a complex design problem that involves design parameters at material and geometrical levels. Although treatise encompasses various designs of ZnO based electrochemical ethylene gas sensors for evaluating fruit maturity post-harvest, there are issues that limit the operation of such sensors that include the following: (i) susceptibility to change in physical conditions like temperature and humidity, (ii) relatively low shelf life, (iii) low selectivity, to mention a few. These issues depend on characteristics of sensing layer, fabrication technique, and process parameters. With the advancements in nano-technology and expansion in the material set for realizing such sensors, it is expected that the performance metrics of ZnO based electrochemical ethylene gas sensors will improve.

References

1. Zhang J, Dong C, Wang B, Khan I, Ni Y (2017a) J Agric Food Chem, 65:7308–7319
2. Tucker G, Yin X, Zhang A, Wang MM, Zhu Q, Liu X et al (2017) Food Qual Saf 1(4):253–267
3. Saraiva LA, Castelan FP, Gomes BL, Purgatto E, Cordenunsi-Lysenko BR (2018) Food Res Int 105:384–392
4. Cai JH, Cheng SC, Luo F, Zhao YB, Wei BD, Zhou Q, Zhou X, Ji SJ (2019) Food Bioprocess Technol 12(5):883–897
5. Meena KV, Mathew R**,** Jyothi L, Ravi Sankar A (2017) Measurement 111:340–350
6. Meena KV, Mathew R, Ravi Sankar A (2017) Biomed Phys Eng Expr 3:045003
7. Mathew R, Nag K, Sharma A, Krishna A, Sathvik S (2019) Second international conference on applied physics, power and material science (APPM) Secunderabad, Telangana, India
8. Vetrivel S, Mathew R, Ravi Sankar A (2016) Microsyst Technol 1–12
9. Navya Sri R, Vetrivel S, Mathew R, Ravi Sankar A (2015) Indian J Sci Technol 8(19)
10. Vetrivel S, Menon A, Mathew R, Ravi Sankar A (2019) IETE J Res
11. Meena KV, Mathew R, Ravi Sankar A (2018) IEEE sensors 2018, New Delhi, India
12. Vetrivel S, Mathew R, Ravi Sankar (2016) A IEEE international conference ICEE 2016, IIT-Bombay, Mumbai
13. Mathew R, Ravi Sankar A (2018) Nano-Micro Lett 10–35 (2018)
14. Mathew R, Ravi Sankar A (2015) J Phys D: Appl Phys 48:205402
15. Mathew R, Ravi Sankar A (2018) J Nano Sci Nano Technol 18:1636–1647
16. Mathew R, Ravi Sankar A (2016) IEEE international conference ICEE 2016, IIT-Bombay, Mumbai, India
17. Mathew R, Ravi Sankar A (2018) J Micromech Microeng 28:085012
18. Mathew R, Ravi Sankar A (2017) AIP Adv 7:035108
19. Mathew R, Ravi Sankar A (2018) J Nanosci Nanotechnol 18:3387–3397
20. Mathew R, Ravi Sankar A (2019) Mater Res Express 6:086304
21. Mathew R, Ravi Sankar A (2020) Microsyst Technol 2020:1–14
22. Mathew R, Ravi Sankar A (2016) Biomed Phys Eng Express 2(5):055012

23. Mathew R, Ravi Sankar A (2018) IEEE Sens 2018, New Delhi, India
24. Pereira L, Pujol M, Garcia-Mas J, Phillips MA (2017) Plant J 91(1):172–183
25. Sklorz A, Janßen S, Lang W (2012a) Procedia Eng 47:486–489
26. Janssen S, Tessmann T, Lang W (2014b) Sens Actuators B: Chem 197(7):405–413
27. Jedermann R, Praeger U, Geyer M, Lang W (2017) Philos Trans 372:1–21
28. Zaidi NA, Tahir MW, Vinayaka PP, Lucklum F, Vellekoop M, Lang W (2016) Procedia Eng 168:380–383
29. Blanke MM, Shekarriz R (2012) Acta Hort 934:255–262
30. Zevenbergen MA, Wouters D, Dam VA, Brongersma SH, Crego-Calama M (2011) Electrochem Sens Ethylene
31. Matic K, Gerald MG, AnE A, Dieter M, Roland W, Gostner JM (2015) Sens 15(11):28088–28098
32. Kathirvelan J, Vijayaraghavan R, Thomas A (2017) Sens Rev 37(2):147–154
33. Pattananuwat P, daoAht-Ong D (2013) J Macromol Sci Part D—Rev Polym Process 52(2):189–194
34. Janssen S, Schmitt K, Blanke M, Bauersfeld ML, Lang W (2017) Philos Trans R Soc A: Math, Phys Eng Sci 372:1–21
35. Biasio MD, Leitner R, Krall C, Krivec M, Wilk A, Mizaikoff B et al (2017) Sensors, pp 1–3
36. Kathirvelan J, Vijayaraghavan R (2017) Infrared Phys Technol 85:403–409
37. Wang Z, Li Z, Ren W (2016) W. Opt Express 24(4):4143–4154
38. Wang Z, Geng J, Ren W (2017) Appl Spectrosc 71(8):1834–1841
39. Li J, Du Z, Zhang Z, Song L, Guo Q (2017) Sens Rev 37(1):82–87
40. Magnotti GKCU, Varghese PL, Barlow RS (2015) J Quant Spectrosc Radiat Transfer 163:80–101
41. Sandfort V, Goldschmidt J, Wöllenstein J, Palzer S (2018) Sensors 18(3):709–725
42. Zhang Z, Zhan Y, Huang Y, Li G (2017c) Spectrochim Acta Part A Mol Biomol Spectrosc 183:312–318
43. Besar K, Dailey J, Katz HE (2017) ACS Appl Mater Interfaces 9(2):1173–1177
44. Khim D, Ryu GS, Park WT, Kim H, Lee M, Noh YY (2016) Adv Mater 28(14):2752–2759
45. Caprioli F, Quercia L (2014) Sens Actuators, B Chem 203(203):187–196
46. Tolentino MAKP, Albano DRB, Sevilla FB (2018) Sens Actuators, B Chem 254:299–306
47. Li Z, Suslick KS (2019) Anal Chem 91(1):797–802
48. Esser B, Swager TM (2010) Angew Chem 122(47):9056–9059
49. Sun M, Yang X, Zhang Y, Wang S, Wong MW, Ni R et al (2019) J Agric Food Chem 67(1):507–513
50. Rao R, Ang Yu, Changlin S, Xingfu Z (2012) ACS Appl Mater Interfaces 4:5346–5352
51. Samanta P, Bagchi S, Mishra S (2015) Mater Today: Proc 2:4499–4502
52. Sholehah A, Fahrezi Faroz D, Huda N, Utari L, Luh N, Septiani W, Yuliarto B (2020) Chemosensors 8:2
53. Shouli B, Chen L, Li D, Wensheng Y, Pengcheng Y, Zhiyong Chen Aifan L, Chiun Liu C (2010) Sens Actuators B 146:129–137
54. Zeng Y, Zhang T, Wang L, Wang R (2009) J Phys Chem C 113:3442–3448
55. Zhang H, Wu J, Zhai C, Du N, Ma X, Yang D (2007) Nanotechnology 18:455604
56. Bhattacharyya P, Basu PK, Mondal B, Saha H (2008) Microelectron Reliab 48:1772–1779
57. Du H, Yang W, Yi W, Sun Y, Yu N, Wang J (2020) ACS Appl Mater Interfaces 12:23084–23093
58. Sholehah A, Faroz DF, Huda N, Utari L, Septiani NLW, Yuliarto B (2019) Chemosensors 8
59. Chen H, Yu H, Cui S, Liu C (2019) Int J Appl Ceram Technol 17:1460–1466
60. Chen Y, Liu B, Liu J, Pei C, Zhao H, Shang Y, Yang H (2020) J Mater Sci-Mater El 31:6118–6129
61. Shi W, Shang Y, Ahmed MM, Zhao R, Li S, Du J, Li J (2020) Mater Lett 270
62. Zevenbergen MAG, Wouters D, Dam V-A T, Brongersma SH, Crego-Calama M (2011) Anal Chem 83:6300–6307
63. Toldra-ReigF, Pastor D, Serra JM (2019) J Electrochem Soc 166(14):B1343–B1355
64. Liu L J Am Chem Soc (2010)

65. FuW, van Dijkman TF, Lima LMC, Jiang F, Schneider GF,´Bouwman E (2017) Nano Lett 17:7980−7988
66. Singkammo S, Wisitsoraat A, Tuantranont A, Phanichphant S, Yodsri V, Liewhiran C(2018) Appl Surf Sci
67. Liu Z, Yang T, Dong Y, Wang X (2018) Sensors 18:3113
68. Fong D, Shao-Xiong L, Andre RS, Swager TM (2020) ACS Cent Sci 6(4):507–512
69. Kathirvelan J, Vijayaraghavan R, Thomas A (2017) Sens Rev, pp 147–154
70. Umar A, Ibrahim AA, Nakate UT, Albargi H, AlsaiariMA, Ahmed F, Alharthi FA, Alghamdi AA, Al-Zaqri N (2021) Chem Phys Lett 763:138204
71. Umar A, Ibrahim AA, Kumar R, Albargi H, Zeng W, Alhmami MAM, Alsaiari MA, Baskoutas S (2021) Mater Lett 286:129232
72. Garcia-Osorio D, Hidalgo-Falla P, Peres HEM, Gonçalves JM, Araki K, Garcia-Segura S, Picasso G (2021) Sensors 21(2):440. https://doi.org/10.3390/s21020440
73. Wang P, Wang SZ, KangYR, Sun ZS, Wang XD, Meng Y Hong MH, Xie WF (2021) J Alloys Compd 854:157152

Ferroelectric Behavior of Mn Substituted KNN Ceramics

Asha Dahiya, Om Prakash Thakur, and Anjani Kumar Singh

Abstract B-site Manganese (Mn) substituted ferroelectric potassium sodium niobate (KNN) ceramics having compositional formula $K_{0.5}Na_{0.5}Mn_xNb_{1-x}O_3$ (KMNN) with x values 2, 4, and 6% were prepared by conventional mixed oxide process. Substitution of Mn^{4+} into KNN also maintained orthorhombic symmetry confirmed from XRD. Ferroelectric properties of substituted samples were investigated by recording *P–E* hysteresis loops with increasing temperature up to 120 °C. Hysteresis loops with varying temperatures for all materials showed considerable changes in ferroelectric nature. The Mn-substitution improves the ferroelectric parameters like coercive field (E_c), remnant polarization (P_r) and squarness (P_r/P_s) of KNN and also shows the high temperature stability which is good for memory device applications.

Keywords Manganese · Ferroelectric · Remanence

1 Introduction

Lead free perovskite ABO_3 structured $K_{0.5}Na_{0.5}NbO_3$, KNN is one of the most prominent ceramic due to high Curie temperature and spontaneous polarization. It is considered as the best substituent for lead based ceramics for last few years which is good for environment. With these properties it shows high temperature stability, higher electromechanical coupling constant [1–4]. The volatile nature of potassium and sodium is the only issue of concern. During sintering at high temperatures, these elements get vaporized and disturb stoichiometry. Then the density of samples gets decreased in comparison to lead based ceramics which leads to large variations in

A. Dahiya (✉)
Department of Applied Sciences, Bharati Vidyapeeth's College of Engineering, New Delhi, India

O. P. Thakur
Material Analysis and Research Lab, Department of Physics, Netaji Subhas University of Technology, New Delhi, India

A. K. Singh
Department of Physics, ARSD College, New Delhi, India

S. B. Krupanidhi et al. (eds.), *Advanced Functional Materials and Devices*, Springer Proceedings in Materials 14, https://doi.org/10.1007/978-981-16-5971-3_25

different properties like dielectric constant, tangent loss, and piezoelectric constant [5–8].

The above mentioned problem can be resolved by using some modification elements like Li, Sr, Cu, Ti, etc., and by using some special synthesis techniques like hot pressing, spark plasma sintering, molten salt synthesis, and others. Manganese (Mn) is one of good modification element because it works as a sintering aid by decreasing the sintering temperature and the dielectric properties also get enhanced on substitution of it. The ionic radius of Mn^{4+} is comparable to Nb^{5+} with the same co-ordination number so it is called B-site substitution [9–15].

The ferroelectric nature with temperature of Mn-modified compositions KMNN, having composition formula $K_{0.5}Na_{0.5}Mn_xNb_{1-x}O_3$ with $x = 0.00$, 0.02, 0.04, and 0.06 which may be useful for memory device applications are studied in this paper.

2 Experimental Details

In this work, Highly pure precursors are used to synthesize $K_{0.5}Na_{0.5}Mn_xNb_{1-x}O_3$ with varying $x = 0.00 - 0.06$, in steps of 0.02 by conventional mixed oxide process. High energy ball mill was used for 5 h to mix powders in Ethanol in which zirconia balls were used as grinding media. The mixtures were dried and calcined at 200 °C and 850 °C for 4 h respectively. Green pellets of KMNN powders having a diameter 15 mm and thickness of about 1.5 mm were sintered at 1050 °C for 3 h in air and cooled in the furnace. Ferroelectric measurements were done after getting silver electroding on surfaces of pellets at 500 °C for 30 min.

X-Ray Diffraction patterns (XRD) were recorded on Bruker, D-8 Advanced model. To get Ferroelectric properties, i.e., polarization versus electric field loops, Swayer–Tower circuit by applying 20 Hz sinusoidal input signal from 25 to 120 °C was used.

3 Results and Discussion

Figure 1 is presenting room temperature XRD patterns of all 850 °C calcined Mn-modified samples. No extra peak in patterns confirms the absence of any pyrochlore-like phase, so all samples show single phase perovskite structure. The room temperature orthorhombic symmetry like to $KNbO_3$ is observed for all samples. The little shifting of peaks, i.e., shifting of (h k l) planes towards the lower 2θ value with increase in value of Mn content is confirmed from Fig. 1. Bragg's equation is used to calculate the lattice parameters. Higher value of lattice parameters (a, b, c) is observed up to $x = 0.04$. Mn^{4+} has little less ionic radius in comparison to Nb^{5+} and also introduces a liquid phase to the system that prohibits grain growth which decrease c/a ratio in $x = 0.06$ composition. The substitution of Mn^{4+} also leads to

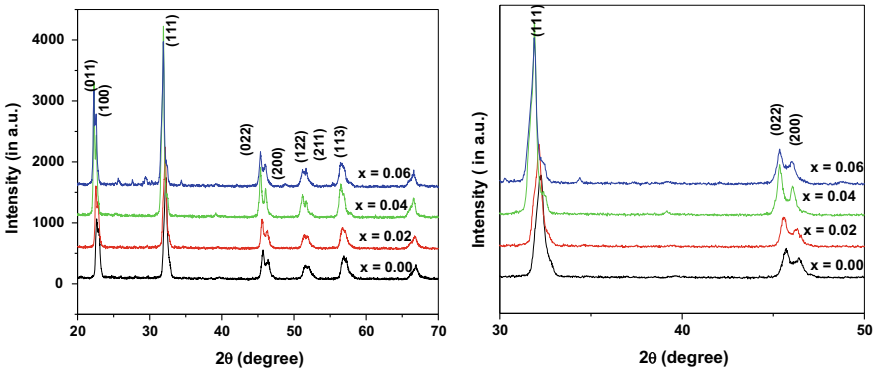

Fig. 1 XRD peaks for calcined compositions with different x values

the shrinkage and smaller grains in the samples which cumulatively results decrease in the bulk densities of all samples.

Ferroelectric behavior at three different electric fields at room temperature (25 °C) for all compositions with $x = 0.00$, 0.02, 0.04 and 0.06 is shown in *a*, *b*, *c* and d part of Fig. 2 respectively. It is observed that substituted samples have good ferroelectric loop with appreciable saturation in comparison to pure samples'. Polarization increases with applied field and reaches saturation at a higher electric field.

P-E loops comparison of all sintered compositions with 25 kV/cm applied field is shown in Fig. 3. Remnant polarization (P_r) was found to decrease with increase in Mn substituted up to $x = 0.04$ with a good value of saturation polarization (P_s). However, value of remnant polarization is maximum for $x = 0.06$ and a symmetric loop is also observed for this case. The room temperature value of remnant polarization (P_r), saturation polarization (P_s), coercive field (E_c), squarness ratio (P_r/P_s), c/a ratio and bulk density for $x = 0.00$ and 0.06 compositions are given in Table 1.

The softening effect of Mn substitution is the reason for reduction of tetragonality for 6 mol % composition. Substitution of Mn relieves the stresses in samples and increase both P_r and P_s [16]. The increase in E_c with a decrease in grain size is reported earlier [17], so increase in coercive field (E_c) for $x = 0.06$ in comparison to $X = 0.02$ and 0.04 can also be explained with average grain size [17–20].

Figure 4 is showing *P–E* hysteresis loops at 30, 70, and 110 °C. Remnant polarization increases for $x = 0.02$ and 0.04 and decrease for $x = 0.06$ ceramics with temperature. This is due to a decrease in the internal energy caused by thermal excitation leading to smaller dipole alignment [21]. The increase in the saturation for $x = 0.06$ with temperature is characteristics of good ferroelectric materials.

Variation of different parameters like E_c, P_r, P_s and P_r/P_s over a range of temperature from 30 to 120 °C for all materials is depicted in Fig. 5. The decrease in E_c and P_r/P_s indicates that material gets softness on heating. Some anomalous trend of all ferroelectric parameters is observed for $x = 0.04$ which may be due to the inhomogeneity in the system. It is noted that value of squarness ratio, i.e., remanence (P_r/P_s)

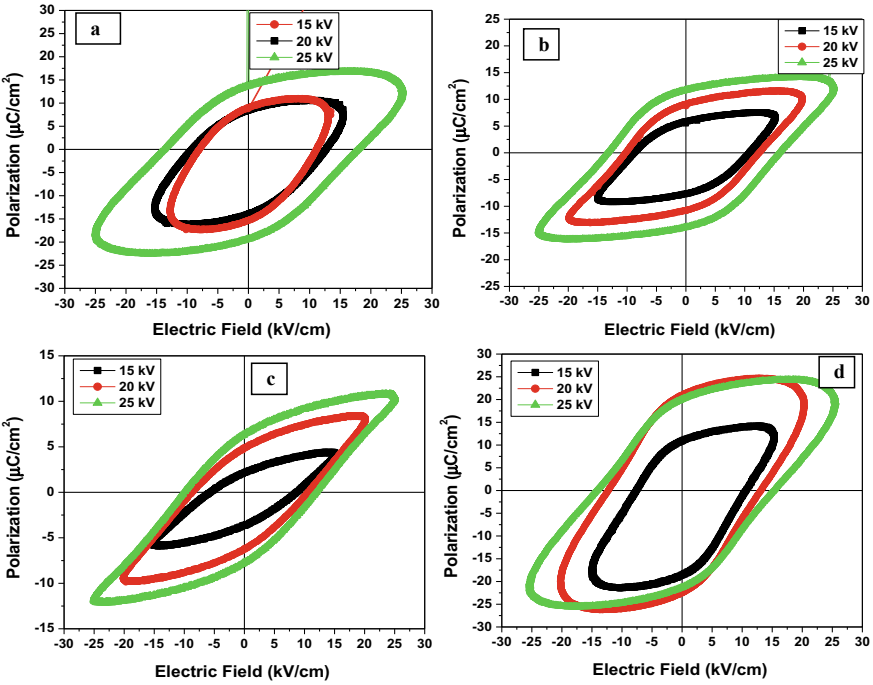

Fig. 2 *P–E* Hysteresis loops of $K_{0.5}Na_{0.5}Mn_xNb_{1-x}O_3$ (KMNN) system with $x = 0.00$, 0.02, 0.04, and 0.06 at different electric fields at 20 Hz in *a*, *b*, *c* and *d* part respectively

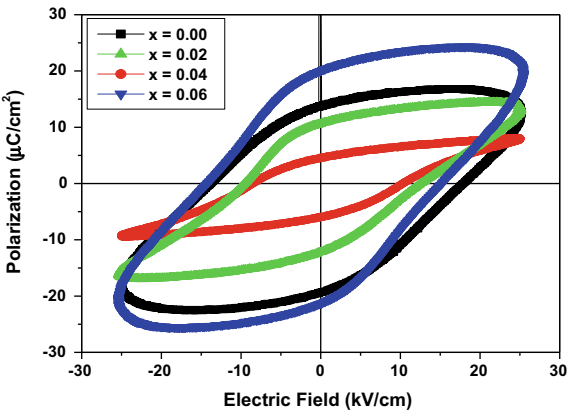

Fig. 3 Room temperature *P–E* Hysteresis loop comparison for different composition of KMNN system at 20 Hz with applied electric field 25 kV/cm

Table 1 Tetragonality (c/a ratio), bulk density, P_r, P_s, E_c, P_r/P_s for $x = 0.00$ and 0.06

S. No.	Value of X	c/a ratio	Bulk density (g/cc)	P_r (μC/cm^2)	P_s (μC/cm^2)	E_c (kV/cm)	P_r/P_s
1	0.00	1.023	3.9516	13.89	16.36	17.67	0.849
2	0.06	1.009	3.8268	19.87	24.19	15.21	0.821

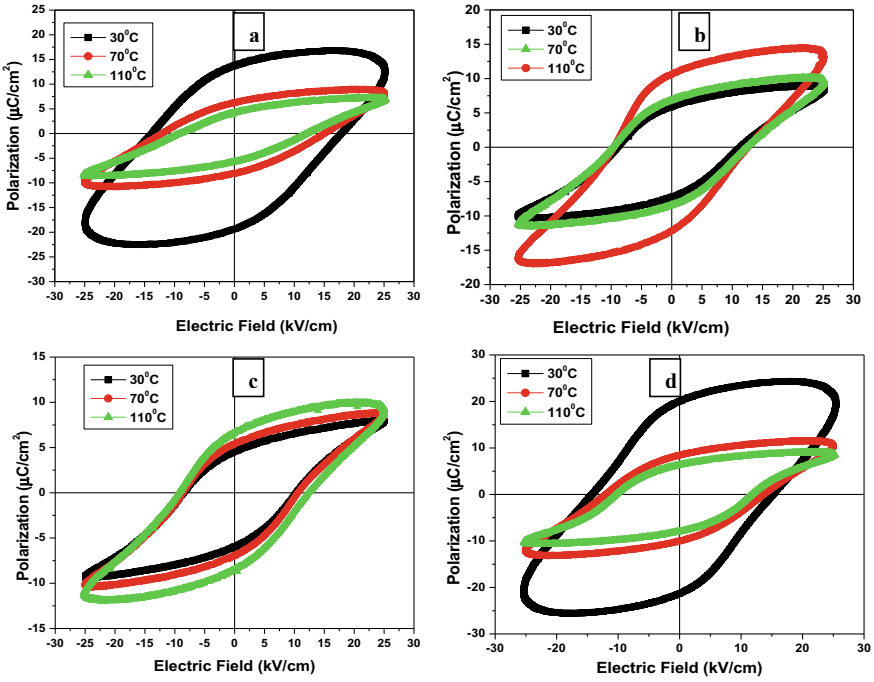

Fig. 4 Temperature dependent hysteresis loops of KMNN systems with $x = 0.00$, 0.02, 0.04 and 0.06 for three different values at 20 Hz and 25 kV/cm

is increased with increase in temperature for $x = 0.04$ but the value is less in comparison to other ceramics systems. The less value of squarness confirmed the less homogeneity in the sample. Higher value of P_r/P_s for $x = 0.06$ attributes the homogenous mixing and accurate fitting of ions at their corresponding lattice site after substitution. It is also observed that all ferroelectric parameters start to increase nearly at 120 °C for substituted ceramics. There may be a dramatic increase in the parameters for further increase in temperature because coexistence of orthorhombic-tetragonal $T_{O\text{-}T}$ phase transition exists in the higher temperature range [22–24].

4 Conclusion

In summary, Pure KNN and Mn substituted KNN, i.e., KMNN ceramics from 0 to 6 mol% substitution with steps of 2 mol% are showing room temperature orthorhombic single phase perovskite structure. P-E plots indicate ferroelectric nature of selected compositions. The comparison of all compositions shows that 6 mol% Mn substitutions can enhance the remnant polarization with lower E_c. 19.87 μC/cm^2 and 15.21 kV/cm are values of P_r and E_c respectively for 6 mol % substituted sample at

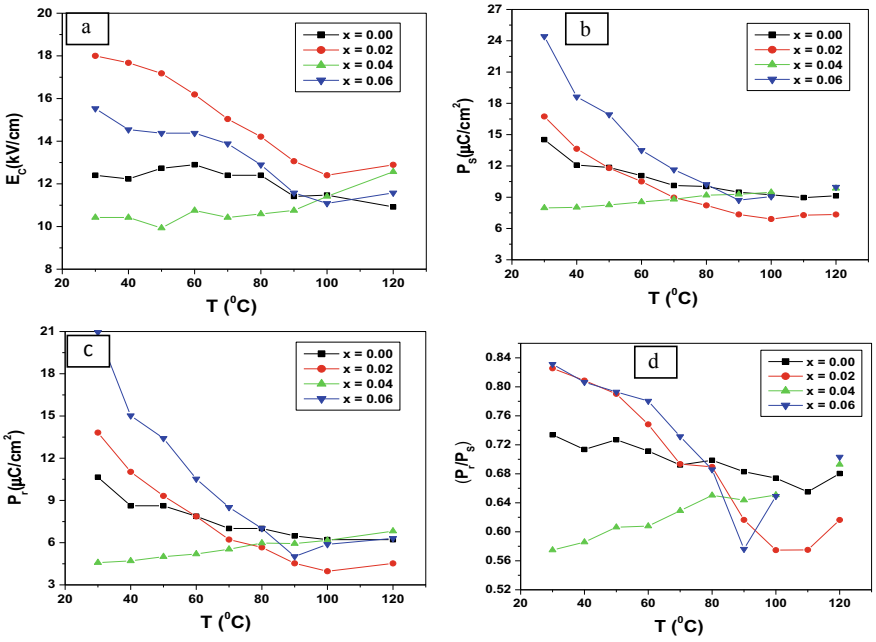

Fig. 5 Plots of E_C, P_r, P_S and P_r/P_S with varying temperatures for KMNN systems at 20 Hz

room temperature. The decrease in coercive field with substitution also indicates that Mn also plays a role of softener for selected initial composition. On basis of present studies, It concludes that composition having 6 mol% Mn is good for ferroelectric memory devices (FERAM) even at higher temperature ranges.

Acknowledgments Asha Dahiya would like to thank ECR Lab., G.V.M Girls College Sonepat for providing research facilities.

References

1. Zuo R, Rodel J, Che R, Li L (2006) Sintering and electrical properties of lead-free $Na_{0.5}K_{0.5}NbO_3$ piezoelectric ceramics. J Am Ceram Soc 89:2010
2. Dahiya A, Thakur OP, Juneja JK, Singh S, Dipti (2014) Comparative study of 2mol% Li- and Mn-substituted lead-free potassium sodium niobate ceramics. Int J Miner Metall Mater 21:1241
3. Hollenstein E, Davis M, Damjanovic D, Setter N (2005) Piezoelectric properties of Li- and Ta-modified $(K_{0.5}Na_{0.5})$ NbO_3 ceramics. Appl Phys Lett 87:182905
4. Ichiki M, Zhang L, Tanaka M, Maeda R, Eur J (2004) Electrical properties of piezoelectric sodium-potassium niobate. Ceram Soc 24:1693
5. Zhang S, Xia R, Shrout TR, Zhang G, Wang J (2006) Piezoelectric properties in perovskite $0.948(K_{0.5}Na_{0.5})$ NbO_3–$0.052LiSbO_3$ lead-free ceramics. J Appl Phys 100:104

6. Yan Y, Cho KH, Priya S (2012) Piezoelectric properties and temperature stability of Mn-doped $Pb(Mg_{1/3}Nb_{2/3})$-$PbZrO_3$-$PbTiO_3$ textured ceramics. Appl Phys Lett 100:132908
7. Poterala SF, Trolier-McKinstry S, Meyer RJ, Messing GL (2011) Processing, texture quality, and piezoelectric properties of <001> C Textured (1-x)$Pb(Mg_{1/3}Nb_{2/3})TiO_3$-xPbTiOc ceramics. J Appl Phys 110:014105
8. Dahiya A, Thakur OP, Singh AK (2021) Transition metal effect on different properties of lead-free KNN ceramics. Mater Today: Proc. 47:1641
9. Chandramani Singh K, Chongtham J, Radhapiyari L, Thakur OP, Bhattacharya DK (2010) Structure and electrical properties of Li- and Ta-substituted $(K_{0.5}Na_{0.5})NbO_3$ lead-free piezoelectric ceramics prepared from nanopowders. J Alloy Compd 496:717
10. Satio Y, Takao H (2006) High performance lead-free piezoelectric ceramics in the (K, Na)NbO_3 – $LiTaO_3$ solid solution system. Ferroelectrics 338:17
11. Guo Y, Kakimoto K, Ohsato H (2004) Phase transitional behavior and piezoelectric properties of $(Na_{0.5}K_{0.5})NbO_3$-$LiNbO_3$ ceramics. Appl Phys Lett 85:4121
12. Li JF, Wang K, Zhang BP, Zhang LM (2006) Ferroelectric and piezoelectric properties of fine-grained $Na_{0.5}K_{0.5}NbO_3$ lead-free piezoelectric ceramics prepared by spark plasma sintering. J Am Ceram Soc 89:706
13. Saito Y, Takao H, Tani T, Nonoyama T, Takatori K, Homma T, Nagaya T, Nakamura M (2004) Lead-free piezoelectric ceramics vs. PZT? Nature 432:84
14. Jaeger RE, Egerton L (1962) Hot pressing of potassium-sodium niobates. J Am Ceram Soc 45:209
15. Carl K (1975) Ferroelectric properties and fatiguing effects of modified $PbTiO_3$ ceramics. Ferroelectrics 9:23
16. Dai X, Xu Z, Li JF, Viehland D (1996) Effects of lanthanum modification on rhombohedral $Pb(Zr_{1-x}Tix)O_3$ ceramics: Part I. Transformation from normal to relaxor ferroelectric behaviors. J Mater Res 11:618
17. Rani R, Sharma S, Rai R, Kholkin AL (2011) Investigation of dielectric and electrical properties of Mn doped sodium potassium niobate ceramic system using impedance spectroscopy. J Appl Phys 110:104102
18. Singh P, Singh S, Juneja J, Raina KK, Pant RP, Prakash C (2010) Effects of samarium doping on the ferroelectric properties of modified lead zirconate titanate ceramics. Int Ferroelectrics 122:23
19. Politova E, Golubko NV, Kaleva GM, Mosunov AV, Sadovskaya NV, Fortalnova EA, Kiselev DA, Ilina TS, Kislyuk AM, Stefanovich SY, Panda PK (2019) Phase transitions, ferroelectric and relaxor properties of nonstoichiometric NBT ceramics. Int Ferroelectrics 196:52
20. Zhang LX, Ren XB (2005) *In situ* observation of reversible domain switching in aged Mn-doped $BaTiO_3$ single crystals. Phys Rev B 71:174108
21. Kumar P, Singh S, Juneja J, Prakash C, Raina KK (2009) Ferroelectric properties of substituted barium titanate ceramics. Physica B 404:1754
22. Dahiya A, Thakur OP, Juneja JK (2013) Sensing and actuating application of potassium sodium niobate. IEEE Xplore 383
23. Mia J, Liu X, Jiang M, Yang H, Chen G, Liu X, Qin L, Luo C (2013) Texture development and dielectric relaxor behavior of $0.80Na_{0.5}Bi_{0.5}TiO_3$-$0.20K_{0.5}Bi_{0.5}TiO_3$ ceramics templated by plate-like $NaNbO_3$ Particles. J Mater Sci: Mater Electron 1676
24. Wang K, Malic B, Wu (2018) Shifting the phase boundary: potassium sodium niobate derivates. J MRS Bull 607

Structural, Electrical and Electrochemical Properties of Fe Doped Orthosilicate Cathode Materials

Nirbhay Singh, Komal Kanwar, Shweta Tanwar, A. L. Sharma, and B. C. Yadav

Abstract We report the paper related to the effect of Fe doping on the $Li_2Fe_xMn_{1-x}SiO_4$ ($x = 0, 0.1, 0.2, 0.3, 0.4, 0.5$) cathode materials synthesized by Sol-Gel technique. X-Ray Diffraction evidences the monoclinic structure with space group *Pn(7)* and crystal size decreases from 43 to 35 nm on doping Fe in Li_2MnSiO_4. Field emission scanning electron microscopy (FESEM) confirms that particle size reduces from 60 to 21 nm with increase of Fe concentration. The impedance analysis shows that highest electrical conductivity was 4.5×10^{-5} Scm^{-1} for $Li_2Fe_{0.4}Mn_{0.6}SiO_4$ cathode material. The initial specific capacity was 152 $mAhg^{-1}$ at the rate of 0.1 C and 131 $mAhg^{-1}$ after the 50th cycle with 86% capacity retention. The doping of Fe enhanced the conductivity by reducing its charge transfer resistance and increasing Li-ion diffusion coefficient than the pure Li_2MnSiO_4 cathode material.

Keywords Orthosilicate · Cathode material · Electrochemical properties · Lithium-ion batteries

1 Introduction

The energy plays a key role in economic development of any nation so each country is trying to set itself as an independent centre in production and storage of energy [1]. Today, the major part of electricity is produced with the help of non-renewable resources which come to ends till 40–70 years, so it is a big challenge in front of the world to generate electricity by using some renewable sources of energy which would be cost effective and easily available [2]. The most popular renewable energy

N. Singh · B. C. Yadav
Department of Physics, BabaSaheb Bhimrao Ambedakar University, Lucknow, UP, India

N. Singh · K. Kanwar · S. Tanwar · A. L. Sharma (✉)
Department of Physics, Central University of Punjab, Bathinda, Punjab, India
e-mail: alsharma@cup.edu.in

K. Kanwar
Department of Physics, Central University of Rajasthan, Ajmer, Rajasthan, India

S. B. Krupanidhi et al. (eds.), *Advanced Functional Materials and Devices*, Springer Proceedings in Materials 14, https://doi.org/10.1007/978-981-16-5971-3_26

resources in order to replace conventional resources produced from hydrocarbon are: solar cells, fuel cells and supercapacitors and Lithium-ion batteries [3]. The Li_2MnSiO_4, shows a higher theoretical capacity of 334 $mAhg^{-1}$ which is obtained on the basis of two redox couples of Mn^{2+}/Mn^{3+} and Mn^{3+}/Mn^{4+} and also provides a higher cell potential at ~4.0 V, than Li_2FeSiO_4 which have a theoretical capacity 166 $mAhg^{-1}$ and cell potential ~3.0 V. On the basis of exhaustive literature reports, it is confirmed that the practical capacity limitation can be improved via doping of Fe in place of Mn cation with different wt% to optimize the concentration.

In the present study, we prepared $Li_2Fe_xMn_{1-x}SiO_4$ cathode material by sol-gel method with different concentrations of Fe doping at 900 °C for 12 h. The effect of Fe doping on the crystal structure, morphology, electrical properties and Li^+ diffusion coefficient was discussed. To improve the poor electronic conductivity of Li_2MnSiO_4 which is ~10^{-15} Scm^{-1} at room temperature [4], we doped Fe in the ratio $x = 0, 0.1, 0.2, 0.3, 0.4$ and 0.5 and investigated the effect of Fe doping on Li_2MnSiO_4 on their electrochemical properties.

2 Experimental

2.1 Precursor Solution

The precursor solution was prepared by dissolving an appropriate amount of $LiNO_3$, $MnCo_3$, $Fe(NO_3)_3$ and SiO_2 in distilled water. To hydrolyze the dissolved solution some droplets of citric acid were added to the precursor solution.

2.2 Preparation of $Li_2Fe_xMn_{1-x}SiO_4$

$Li_2Fe_xMn_{1-x}SiO_4$ was prepared by **sol-gel** synthesis method. The prepared cathode material is label as LFMS and it is prepared for varying the concentration of Fe for $x = 0.1, 0.2, 0.3, 0.4, 0.5$ so label as LFMS-1, LFMS-2, LFMS-3, LFMS-4, LFMS-5 respectively (Fig. 1).

2.3 Characterization Technique

The crystal structure of $Li_2Fe_xMn_{1-x}SiO_4$ was identified by X-Ray powder diffraction (model: Philips. Field emission scanning electron microscopy (FESEM; Merlin Compact). Fourier Transform Infra-red (FTIR) Spectroscopy (Model: Tensor 27. Electrical properties measurements are carried out by CH instrument (Model: 760) from which Electrical Impedance Spectroscopy (EIS) is used to calculate the electrical conductivity of prepared material, Cyclic Voltammetry (CV) is used to find out the power capacity of the prepared materials.

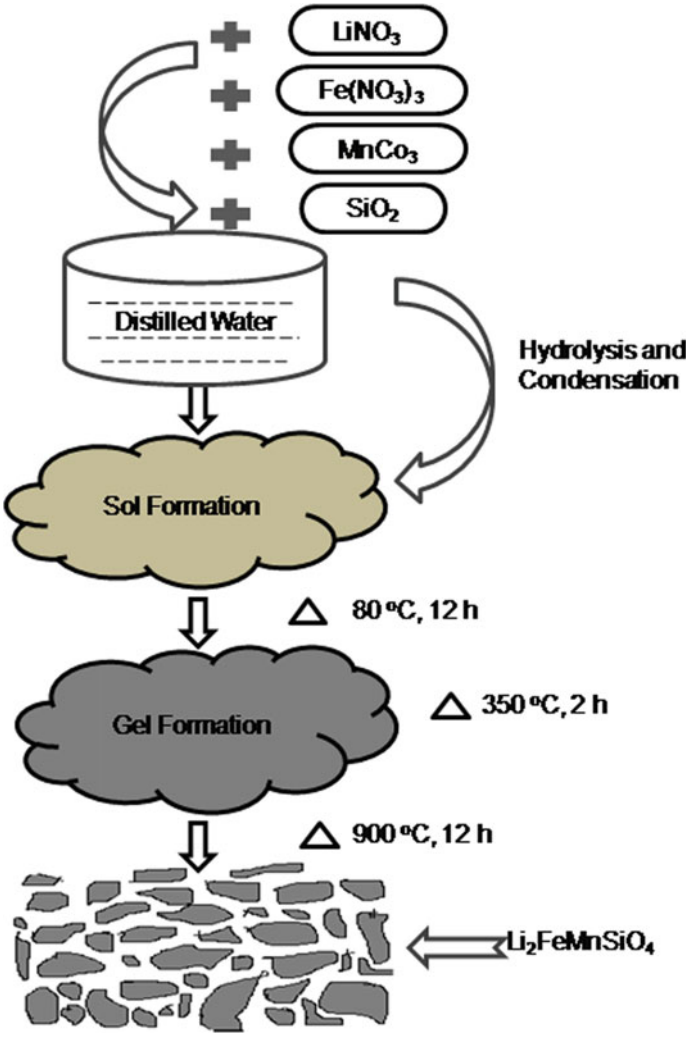

Fig. 1 Schematic diagram of Sol-gel method

3 Results and Discussion

1. **X-Ray Powder Diffraction Analysis (XRD)**
   The X-ray powder diffraction (XRD) of dilithium silicate materials comprising of $Li_2Fe_xMn_{1-x}SiO_4$ ($x = 0$, 0.1, 0.2, 0.3, 0.4 and 0.5) synthesized by sol-gel method at 900 °C are given in Fig. 2. The diffraction analysis has been performed in the wide angle $2\theta = 10°$ to 80^0. The diffraction peaks at 27°, 33°, 38°, 42°, 55° and 65° are associated with the planes (012), (131), (112), (240), (161) and (023) respectively. All the obtained peak intensity closely matches with JCPDS [file

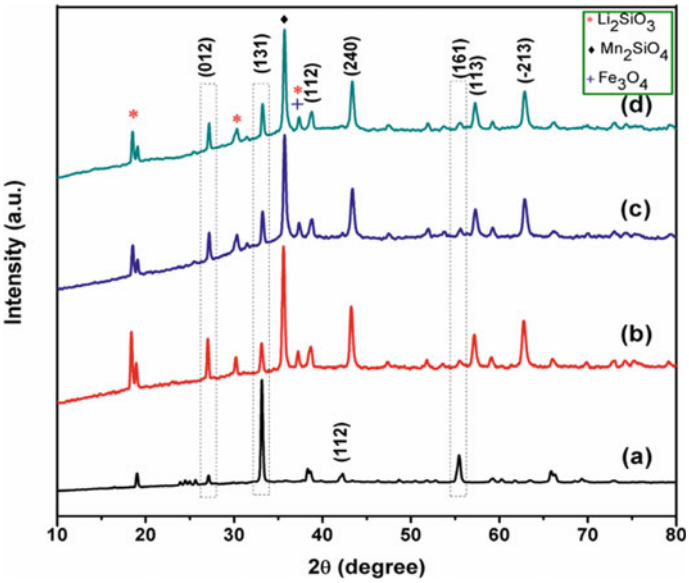

Fig. 2 X-ray diffraction pattern of $Li_2Fe_xMn_{1-x}SiO_4$ **a** $x = 0$, **b** $x = 0.3$, **c** $x = 0.4$ and **d** $x = 0.5$

no. 00-055-0704] file which confirms the monoclinic structure of the samples with space group *Pn(7)*. The impurity phases like Li_2SiO_3 was also presents at an angle 19°, 30°, 37° and Mn_2SiO_4 at angle 35° [5] and Fe_3O_4 at angle 37° in $Li_2Fe_xMn_{1-x}SiO_4$ which are unavoidable. The sifting in peaks occurs firstly at a higher angle (from $x = 0$ to 0.4) after that it starts sifted towards a lower angle (from $x = 0.4$ to 0.5). The shifting in peaks directly correlate with the particle size which shows firstly the crystal size decrease as dopant concentration increases from $x = 0$ to 0.4. The lowest value of size for the $x = 0.4$ will enhance its electrochemical properties like electrical conductivity, energy density, cycle life, etc. which will be analyzed later. The intensity of peaks also first increase from $x = 0$ to 0.4 and after that decreases from $x = 0.4$ to 0.5. All the major peaks of pure Li_2MnSiO_4 are also present after the Fe doping, so there is no strong evidence is observed for structure changes after doping of Fe in pure Li_2MnSiO_4 material.

2. **Field Emission Scanning Electron Microscopy (FESEM) Analysis**

The morphological study was studied by using FESEM. The Fig. 3a shows the surface morphology of pure Li_2MnSiO_4 cathode material. There is no agglomeration between the particles and the calculated average size is about 47 nm. Figure 3b-f shows the surface morphology of $Li_2Mn_xFe_{1-x}SiO_4$ cathode material ($x = 0.1, 0.2, 0.3, 0.4$ and 0.5). As the concentration of Fe increases, particle size reduces because of this the lithium-ion path length decreases and this results in improvement in electrochemical Properties [6]. The possible reason for the reduction in particle size is the decrease in internal stress may increase its binding

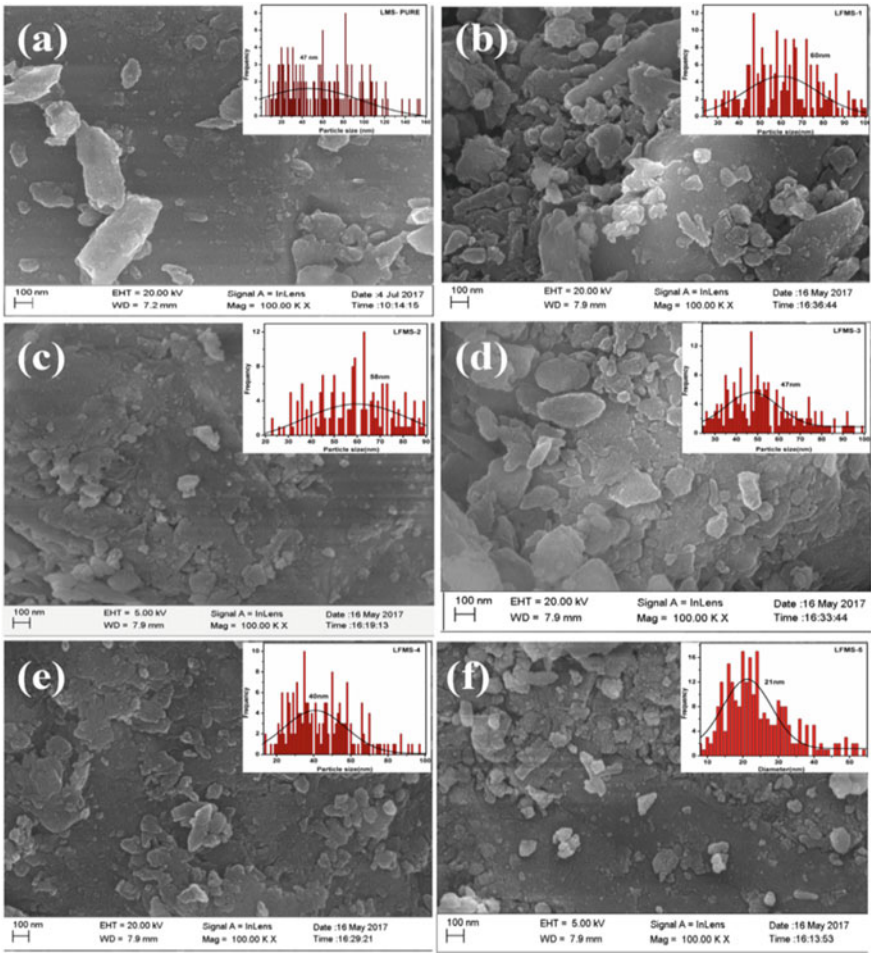

Fig. 3 FESEM images of $Li_2Fe_xMn_{1-x}SiO_4$ **a** $x = 0$, **b** $x = 0.1$, **c** $x = 0.2$ and **d** $x = 0.3$, **e** $x = 0.4$, **f** $x = 0.5$

force with a relative area of its grain boundaries. Particle size calculated from the FESEM is 47, 60, 58, 47, 40 and 20 (all in cm) for LMS, LFMS-1, LFMS-2, LFMS-3, LFMS-4 and LFMS-5 respectively.

3. **Fourier Transform Infra-red Radiation (FTIR)**
FTIR is a powerful technique to identify the functional group, impurity and their bonding with the host material present in the material. FTIR was done in the wavenumber range 400–4000 cm^{-1} with the transmission mode for $Li_2Fe_xMn_{1-x}SiO_4$ material which is given in Fig. 4. The transmission peaks are obtained at 525, 550, 619, 737, 852, 951 and 1070 cm^{-1}. The presence of tetrahedral SiO_4 group was confirmed by FTIR. The vibrational peaks observed

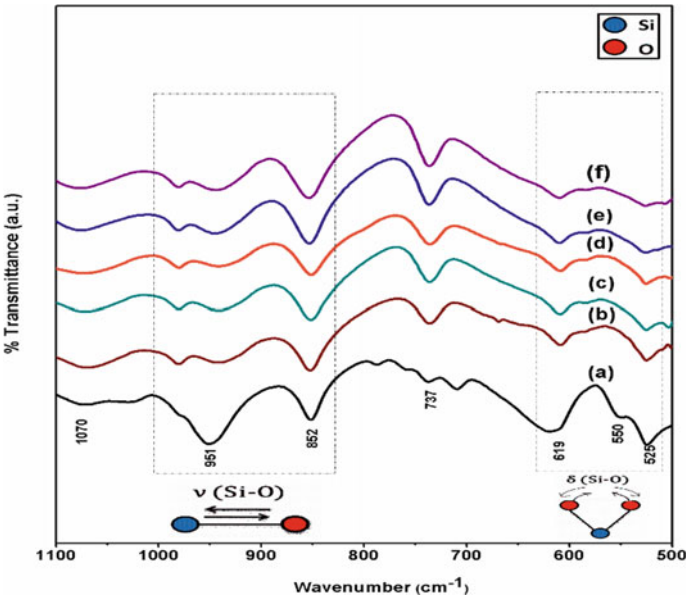

Fig. 4 FTIR spectra of $Li_2Fe_xMn_{1-x}SiO_4$ **a** $x = 0$, **b** $x = 0.1$, **c** $x = 0.2$ and **d** $x = 0.3$, **e** $X = 0.4$, **f** $x = 0.5$

at 951 and 852 cm^{-1} are associated with the stretching vibration of O–Si–O bonds in tetrahedral SiO_4 group. The minor peak at 737 cm^{-1} in Fig. 4 is attributed to bending vibrations of Si–O–Si bonds. There is also an increase or decrease in peak intensity which occurs due to an increase or decrease in the amount of material present in the material. Here, the intensity of peak at 737 cm^{-1} is increases with an increase in the Fe dopant concentration. The vibrational bands at 525, 550 and 619 cm^{-1} is corresponds to bending vibrations of O–Si–O bonds in tetrahedral SiO_4 group [7]. There is a decrease in the peak intensity. The vibrational bands at 1070 cm^{-1} can correspond to Si–O vibrations in Li_2SiO_3. The shifting in peaks also occurs at higher wavenumber as the dopant concentration increases.

Electrochemical Analysis

These analyses are done with an electrochemical workstation CH-760 instrument. The main technique performed are EIS (Electrochemical Impedance Spectroscopy), CV (Cyclic Voltammetry) and GCD (Galvonostatic charge and discharge).

4. **Impedance Spectroscopy Study**

The impedance spectroscopy (Nyquist plot) is performed between the real part and imaginary part of impedance. The prepared cathode materials were sandwiched between two blocking (stainless steel) electrodes and small ac voltage (10 mV) applied in frequency range of 1 Hz to 1 MHz. Figure 5

shows the impedance spectroscopy results of $Li_2Fe_xMn_{1-x}SiO_4$ materials [8]. In order to validate the experimentally obtained data, a nonlinear least square fitting means of ZSImpWin software is performed. On fitting, it is observed that all the experimental data fitted with a series combination of constant phase elements with resistance followed by parallel combination of another constant phase element. Constant phase element (CPE) may be considered as the practical representation of capacitance. In general, it is intermingling of both (resistance and capacitance). The constant phase element can be represented by the formulae:

$$\text{CPE} = \frac{1}{(\omega Q_o)^n}$$

where ω is angular frequency and 'n' is power exponent. The value of $n = 1$ represent the CPE is pure capacitance, $n = 0$ pure resistance and $n = -1$ represents pure inductance. If the n value lies in between 0 and 1 that represents the presence of resistance and capacitance both. The estimated value of bulk resistance from the experiment as well as through fitting was obtained in the range of 6–12 kΩ.

5. **Electrical Conductivity Analysis**

The electrical conductivity of all prepared cathode material samples is obtained using the above discussed impedance spectroscopy results. As the bulk resistance obtained by the line joining of intercept of lower frequency spike and high frequency small semi-circular arc. The formula for estimation of bulk electrical conductivity (σ_{dc}) from bulk resistance is given below:

$$\sigma_{dc} = \frac{1}{R_b}\frac{\ell}{A}$$

where ℓ is sample thickness, A is contact area of electrode and R_b is the bulk resistance of the material calculated from Nyquist plot [9].

From Fig. 5a–f, the estimated value of bulk resistance of LMS, LFMS-1, LFMS-2, LFMS-3, LFMS-4 and LFMS-5 are 6931, 6043, 4708, 3674, 416 and 12,063 Ω respectively with the thickness value $t = 0.02$ cm and $A = 1.07$ (cm^2) for each sample. Conductivity calculated from the bulk resistance is of the order of 2.7×10^{-6}, 3.1×10^{-6}, 4.0×10^{-6}, 5.1×10^{-6}, 4.5×10^{-5} and 1.6×10^{-6} S cm^{-1} for LMS, LFMS-1, LFMS-2, LFMS-3, LFMS-4 and LFMS-5 respectively. As the concentration of dopant-Fe increases, value of electrical conductivity increases this may be possible. The conductivity of the doped sample material is one order higher than the pure material recorded.

6. **Cyclic Voltammetry Analysis**

Cyclic voltammetry (CV) is generally performed in between the definite electrochemical potential through charging and discharging of complete

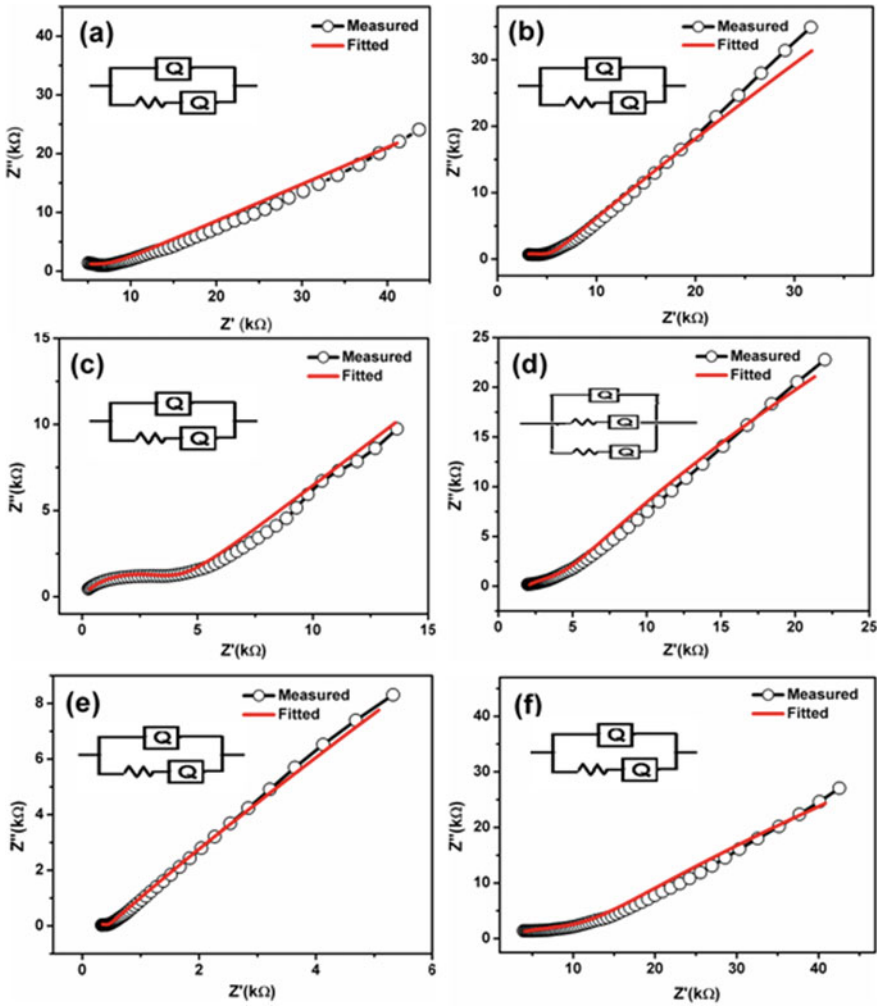

Fig. 5 Impedance spectra of $Li_2Fe_xMn_{1-x}SiO_4$ **a** $x = 0$, **b** $x = 0.1$, **c** $x = 0.2$ and **d** $x = 0.3$, **e** $x = 0.4$, **f** $x = 0.5$

system. It is performed on different scan rates depend upon the current (sensitivity) limit. CV measurement is done between current (Y axis) and potential (X axis) on certain scan rate. The area under the curve directly useful in estimating the energy of the system. The energy density of the system can also be estimated in unit volume or mass based on necessity. During this charging and discharging oxidation and reduction takes place at the anode and cathode invariably. The liberation and deintercalation of lithium ions taken place due to the use of variable oxidation state transition metal ions. This redox reaction use to determine using this technique [10].

Figure 6 shows the cyclic voltammogram of di lithium manganese silicate (Li_2MnSiO_4) and Fe doped di lithium manganese silicate with different weight percent concentrations. Cyclic voltammetry graphs are studied at different scan rates (~0.1 mV/s) for different prepared materials shown in Fig. 6. The power capacity is calculated by multiplying the area of CV curve and current which is 96, 106, 263, 311, 357 and 239 for x = 0, 0.1, 0.2, 0.3, 0.4 and 0.5 respectively. The power capacity is larger for $Li_2Fe_{0.4}Mn_{0.6}SiO_4$ cathode material than the pure sample which indicates that this material is having highest capacity for lithium intercalation or deintercalation process.

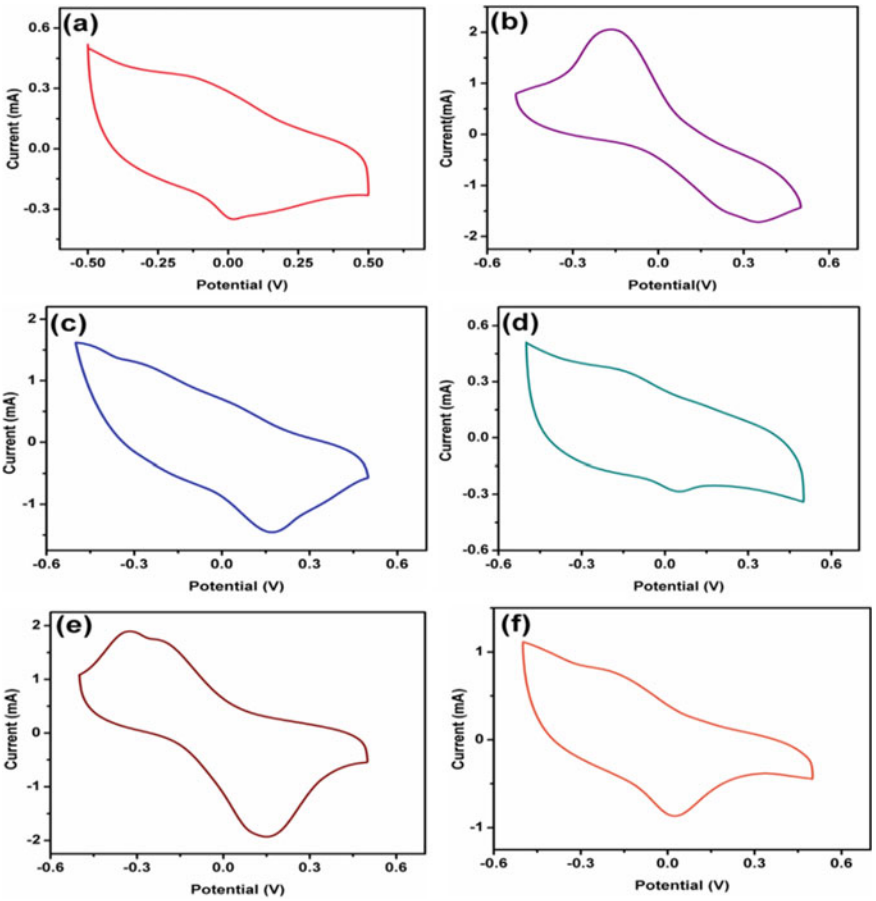

Fig. 6 Cyclic—voltammetry graphs of $Li_2Fe_xMn_{1-x}SiO_4$ **a** $x = 0$, **b** $x = 0.1$, **c** $x = 0.2$ and **d** $x = 0.3$, **e** $x = 0.4$, **f** $x = 0.5$

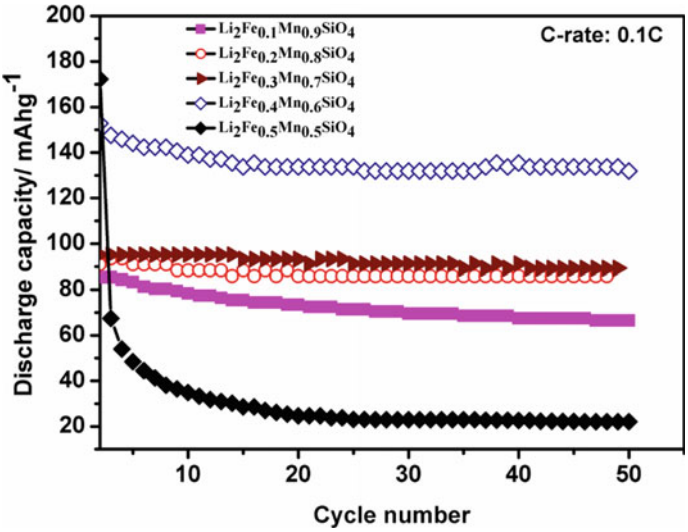

Fig. 7 Retention capacity graphs of $Li_2Fe_xMn_{1-x}SiO_4$ **a** $x = 0.1$, **b** $x = 0.2$, **c** $x = 0.3$ and d $x = 0.4$, **e** $x = 0.5$

Capacity Retention Analysis

This study provides the capacity retention behaviour in Charging and discharge cycle. Here it is observed on increasing the Fe concentration the value of Discharge capacity increases which is in correlation with electrochemical analysis other studies like CV.

The $Li_2Fe_{0.4}Mn_{0.6}SiO_4$ cathode material gives remarkable results with a discharge capacity 152 mAh/g initially and it is stable after 50 cycles up to 131 mAh/g value of discharge capacity. This material is meeting our expectations. So this material shows good cyclic stability behaviour. For the cathode material Li_2MnSiO_4 if we enhance its all properties then we have to dope Fe at the concentration of 0.4.

The discharge capacity for $Li_2Mn_xFe_{1-x}SiO_4$ is 85, 93, 95, 152, 172 and after 50 cycle it is 66, 85, 89, 131, for $x = 1$, 0.1, 0.2, 0.3, 0.4 and 0.5 respectively (Fig. 7).

References

1. Joshua KP, Mohanalin J, Christa SJ, Bhuvanesh A (2021) A novel autonomous energy management system: solution for a fossil fuel free future. In: Advances in automation, signal processing, instrumentation, and control: select proceedings of i-CASIC 2020, 163
2. Wu W, Sun Z, He Q, Shi X, Ge X, Cheng J, Zhang Z (2021) Boosting lithium-ion transport kinetics by increasing the local lithium-ion concentration gradient in composite anodes of lithium-ion batteries. ACS Appl Mater Interfaces
3. Jacome A, Dépature C, Boulon L, Solano J (2021) A benchmark of different starting modes of a passive fuel cell/ultracapacitor hybrid source for an electric vehicle application. J Energy Storage 35:102280

4. Liu P, Gong Y, Nie S, Fu Q, Li L, Liu N, Chen J (2019) The porous spherical Mn and Ti co-doped Li_2FeSiO_4/C cathodes material for lithium-ion batteries. Ionics 25(8):3611–3621
5. Hergett W, Neef C, Meyer HP, Klingeler R (2021) Challenges in the crystal growth of Li_2FeSiO_4. J Cryst Growth 556:125995
6. Qiu H, Jin D, Wang C, Chen G, Wang L, Yue H, Zhang D (2020) Design of Li_2FeSiO_4 cathode material for enhanced lithium-ion storage performance. Chem Eng J 379:122329
7. Hsu CH, Du TR, Tsao CH, Lin HP, Kuo PL (2019) Hollow Li_2FeSiO_4 spheres as cathode and anode material for lithium-ion battery. J Alloy Compd 797:1007–1012
8. Duan WY, Li T, Li SD, Gao K (2019) Energy storage mechanism of powdery and nano-fibrous Li2FeSiO4 as aqueous capacitor electrode. Mater Lett 250:79–83
9. Thayumanasundaram S, Rangasamy VS, Seo JW, Locquet JP (2019) Novel strategies to improve the structural and electrochemical stability of Li_2CoSiO_4 during cycling. Solid State Ionics 337:161–169
10. Yang F, Xia Z, Huang S, Zhang X, Song Y, Xiao G, Shao G, Liu Y, Deng H, Jiang D, Ouyang Z (2020) High field phase transition of cathode material Li2MnSiO4 for lithium-ion battery. Mater Res Expr 7(2):026104

AdS/CFT Duality and Condensed Matter System: a Brief Overview

Neha Bhatnagar and Sanjay Siwach

Abstract Strongly coupled systems are an important area of research as we still lack a complete theoretical framework to explain their observed novel features. AdS/CFT duality is the most applied theoretical tool to investigate the transport phenomenon of these condensed matter systems. We can also apply this duality to diverse area of research like to explore different phases of Quark Gluon Plasma to study high T_c superconductors and even to explore the dark matter physics. In this work, we had made a small attempt to explore transport coefficients of a non-relativistic condensed matter systems using the duality. We consider Einstein Maxwell Dilaton (EMD) theory and incorporate momentum relaxation in the system by introducing two linear axionic fields and obtain the expressions for finite conductivty, Hall's angle, Lorenz number, and Nernst signal for the boundary theory.

Keywords Strongly coupled system · High T_c superconductor · transport coefficients · EMD theory

1 Introduction

With the advancement in technology, many novel features of strongly coupled condensed matter systems have been observed in the laboratory. But the difficulty arise in realizing these features using traditional theoretical approaches. AdS/CFT duality or commonly called as holography [1] is the only reliable tool available which has successfully captured the salient features of these systems [2]. Using AdS/CFT duality, one can study the dynamics of strongly coupled systems in dimension from a weakly coupled dual gravity theory in $(d + 1)$ dimensions. In the same line of work, features like Hall effect and Nernst effect for the boundary theory have also

N. Bhatnagar (✉)
School of Sciences, Auro University, Surat, Gujarat 394510, India
e-mail: neha.bhatnagar@aurouniversity.edu.in

S. Siwach
Department of Physics, Institute of Science, BHU, Varanasi 221005, India

S. B. Krupanidhi et al. (eds.), *Advanced Functional Materials and Devices*, Springer Proceedings in Materials 14, https://doi.org/10.1007/978-981-16-5971-3_27

been explored [3, 4]. Also, by introducing a charged scalar field in the bulk, it was discovered [5] that one could capture the essential features of a superconductor.

In this work, we have used the holographic EMDA (Einstein Maxwell Dilaton Axion) model to study different transport coefficients of (2+1) dimensional boundary system. Anisotropic scaling betwen spatial and temporal component in the gravity set-up is used to study realistic boundary theory and external magnetic field is applied to study the different effcets. The approach used in this work is phenomological simpler and able to capture transport properties for the boundary theory [6, 7].

2 Holographic Model: EMDA System

We have considered the following gravity action using EMD theory with two different gauge fields and two scalar fields [7],

$$S = \int \mathrm{d}^4x\sqrt{-g}\left(R - \frac{1}{2}(\partial\phi)^2 + V(\phi) - \frac{1}{4}e^{\lambda_1\phi}F_1^2 - \frac{1}{4}e^{\lambda_2\phi}F_2^2 - e^{\lambda_3\phi}\sum_{i=1}^{2}\partial\chi_i^2\right), \tag{1}$$

where F_1 is introduced in the bulk to break Lorentz-symmetry and F_2 incorporate charge in the set-up. $V(\phi) = -2e^{\lambda_0\phi}\Lambda$ is the dilatonic potential and χ_1, and χ_2 are two scalar fields or as called axionic fields. The Einstein field equation using the gravity action is given by,

$$\begin{aligned} R_{\mu\nu} = {} & \frac{1}{2}\partial_\mu\phi\partial_\nu\phi + \Lambda e^{\lambda_0\phi}g_{\mu\nu} + \frac{1}{2}e^{\lambda_3\phi}(\partial_\mu\chi_i\partial_\nu\chi_i) + \frac{1}{2}e^{\lambda_1\phi}(F_{1\mu\rho}F_{1\ \nu}^{\rho} - \frac{1}{4}F_1^2 g_{\mu\nu}) \\ & + \frac{1}{2}e^{\lambda_2\phi}(F_{2\mu\rho}F_{2\ \nu}^{\rho} - \frac{1}{4}F_2^2 g_{\mu\nu}). \end{aligned} \tag{2}$$

The matter fields equations of motion are,

$$\Box\phi = \frac{1}{2}\lambda_3\sum_{i=1}^{2}(\partial\chi_i) + \frac{1}{4}\lambda_1 e^{\lambda_1\phi}F_1^2 + \frac{1}{4}\lambda_2 e^{\lambda_2\phi}F_2^2 + 2\lambda_0\Lambda e^{\lambda_0\phi}, \tag{3}$$

$$\nabla_\mu\left(e^{\lambda_1\phi}F_1^{\mu\nu}\right) = 0, \quad \nabla_\mu\left(e^{\lambda_2\phi}F_2^{\mu\nu}\right) = 0, \tag{4}$$

$$\nabla_\mu\left(e^{\lambda_3\phi}\nabla^\mu\chi_i\right) = 0. \tag{5}$$

The metric ansatz [8–10] used for the above action (1) is,

$$\mathrm{d}s^2 = r^\theta\left(-r^{2z}f(r)\mathrm{d}t^2 + \frac{\mathrm{d}r^2}{r^2 f(r)} + r^2(\mathrm{d}x^2 + \mathrm{d}y^2)\right). \tag{6}$$

and,

$$A_2 = A_2(r)\mathrm{d}t + Bx\mathrm{d}y. \tag{7}$$

where B is the external magnetic field applied, $\chi_1 = \alpha x$ and $\chi_2 = \alpha y$ and α is the strength of the momentum relaxation.

The parameters of this model as obtained from gravity solutions are [10],

$$\gamma = \sqrt{(\theta + 2z - 2)(\theta + 2)}, \qquad \lambda_0 = \frac{-\theta}{\gamma}, \qquad \lambda_1 = \frac{-(4+\theta)}{\gamma}, \tag{8}$$

$$\lambda_2 = \frac{(\theta + 2z - 2)}{\gamma}, \qquad \lambda_3 = \frac{-\gamma}{2+\theta}, \qquad q_1 = \sqrt{2(\theta + z + 2)(z-1)}, \tag{9}$$

with $\Lambda = \frac{-1}{2}(\theta + z + 2)(\theta + z + 1)$ and $\phi = \log r\gamma$. Using A_t component of above gauge field Eq. (4) as called q_i we obtain,

$$J_i^t = r^{-z+3} e^{\lambda_i \phi} (A_i)_t', \tag{10}$$

The black hole factor is given as,

$$f(r) = 1 - \frac{m}{r^{\theta+2+z}} + \frac{\alpha^2}{(z-2)(\theta+2)r^{2z+\theta}} + \frac{B^2 + q_2^2}{2(2+\theta)(\theta+z)r^{2(\theta+z+1)}}. \tag{11}$$

Thus, the expression for Hawking temperature is,

$$T = \frac{2+\theta+z}{4\pi} r_h^z - \frac{q_2^2}{8\pi(\theta+2)} \frac{1}{r_h^{2+z+2\theta}} - \frac{\alpha^2}{4\pi(\theta+2)} \frac{1}{r_h^{\theta+z}}. \tag{12}$$

For numerical calculation, the range for Lifshitz scaling is $1 \leq z < 2$, and $0 \leq \theta < 1$ to maintian the consistency of the equation. After introducing the perturbation in the bulk theory, we capture the features of the boundary theory by studying the response. The coupled equations of motion for the bulk fields are,

$$\begin{aligned}
0 &= (r^{z-3-\theta} f a_{1i}')' + q_1 h_{ti}' + \frac{\omega^2 a_{1i}}{r^{5+z+\theta} f}, \\
0 &= (r^{3z-1+\theta} f a_{2i}')' + q_2 h_{ti}' + \frac{\omega^2 a_{2i}}{r^{3-z-\theta} f} + \epsilon_{ij} \frac{i\omega B h_{tj}}{f r^{3-z-\theta}}, \\
0 &= (r^{5-z} f b_i')' + \frac{\omega^2 b_i}{f r^{3z-3}} - \frac{i\omega\alpha h_{ti}}{f r^{3z-3}}.
\end{aligned} \tag{13}$$

$$\begin{aligned}
0 = (r^{5-z+\theta} h_{ti}')' - q_1 r^{z-1-\theta} a_{1i}' - q_2 r^{z-1-\theta} a_{2i}' + \frac{(\alpha^2 r^{-\theta-2z+2} + B^2 r^{2z-4}) h_{ti}}{f} \\
+ \frac{i\alpha\omega r^{-\theta-2z+2} b_i}{f} + \epsilon_{ij} \frac{i\omega B r^{2z-4} a_{2i}}{f}.
\end{aligned} \tag{14}$$

where ϵ_{ij} is the Levi-Civita tensor.

3 Methodology

To explore the transport properties of boundary system, we have to solve the coupled equations of motion (13) and (14) obtained [6]. The Onsager relation ($J = \tau X$) is used in the matrix form with 'X_i' representing the linear sources and 'J_i' the responses,

$$\begin{pmatrix} J_{1i} & J_{1j} \\ J_{2i} & J_{2j} \end{pmatrix} = \tau \begin{pmatrix} X_{1i} & X_{1j} \\ X_{2i} & X_{2j} \end{pmatrix}, \tag{15}$$

τ contain different transport coefficients. Thus, linearized equations of motion (13) and (14) in metric form are given as,

$$\tau = \begin{Vmatrix} -r^{z-3-\theta} f a_{1i'} \\ -r^{3z-1+\theta} f a'_{2i} \\ -r^{5-z} f b'_i \\ -r^{5-z+\theta} h'_{ti} \end{Vmatrix} \begin{Vmatrix} i\omega a_{1i} \\ i\omega a_{2i} \\ i\omega b_i \\ i\omega h_{ti} \end{Vmatrix}^{-1} \tag{16}$$

Working in limiting condition, $f(r_h) = 0$ we obtain τ_h.

$$\tau_h = \begin{pmatrix} r_h^{-3-z} & 0 & 0 & 0 \\ 0 & r_h^{-3+3z} & 0 & \frac{-Br_h^{-3+3z}}{\omega} \\ 0 & 0 & r_h^{-2z+4} & \frac{\alpha r_h^{-2z+4}}{i\omega} \\ \frac{q_1}{i\omega} & \frac{iBr_h^{-3+2z}+q_2}{i\omega} & \frac{r_h^{4-2z}}{i\omega} & -\frac{B^2 r_h^{3z-3}+\alpha^2 r_h^{4-2z}-iq_2 B}{\omega^2} \end{pmatrix} \tag{17}$$

By substituting τ_h in Eq. (16), our flow equations gets simplified to first order in the near horizon limit,

$$\begin{aligned} (-r_h^{-2} f a_{1i})' &= r_h^{-3-z} i\omega a_{1i}, \\ (-r_h^{4z-2} f a_{2i})' &= r_h^{-3+3z} i\omega a_{2i} + \epsilon_{ij} iB r_h^{-3+3z} h_{tj}, \\ (-r_h^{5-z} f b_i)' &= r_h^{-2z+4} i\omega b_i + \alpha r_h^{-2z+4} h_{ti}, \\ (-r_h^4 h_{ti})' &= (iBr_h^{-3+3z} + q_2) a_{2i} + r_h^{4-2z} \alpha b_i + q_1 a_{1i} \\ &\quad - \frac{(iB^2 r_h^{3z-3} + \alpha^2 r_h^{4-2z} + q_2 B) h_{tj}}{\omega}. \end{aligned} \tag{18}$$

$$\begin{aligned} h_{ti}|_{r=r_h} = &-i\omega \frac{(q_1 r_h^{-z-1}) a_{1i} + \epsilon_{ij}(q_2 r_h^{-z-1} + iBr_h^{2z-4}) a_{2j}}{(B^2 r_h^{2z-4} + \alpha^2 r_h^{-3z+3}) - iq_2 B r_h^{-z-1}} \\ &- \frac{i\alpha\omega r_h^{-3z+3} b_i}{(B^2 r_h^{2z-4} + \alpha^2 r_h^{-3z+3}) - iq_2 B r_h^{-z-1}}. \end{aligned} \tag{19}$$

3.1 DC Conductivity

The expression for conserved currents for A_1 is obtained using the gauge field Eq. (13), $J_{1i} = -r^{z-3-\theta} f a'_{1i} - q_1 h_{ti}$. On substituting Eq. (18), the expression takes the form,

$$J_{1i} = r_h^{-3-z} i\omega a_{1i} - q_1 h_{ti}. \tag{20}$$

From Eq. (19), we obtain the expression for DC conductivity,

$$\sigma_{ij} = \frac{\partial J_i}{\partial E_j}, \qquad \text{where} \quad E_j = i\omega a_j. \tag{21}$$

Thus,

$$\sigma_{xx}^{11} = \sigma_{yy}^{11} = r_h^{-3-z} + \frac{q_1^2 \left(B^2 r_h^{z-5} + \alpha^2 r_h^{-4z+2}\right)}{(B^2 r_h^{2z-4} + \alpha^2 r_h^{-3z+3})^2 + B^2 q_2^2 r_h^{-2z-2}}, \tag{22}$$

Also, since we have used two different gauge fields in the set-up, we have some mixed terms for DC conductivity given as,

$$\sigma_{xx}^{12} = \sigma_{yy}^{12} = \frac{q_1 q_2 \alpha^2 r_h^{-4z+2}}{(B^2 r_h^{2z-4} + \alpha^2 r_h^{-3z+3})^2 + B^2 q_2^2 r_h^{-2z-2}}, \tag{23}$$

$$\sigma_{xy}^{12} = -\sigma_{yx}^{12} = q_1 B \frac{B^2 r_h^{4z-8} + \alpha^2 r_h^{-z-1} + q_2^2 r_h^{-2-2z}}{(B^2 r_h^{2z-4} + \alpha^2 r_h^{-3z+3})^2 + B^2 q_2^2 r_h^{-2z-2}}. \tag{24}$$

For A_2, the expression for conductivity obtained is as follows,

$$\sigma_{xx}^{22} = \sigma_{yy}^{22} = \frac{\alpha^2 r_h^{2z-4} [B^2 + r_h^{-5z+7} (q_2^2 r_h^{-z-1} + \alpha^2)]}{B^2 q_2^2 r_h^{-2z-2} + (B^2 r_h^{2z-4} + \alpha^2 r_h^{-3z+3})^2}, \tag{25}$$

$$\sigma_{xy}^{22} = -\sigma_{yx}^{22} = \frac{q_2 B r_h^{4z-8} \left[B^2 + r_h^{-5z+7} \left(q_2^2 r_h^{-z-1} + 2\alpha^2\right)\right]}{B^2 q_2^2 r_h^{-2z-2} + \left(B^2 r_h^{2z-4} + \alpha^2 r_h^{3-3z}\right)^2}, \tag{26}$$

3.2 Halls Angle θ_H

The expression for θ_{H} is obtained using conductivity Eqs. (25) and (26), $\tan\theta_H = \frac{\sigma_{xy}^{22}}{\sigma_{xx}^{22}}$

$$\theta_H = \frac{q_2 r_h^{2z-4} B \left[r_h^{7-5z} \left(q_2^2 r_h^{-z-1} + 2\alpha^2\right) + B^2\right]}{\alpha^2 \left[r_h^{7-5z} \left(q_2^2 r_h^{-z-1} + \alpha^2\right) + B^2\right]} \tag{27}$$

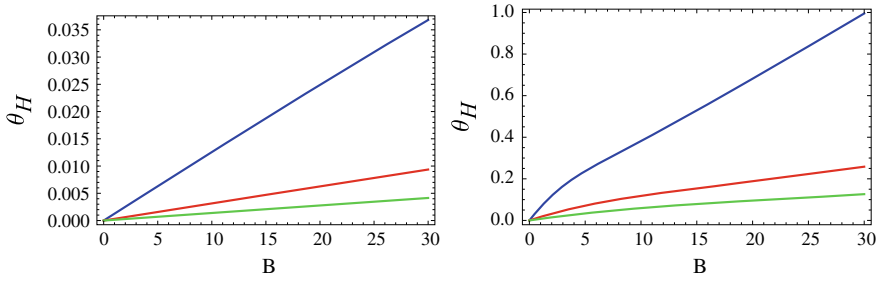

Fig. 1 Variation of θ_H with B for $z = 1$ (left plot) and $z = 4/3$ (right plot) for $\alpha = 3$ (blue), 6 (red) and 9 (green)

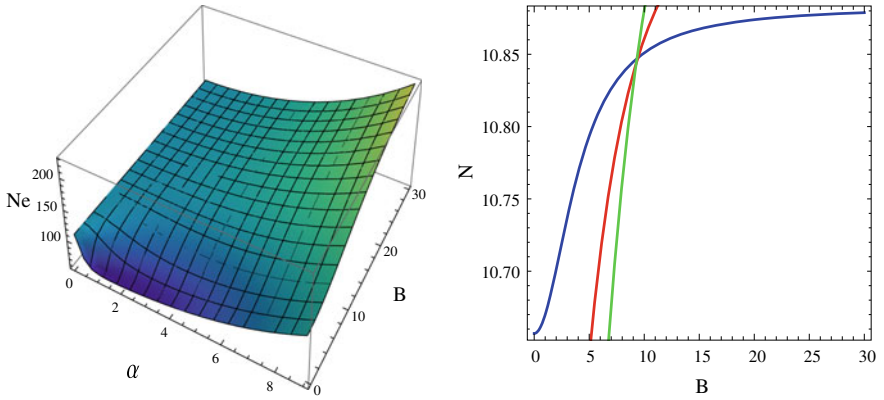

Fig. 2 Variation of N_e with B and α

We can obtain the temperature dependence of θ_H from the above expression as,

$$\text{For } z = 1, \theta_{\text{H}} \sim 1/T^2, \quad z = 4/3, \theta_{\text{H}} \sim 1/T \quad \& \quad z \to 2, \theta_{\text{H}} \sim 1/T^0$$

We have plot the dependence of Hall angle and magnetic field as shown in Fig. 1. We have kept the other parameters as constant and observed the difference in pattern for non-trivial z scaling, which could be related to strange metals behavior.

The expression for the Nernst signal is obtained using, $N_e = -(\sigma^{-1}\alpha)^x_y$,

$$N_e = \frac{4\pi r_h^{z+1}\left(B^2 r_h^{6z} + {q_2}^2 r_h^6 + \alpha^2 r_h^{z+7}\right)}{q_2\left(B^2 r_h^{6z} + q_2^2 r_h^6 + 2\alpha^2 r_h^{z+7}\right)} \tag{28}$$

The variation of Nernst signal with B and the momentum dissipiation strength is shown in Fig. 2. In 3D plot (left side Fig. 2), we have observed the dependence of Nernst signal on B applied and momentum dissipitaion strength. In 2D plot (right side Fig. 2), we have explicitly show the Nernst signal strength for different momentum relaxation condition, α 0.5 (blue), 1 (red), and 1.5 (green).

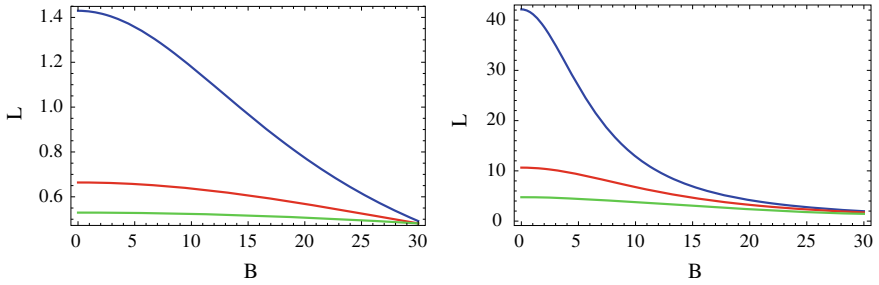

Fig. 3 Variation of θ_H with B for $z = 1$(left) and $z = 4/3$(right) for $\alpha = 3$(blue),6(red) and 9(green)

3.3 Lorenz Ratio

To obtain the expression for Lorenz ratio, we use the expression of thermal conductivity and DC conductivity as shown,

$$L = \frac{\bar{\kappa}_{xy}}{\sigma_{xy} T} = \frac{16\pi^2 r_h^{8+2z}}{q_2^2 r_h^6 + B^2 r_h^{6z} + 2\alpha^2 r_h^{7+z}}, \tag{29}$$

For limiting condition, i.e, $T = 0$ and $B \to 0$ for $z = 1$ we obtain,

$$\bar{L} = \frac{\bar{\kappa}_{xx}}{\sigma_{xx} T}|_{B,T\to 0} = \frac{4}{3}\pi^2 \left(1 + \frac{\alpha^2}{\sqrt{12q_2^2 + \alpha^4}}\right) \tag{30}$$

The expression for Lorenz ratio at $B = 0$ states that the Wiedemann-Franz (WF) law is valid and one can conclude Fermi-liquid type behavior for the system. In our case, we have observed metal like behavior for $z = 1$. But with the nontrivial z scaling, the strange metals behavior as shown in Fig. 3 is observed, and WF law is stated violated.

4 Results and Discussion

In this work, we have given a brief overview on how a holographic technique can be used to establish a connection between strongly coupled condensed matter systems and weakly coupled gravitational theory. We have obtained the expression of transport coefficients for realistic condensed matter system using the flow equations. The main aim is to develop the models in the same universality class as of strongly correlated condensed matter systems. The scalar fields introduced in the bulk models helped in capturing the finite DC conductivity by introducing the momentum relaxation in the system. Non-trivial scaling of dynamical exponent z has captured

many novel features of a boundary theory. The established relation between different parameters of the model and the transport properties of the system indicates that holography is a powerful tool, and we are on a right path to probe any strongly coupled system.

References

1. Maldacena JM (1999) The large N limit of superconformal field theories and supergravity. Int J Theor Phys 38:1113–1133
2. Hartnoll SA, Herzog CP, Horowitz GT (2008) Holographic Superconductors. JHEP 12:015
3. Hartnoll SA, Kovtun P (2007) Hall conductivity from dyonic black holes. Phys Rev D 76:066001
4. Hartnoll SA, Kovtun PK, Muller M, Sachdev S (2007) Theory of the Nernst effect near quantum phase transitions in condensed matter, and in dyonic black holes. Phys Rev B 76:144502
5. Gubser SS, Karch A (2009) From gauge-string duality to strong interactions: a pedestrian's guide. Ann Rev Nucl Part Sci 59:145–168
6. Tian Y, Ge XH, Wu SF (2017) Wilsonian RG-flow approach to holographic transport with momentum dissipation. Phys Rev D 96(4):046011
7. Bhatnagar N, Siwach S (2018) DC conductivity with external magnetic field in hyperscaling violating geometry. Int J Mod Phys A 33(04):1850028
8. Alishahiha M, Colgain EO, Yavartanoo H (2012) Charged black branes with hyperscaling violating factor. JHEP 1211:137
9. Gouteraux B (2014) Charge transport in holography with momentum dissipation. JHEP 1404:181
10. Cremonini S, Liu HS, Lu H, Pope CN (2017) DC conductivities from non-relativistic scaling geometries with momentum dissipation. JHEP 1704:009

Determination of Superdeformed Magic Numbers Using Nilsson Potential

Poonam Jain and Yogesh Kumar

Abstract The single-particle states having axis ratio 2:1 and quadrupole deformation (0.6) in a strongly elongated nuclei using Nilsson potential are investigated. It is observed that large gaps of energy create to deformed magic number over a wide spectrum of quadrupole deformation. We are able to point out the most probable superdeformed (SD) magic numbers for both proton and neutron. The results are compared with other theoretical and experimental works and found a good agreement.

1 Introduction

Structure of a nucleus is a complex entity consists of neutrons and protons. The apparent success of shell model along with the theoretical and experimental finding help researchers to understand the nuclear structure physics. Nuclei undergoes certain changes in variety of shapes and excitation modes due to rotation effect from spherical to superdeformed. The superdeformed (SD) shapes occur possibly by the influence of shell structure effects [1–5]. The work on SD nuclear states is investigated at the cutting edge of nuclear structure. Among many existing theoretical models for SD studies [6–14], a superdeformed nucleus is the one which have shape in ellipsoid form having major to minor axis ratio ≈2:1. The stabilization of such shapes are due to the new shell closures corresponding to magic numbers. It is declared that there are approximately 350 SD bands found in mass land A ∼190,150,130 and even at lower mass regions.

P. Jain (✉)
Department of Physics, Sri Aurobindo College, University of Delhi, Malviya Nagar, New Delhi 110017, India
e-mail: poonam.jn1@gmail.com

Y. Kumar
Department of Physics, Deshbandhu College, University of Delhi, Kalkaji, New Delhi 110019, India
e-mail: ykumar@db.du.ac.in

S. B. Krupanidhi et al. (eds.), *Advanced Functional Materials and Devices*, Springer Proceedings in Materials 14, https://doi.org/10.1007/978-981-16-5971-3_28

A prolate or oblate shape of deformed nuclei was also suggested by Nilsson. The highly elongated nuclei with high deformation (0.6) are known as superdeformed nuclei. Since long, SD rotational bands attracted experimentalists and theoreticians to explore the properties of these bands [15, 16]. In this work, we have focused to calculate the magic numbers (energy gaps) at high deformation using Nilsson model. We have performed the calculations for the single-particle energies for deformed shapes by varying quadrupole deformations.

We organize our paper as follows: In Sect. 2, the theoretical framework of Nilsson potential model is introduced, and the relevant formulas are presented. The results of this model are presented and compared for the SD bands in Sect. 3. Finally, Sect. 4 contains the discussion.

2 Theoretical Framework

The work is mainly based on the investigation of fast rotation of nucleus that may influence the nuclear shell structure. With the help of Nilsson potential, we explored the large gaps of energy spectra, and at the same time, the nuclear spins at which the energy gaps occur.

The beginning point for the description of the intrinsic degrees of freedom is the study of single-particle motion in anisotropic potential with the symmetry and shape exhibited by the observed rotational spectra. The theoretical energy of single-particle eigen values plotted with respect to the quadrupole deformation parameter ($\epsilon_2 = 0.6$) is known as Nilsson diagram [14]. It is observed that large gaps of energy create deformed "magic" numbers over a range of deformations. It is found that an extreme deformations can exist at low excitation energies in which a nucleus possesses magic numbers for neutrons and protons at the same deformation.

We have used Nilsson potential which comprises of the anisotropic harmonic oscillator (AHO) potential in addition to the spin-orbit and centrifugal potentials. It is represented as,

$$H_o = H_o^o + H_\delta \ , \tag{1}$$

where H_o^o, the spherical part is defined as,

$$H_o^o = \frac{1}{2}\hbar\omega_o \left[-\nabla^2 + r^2\right] \ , \tag{2}$$

and H_δ, the deformed part is given as,

$$H_\delta = -\delta\hbar\omega_o \frac{4}{3}\sqrt{\frac{\pi}{5}} r^2 Y_{20} \ , \tag{3}$$

where $r^2 = X^2 + Y^2 + Z^2$ and Y_{20} are the spherical harmonics [17]. The coordinates X, Y, and Z are taken as,

$$X = \sqrt{\frac{m\omega_o}{\hbar\hbar}}x \; ; \; Y = \sqrt{\frac{m\omega_o}{\hbar\hbar}}y \; ; \; Z = \sqrt{\frac{m\omega_o}{\hbar\hbar}}z, \tag{4}$$

The total Hamiltonian by including spin orbit and centrifugal terms is written as,

$$H_o = H_o^o + H_\delta + C\overrightarrow{\ell}.\overrightarrow{s} + D\overrightarrow{\ell}^2. \tag{5}$$

In the above equation, C is the constant defines the spin-orbit force strength and $D\overrightarrow{\ell}^2$ shifts the levels downwards with the higher values of ℓ. The diagonal operators in this case are $\overrightarrow{\ell}^2$, ℓ_z, s_z and j_z with the corresponding quantum numbers being l, Λ, Σ and Ω, respectively. With the constraint $\Omega = \Lambda + \Sigma$, we can choose the base vector to be $\mid Nl\Lambda\Sigma >$.

Matrix element of H_o^o and $\overrightarrow{\ell}^2$ is diagonal. One can expand $\overrightarrow{\ell}.\overrightarrow{s}$ in terms of the ladder operators as,

$$\overrightarrow{\ell}.\overrightarrow{s} = \frac{1}{2}\left(\overrightarrow{\ell}_+\overrightarrow{s}_- + \overrightarrow{\ell}_-\overrightarrow{s}_+\right) + \overrightarrow{\ell}_z\overrightarrow{s}_z \tag{6}$$

which leads to the matrix elements,

$$\begin{aligned}\langle\Lambda'\Sigma'|\overrightarrow{\ell}.\overrightarrow{s}|\Lambda\Sigma\rangle &= \frac{1}{2}\sqrt{(\ell-\Lambda)(\ell+\Lambda+1)}\delta_{\Lambda'\Lambda+1}\delta_{\Sigma'\Sigma-1} \\ &+\frac{1}{2}\sqrt{(\ell+\Lambda)(\ell-\Lambda+1)}\delta_{\Lambda'\Lambda-1}\delta_{\Sigma'\Sigma+1} + \Lambda\Sigma\delta_{\Lambda'\Lambda}\delta_{\Sigma'\Sigma}\,.\end{aligned} \tag{7}$$

Using the Wigner-Eckart theorem of angular momentum, we may write the matrix elements of the spherical harmonics as,

$$\left\langle\ell'\Lambda'|Y_{20}|\ell\Lambda\right\rangle = \sqrt{\frac{5(2\ell+1)}{4\pi(2\ell'+1)}}\begin{pmatrix}\ell & 2 & \ell \\ \Lambda & 0 & \Lambda'\end{pmatrix}\begin{pmatrix}\ell & 2 & \ell \\ 0 & 0 & 0\end{pmatrix} \tag{8}$$

With all the matrix elements available, we set up the Hamiltonian matrix by properly varying the quantum numbers of the basis $|N\ell\Lambda\Sigma >$. Diagonalization of these matrices leads to the energy eigen values which are the energies of single-particle nuclei within the Nilsson model.

3 Results

We have calculated the single-particle states in superdeformed nuclei in which a quadrupole deformation is taken as 0.6 (axis ratio 2:1). Single-particle energy spectrum for anisotropic harmonic oscillator potential is shown in Fig. 1 by circle. Interestingly, we noticed that the magic number for proton generated by Nilsson potential

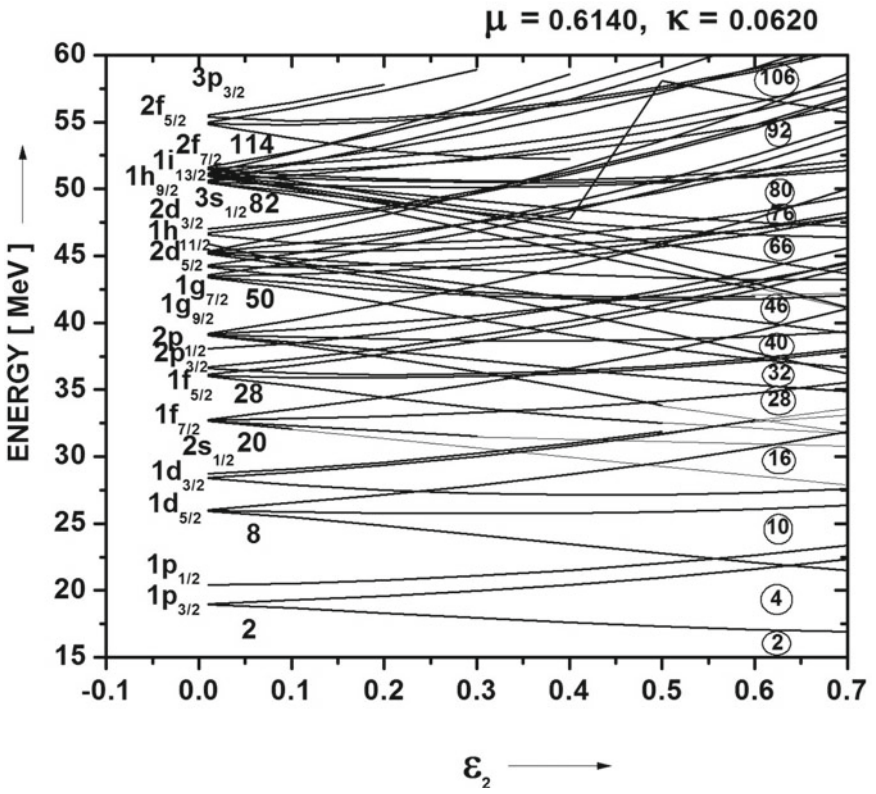

Fig. 1 Energies of single-particle orbitals with respect to function of deformation for proton at deformation 0.6 are shown

are 2, 4, 10, 16, 28, 32, 40, 46, 66, 76, 80, 92, 106. We searched for large gaps which give rise to magic number at higher deformation ($\epsilon_2 = 0.6$) by taking μ and κ in standard values, i.e., 0.6140 and 0.0620, respectively, in the spectrum. We compared our results for proton with the results of Dudek et al. [18] in which the single-particle energy orbitals are plotted by using deformed Nilsson cranked potential and Wood-Saxon potential. In addition to this, the magic numbers at higher deformation shown by Aberg [19] in Fig. 2 are also compared with our results. Thus, our outcomes are significant with these works.

In Fig. 3, we observed the single-particle states for neutron in superdeformed nuclei for quadrupole deformation $\epsilon_2 = 0.6$ with μ and κ are 0.393 and 0.0636, respectively. On comparison, the magic numbers generated by Nilsson potential, i.e., $N = 2, 4, 10, 16, 20, 28, 32, 38, 42, 44$ for lower energy region are in good agreement with the work conducted by Dudek et al. [18] using Nilsson cranked and Wood-Saxon potentials, although there is some anomaly in the higher energy region which needs more analysis. Finally, we are able to provide the total possible SD magic numbers $N = 2, 4, 10, 16, 20, 28, 32, 38, 42, 44, 58, 60, 78, 88$ for neutron.

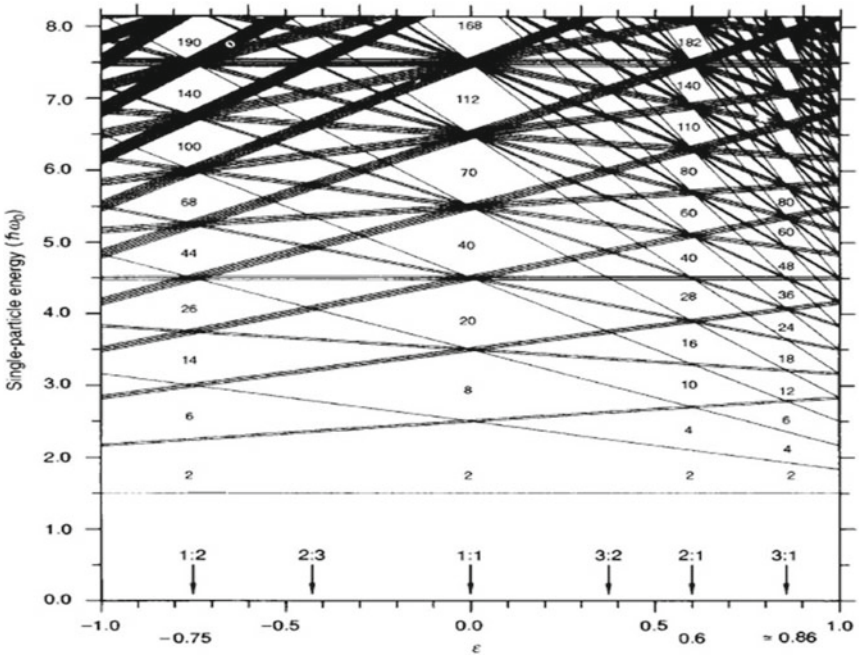

Fig. 2 Energy of single particle with deformation ratio 2:1 at deformation 0.6 is shown

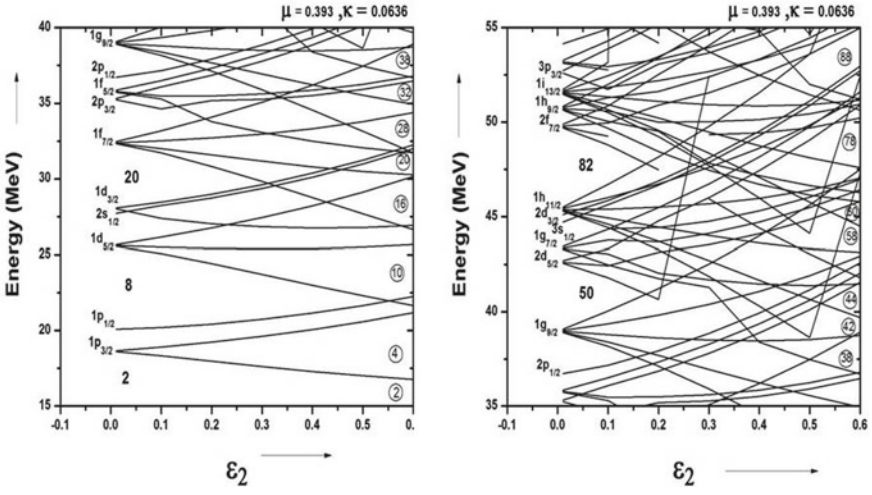

Fig. 3 Energies of single-particle orbitals as a function of deformation for neutron at deformation 0.6 are shown

The results are in conformity with other works up to magic number, 44 as higher region does not have clear indication.

Overall, the magic numbers produced by Nilsson model for proton and neutron are in well agreement as plotted in Figs. 1 and 3. However, we are able to probe the magic numbers for neutron in lower energy region only and found some inconsistency at higher energy. To understand this phenomenon better, more investigations are required in near future.

4 Discussion

The results show that at large nuclear elongations, with an axis ratio 2 : 1, a strong effects of shell are believed at mentioned values of Z and N. Our results furnish the outstanding agreement with the magic number generated using Nilsson cranked and Woods-Saxon potential for proton and in the lower energy region for neutron. The results are also compared with the other works [15, 16, 18, 19]. Overall, the magic numbers are found successfully for SD nuclei using Nilsson potential as well. Significantly, the gaps of energy are achieved by Nilsson potential, and results are in good agreement with both Wood-Saxon and Nilsson cranked potentials.

Acknowledgements The authors are thankful to Delhi University for providing the research facilities to pursue research work in the field of nuclear physics.

References

1. Bengtsson R et al (1975) Yrast bands and high-spin potential-energy surfaces. Phys Lett 57B:301. https://doi.org/10.1016/0370-2693(75)90455-4
2. Andersson CG et al (1976) Nuclear shell structure at very high angular momentum. Nucl Phys A 268:205. https://doi.org/10.1016/0375-9474(76)90461-9
3. Nergaard K, Pashkevich VV (1975) Shell corrections to the deformation energies of very high spin nuclei (I $\leq$ 100). Phys Lett 59B:218. https://doi.org/10.1016/0370-2693(75)90030-1
4. Nergaard K, Pashkevich VV, Frauendorf S (1976) Shell energies of rapidly rotating nuclei. Nucl Phys A 262:61. https://doi.org/10.1016/0375-9474(76)90440-1
5. Ragnarsson I, Bengtsson T, Leander G, Aberg S (1980) Nilsson-Strutinsky model of very high spin states. Nucl Phys A 347:287. https://doi.org/10.1016/0375-9474(80)90530-8
6. Aberg S, Flocard H, Nazarewicz W (1990) Nuclear shapes in mean field theory. Ann Rev Nucl Part Sci 40:439. https://doi.org/10.1146/annurev.ns.40.120190.002255
7. Afanasjev AV, Ragnarsson I (1996) The coexistence of the intruder vi_{132}, superdeformed and terminating bands in the A$\sim$135 mass region. Nucl Phys A 608:176. https://doi.org/10.1016/0375-9474(96)00257-6
8. Terasaki J et al (1995) Superdeformed rotational bands with density dependent pairing interactions. Nucl Phys A 593:1. https://doi.org/10.1016/0375-9474(95)00316-S; (1997) Superdeformed bands of odd nuclei in A=190 region in the quasiparticle picture. Phys Rev C 55:1231. https://doi.org/10.1103/PhysRevC.55.1231
9. Ring P (1996) Relativistic mean field theory in finite nuclei. Prog Part Nucl Phys 37:193. https://doi.org/10.1016/0146-6410(96)00054-3

10. Afanasjev AV, Konig J, Ring P (1996) Superdeformed rotational bands in the A∼140–150 mass region: a cranked relativistic mean field description. Nucl Phys A 608:107. https://doi.org/10.1016/0375-9474(96)00272-2; (1996) Cranked relativistic mean field description of superdeformed bands in ^{83}Sr. Phys Lett B 367:11. https://doi.org/10.1016/0370-2693(95)01414-4
11. Sun Y, Guidry MW (1995) Quantitative description of superdeformed bands with the projected shell model. Phys Rev C 52:R2844. https://doi.org/10.1103/PhysRevC.52.R2844
12. Sun Y, Zhang JY, Guidry MW (1997) Systematic description of Yrast superdeformed bands in even-even nuclei of the mass-190 region. Phys Rev Lett 78:2321. https://doi.org/10.1103/PhysRevLett.78.2321
13. Hara K, Sun Y (1995) Projected shell model and high-spin spectroscopy. Int J Mod Phys E 4(4):637. https://doi.org/10.1142/S0218301395000250
14. Bohr A, Mottelson BK (1975) Nuclear structure, vol II: Nuclear Deformations, Benjamin, Reading, MA
15. U Garg, B Kharraja (2000) Spectroscopy of nuclei under extreme rotation and deformation with large detector arrays. PINSA, 66A, No. 6, 545
16. Sharma N et al (2013) Empirical evidence for magic numbers of superdeformed shapes. Phys Rev C 87:024322. https://doi.org/10.1103/PhysRevC.87.024322
17. Nilsson SG et al (1969) On the nuclear structure and stability of heavy and superheavy elements. Nucl Phys A 131:1. https://doi.org/10.1016/0375-9474(69)90809-4
18. Dudek J et al (1982) Possible superdeformed states in rare earth nuclei studied using the Nilsson and Woods-Saxon potentials. Phys Lett 112B:1. https://doi.org/10.1016/0370-2693(82)90892-9
19. Aberg S (1993) Superdeformed nuclei. Nucl Phys A 557:17c. https://doi.org/10.1016/0375-9474(93)90528-6

Optimization of Mask-Less Laser Lithography

Manisha Bharati, Lokesh Rana, Reema Gupta, Monika Tomar, and Vinay Gupta

Abstract The hybrid microcircuits with small size and low weight are advantageous in medical electronics, space electronics, and other applications. Miniaturization of these circuits makes it convenient for mass scale production and portability, etc. The key step in miniaturization of the devices is lithography which is used to transfer geometric patterns to a substrate or film. The type of lithography used is decided by the minimum dimension of the geometric pattern being used. Present work is focused on the use of Laser lithography technique for the fabrication of microelectronic devices. In the laser lithography technique, the power and focus of the laser light play a very important role. In the present work, results obtained on optimization of the laser power, focus, thickness of the polymer layer, and developing time are presented.

1 Introduction

Lithography is the technique of transference of a geometric pattern on a substrate or a thin film, where dimension of one or more features lies in micrometers or lower range. There are various lithography techniques like photolithography, laser lithography and electron beam lithography which can be utilized for device fabrication [1–4]. Basic steps involved in the lithography technique include coating of a polymer layer on the substrate, exposure of the geometric pattern on the polymer, and developing of the exposed pattern. The polymers used for the lithography technique are called photoresists. It is named so, as when exposed to light it changes its property and becomes susceptible to a certain etchant, i.e., developer. The photoresists are positive or negative depending on its behavior after exposure to light. A positive photoresist get dissolved in the developer when exposed to light due to the weakening of its bond while in the negative photoresist, polymerization of the exposed photoresist occurs

M. Bharati · L. Rana · R. Gupta · V. Gupta (✉)
Department of Physics and Astrophysics, University of Delhi, Delhi-110007, India
e-mail: vgupta@physics.du.ac.in

M. Tomar
Department of Physics, Miranda House, University of Delhi, Delhi-110007, India

S. B. Krupanidhi et al. (eds.), *Advanced Functional Materials and Devices*, Springer Proceedings in Materials 14, https://doi.org/10.1007/978-981-16-5971-3_29

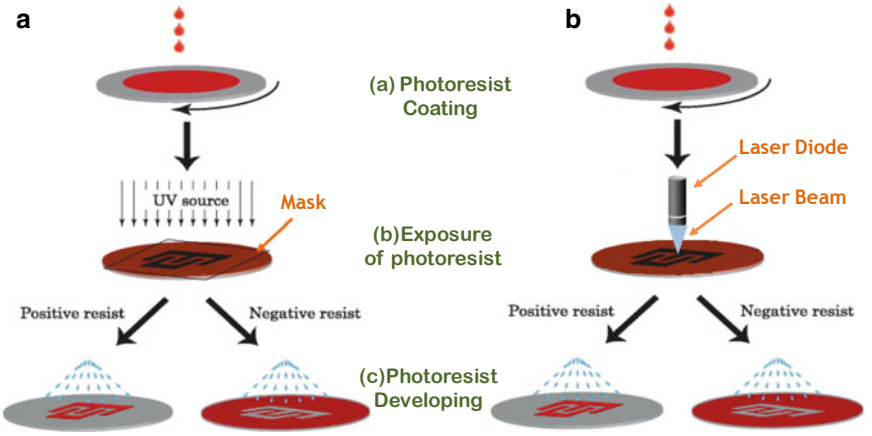

Fig. 1 Schematic of **a** UV photolithography and **b** Mask-less Laser lithography

and the unexposed part gets dissolved in the developer [5, 6]. In the present work, S1813 positive photoresist has been used. Spin coating of the photoresist was done at a speed of 6000 rpm, resulting in a thickness of 1.3 μm.

Figure 1a shows schematic of UV photolithography using a mask and Fig. 1b shows mask-less laser lithography.

There are several advantages of mask-less laser lithography over other lithographic techniques. The minimum resolution size obtained in laser lithography technique is much lower than that of UV photolithography. Also, elimination of the use of masks increases the yield of lithography. Unlike mask-less laser lithography, there is a possibility of obtained 3D patterning in the photoresist, called grayscale lithography. This is possible with varying laser power at different places during the exposure, resulting in the variation of the height of developed photoresist. This technique can be used for fabrication of photomasks used in photolithography. Additionally, power consumption in laser lithography is much less than the e-beam lithography with much faster writing speed.

2 Mask-Less Laser Lithography

Figure 2 shows the schematic of laser lithography unit (Make: Heidelberg Instrument; μPG101) and Table 1 summarizes the different parts of the laser lithography system. To achieve different resolutions, 3 different write heads are being used. Specifications of these write heads are given in Table 2 [7]. For the exposure of a pattern, the photoresist coated sample is kept on the stage below the write head. A softcopy of the pattern is fed and the laser exposes the photoresist accordingly.

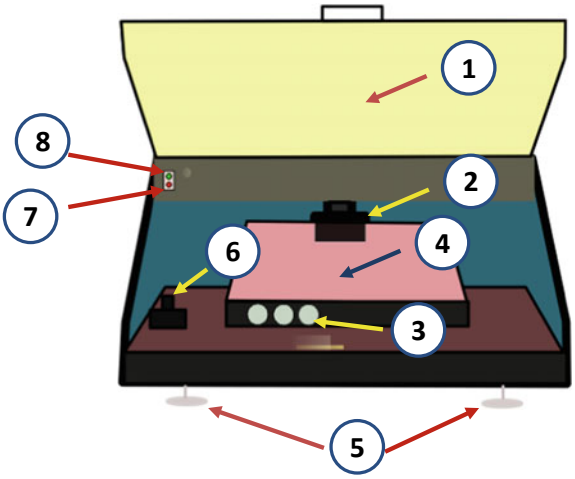

Fig. 2 Schematic of laser lithography unit

Table 1 Different parts of the Laser lithography unit as shown in Fig. 2

1	Cover lid with interlock circuit
2	Write head
3	Vacuum field adjustment screw
4	Stage
5	System base
6	Vacuum switch
7	Safety interlock lamp
8	Power On/Off indicator lamp

Table 2 Specifications of write heads

Parameters	Write head I	Write head II	Write head III
Laser wavelength (nm)	375	375	375
Focal length (mm)	2	4	10
Minimum structure size (μm)	0.6	1.0	2.5
Write speed (mm^2/minute)	1	5	35

3 Optimization of Lithography

For the optimization, 1.3 μm thick positive photoresist layer was coated using a spin coater at 6000 rpm on a silicon substrate. The photoresist coated sample was

prebaked at 90 °C for 30 min. Laser focus and power were optimized using write head III keeping the developing time constant at 1 min. Images of the developed patterns were grabbed using an optical microscope (Make: Leica, Model:DFC 295).

(i) Focus optimization:

Distance of the substrate from the write-head, i.e., focus, plays an important role in obtaining the exact shape and size of the pattern. The write head of the system is connected with a stepper motor which adjusts the distance between it and the sample. This distance, i.e., focus, is being mentioned in terms of arbitrary units here. Poor focus leads to blur edges, which cannot distinguish between a triangle and a circular pattern. Figure 3a shows an exposed pattern with, a focus value of 9, where the contrast between exposed and non-exposed parts is not much. It shows a quite poor focusing. Figure 3b has the sample image with a focus value of 4, which shows improved focusing and where the exposed part has better contrast with sharp edges.

(ii) Power optimization:

After obtaining a good focus, values for the exposed power was varied from 7 to 13mW. Figure 4a shows the image of the sample exposed with a power of 7mW, where, though outlines of the exposed patterns were good due to the good focus value, the photoresist was not exposed throughout owing to poorly developed patterns. Figure 4b shows the sample image, exposed with a power of 13mW, where the power is a little high, leading to the exfoliation of the pattern as visible in the right half of the image. Figure 4c contains the sample image, exposed at a power of 11.8mW, which has better contrast and a clear pattern.

(iii) Developing time:

Developing time of exposed patterns is another important parameter to play with. While optimization of power and focus was done the developing time was kept fixed at 1 min. With optimized value of power and focus developing time was further varied to obtain better resolution. Also for the different write heads, it was imperative to vary

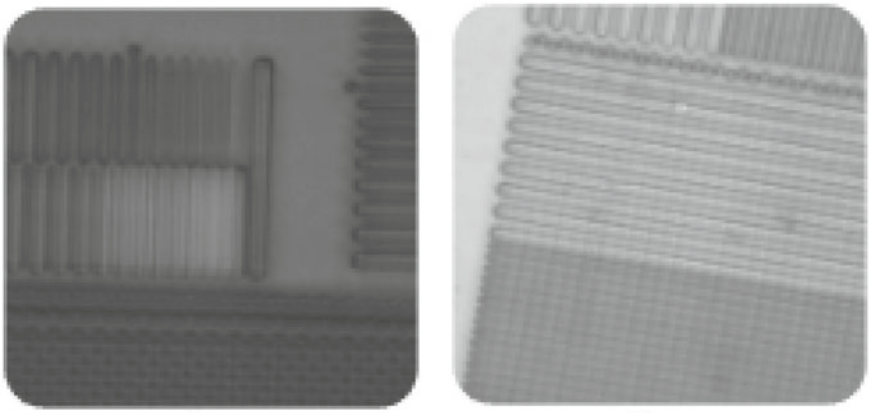

Fig. 3 Exposed sample images with **a** very poor focus and **b** improved focus

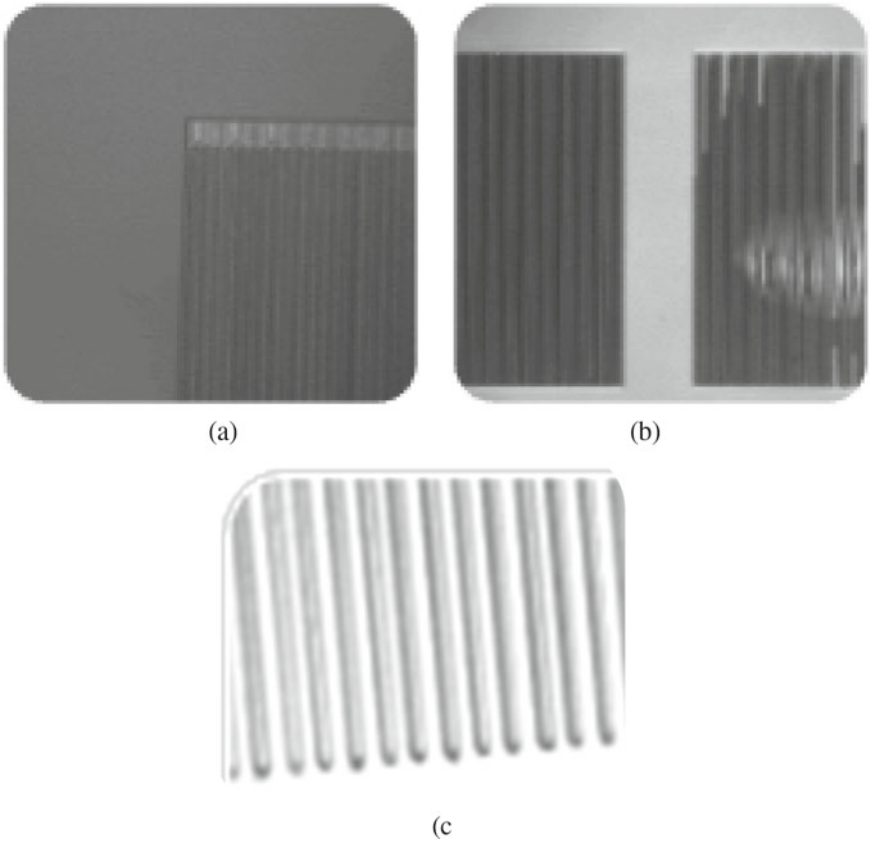

Fig. 4 Exposed sample images with **a** very low power **b** high power and **c** optimized power

the developing time as well. Figure 5a shows the exposed pattern which is slightly underdeveloped, where photoresist from the edges of the pattern is not removed owing to the thinning of the desired pattern. Figure 5b shows the pattern which is slightly overdeveloped leading to undercutting of photoresist and broadening of exposed patterns. Figure 5c is the excessively developed sample image, leading to removal of an almost complete pattern. Figure 5d is the pattern with optimized value of developing time, with the desired dimension of pattern.

4 Discussions

The optimized focus and power of the laser along with the optimized developing time are required for obtaining the correct pattern on substrate. Poor focus adjustment leads to inaccurate imprinting of the pattern on the photoresist with blunt

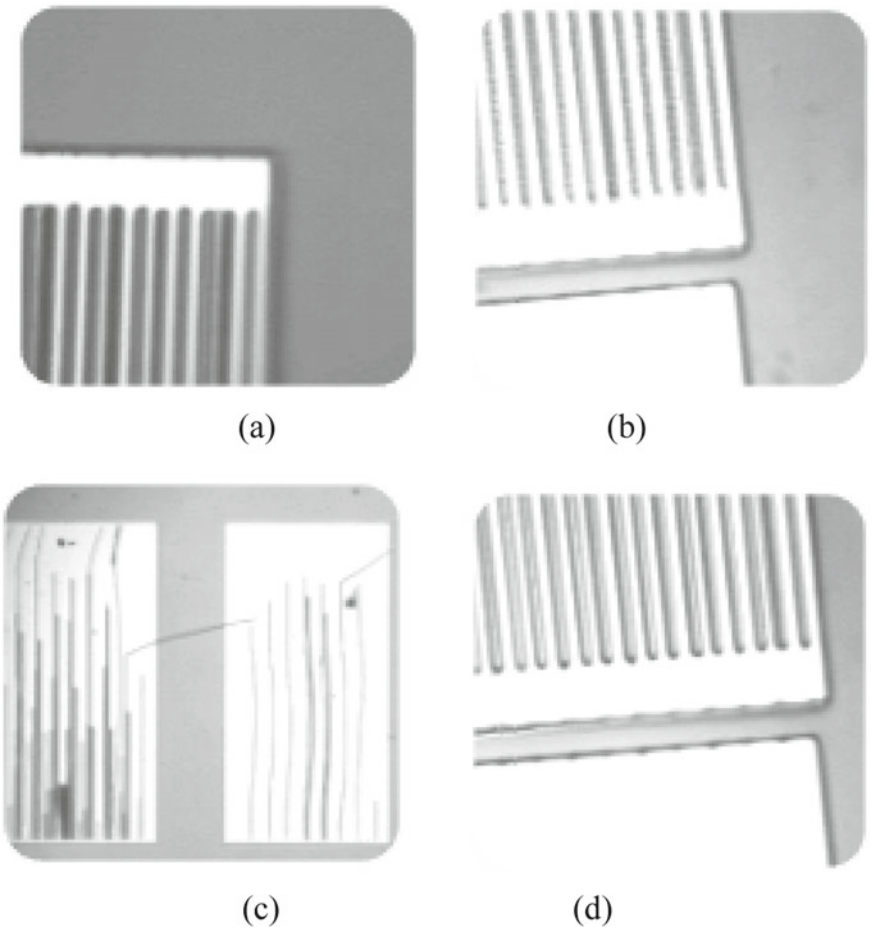

Fig. 5 Exposed sample images with **a** underdeveloped pattern **b** overdeveloped pattern **c** highly overdeveloped pattern and **d** nicely developed patterns

Table 3 Summary of optimized values

Parameters	Write head I	Write head II	Write head III
Focus (a.u.)	11	7	4
Power	1.8 mW	5.8 mW	11.31 mW
Developing time	30 s	40 s	1 min 20 s

edges, while the appropriate power is required for a properly developed pattern. These optimizations were carried out for all three write heads. Additionally, any dust particle in the exposure path leads to scattering of the laser beam, leading to inappropriate pattern development, which calls for the requirement of clean room for the designing of microcircuits. Table 3 summarizes the values of optimized focus power

and developing time for the three different write heads.

Acknowledgments Authors would like to thank DRDO, the Government of India for providing the financial grant to carry out this research work and one of the authors, Manisha Bharati, is thankful to CSIR for research fellowship.

References

1. Ito T, Okazaki S (2000) Pushing the limits of lithography. Nature 406(6799):1027–1031
2. Rana L, Gupta R, Sharma A, Tomar M, Gupta V (2018) Development of MEMS-based lamb wave acoustic devices. IEEE Trans Electron Devices 65(4):1523–1528
3. Radtke D, Duparré J, Zeitner UD, Tünnermann A (2007) Laser lithographic fabrication and characterization of a spherical artificial compound eye. Opt Express 15(6):3067–3077
4. Vieu C, Carcenac F, Pepin A, Chen Y, Mejias M, Lebib A, Manin-Ferlazzo L, Couraud L, Launois H (2000) Electron beam lithography: resolution limits and applications. Appl Surf Sci 164(1–4):111–117
5. Bhagyaraj SM, Oluwafemi OS, Kalarikkal N, Thomas S, editors (2018) Synthesis of inorganic nanomaterials: Advances and key technologies
6. Tilli M, Paulasto-Kröckel M, Petzold M, Theuss H, Motooka T, Lindroos V, editors (2020) Handbook of silicon based MEMS materials and technologies. Elsevier
7. Heidelberg Instruments, μPG101, User guide Manual

Innovative Design for Efficient Solar Cell

Mukesh Kumar, Lokesh Rana, and Amruta Pattnaik

Abstract With increasing population and industrialization, interest in energy is expanding day by day. Knowing the limitations of fossil energy, a lot of researchers are continuing to investigate the different wellsprings of energy. Among different energy sources, for example, sun-oriented energy, wind energy, tidal energy, and biomass energy: Solar energy is the most appealing as the sun is the enormous source of energy. Solar energy can be utilized to produce power legitimately, utilizing photovoltaic cells, or can be utilized as warm energy. Immense exploration is going on in the field of sun-powered photovoltaic cells and still, there is a great scope of extension to increase the effectiveness of solar cells and henceforth decreasing the expense of non-renewable energy. The various factors such as cell Geometry, numbers of absorbing layers, heat generated, and other forms of energy loss affect the efficiency of cells. This paper revolves around the different innovative approaches to investigate several types of losses to increase the productivity of solar cells.

Keywords Solar energy · Solar losses · Energy efficiency · Cell design

1 Introduction

Energy is the need of great importance and everybody is searching for increasingly proficient and dependable strategies and hunger for energy assets too to take care of the requirements of residents. Further, their expanded non-sustainable power source assets abuse is thoroughly destroying the biological parity and nature. The energy age isn't just a tricky issue yet in addition to their productive use and their protection as well. To have financially savvy, dependable, proficient, and naturally, benevolent answers for our energy needs—sun-oriented energy, a boundless type of sustainable

M. Kumar (✉)
Physics Department, SSNC, University of Delhi, New Delhi, India

L. Rana
Physics Department, Zakir Husain College, University of Delhi, New Delhi, India

A. Pattnaik
Department of Electrical & Electronics Engineering, ADGITM, New Delhi 110053, India

S. B. Krupanidhi et al. (eds.), *Advanced Functional Materials and Devices*, Springer Proceedings in Materials 14, https://doi.org/10.1007/978-981-16-5971-3_30

power source and can meet the developing energy needs of current civic establishments. Sun-based photovoltaic (PV) innovation is the most famous innovation. Sun-oriented cells have two points of interest and restrictions depending on their accessibility, activity, and guideline. Many generations of solar cells have been proposed since their exploitation. The productivity on a mechanical scale is roughly 12–15%, and consequently leaves a great deal of space for additional improvement [1]. The low effectiveness is due to related misfortunes, for example, range losses, reflection loss, transmission misfortune, region misfortune, assortment misfortune, opposition misfortune, and so forth. These misfortunes are represented by different laws of material science and the wise and creative employments of material, size, multi-intersection cells and range change are numerous ways, which can assume a significant job in limiting misfortune and thus expand the effectiveness of sun-oriented cells.

So this work centres around to what degree the new energy assets limit, energy wastage, and earth safe assets for dealing with the circumstance of expanded weight on characteristic assets and natural corruption for a capable humanized society.

2 Solar Cell and Associated Loss

Where the energy of the solar photon is equal to or greater than the bandgap of the material, it is absorbed into the material accompanied by excitation of an electron to the conduction band and creating a hole in the valence band. For a combination of p and n-type materials, a p–n junction is formed which allows only one type of carrier to pass through it, acting as a semipermeable membrane. In this way, three processes take place: electron-hole generation. Charge separation, Diffusion, and drift of carriers [2].

An ideal solar cell can be represented as a function of the series resistance, shunt resistance, temperature, and irradiation. The current I in the external circuit is written as [2]

$$I = I_0(e^{qV/KT} - 1) - I_L \tag{1}$$

where I_0 is the dark saturation current, V is the bias voltage, q is the charge of an electron, k is the Boltzmann's constant, and T is the temperature in K and I_L is the photocurrent. For the same irradiation and cell junction temperature, the generated output current is found to be a function of applied voltage. It involves various extreme value factors like short circuit current (I_{SC}) and open-circuit voltage (V_{OC}). The I_{SC} becomes negative of I_L for no applied voltage. It is because of the generation and collection of the light-generated carriers and signifies the maximum value of current drawn from the solar cell. To achieve maximum I_{SC}, there should be minimum transmission losses, minimum front surface reflection along the minimum surface, and bulk recombination. The open-circuit voltage V_{OC} takes value $\frac{kT}{q} \ln\left(\frac{I_L}{I_0} + 1\right)$

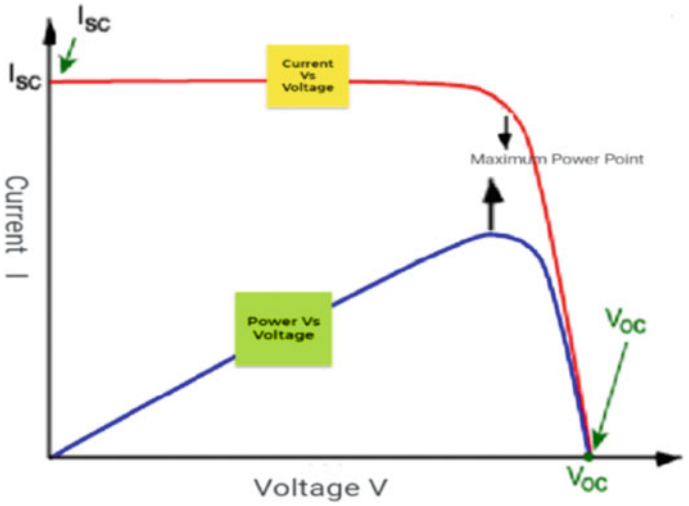

Fig. 1 IV characteristics of solar cells [11]

for no current drawn. It corresponds to the value of forwarding bias due to the biasing of solar cell junction with the light-generated photocurrent. To achieve maximum V_{oc} for the low value I, doping densities should be high along with low surface recombination velocities and large diffusion length (Fig. 1).

Both parameters I_{SC} and V_{oc} corresponding to the zero power value from the solar cell. A parameter Fill Factor is used, that is a product of maximum point value $V_{mp}I_{mp}$ to the value $V_{oc}I_{SC}$. It reflects the overall quality of solar cells. Graphically, it measures the "squareness" of the solar cell and is like a Carnot cycle in thermal physics. To achieve a high value of fill factor, shunt resistance should be high and the series resistance should be low, which causes less current dissipation as internal losses. Fill factor increases as the bandgap of the semiconductor increases and for a good solar cell, the efficiency (η) is determined as the fraction of incident power, converted to electricity that is [3]:

$$\eta = \frac{P_{\text{maximum}}}{P_{\text{incident}}} = \frac{V_{\text{oc}} I_{\text{sc}}}{P_{\text{incident}}} \tag{2}$$

Like Carnot engines, which depend on the source and sink parameters, solar cells in addition to the material property also depend on solar radiation. The solar radiation spectrum is very wise and every photon does not have energy equal to the band of absorber material. This leads to external and internal quantum efficiency limits of solar cells such as the Shockley–Quisser limit [4]. Various factors, such as temperature, spectral distribution, and resistive load influence the output power of the solar cells. The conversion efficiency of a solar cell gets affected by reflection, thermodynamics, charge carrier generation, and conduction.

Although the efficiency of solar cells has improved significantly with the continuous efforts of researchers, still a large gap exists between the experimentally achieved efficiency and the theoretically predicted limit. Improvement in the efficiency of solar cells even fractionally makes a lot of difference in the power generated per input cost and thereby makes solar power consumption more feasible.

3 Minimization of Solar Cell Losses

Numerous presumptions are related to the said limitation in the above segment to the pertinence of a wide range of solar cells. Even though there are various standards in progress to discover ways around such cut-off points, everything has scope for productivity upgrade of the sunlight-based cells available today. For this one needs to recollect that impediment on semiconductor material sun-powered cell, single p/n intersection per sun-oriented cell just thought daylight because of a "one sun" source and energy is changed over to warm from photons more prominent than the band hole. This records for just about lost two-third of energy [1]. The greater part of sun-powered energy gets changed over to warm, though some daylight is lost in neighbourhood recombination or reflected off the outside of the cell, infrared/microwave, and radio waves go through the sunlight-based cell and a few misfortunes because of electrical transportations.

The following few proposed modifications or strategies can help to obtain better efficiencies than the limit proposed by various principles in Sect. 1. All these do not violate these limits, but use discretization of energy.

3.1 Transmission Losses

Usually, the bandgap of a solar cell is fixed and the photons with energy higher than the bandgap of solar cell material get transmitted without being absorbed and such losses are termed as transmission losses [5]. This kind of loss can be reduced by using multiple channels for a collection like old rahat irrigation systems and farmers collecting efficiently maximum water for cultivation from a single water source. This situation is similar to maximum solar light collection from a single sun. The main difference here is the nature of the material collected, i.e., water and solar light. The underlying problem is due to the vast frequency range of the solar spectrum from ultraviolet to infrared and not having a single trapping material for different frequencies.

Moreover, much work [6, 7] has been done in this direction &and their light capture technique. This type of issue can be tackled up to a level through the use of multifunction cells or different material combinations. The different layers of cells have to fulfil various requirements for minimum light scattering and maximum energy utilization because of the law of conservation of energy.

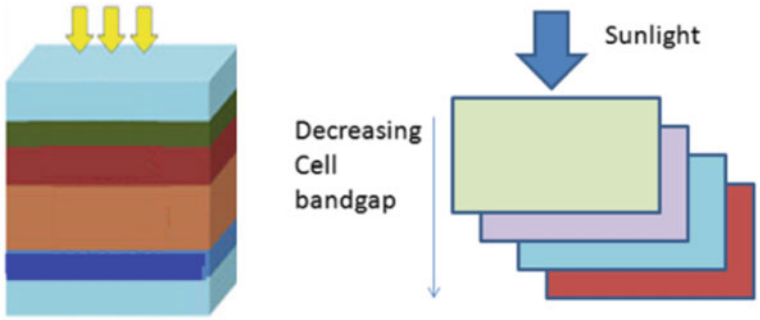

Fig. 2 Multiple P-N junction order

First, these layers shall have good ohmic contact for the charge extraction and facilitation of recombination of collected holes and electrons without any introduction of resistive losses. Secondly, layers must be optically transparent to avoid parasitic absorption of light. Lastly, these layers must have buffer layers to protect them and have sufficient barriers to penetration to prevent any re-dissolution of underlying layers [8] (Fig. 2).

So the use of multiple P-N junctions with different solar spectrum frequency tuned can resolve such issues to a vast extent. To optimize each section of the spectrum, band gaps are maintained nearly of the same width as their wavelength. The top layer is made very thin and highly transparent to longer wavelengths, which captures the shortest wavelengths. The junction between different layers allows the electrons to flow between the cells and it also separates the electric fields of the two cells.

Most of the present research focuses on Tandem solar-individual cells connected in series. The work contribution of Bremner [1], is remarkable in this direction. Through such methodology, solar cells can enhance efficiency to some extent.

3.2 Solar Cell Geometry

The quality and quantity of reflected and transmitted radiation depend on the angle of incident and medium. The angle of the incident indirectly depends on geometry. The incident angle should be minimum or equal to zero for a maximum amount of direct or diffuse radiation collection. Such solar tracking requires spherical trigonometry optimization such as tilt angle, zenith angle, azimuth angle tracking, etc. Such tracking is a mandatory process for focusing and many panels are also powering by tracking elements to generate more electricity. In perfect tracking, the surface azimuth should be equal to the solar azimuth angle and the tilt angle should be equal to the zenith angle [9]. In a reverse way, one can say that the geometry of the solar cell also affects sun tracking and light collection.

One can inspire from plant structures that absorb sunlight in all directions, which are difficult to interpret. The architectural design of a leaf in a given plant must provide margins to increase the efficiency of solar cells. The different leaves capture different amounts of sunlight depending on their thickness, geometry, and size. The photosynthesis light conversion efficiency of plants is found much higher than a solar cell. This suggests that some curve leaves like the geometry of a cell introduce some improvement in solar efficiency in contact with flat solar panels. A curved solar panel incorporating circular lens facets is a relatively simple and inexpensive optical concentration to increase solar efficiency, more power per unit of surface area. This curved solar has energy many times its normal intensity depending on its curvature. The flexible nature of cell geometry digs another nail to harness the sun's energy. A flexible substrate must be chosen such that the desired geometry will help in focussing sunlight to improve efficiency. All intensity-related deficiency can be tackled through some changes in the geometrical shape of solar cells because of thermodynamic limit as suggested by the work of Vital Borblik [10]. The work of Darren Quick gives another look at heat loss through the concept of PETE. The area of the surface, an area between two materials, etc. play is an important factor for efficiency calculation. The olive tree leaves like shapes optimize sunlight harvesting.

3.3 Thermalisation Loss

Sun is an ample source of energy and the earth receives around 174 petawatts of irradiation before entering the atmosphere. On entering the atmosphere sunlight gets absorbed as well as scattered by air molecules, the amount of absorption and scattering depends on the path travelled. The path travelled by radiations is least when the sun is overhead at a location and hence the scattering and absorption of radiations is minimum. On passing through the air mass there are different changes in radiations and hence the radiations are labelled at various positions. AM_0 is the radiation just before entering the atmosphere, AM_1 is the radiation reaching a point on earth when the sun is overhead. If the sun is not overhead, sunrays need to take an extra path before reaching a point and hence suffer extra absorption and scattering. For sun rays reaching at a point making an angle theta with the vertical, AM is given as [11]:

$$\mathrm{AM} = \frac{1}{\cos\theta} \tag{3}$$

Solar radiations reaching at the surface in units of W/m^2 for AM_0, AM_1, $AM_{1.5,}$ and AM_2 are 1376, 1105, 1000, and 894 respectively.

It is important to note here that when the radiations are maximum, absorption and scattering are minima and vice versa. So, when the sun is not overhead we have with us scattering and absorption of sun's energy in air molecules, which appear to us in the form of heat and wind. The discrepancy between the broad range of the solar

spectrum and the energy absorption of the cell bandgap leads to the non-absorption of photons radiation outside the bandgap. These interactions with the charge carrier result in the loss of incident energy through thermalization loss [12]. So radiation absorbers become heat emitters and further reduce conversion. The channelization of generated heat and its reuse can help to enhance the efficiency of solar cells.

Thermoelectric devices help in converting the temperature difference into electricity and it is also reversible, i.e., applied electricity can produce a temperature difference. This can be used for generated thermal energy conversion into electrical work otherwise it decreases cell efficiency [13]. Its reversibility principle can be used for applications, such as powering small temperature sensors and cooling mini-fridges. The various work of [10] thermionic converters are made using solar concentrations as their source of energy and using solar photon energy and heat. A process called PETE (Photon Enhanced Thermionic Emission) can harness this heat energy to increase the efficiency of solar cells, about 25% at 200 °C and higher efficiencies at higher temperatures [10]. Solar thermal efficiency is limited according to Carnot theorem and is given as:

$$T_\eta = 1 - \left(T_a / T_c\right)$$

where T_c is receiver temperature and T_a is ambient temperature (Fig. 3).

The ample heat energy can be harnessed using various techniques such as thermo-photovoltaic, thermoelectric, hot carrier cells, and thermionics as discussed in detail by Green in his report [7].

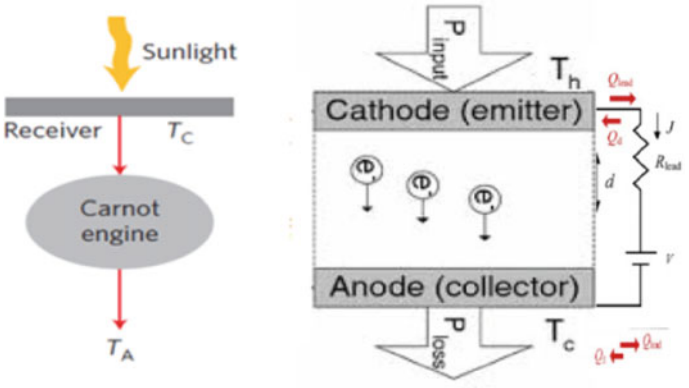

Fig. 3 Thermoelectric model of solar cell

3.4 Metal Coverage Loss

Some part of the cell is devoid of radiations because of metal contacts for the collection of charges on the top of the cell and termed as metal coverage losses. Such losses can be reduced by using transparent electrodes such as Indium tin oxide [14].

3.5 Losses Due to Lower Thickness

Thin film-based solar cells suffer from the disadvantage of smaller thickness as compared to bulk as the thickness of material required to absorb the radiations completely depends on the absorption coefficient of the photon of some specific energy and is given by:

$$d = 1/\alpha \tag{4}$$

where d is the thickness of absorbing material and α is the absorption coefficient of material for some specific energy of photon [15]. Absorption coefficients of specific materials can be improved if we go down to nano-dimensions and thereby reduce the minimum thickness required for the complete absorption of radiations [16, 17].

4 Synthesis of Losses to Gain Efficiency

The different possible solutions to energy losses of a solar cell under the illumination of the solar spectrum are described in the previous section. The laws of thermodynamics put some limits on such power conversion, but also leave some scope for improvement through multiple loss minimizations.

One such energy waste solution is due to the Tandem/Multijunction solar cell, which is a multilayer vast spectrum absorber and finds a single set of solutions to spectrum loss problems. Nature inspiration focuses on disorderly highly ordered small curved surface geometry like olive. So smaller, more elongated, small curved and multilayer cell geometry can capture more sunlight. These multilevel elongated shapes capture direct radiation and diffuse radiation. The introduction of thermionic converters helps in reducing thermalization losses and hence improving efficiency.

In this novel solar cell design, multilevel tandem cell junctions can be fabricated to drastically reduce transmission losses. The leaf-like structure and a thermionic generator thereby leading to enhanced sensitivity. To collect solar energy transparent electrodes of material such as indium tin oxide will be used to further improve the transparency of the top surface. On the top of the cell, the anti-reflective coating can be used to reduce reflection losses [18, 19]. This kind of texturing of the rear surface will not be required to achieve total internal reflection as the surface of flexible

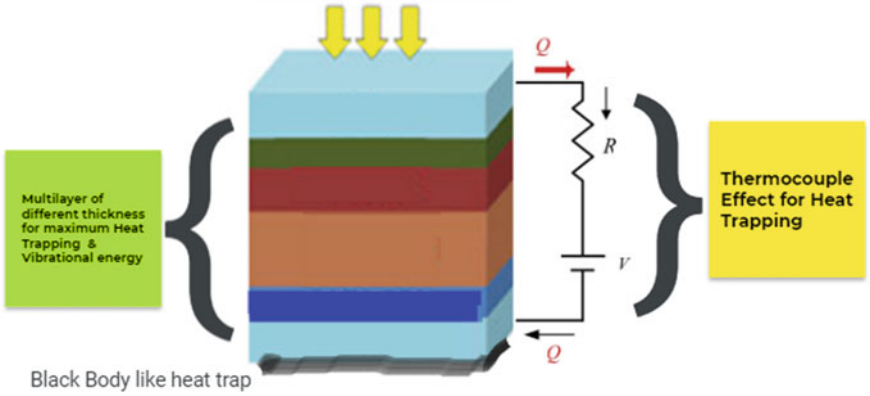

Fig. 4 Solar cell model

materials is already rough. Recombination losses can also be reduced by surface passivation using layers such as aluminium nitride. Using metal nanoparticles on the top of the solar cell improves the efficiency drastically as it will scatter the light in different directions due to the plasmonic effect [20]. Also, there are reports on multilayer thin film-based solar cells to increase efficiency [21–23].

Lastly, apart from the active energy from the sun, i.e., radiations which are used to generate electricity, the sun is the ample source of indirect energy such as wind and heat. The flexible nature of coated piezoelectric solar cells helps in harnessing wind energy throughout day and night [11]. The heat energy can be converted simultaneously into electric energy using the thermal energy of radiation. The heat traps can be used to trap the heat of radiation and can be connected to other cold electrodes to collect the charge generated. The various designs that can be employed are discussed in detail by green in his report [7]. The synchronization of solar energy with heat energy and wind energy supply a continuous supply of energy even at night or when the sun is covered with clouds [24].

Another sun-based cell configuration delineated in Fig. 4 is proposed to improve the proficiency of commercial solar cells utilized presently. This cell proposes solar cells to trap the greatest spectrum range, heat misfortune catching, better sun radiation inclination, and wind energy trap.

5 Results and Discussion

The combination of all these approaches not only minimizes the energy dissipation but also gives a multi-renewable energy harvesting option combination. Our proposed model uses various schools of thought like conversion of heat to usable energy, loss of spectrum by multijunction cells, and utilization of wind power, sun-associated energy. In this situation Eq. (1) becomes a function of thermal generated current I_T

and wind-generated current I_w in addition to PV cell generate current. It can be easily in phase such as generated power

$$I = I_0(e^{qV/KT} - 1) - I_L + I_T + I_w \tag{5}$$

The measure of extra created current I_T and I_w will be little in contrast with top hour PV produced current I. The wind delicate nature of the upper layer of cells helps in producing current even without light. This model depends on waste recovery which is in any case being squandered and going to debase our condition. The open-circuit voltage V_{OC} and I_{SC} continue as before. However, just some extra force is produced from the sun-oriented cell squander. Changed proficiency becomes:

$$\eta^1 = \frac{\text{modified}\, P_{\text{maximum}}}{P_{\text{incident}}} = \frac{V_{\text{oc}}(I_{\text{sc}} + I_{\text{sT}} + I_w)}{P_{\text{incident}}} > \eta \tag{6}$$

The synchronization of different generated currents can give us some significant value to solar cell output. The regeneration % still needs to explore, one thing sure here is that the fraction of output which is converted to electricity is going to increase. It is not only a step to save fossil fuels that are going to end very soon but also gives a way to save our environment that is going to degrade by using conventional fuel.

Acknowledgements The authors would like to acknowledge the guidance of Late Sh. Prof. Vinay Gupta for their valuable remarks. We dedicate this work to him and his research laboratory.

References

1. Capar S (2005) Photovoltaic power generation for polycrystalline solar cells and turning sunlight into electricity thesis. University of Gaziantep, Engineering Physics
2. Haverkort JEM, Garnett EC, Bakkers, EPAM (2018) Fundamentals of the nanowire solar cell: Optimization of the open circuit voltage. Applied Phy Rev 5:031106. https://doi.org/10.1063/1.5028049
3. Luque A, Hegedus S (Eds) (2011) Handbook of photovoltaic science and engineering. Wiley
4. Natarajan M, Srinivas T (2015) Study on solar geometry with tracking of collector. Appl Solar Energy 51:274–282
5. Pattnaik A, Jha S, Tomar M, Gupta V, Prasad B, Mondal S (2018) Improving the quantum efficiency of the monocrystalline silicon solar cell using erbium-doped zinc sulphide nanophosphor in downshift layer. Materials Res Exp 5(9):095014
6. Kumar M, Rana L, Kesari JP (2020) Flexible solar power tree—A Concept. Int J Engineering Appl Sciences Tech 5(2):217–221
7. Green MA, Bremner SP (2016) Energy conversion approaches and materials for high-efficiency photovoltaics. Nature Mat, 20 December. https://doi.org/10.1038/NMAT4676
8. Jain S, Paliwal A, Gupta V, Tomar M (2020) Plasmon-assisted crystalline silicon solar cell with tio 2 as anti-reflective coating. Plasmonics, 1–11
9. Kinsey GS, Hebert P, Barbour KE, Krut DD, Cotal HL, Sherif RA (2008) Concentrator multijunction solar cell characteristics under variable intensity and temperature. Prog Photovoltaics Res Appl 16(6):503–508

10. Quick D (2010) New process that harnesses heat energy could double efficiency of solar cells, August
11. Solanki CS (2015) Solar photovoltaics: fundamentals, technologies and applications. PHI Learning Pvt. Ltd.
12. Pattnaik A, Tomar M, Gupta V, Prasad B, Mondal S (2018) Optical study of zns nano spheres with varying amounts of ethylenediamine for photovoltaic application. Integr Ferroelectr 194(1):135–144
13. Hirst LC, Ekins-Daukes NJ (2011) Fundamental losses in solar cells. Prog Photovoltaics Res Appl 19(3):286–293
14. Roshko VY, Kosyachenko LA, Grushko EV (2011) Theoretical analysis of optical losses in cds/cdte solar cells. Acta Phys Pol A 120(5):954–956
15. Mcmeekin DP, Mahesh S, Noel NK, Klug MT, Lim J, Warby JH, Snaith HJ (2019) Solution-processed all-perovskite multi-junction solar cells. Joule 3(2):387–401
16. Atwater HA, Polman A (2011) Plasmonics for improved photovoltaic devices. In: Materials for sustainable energy: A collection of peer-reviewed research and review articles from Nature Publishing Group (pp 1–11)
17. Mehta BR, Kruis FE (2005) A graded diameter and oriented nanorod–thin film structure for solar cell application: a device proposal. Sol Energy Mater Sol Cells 85(1):107–113
18. Rühle S (2016) Tabulated values of the Shockley-Queisser limit for single junction solar cells. Sol Energy 130:139–147
19. Sharma S, Tomar M, Puri NK, Gupta V (2016) Bifeo3/batio3 Multilayer Structures for Solar Energy Harvesting Application. Energy Harvesting and Systems 3(3):237–243
20. Varlamov S, Rao J, Soderstrom T (2012) Polycrystalline silicon thin-film solar cells with plasmonic-enhanced light-trapping. J Visualized Exp 65:e4092
21. Bremner SP, Levy MY, Honsberg CB (2008) Analysis of tandem solar cell efficiencies under {AM1.5G} spectrum using a rapid flux calculation method. Progress in Photovoltaics: Res Appl 16:225–233 (2008)
22. Borblik V (2016) Effect of circular p-n junction curvature on the diode current density. J Electronic Mat 45(8):4117–4121. https://doi.org/10.1007/s11664-016-4597-z
23. Dhankhar M, Singh OP, Singh VN (2014) Physical principles of losses in thin film solar cells and efficiency enhancement methods. Renew Sustain Energy Rev 40:214–223
24. Gupta R, Rana L, Sharma A, Gupta V, Tomar M (2019) Fabrication of micro-cantilever and its theoretical validation for energy harvesting applications. Microsyst Technol 25(11):4249–4256

Development of La and Mo Co-Doped $SrTiO_3$ as Novel Anode Material for Solid Oxide Fuel Cell Applications

Saurabh Singh, Raghvendra Pandey, Onkar Nath Verma, and Prabhakar Singh

Abstract The structural, thermal and electrical attributes of co-doped $SrTiO_3$ system (La^{3+} at Sr-site and Mo^{6+} at Ti-site) were studied. The solid solution limit of La in $SrTiO_3$ and Mo in $La_{0.3}Sr_{0.7}Mo_xTi_{1-x}O_{3-\delta}$ was around 30 mol percent and 5 mol percent, respectively. Mo-doping in $La_{0.3}Sr_{0.7}TiO_{3-\delta}$ at 1000 °C resulted in improved crystallinity. The impure phase of Pyrochlore ($La_2Ti_2O_7$) and MoO_3 were resulted at a doping concentration of $x \geq 0.05$. As a result, the amount of Mo increases, the structural changes are observed. The electrical conductivity of co-doped $La_{0.3}Sr_{0.7}Mo_{0.05}Ti_{0.95}O_{3-\delta}$ was found to be 7.3×10^{-5} S.cm^{-1} at 700 °C in air, indicating its potential as an anode candidate for applications in solid oxide fuel cell (SOFC).

Keywords SOFC · Anode · $SrTiO_3$ · Co-doping · Impedance

1 Introduction

Solid oxide fuel cell is an electrochemical device, known as a converter of chemical energy to electrical energy. It has substantial benefits over conventional power-generating systems in terms of performance, stability, modularity, fuel flexibility and environmental impact due to the use of solid components [1]. Furthermore, SOFCs allow for cogeneration with gas turbines as a source of energy, allowing for full use of both power and heat, resulting in a 70% efficiency increase. Two porous electrodes

S. Singh (✉) · P. Singh
Department of Physics, Indian Institute of Technology (BHU) Varanasi, Varanasi 221005, India

S. Singh
Department of Physics, Teerthanker Mahaveer University, Moradabad, India

R. Pandey
Department of Physics, A.R.S.D. College, University of Delhi, Dhaula Kuan, New Delhi 110021, India

O. N. Verma
Department of Physics and Astronomical Sciences, Central University of Jammu, Jammu and Kashmir 181143, India

S. B. Krupanidhi et al. (eds.), *Advanced Functional Materials and Devices*, Springer Proceedings in Materials 14, https://doi.org/10.1007/978-981-16-5971-3_31

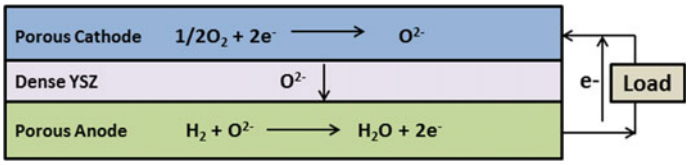

Fig. 1 A schematic sketch depicting the operation of a hydrogen-powered solid oxide fuel cell

(anode and cathode) are separated by a thick, oxygen-conducting electrolyte in a single SOFC cell. The working mechanism of SOFC cell is depicted in Fig. 1. On the cathode (air electrode), oxygen combines with the electrons to form oxygen ions, which then travel over the electrolyte. The incoming oxygen ions which are migrated through the electrolyte and reached anode (fuel electrode) where fuel is oxidised, the resultant electrons are released and move through an external electrical circuit [2]. Ionic current flow within the electrolyte balances the external circuit's charge flow.

More crucially, at the cathode/electrolyte contact, oxygen is dissociated and transformed to oxygen ions, whereas at the anode/electrolyte contact, fuel is electrochemically oxidised. According to the Nernst equation, the ideal voltage (E°) of a single cell in an open circuit has a voltage of around 1.0 V dc. The usable voltage output (V) is provided by Eq. (1) when it is loaded [2].

$$V = E^{\circ} - \mathrm{IR} - \eta_c - \eta_a \tag{1}$$

where I is the current running through the cell, R is the cell's electrical resistance and η_c and η_a the polarisation losses associated with the cathode and anode, respectively. Internal electrical resistance causes voltage loss, which includes contributions from electrodes and electrolytes, with the electrolyte accounting for the majority of the contribution due to its natural ionic conduction. To reduce IR leakage, it's becoming more common to make a dense, gas-tight electrolyte membrane, i.e. as thin as possible [3, 4]. The porous anode is a component of SOFC stacks that provides electrochemical reaction sites by fuel oxidation, a channel for electrons to be carried from the electrolyte/anode reaction sites to the interconnect and permits fuel and by products to be provided and removed from surface sites [5]. A component that links the anode of one cell to the cathode of another to boost the voltage output for practical usage is called an interconnect. In this work, we have studied the co-doping effect on $SrTiO_3$ based anode system.

2 Experimental

Strontium carbonate, $SrCO_3$, (>99%, Sigma Aldrich), Lanthanum oxide, La_2O_3, (99%, Sigma Aldrich), Molybdenum trioxide, MoO_3, (99.5%, Sigma Aldrich) and titanium dioxide, TiO_2, (99.5% Sigma Aldrich) were used to make polycrystalline

samples of $La_{0.30}Sr_{0.70}Mo_xTi_{1-x}O_{3-\delta}$ (x = 0.02, 0.05, 0.07, 0.10) abbreviated as LSMT2, LSMT5, LSMT7 and LSMT10 respectively. Powders were weighed in the requisite stoichiometric ratios and blended in ethanol with ZrO_2 media for 24 h by ball milling at 350 rpm [6]. The powders were ball milled before being calcined for 10 h at 1000 °C. To make pellets, the calcined powders were uniaxially pressed at a hydraulic pressure of 5 tons/m^3 (diameter 12 mm). The electrical conductivities of the LSMT pellets were tested after sintered at 1400 °C for 6 h in air.

3 Results and Discussion

Figure 2 shows a simultaneous DT/TGA plot of calcined powder for representative compositions with x = 0.02 in the LSMT system ($La_{0.3}Sr_{0.7}Mo_xTi_{1-x}O_{3-\delta}$) in the temperature range of 20 °C to 1000 °C. Similar patterns were obtained for other compositions. The DTA curve steadily grows with temperature up to the peak value of 560 °C due to the dissolution of metal nitrates and citric acid then begins to decrease in a parabolic manner with abrupt dips [7, 8]. The TGA curve depicts the sample disintegration in three stages, which is caused by the thermal change of water evaporation, organic species and metal nitrates [9, 10]. Single-phase perovskite-type LSMT crystallises with a weight loss of 2% after a rapid start and offsets breakdown between temperatures of 800–880 °C. There is no weight loss when the temperature exceeds 880 °C, implying that the ultimate product is developing or crystallising. As can be seen from the XRD results, calcined precursor powders at 1000 °C produce nicely crystalline of all compositions.

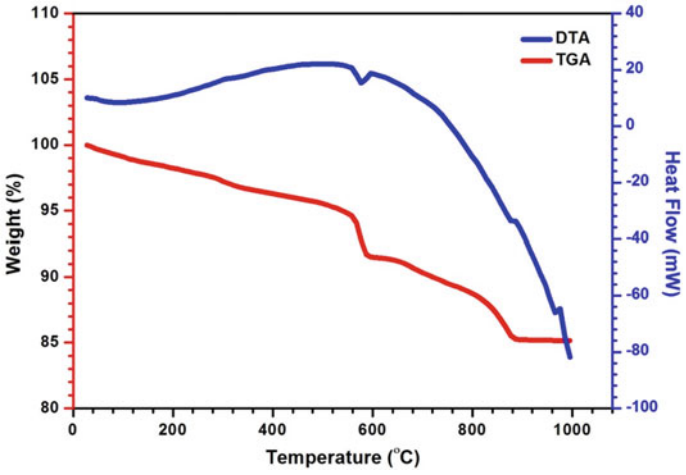

Fig. 2 Consecutive DT/TGA profile for LSMT2 system

The Powder XRD was performed at various phases of the synthesis and processing of prepared samples (e.g. as self-ignited ash, calcined and sintered). Mortar and pestle were used to grind the samples $La_{0.3}Sr_{0.7}Mo_xTi_{1-x}O_{3-\delta}$ (x = 0.02, 0.05, 0.07 and 0.10). The resulting powders were calcined and sintered pellets were reground to analyse powder X-ray diffraction patterns, which were recorded using an X-ray diffractometer (Rigaku, MiniFlex 600) with Cu-Kα radiation from 20° to 80° Bragg's angle (2θ). The cubic $SrTiO_3$ perovskite structure with the Pm $\bar{3}$ m space group can be indexed to all diffraction peaks (JCPDS Card Number: 86–0178). As shown in Fig. 3, the sample with x = 0.02 has a single perovskite structure, but the sample with x = 0.05 has a trace amount of pyrochlore phase ($La_2Ti_2O_7$) and the sample with x = 0.07 contains a minor impurity phase (MoO_3) in addition to the pyrochlore phase. However, as the Mo concentration increased, the XRD peak of the samples

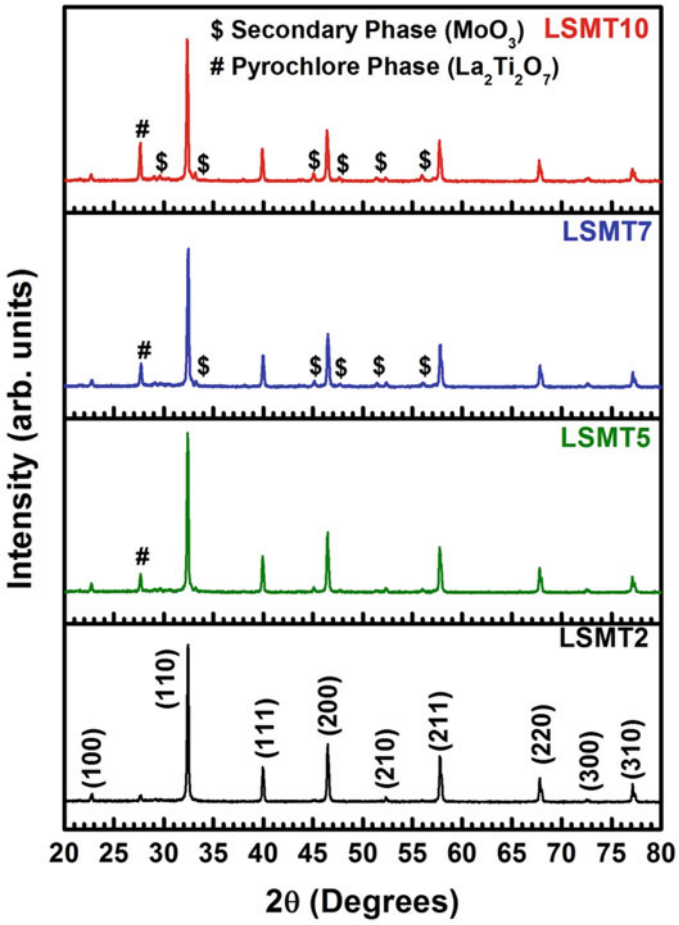

Fig. 3 X-ray diffraction pattern of LSMT series compositions

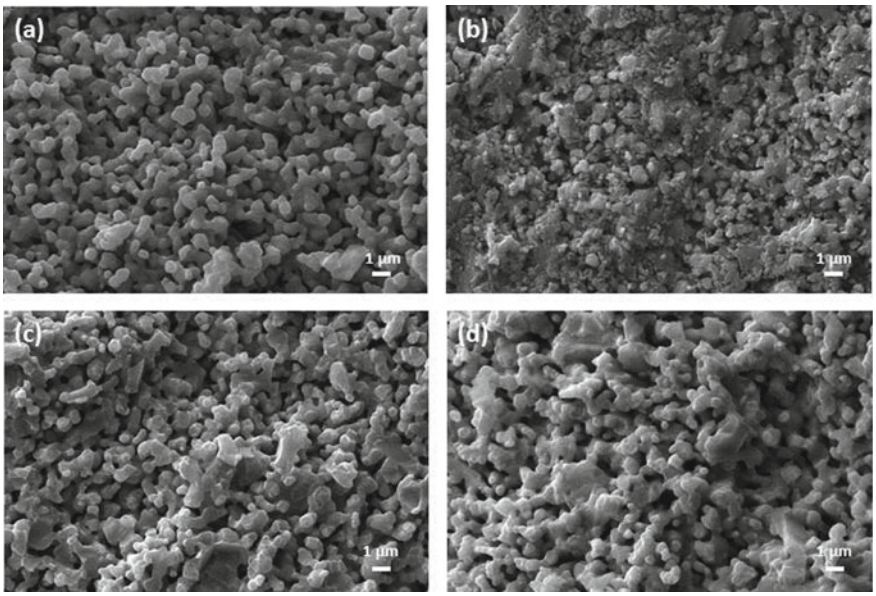

Fig. 4 The SEM micrographs of **a** LSMT2, **b** LSMT5, **c** LSMT7 and **d** LSMT10 fractured samples

($La_{0.3}Sr_{0.7}Mo_xTi_{1-x}O_{3-\delta}$) migrated to the left, indicating that the lattice parameter increased [11]. This is because the ionic radii of dopant element of La^{3+} (1.36 Å) are substantially bigger than the other dopant element of Mo^{6+} (0.590 Å). The ionic radii of Mo^{6+} (0.590 Å) is much smaller than Ti^{4+} (0.605 Å) and Ti^{3+} (0.670) [9, 12]. As a result, the redox coupling (Ti^{4+}/Ti^{3+}) renders the pyrochlore phase ($La_2Ti_2O_7$) and secondary phase (MoO_3) at high sintering temperatures [13, 14].

Scanning Electron Micrograph (SEM) pictures of shattered samples in Fig. 4 demonstrate the grain orientation and texture. It was discovered that as the Mo content increases, the porosity of the samples falls up to $x = 0.05$ and then increases. This suggests that Mo-doping may boost the samples sintering activity [15]. On the other hand, the sample $x = 0.05$ is less porous than the rest. Porosity indicates the presence of a triple phase barrier for electrochemical reactions [16].

Impedance spectroscopy is a powerful method for studying the electrochemical properties of materials. Electrical conductivity is measured in two different ways: dc conductivity (σ_{dc}) and ac conductivity (σ_{ac}) respectively. The dc conductivity of polycrystalline materials is based on a single dynamic response with frequency-independent behaviour. Conductivity measurements are often performed with a dc bias across materials that exhibit polarisation at the electrode/electrolyte contact [17]. Grain, grain boundary and electrode-specimen interface contributions provide the electrical conductivity relaxation in polycrystalline materials. In the case of electroceramics, frequency dependant conductivity spectra are divided into two dispersion regimes: a low frequency plateau (or frequency-independent regime) that represents dc conductivity and a high frequency (frequency-dependent dispersive) region that

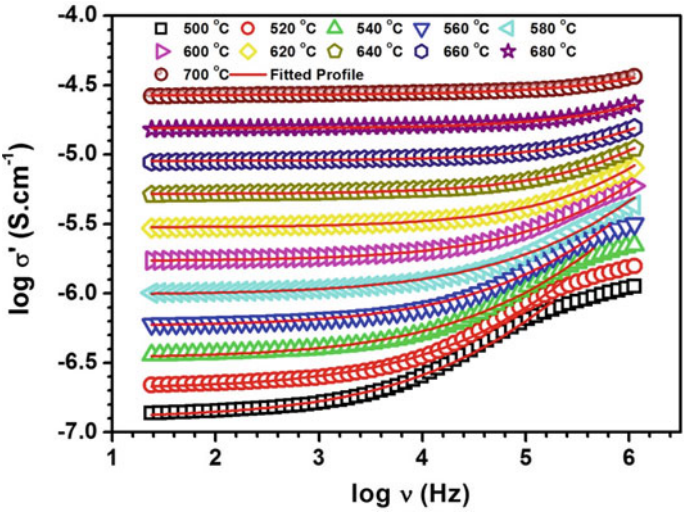

Fig. 5 The conductivity spectra of LSMT5 sample throughout a temperature range 500–700 °C with frequency regime 20 Hz to 1 MHz using Jonscher's power law

represents ac conductivity, as shown in Fig. 5. In the presence of electrode polarisation processes, both regions are attributed to the grain and grain boundary relaxation combined impact [18]. The system's dc conductivity (σ_{dc}) was calculated from the conductivity spectra of low frequency plateau and displayed in Arrhenius fashion, with a comparatively low value due to electrode polarisation dominating at low frequencies. The frequency-independent part, which is caused by the random motion of the mobile charge carriers and the frequency-dependent component (dispersion regime), which is generated by the hopping motion of the mobile charge carriers in grains and grain borders, are the two sections of the conduction process [19]. In most polycrystalline ceramic materials, the frequency-dependent real part of the conductivity spectra is given by

$$\sigma' = \sigma_{dc} + \sigma_{ac} \tag{2}$$

where the ac conductivity (σ_{ac}) can be written with general formula

$$\sigma_{ac}(v, T) = A(T).v^{n(T)} \tag{3}$$

where A is a constant and also depends on various factors. The real part of electrical conductivity σ' can be explained by Jonscher's power law.

$$\sigma' = \sigma_{dc}\left[1 + \left(\frac{v}{v_H}\right)^n\right] \tag{4}$$

where v_H parameter is the hopping frequency, v is the frequency and n is an exponent factor that is smaller than one. We can fit the conductivity spectra of the LSMT system using Eq. (4), as illustrated in Fig. 5. By fitting the conductivity spectra with Jonscher's power law, the values of σ_{dc}, v_H and n can be simply calculated.

The real part of the total conductivity and Jonscher's power law can be demonstrated by the Eqs. (2), (3) and (4) with the hopping frequency as given by:

$$v_H = \left(\frac{\sigma_{dc}}{A}\right)^{1/n} \tag{5}$$

In the conductivity spectra, it marks the commencement of conductivity dispersion. The Almond and West representation of Jonscher's power law is also known as Eq. (4) [20–22].

The total electrical conductivity was explored using complex plane impedance analysis and computed using observed parameters of conductance (G) and dielectric constant (D) using an impedance analyser in the range of 20 Hz to 1 MHz frequency. The following formula given by Eq. (6) can be used to compute the real component of the impedance Z' and the imaginary part of the impedance Z" [23].

$$Z' = \frac{D^2}{G(D^2+1)} \quad \text{and} \quad Z'' = \frac{Z'}{D} \tag{6}$$

In a Nyquist plot, three semi-circular depressed arcs may occur. In general, the arc passing through the origin corresponds to the grain contribution in the highest frequency range. The contribution of grain boundaries at intermediate frequencies is shown by the second arc, whereas the contribution of the electrode-specimen contact at low frequencies is shown by the third arc. The grains, grain boundaries and electrode-specimen contact contribute to the overall resistance in decreasing order of frequency when these arcs are intercepted on the real impedance axis [24, 25].

Figure 6 shows the complex impedance graphs (also known as Nyquist plots) for the LSMT system at various temperatures in air. At a higher temperature, it was observed that the sample has the lowest impedance. All other samples investigated show similar behaviour in the complex impedance graphs [26]. Among the samples, LSMT5 sample showed the highest conductivity (7.3×10^{-5} S.cm^{-1}) in air at the operating temperature, i.e. 700 °C as shown in Fig. 6b. The electrical conductivity of LSMT samples may also be calculated by the Eq. (7).

$$\sigma_t = \frac{1}{R_t} \cdot \frac{l}{S} \tag{7}$$

where σ_t is the total conductivity, l is the thickness of pellet and S is the surface area of the pellet. Due to the presence of secondary phase in high amounts, the conductivity of LSMT7 and LSMT10 samples diminishes.

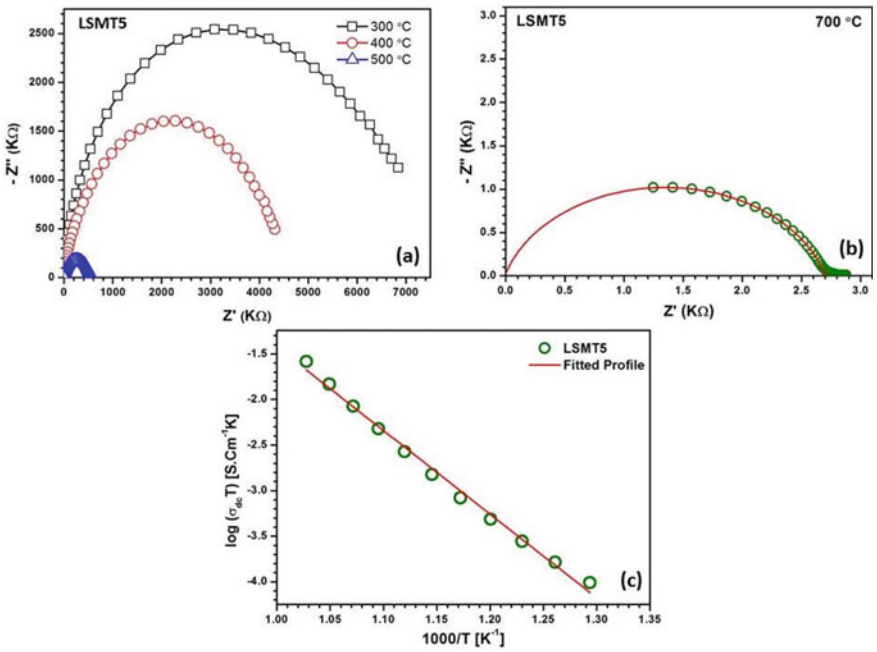

Fig. 6 Impedance spectra for LSMT5 sample **a** at various temperatures, **b** at 700 °C in air and **c** Arrehenius plot of the LSMT5 sample for activation energy

In air, the activation energy (E_a) for each regime was calculated using the Eq. (8) given below to investigate the mechanism of conductivity [27, 28].

$$\sigma = \frac{\sigma_{\mathrm{dc}}}{T} \cdot \exp\left(-\frac{E_a}{\mathrm{KT}}\right) \tag{8}$$

where σ_{dc} is a dc conductivity, E_a is the activation energy for conduction, k is the Boltzmann constant and T is an absolute temperature.

In Fig. 6c, the Arrhenius plot of log $\sigma_{dc}T$ *vs.* 1000/T was plotted for LSMT5 sample in air atmosphere. The activation energy of the LSMT5 sample was 1.82 eV, which was similar to the activation energy of the LSMT2 sample (1.84 eV), as shown in Table 1. Similar type of conduction behaviour of the samples was found in the temperature range of 300 ℃ - 700 ℃. The values of electrical conductivity at 700 °C in air and activation energy for the studied samples are listed in Table 1.

Table 1 Electrical conductivity and activation energy of the investigated samples

Cpmpositions	Activation energy E_a (eV)	Conductivity (σ, Scm^{-1}) at 700 °C
LSMT2	1.84	6.3×10^{-5}
LSMT5	1.82	7.3×10^{-5}
LSMT7	1.93	4.9×10^{-5}
LSMT10	2.17	2.7×10^{-5}

4 Conclusion

The increase in porosity with increasing Mo concentration was observed in SEM micrographs, all the samples (except LSMT5). The activation energy was determined using the slope of the Arrhenius plot. As a result, the value of activation energy for additional doping of Mo amounts reduces till $x \leq 0.05$. The variations in conductivity were found owing to the variation in the unit cell volume with increasing Mo substance in the composition $La_{0.3}Sr_{0.7}Mo_xTi_{1-x}O_{3-\delta}$. At higher doping concentration, a slight decrease in conductivity was found that may be due to increase in Mo^{6+} concentration which could be resulted an association of defects. Dopant concentration and composition can alter grain characteristics and grain boundaries. This has an impact on the effectiveness of dopants as well as the properties of grain boundaries, which may vary with grain size and density. However, the compositions of $La_{0.3}Sr_{0.7}Mo_xTi_{1-x}O_{3-\delta}$ system with $x = 0.02$ (i.e. LSMT2) and $x = 0.05$ (i.e. LSMT5) could be used as possible anode materials. On the basis of results, LSMT5 having the highest electrical conductivity (7.3×10^{-5} S.cm^{-1}) with sufficient porosity for triple phase boundary reaction. Therefore, LSMT5 may be used as a promising novel anode material for SOFC applications.

Acknowledgements The lab facilities generously provided by Department of Physics and the Central Instrument Facility Centre for XRD and SEM characterizations, at Indian Institute of Technology (BHU), Varanasi.

References

1. Minh NQ (1993) Ceramic fuel cells. J Am Ceram Soc 76(3):563–588
2. Williams MC (2011) "Fuel cells," in Fuel cells: technologies for fuel processing, Elsevier, pp 11–27
3. Tuller H (2017) "Ionic conduction and applications," pp 1–1
4. Lang M, Bohn C, Henke M, Schiller G, Willich C, Hauler F (2017) Understanding the current-voltage behavior of high temperature solid oxide fuel cell stacks. J Electrochem Soc 164(13):F1460–F1470
5. Bharadwaj SR, Varma S, Wani BN (2012) "Electroceramics for fuel cells, batteries and sensors," in Functional materials, Elsevier, pp 639–674

6. Singh S, Jha PA, Varma S, Singh P (2017) Large polaron hopping phenomenon in lanthanum doped strontium titanate. J Alloys Compd 704:707–716
7. Stucky A et al (2016) Isotope effect in superconducting n-doped $SrTiO_3$. Sci Rep 6(1):37582
8. Lu Z, Zhang H, Lei W, Sinclair DC, Reaney IM (2016) High-figure-of-merit thermoelectric La-Doped A-Site-Deficient $SrTiO_3$ ceramics. Chem Mater 28(3):925–935
9. Rocca A, Licciulli A, Politi M, Diso D (2012) Rare Earth-Doped $SrTiO_3$ perovskite formation from xerogels. ISRN Ceram 2012:1–6
10. Kim J, Duy LT, Lee SY, Ko M, Seo H (2020) Thermoelectric properties of Nb-doped $SrTiO_3$ films prepared by co-sputtering. J Asian Ceram Soc 8(4):1135–1146
11. Prasetya AD, Rifai M, Mujamilah, Miyamoto H (2020)"X-ray diffraction (XRD) profile analysis of pure ECAP-annealing nickel samples," J Phys Conf Ser 1436:012113
12. Zulueta YA, Lim TC, Dawson JA (2017) Defect clustering in rare-earth-doped $BaTiO_3$ and $SrTiO_3$ and Its influence on dopant incorporation. J Phys Chem C 121(42):23642–23648
13. Blennow P, Hagen A, Hansen K, Wallenberg L, Mogensen M (2008) Defect and electrical transport properties of Nb-doped $SrTiO_3$. Solid State Ionics 179(35–36):2047–2058
14. Shannon RD (1976) Revised effective ionic radii and systematic studies of interatomic distances in halides and chalcogenides. Acta Crystallogr Sect A 32(5):751–767
15. Kalem V (2016) Structural and electrical properties of $SrTiO_3$-modified $Bi_{0.5}(Na, K)_{0.5}TiO_3$ lead-free ceramics. J Mater Sci Mater Electron 27(8):8606–8612
16. Lu X et al (2017) Correlation between triple phase boundary and the microstructure of solid oxide fuel cell anodes: the role of composition, porosity and Ni densification. J Power Sources 365:210–219
17. Raghvendra, Singh P (2015) "Influence of Bi_2O_3 additive on the electrical conductivity of calcia stabilized zirconia solid electrolyte," J Eur Ceram Soc 35(5):1485–1493
18. Li X, Zhao H, Gao F, Zhu Z, Chen N, Shen W (2008) Synthesis and electrical properties of Co-doped $Y_{0.08}Sr_{0.92}TiO_{3-\delta}$ as a potential SOFC anode. Solid State Ionics 179(27–32):1588–1592
19. Satpathy SK, Mohanty NK, Behera AK, Behera B, Nayak P (2013) Electrical conductivity of Gd doped $BiFeO_3$-$PbZrO_3$ composite. Front Mater Sci 7(3):295–301
20. Almond D, Duncan G, West A (1983) The determination of hopping rates and carrier concentrations in ionic conductors by a new analysis of ac conductivity. Solid State Ionics 8(2):159–164
21. Almond D, West A (1983) Mobile ion concentrations in solid electrolytes from an analysis of a.c. conductivity. Solid State Ionics 9–10:277–282
22. Dwivedi RK, Kumar D, Parkash O (2001) Valence compensated perovskite oxide system $Ca_{1-x}La_xTi_{1-x}Cr_xO_3$ Part I Structure and dielectric behaviour. J Mater Sci 36(15):3641–3648
23. Jacob R, Nair H, Isac J (2015) Impedance spectroscopy and dielectric studies of nanocrystalline iron doped barium strontium titanate ceramics. Process. Appl. Ceram. 9(2):73–79
24. Singh S et al (2018) Structural and electrical conduction behaviour of yttrium doped strontium titanate: anode material for SOFC application. J Alloys Compd 748:637–644
25. Sen S, Choudhary RN, Pramanik P (2007) Structural and electrical properties of Ca^{2+}-modified PZT electroceramics. Phys B Condens Matter 387(1–2):56–62
26. Dhahri A, Dhahri E, Hlil EK (2018) Electrical conductivity and dielectric behaviour of nanocrystalline $La_{0.6}Gd_{0.1}Sr_{0.3}Mn_{0.75}Si_{0.25}O_3$. RSC Adv 8(17):9103–9111
27. Singh S et al (2019) Suitability of Sm^{3+}-substituted $SrTiO_3$ as anode materials for solid oxide fuel cells: a correlation between structural and electrical properties. Energies 12(21):4042
28. Li X, Zhao H, Xu N, Zhou X, Zhang C, Chen N (2009) Electrical conduction behavior of La, Co co-doped $SrTiO_3$ perovskite as anode material for solid oxide fuel cells. Int J Hydrogen Energy 34(15):6407–6414

Tailoring Surface Plasmons in Metal Nanoparticles

Hira Joshi

Abstract Surface plasmon resonance affects the optical properties of metal nanoparticles. The resonant wavelength, which is characteristic property of localised surface plasmon resonance, depends on dielectric function of the metal and also on size, shape, composition and external matrix of nanoparticle. Optical constants of metal nanoparticles are studied theoretically using different theories like Mie, Gans, EMGM and MEM. It is shown that size of nanoparticle shows its effect only in EMGM theory. Absorption spectrum is shown to be redshifted with increase in both size of nanoparticle and refractive index of external matrix. This redshift observed in the nanocomposites is supported using Mie's simulation and extended Maxwell–Garnet–Mie theory (EMGM). Redshift in resonant wavelength, due to change in external matrix, is utilised in sensors and in various devices.

Keywords SPR · Nanoparticles · EMGM · Gans

1 Introduction

Surface plasmons are collective and coherent oscillations of conduction electrons of metal nanoparticles. Localised surface plasmon resonance (LSPR) is the prominent property of noble metal nanoparticles in the vicinity of UV–Visible absorption spectrum [1, 2]. The amplitude, spectral location and width of the SPR band depend on the metal particle size, shape and concentration in the medium, respectively [3, 4]. The SPR is responsible for the enhancement of local electromagnetic field in the particles, which results in various applications such as SERS, sensing, imaging and amplification [5–10]. Also, strong redshift with broadening and damping of resonance band can be seen with the variation in refractive index of external medium [11]. This variation in refractive index can be achieved by different choice of matrices or subjecting the sample to external treatment that can modify the dielectric constant of the medium. Here, we have tailored surface plasmons with the help of size of nanoparticles (nps), their shape and the external matrix in which nps are placed.

H. Joshi (✉)
Department of Physics, Gargi College, University of Delhi, Delhi, India

S. B. Krupanidhi et al. (eds.), *Advanced Functional Materials and Devices*, Springer Proceedings in Materials 14, https://doi.org/10.1007/978-981-16-5971-3_32

Optical response of nanoparticles is studied, based on different theories, and has thereby theoretically shown the effect of physical parameters and external matrix on optical constants such as extinction coefficient of noble metal nps. Optical constants of different noble metals like Au and Ag are also compared.

2 Results and Discussion

According to Mie's theory [12], extinction coefficient (which is sum of absorption and scattering) in quasi-static limit ($2r << \lambda$, r is radius of the particle, and λ is the wavelength of light in medium), for spherical nanoparticles of volume, V, is

$$C_{\text{ext}} = \frac{9\omega(\varepsilon_{\text{M}})^{\frac{3}{2}} V\varepsilon_2}{C\left[(\varepsilon_1 + 2\varepsilon_{\text{M}})^2 + \varepsilon_2^2\right]} \tag{1}$$

$\varepsilon(\omega) = (\varepsilon_1 + \varepsilon_2)$, ε_1 and ε_2 are real and imaginary parts of dielectric function of the metal which is placed in a surrounding medium with dielectric constant, ε_{M}. ω is the angular frequency of the oscillating radiations.

3 Drude Model

Size dependence can be added in Drude model by assuming size-dependent material dielectric function $\varepsilon(\omega, r)$

$$\begin{aligned} \varepsilon(\omega, r) &= 1 - \omega_p^2/\left(\omega^2 + i\omega\Gamma\right) \\ \Gamma &= \Gamma_{\text{o}} + AV_f/r \end{aligned} \tag{2}$$

Here, Γ and Γ_{o} are phenomenological and bulk damping constants, respectively [13, 14].

$$\varepsilon(\omega, r) = 1 - \omega_p^2/\left(\omega^2 + i\omega\left(\Gamma_{\text{o}} + AV_f/r\right)\right] \tag{3}$$

$$\varepsilon(\omega) = \varepsilon_{\text{bulk}} - \varepsilon_{\text{D}}(\omega) + \varepsilon_{\text{D}}(r, \omega), \qquad D = \text{Drude}$$

$$\varepsilon_D(\omega) = \omega_p^2/\left(\omega^2 + i\omega\Gamma\right) \tag{4}$$

$$\varepsilon_D(r, \omega) = \omega_p^2/\left(\omega^2 + i\omega[\Gamma + AV_F/r]\right) \tag{5}$$

Modified dielectric functions according to EMGM theory [15]:

$$\mathrm{Re}\,\varepsilon_D(r,\omega) = \varepsilon_{\mathrm{bulk}} - {\omega_p}^2/\left(\omega^2 + \Gamma^2\right) + \omega_p^2/\left(\omega^2 + [\Gamma + AV_F/r]^2\right) \quad (6)$$

$$\mathrm{Im}\,\varepsilon_D(r,\omega) = {\omega_p}^2\Gamma/\left[\omega\left(\omega^2 + \Gamma^2\right)\right] + {\omega_p}^2[\Gamma + AV_F/r]/\left\{\omega\left(\omega^2 + [\Gamma + AV_F/r]^2\right\}\right. \quad (7)$$

Gans theory is used to account for shape dependence of nps in calculating extinction coefficient as this theory takes into account other shapes of nanoparticles than spherical, for example, nanorods [16].

Optical constants like extinction coefficient for noble metals [17–19] are calculated theoretically, using Mie's formalism for spherical nanoparticles. Dielectric constants data are taken from JC [18] and Sh [20] for Ag and Au, in case of Drude and Drude with size of np variation. To show effects on LSPR due to Gans and EMGM, data for different optical constants are taken from references [9, 10].

In Fig. 1, comparison of real and imaginary parts of permittivity of metal nanoparticles from different theories: Drude (D), Drude with size variation (Dr), EMGM (T), Sh [20] and JC [18] is shown. For ε_1, JC and Dr match exactly but not in ε_2.

In Fig. 2a is shown the variation of extinction spectrum in Ag for different sizes of nanoparticle (np) in Drude model. It is shown that extinction coefficient amplitude is varying with the size of nanoparticle but resonant wavelength remains constant. Figure (b) extinction spectrum in Ag nanoparticle (np) in EMGM for fixed external matrix having refractive index as 1.769 is having variation in amplitude and resonant wavelength. As size is increasing, both amplitude and resonant wavelength are redshifted.

Variation of extinction spectrum for different sizes of nanoparticle but for fixed external matrix is shown in Fig. 3. In Fig. 3a is shown size independence of resonant

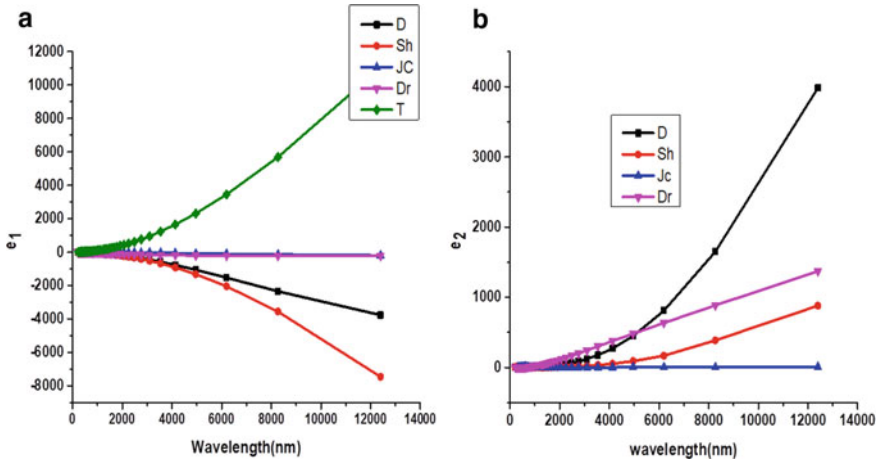

Fig. 1 Variation of dielectric constants from different theories for Ag. D—Drude, Dr—when r variation in Drude, T-MEM sh—Data from Shaista et al. [21], JC—Data from Johnson and Christy [20]

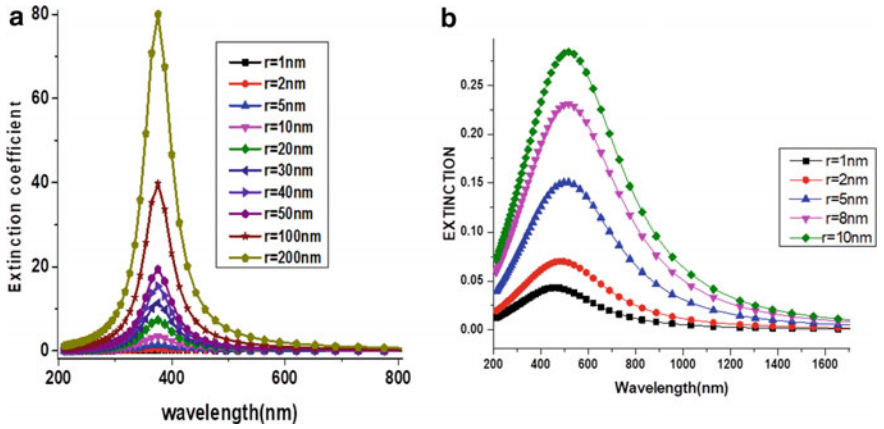

Fig. 2 Variation of extinction spectrum in Ag for different sizes of nanoparticle (np) in Drude model (**a**) and for EMGM in (**b**) for a fixed external matrix

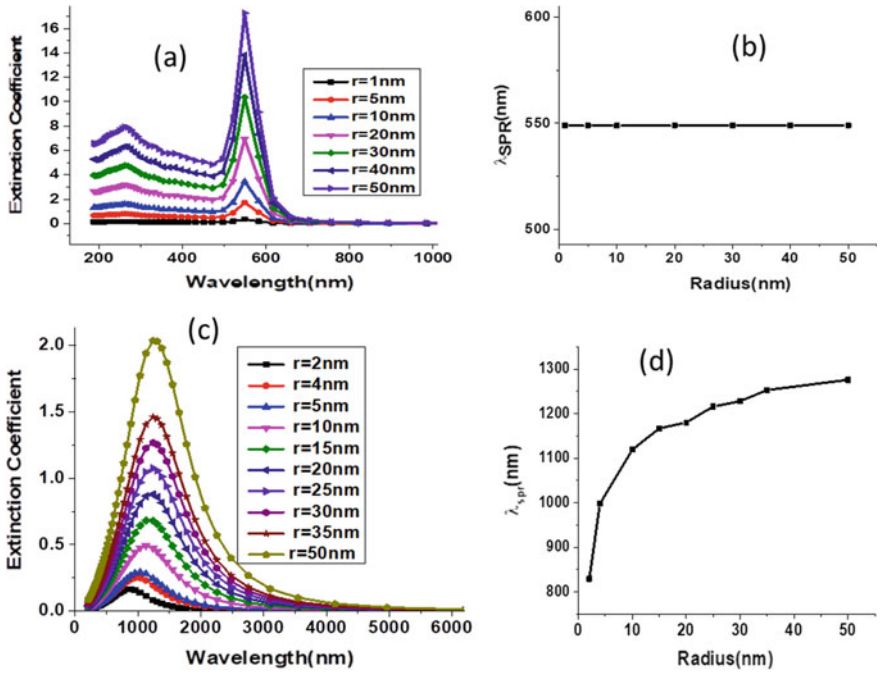

Fig. 3 **a** Variation of extinction spectrum in Au for different sizes of nanoparticle (np) in Drude model data JC and in (**c**) EMGM. **b** Resonant wavelength variation with size of nanoparticle for D and (**d**) for EMGM

wavelength according to Drude model. In Fig. 3c is shown the variation of extinction coefficient with size in EMGM. As the size of particle increases, the resonant wavelength and peak of extinction coefficient vary. Fig. 3b, d shows variation of resonant wavelength in LSPR with size of np. In Drude model, the wavelength is found to be independent of size of np, but in EMGM, resonant wavelength increases with size of np.

In Fig. 4 is shown the variation of extinction coefficient with refractive index of external matrix at fixed size (10 nm) of nanoparticle in Au. In (a), this variation is shown for Dr and in (c) for EMGM. In Dr, resonant wavelength increases with refractive index of external matrix but not systematically as in EMGM case. There is redshift in wavelength with refractive index in both cases which can be utilised in sensors. Figure 4b, d shows variation of resonant wavelength with external matrix refractive index showing smooth increase in EMGM as compared to Dr.

Figure 5 shows variation of absorptance for Au nanorod in (a) for different aspect ratio (length/width) when external medium is fixed. It is shown that when aspect ratio of Au nanobar is changed from 1 to 4, LSPR longitudinal mode shifts, while transverse mode does not show any shift. Figure (b) shows variation of absorptance with external medium for a fixed aspect ratio as 4. Data for dielectric constants are

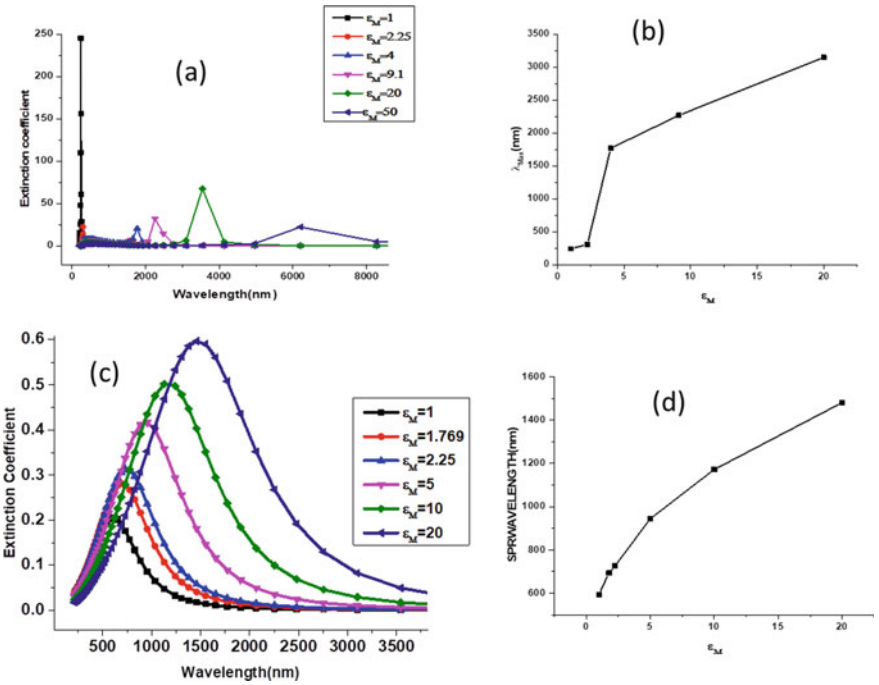

Fig. 4 Variation of extinction coefficient with different external media for fixed size 10 nm of Au nanoparticle in (**a**) Drude model (Dr) and in (**c**) EMGM. Variation of SPR wavelength with permittivity of external medium for fixed size of nanoparticle in (**b**) for Dr and in (**d**) EMGM

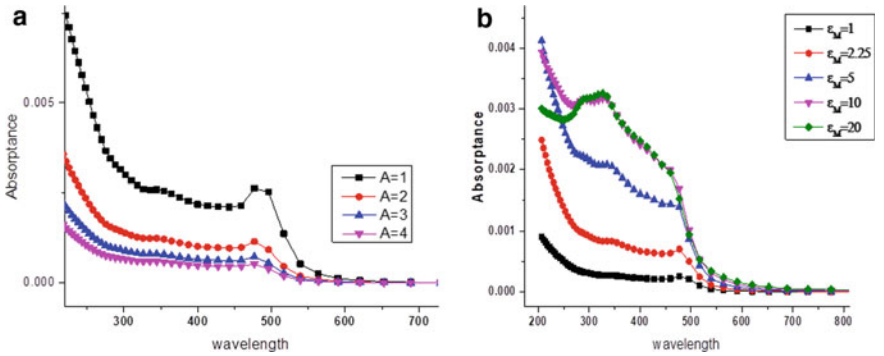

Fig. 5 **a** Variation of absorptance for different aspect ratios at a fixed value of external matrix as 1.77 for Au. **b** Variation of absorptance of Au as a function of external matrix at a fixed aspect ratio as 4

taken from JC [18]. It is shown that longitudinal mode wavelength changes with external medium of nanorod.

Effect of each size of np and external matrix is to increase the resonant wavelength in LSPR. Redshift in resonant wavelength, due to change in external matrix, is utilised in sensors and in various devices. It is shown that surface plasmons can be tailored by different physical parameters like size, shape, composition and external matrix around nanoparticles.

4 Conclusion

Surface plasmons can be controlled not only by physical parameters of nps but also with external matrix. By changing aspect ratio of nanorods, the resonant frequency can be tuned systematically. It is shown that LSPR is very sensitive to size, shape and external matrix. Thus, the optical properties of noble metals can be controlled over a given range of wavelengths by changing physical parameters. It is concluded, that modifications in physical parameters and external matrix affect surface plasmons in metal nanoparticles in a big way.

References

1. Walters G, Parkin IP (2009) The incorporation of noble metal nanoparticles into host matrix thin films: synthesis, characterisation and applications. J Mater Chem 19:574590
2. Wang J, Lau WM, Quan L (2005) Effects of Particle Size and spacing on the optical properties of gold nanocrystals in alumina. J Appl Phys 97:114303–114308
3. Coronado EA, Gc S (2003) Surface plasma broadening for nanoparticles. J Chem Phys 119(7):3926–3934

4. Lee KS, El-Sayyed MA (2006) Gold and silver nanoparticles in sensing and imaging: sensitivity of plasmon response to Size, shape, and metal Composition. J Phys Chem B 110:19220–19225
5. Aslan K, Lakowicz JR, Geddes CD (2005) Plasmon light scattering in biology and medicine: new sensing approaches, visions and perspectives. Curr Opin Chem Biol 9:538–544
6. Willets K, Van Duyne R (2007) Localized surface plasmon resonance spectroscopy and sensing. Annu Rev Phys Chem 58:267–297
7. Pinçon N, Palpanta B, Prot D, Charron E, Debrus S (2002) Third-order nonlinear optical response of Au: SiO_2 thin films: Influence of gold nanoparticle concentration and morphologic parameters. Eur Phys J D 19:395–402
8. Thomas S, Nair SK, Jamal EM, Al-Harthi SH, Varma MR, Anantharaman MR (2008) Size-dependent surface plasmon resonance in silver silica nanocomposites. Nanotechnology 19:075710-075717
9. Derkachova A, Kolwas K, Demchenko I (2016) Dielectric function for gold in plasmonics applications: size dependence of plasmon resonance frequencies and damping rates for nanospheres. Plasmonics 11:941–951
10. Kolwas K, Derkachova A (2010) Plasmonic abilities of gold and silver spherical nanoantennas in terms of size dependent multipolar resonance frequencies and plasmon damping rates. Opto−Electron Rev 18(4):429–437
11. Jain PK, Sayed MAE (2008) Noble metal nanoparticle pairs: effect of medium for for enhanced nanosensing. Nano Lett 8:4347–4352
12. Mie G (1908) Beitrage zur Optik truber Medien, speziell kolloidaler Metallosungen. Ann Phys 25(3):376–445
13. Kreibig U, Vollmer M (1995) Optical properties of metal clusters. Springer, Berlin Heidelberg New York
14. Jain K, Eustis S, El-Sayed M (2006) Optical properties of metal clusters (springer series in material science). J Phys Chem B 110:18243
15. Battie Y, Resano A-Garcia, Chaouli N, Zhang Y, Nacini A (2014) Extended Maxwell-Garnett-Mie formulation applied to size dispersion of metallic nanoparticles embedded in host liquid matrix. J Chem Phys 140:044705–044709
16. Eustis S, El-Sayed MA (2006) Determination of the aspect ratio statistical distribution of gold nanorods in solution from a theoretical fit of the observed inhomogeneously broadened longitudinal plasmon resonance absorption spectrum. J Appl Phys 100:044324–044328
17. Maaza M, Nemraoui O, Sella C, Beye AC (2005) Surface plasmon resonance tunability in Au−VO2 thermochromic. Nano-compos Gold Bull 38(3):100–106
18. Derkachova A, Kolwas K (2013) Simple analytic tool for spectral control of dipole plasmon resonance frequency for gold and silver nanoparticles. Photon Lett Poland 5(69–71):15
19. Bakhti S, Destouches N, Tishchenko AV (2015) Singular representation of plasmon resonance modes to optimize the near- and far-field properties of metal nanoparticles. Plasmonics:1–9, 16
20. Johnson PB, Christy RW (1972) Optical constants of noble metals. Phys Rev B 6:4370–4379
21. Baber S, Weaver JH (2015) Optical constants of Cu, Ag, Au revisited. Appl Opt 54(3):477–487